

# **Material Properties of Cerium Doped Yttrium Silicate ( $Y_2SiO_5: Ce^{3+}$ ) by Pulsed Laser Deposition Method for Display Applications**

By: Hagos Tsegay Haile

A thesis submitted for the fulfilment of the requirements for the degree of  
**PHILOSOPHIAE DOCTOR**

in the  
Faculty of Natural and Agricultural Sciences

Department of Physics

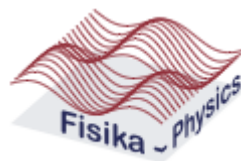
at the



University of the Free State

Republic of South Africa

Promoter: Prof. F.B. Dejene



November 2020

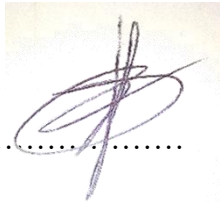
## Declaration

This research has not been previously accepted for any degree and is not being currently considered for any other degree at any other university. I declare that this thesis contains my own research work except where specifically acknowledged.

Name: Hagos Tsegay Haile

Student number: 2016444677

Signature: .....



03/03/2021  
Date: .....

## Approval

“**Material Properties of Cerium Doped Yttrium Silicate ( $Y_2SiO_5: Ce^{3+}$ ) by Pulsed Laser Deposition Method for Display Applications**”, a thesis prepared by Hagos Tsegay Haile for the degree, Doctor of Philosophy (PhD) in Physics, has been approved and accepted by the Thesis Committee for examination.

Promoter: Prof. F.B Dejene

.....

.....

Signature

Date

Subject Head:

.....

.....

Signature

Date

Dean of Faculty:

.....

.....

Signature

Date

## **Dedication**

This thesis is dedicated to my loving wife Rahwa Hagos, my daughter Arsemawit Hagos, my Son Ezana Hagos, and my Parents.

## **Acknowledgements**

First and foremost, I would like to thank my almighty God for keeping me safe, for his deepest love and guiding's. Thanks God, for all your blessings to my family, for the strength you give me each day and all the people who were around me in making my life more meaningful.

My special acknowledgement goes to my Promoter Prof. Francis B. Dejene for the opportunity he gave me to work with his research group. Thank you for your esteemed guidance, encouragement, invaluable help and fruitful recommendations throughout my whole studies. From his vast experience in the field of material science, his scholastic insights and remarks he has, I have learnt very important ideas and insight looking's which could help me in my future career. Moreover, the advice and motivation he was giving us as a group and individuals helps me to rely on my own way, makes me self-esteemed. I also thank him for securing my funds during my entire study period and allowing me to access the important research materials, measurement machines that allow me to complete my study successfully.

I would like to acknowledge the African Laser Centre (ALC), South Africa and the Ministry of science and higher education, Ethiopia for their financial support and their arrangements for the students' workshop with full material and technical support.

My in-depth appreciation goes to members of the department of physics, University of the Free State, for their assistance during my entire study. The administrative staff: Karen Cronje, Meiki Lebobo and Semakaleng for their support during my study. I would also like to thank the members of the UFS QwaQwa campus physics academic staffs Dr. K.G. Tshabalala, Dr. L.F. Koao, Dr. S.J. Motlounge, and Dr. R. Ocaya, for their continuous support during my period of study. I would like to thank Mr. Lucas Erasmus for his continuous assistance and support during pulsed laser deposition at University of the Free State (UFS), Bloemfontein. I would also like to express my gratitude to the UFS QwaQwa campus chemistry department for letting me use their equipment's in doing part of the characterization of my samples; Chelly Ann who helped me in the SEM/EDS measurement and Mr. Lee of Bloemfontein campus who helped me in carry out my SEM/EDS measurements. My appreciation also goes to Post Doc students: Dr. Fekadu Gashaw and Dr. Obi Echendu for their scholastic support and their meaningful discussions we had made in different points. I would like to express my sincere appreciation to Dr. Fekadu Gashaw for being a bridge for my PhD studies in opening the door, thank you very much. My appreciation and acknowledgement go to my Ethiopian Friends; Abebe Getachew, Megersa Kasim, Edris Taju, Solomon Zerihun and Desta Golja, thank you for your friendship, fruit full discussion we had in different aspects and love we have shared during our study. I got also a golden chance to introduce myself with other African Fellows: Dr.

Jatani Ungula, Dr. Winfred Mulwa, Sharon Kiprotich, Donald Hile, Michael Musembi, Dorah Kawira, Peter Korir and Munguti Lawrence, thank you for your useful academic and social supports. Especial appreciation and acknowledgement go to Peter Korir for his kind support and guidance he gave me when I was introducing myself to the PLD system. The support and love from my families gives me strong spirit, no feeling of loneliness and feels courage in my study. Thank you, all my lovely wife Rahwa Hagos, my lovely kids Arsemawit and Ezana Hagos for your continuous love and encouragement you feed me daily in my entire stay away from you, I'm very happy and lucky to have you. Thanks to my parents (Mami, father, sisters and brothers) for your prayer and love.

## Abstract

The thin film phosphor  $\text{Y}_2\text{SiO}_5:\text{Ce}^{3+}$  were deposited on the Si (100) substrates using 266 nm Nd: YAG pulsed laser. The conditions used for deposition were; substrate to target distance, substrate temperature, variable deposition gases, variable deposition pressure and variable deposition time to characterize the material properties on the thin films.

When the material characterises by varying the distance of the substrate from the target, the crystalline size was found to be 19.93 nm. A substantial reduction in thickness were observed as a function of increasing substrate to target distance. This attributes to the semicircular diffusion of the plasma plume due to the reduction of particle species flow over the deposition area of the substrate. In all deposition conditions, the PL emission has been observed in the blue region. This emission is attributed to the electronic transition of  $5d \rightarrow 4f$  in the  $\text{Ce}^{3+}$  orbitals. Where the excited state  $5d$  orbital further splits in to  $^2D_{3/2}$  and  $^2D_{5/2}$  closed states. The scanning electron microscopy (SEM) and atomic force microscopy (AFM) measurements has been observed with different textures which varies with deposition parameters. In all deposition conditions the particles have been observed spherical in shape. When the thin films are deposited by varying the temperature of the substrate, it was deposited at 150, 250, 350, 450 and 600 ° C to characterize the material properties of the thin films of  $\text{Y}_2\text{SiO}_5:\text{Ce}^{3+}$  at these deposition temperatures. The resulted material was structurally monoclinic with a prominent diffraction peak of  $29.2^\circ$ . An increment in surface thickness was observed from a deposition temperature of 150 to 450 ° C and began to decrease from 450 ° C to 600 ° C. The decrease in surface thickness ascribes to reduction in deposition rate. Similar emission and excitation were observed at 465 and 337 nm respectively which is in the same range with the thin films deposited at variable substrate to target distance. The maximum decay time has been observed at a deposition temperature of 450 °C. SEM images and EDS measurements show a significant change in morphology among each image and stoichiometric variations resulting from the change in substrate temperature respectively. When the films are deposited at different background gases (Vacuum, Nitrogen, Argon and Oxygen), a prominent peak at a diffraction peak of  $15.7^\circ$  were observed. The PL emission was also observed at the blue spectral region. The thin films show uniform distribution of grains with small agglomerated topographic areas. Maximum UV-VIS absorbance was observed at Argon depositions. The energy bandgap varies between 3.14 and 4.33 eV. The activation energy was obtained in the range of 0.1733 and 0.1938 eV. The maximum activation energy was obtained under the argon deposition.

The influence of oxygen deposition gases on the material properties of thin films at a deposition pressures of 1.5, 20, 40, 60 and 100 mTorr with substrate temperature of 250 °C was also investigated. The deposited material was structurally monoclinic with prominent diffraction peak of

28.9<sup>0</sup>. The Raman spectroscopy measurement also shows prominent emission intensity which could be resulted from the crystallized surface of the films. Spherical nano particles have been observed in all depositions. The surface roughness and agglomeration of the thin films have showed variation as a function of deposition pressures. The excitation and emission wavelengths were observed at 244 and 470 nm respectively. The average nanoparticles size varies between 25.71 to 40.4 nm. Maximum average activation energy of 0.438 eV was obtained at a deposition pressure of 1.5 mTorr. Moreover, the influence of deposition time on the structural, photoluminescence, morphological and optical properties of Y<sub>2</sub>SiO<sub>5</sub>:Ce<sup>3+</sup> thin films was also investigated at a deposition time of 30, 60, 90, 120 and 150 minutes. The deposited material was structurally end centered monoclinic with a prominent diffraction angle observed at 30.6<sup>0</sup>. Maximum crystallite size was observed at a deposition time of 60 minutes. The Rayleigh, stokes and anti-stokes scattering were observed at 536, 6.9 and 980 Cm<sup>-1</sup> respectively. The nanoparticles are uniformly distributed with a size of 0.2 to 0.4 μm. The calculated band gap from the deposition time of 90 and 120 minutes were 2.49 and 1.79 eV respectively. The excitation wavelengths were observed at 269 and 282 nm which ascribes to the two crystallographic sites of Ce<sup>3+</sup> and the emission wavelength was observed at 473 nm which might be due to the recombination probability of the excited Ce<sup>3+</sup> electrons from the excited state to the holes created in the ground state.

The phosphor powder was synthesised by combustion route by various molar concentration of TEOS. All the samples were annealed at a temperature of 800<sup>0</sup>C for about 4 hours. The average nanoparticle size from the TEM measurement was found to be 13.8 nm. High percentage of weight loss were observed at 0.014 M. The deionized water and residual organic materials were evaporated at 95<sup>0</sup>C and 600<sup>0</sup>C respectively. The excitation wavelength was observed at 220, 308 and 340 nm and a single emission wavelength has been observed at 483 nm. Maximum TL emission were observed at a TEOS concentration of 0.021 M. More over the maximum activation energy were observed at 0.014 and 0.015 M respectively which is related to the trap depth of the trapped electrons.



## Keywords

Y<sub>2</sub>SiO<sub>5</sub>:Ce<sup>3+</sup>, Pulsed laser deposition, thin films, photoluminescence, RE ions, electronic transition, phosphor, emission/excitation, morphology, decay time, atomic force microscopy, scanning electron microscopy, Grazing X-ray diffraction, thermoluminescence.

## Abbreviations

- PL- Photoluminescence
- CL – Cathodoluminescence
- TL-thermoluminescence
- TEM- Transmission electron microscopy
- TGA/DTGA-differential thermogravimetry
- CBD-chemical bath deposition
- CVD-chemical vapor deposition
- GIXRD-grazing incidence x-ray diffraction
- UV-Vis-ultraviolet visible spectroscopy
- XRD -X-ray diffraction
- SEM- Scanning electron microscopy
- EDS/EDXS -Energy dispersive spectroscopy
- PLD -Pulsed laser deposition
- AFM- Atomic force microscopy
- RE- RE
- VB-Valence band
- CB-Conduction band
- CIE-Commission International del'Eclairage
- RE- RE
- FWHM- Full Width at Half Maximum
- Ce<sup>3+</sup>-Trivalent cerium ion (dopant)
- JCPDS-Joint Committee on Powder Diffraction Standards

## List of Figures

Fig 2.1: schematic diagram of excitation and emission characteristics.....	2
Fig. 2.2: Schematic diagram of the TL process after the thermal activation of trapped charge carriers [29].....	5
Fig. 2.3 (a),(b)and (c) shows the ground and excited states of a molecule [35].....	7
Fig. 2.4: A spectrometer can be used to display the spectrum of a light source on a screen. ....	8
Fig. 2.5: Diagram of a discharge tube. ....	8
Fig. 2.6: Energy levels of hydrogen atom and various emission transitions [36]. ....	9
Fig. 2.7. Energy-level diagram of the mirror image of absorption and emission spectra [40].....	11
Fig. 2.8: Schematic diagram showing elements used to measure photoluminescence spectra[41].	11
Fig. 2.9: Representation of luminescence process: (a) activator (A) in a host (H) and (b) sensitizer (S) and activator (A) in a host (H)[43]. ....	12
Fig. 2.10: Major application of phosphors [6].....	13
Fig. 2.11a: schematic crystal structure of $Y_2SiO_5$ [60].....	15
Fig. 2.11b: schematic diagram shows the sites of Y in the complex crystal structure of $Y_2SiO_5$ ...	15
Fig. 2.12: Schematic illustration of (a) $SiO_4$ -tetrahedron and (b) $Y_1$ and $Y_2$ centred polyhedron in the structures of $Y_2SiO_5$ [61]. ....	16
Fig. 2.13: Angular dependence functions of d-orbitals [64].....	18
Fig. 2.14: Energy splitting of the five d orbitals for octahedral crystal field and the orbits of the free ion.....	19
Fig. 2.15(a) and (b): Crystal field splitting diagrams for high and low spin orbit .....	19
Fig. 2.16: Energy levels of the $4f^n$ configuration of the trivalent lanthanides(Dieke diagram)[65]. ....	21
Fig.2.17: Scheme and crystal field splitting of the $Ce^{3+}$ ion ( $4f^1$ )[67]. ....	23
Fig. 2.18: Schematic diagram of the splitting of RE energy levels due to the electrostatic, spin-orbit and crystal field interactions[6].....	25
Fig. 3.1: possible configuration of a PLD deposition chamber. ....	33
Fig. 3.2: Schematic diagram of crystalline and amorphous solids .....	39
Fig. 3.3: Schematic diagram of the X-ray diffractometer[98]. ....	39
Fig. 3.4: Characteristic X-ray radiations[99]. ....	40
Fig. 3.5: The geometry of Bragg's law[96]. ....	40
Fig. 3.6: Spectroscopic measurement apparatus[105]. ....	43
Fig. 3.7: Basic construction of spectrometer .....	44
Fig. 3.8. Schematic representation of the basic SEM components[112]. ....	46

Fig. 3.9. Different types of signals used by a SEM and the area from which they originate[113].	48
Fig. 3.10: schematic diagram of AFM setup[116].	49
Fig. 4.1: XRD pattern for phosphor thin film of $Y_2SiO_5:Ce^{3+}$	56
Fig. 4.2: Intensity and FWHM of the intense peak (022) as a function of substrate distance	57
Fig. 4.3: SEM micrograph of (a) $d= 4.0$ cm (b) $d= 5.0$ cm and (c) $d= 6.0$ cm respectively	58
Fig. 4.4: EDS spectrum for (a) $d = 4.0$ cm (b) $d = 5.0$ cm (c) $d = 6.0$ cm respectively	59
Fig. 4.5: The average roughness and Root mean square of the thin films measured by Gwyddion2.50 software [146].	60
Fig. 4.6: UV-VIS absorbance of $Y_2SiO_5:Ce^{3+}$ thin film	61
Fig.4.7: Excitation and emission bands of $Y_2SiO_5:Ce^{3+}$ thin film at 438 nm and 356 nm respectively	62
Fig. 4.8: Deconvoluted emission of $Y_2SiO_5:Ce^{3+}$ thin film at $d=5.0$ cm	63
Fig. 4.9: Energy diagram for the $Y_2SiO_5:Ce^{3+}$ thin film for the excitation and emission spectra's	64
Fig.4.10: (a) CIE coordination graph for all samples emitted at excitation wavelength of 356 nm (b) max PL emission for the corresponding excitation wavelengths.	65
Fig. 5.1: XRD pattern of the $Y_2SiO_5: Ce^{3+}$ phosphor thin films.	69
Fig. 5.2: SEM graphs of thin film phosphor at a substrate temperature of (a) $150^0$ C (b) $450^0$ C and (c) $600^0$ C	71
Fig. 5.3: EDS micrographs the thin film phosphor at a substrate temperature of (a) $150^0$ C (b) $450^0$ C and (c) $600^0$ C	72
Fig. 5.4: Elemental maps of the thin film phosphors at a substrate temperature of (a) $150^0$ C (b) $450^0$ C and (c) $600^0$ C	73
Fig. 5.5: Absorption graph of UV-Vis for the $Y_2SiO_5:C^{3+}$ thin film phosphors	74
Fig. 5.6: PL excitation graph probed with the emission peak at 465 nm	75
Fig. 5.7: PL emission spectra at an excitation of 337 nm	76
Fig. 5.8: decay curve for the $Y_2SiO_5: Ce^{3+}$ thin films	77
Fig. 5.9: CIE of the $Y_2SiO_5: Ce^{3+}$ thin film phosphor	78
Fig. 6. 1: XRD diffraction patterns for the $Y_2SiO_5: Ce^{3+}$ thin films deposited at different gases	83
Fig. 6.2: Effect of deposition gases on the crystallite size and FWHM of the $Y_2SiO_5: Ce^{3+}$ thin films	83
Fig. 6.3: SEM micrographs of $Y_2SiO_5:Ce^{3+}$ thin films deposited at different gases: (a) vacuum (b) nitrogen (c) argon and (d) oxygen	85
Fig. 6.4: Distribution of nanoparticles	85
Fig. 6.5: EDS spectra of the $Y_2SiO_5: Ce^{3+}$ thin films deposited at different background gases (a) Oxygen (b) Argon and (c) Nitrogen (d) powder	87

Fig. 6.6: Absorbance graphs of $Y_2SiO_5: Ce^{3+}$ thin films deposited at different deposition gases...	88
Fig. 6.7: Dependence of $(\alpha h\nu)^2$ on the photon energy ( $h\nu$ ) for $Y_2SiO_5: C^{3+}$ thin films deposited at different deposition gases. ....	89
Fig. 6.8: Excitation and emission spectra of $Y_2SiO_5: Ce^{3+}$ thin films .....	91
Fig. 6.9: Deconvoluted emission peak of $Y_2SiO_5: Ce^{3+}$ thin film for oxygen deposition .....	91
Fig. 6.10: The CIE chromaticity diagram for the $Y_2SiO_5: Ce^{3+}$ thin films excited at 370 nm .....	92
Fig. 6.11: Effect of deposition gases on TL intensities of $Y_2SiO_5:Ce^{3+}$ thin film phosphors .....	94
Fig.7.2 Effect of oxygen deposition pressure on the crystal size of the thin films.....	100
Fig. 7.3: Raman spectra of $Y_2SiO_5:Ce^{3+}$ thin films deposited at different oxygen pressure .....	102
Fig. 7.5: Distribution of nanoparticles (NPs) in diameter (nm).....	105
Fig. 7.6: Gaussian distribution of nanoparticles on the substrate .....	105
Fig. 7.7: EDS spectrum of $Y_2SiO_5:Ce^{3+}$ thin films for different oxygen deposition pressure: (a) 1.5mT, (b) 20mT (c) 60mT and (d) 100mT .....	106
Fig. 7.8: 2D and 3D AFM images of $Y_2SiO_5:Ce^{3+}$ thin films for different oxygen deposition pressures (a)1.5mT, (b) 20mT (c) 60mT and (d) 100mT .....	108
Fig. 7.9: UV-VIS for $Y_2SiO_5:Ce^{3+}$ thin films deposited at different oxygen pressure.....	109
Fig. 7.10: Excitation spectrum of $Y_2SiO_5:Ce^{3+}$ thin films for different Oxygen deposition pressures .....	110
Fig. 7.11: Emission spectrum of $Y_2SiO_5:Ce^{3+}$ thin films grown at different Oxygen deposition pressures. ....	111
Fig. 7.12: UV-irradiated TL glow curve of $Y_2SiO_5:Ce^{3+}$ thin films deposited at different oxygen pressures. ....	112
Fig. 8.1: GIXRD diffraction pattern of $Y_2SiO_5:Ce^{3+}$ thin films at different deposition time.....	117
Fig. 8.2: effect of deposition time on FWHM and crystallinity size .....	117
Fig. 8.3: Raman spectroscopy of $Y_2SiO_5:Ce^{3+}$ thin films deposited at different time.....	119
Fig. 8.4: SEM micro images for: (a) 30 minute (b) 60 minute (c) 90 minute and (d) 150 minutes .....	120
Fig. 8.5: Nano particles' distribution of $Y_2SiO_5:Ce^{3+}$ thin films in the mentioned deposition ....	120
Fig. 8.6: EDS spectrum for: (a) 30 minute (b) 60 minute (c) 90 minute and (d) 150 minutes.....	121
Fig. 8.7: UV-VIS absorption of thin films deposited at different time deposition.....	123
Fig. 8.8: Band gap of thin films deposited at a deposition time of 90 and 120 minutes .....	124
Fig. 8.9: Excitation spectrum of $Y_2SiO_5:Ce^{3+}$ thin films deposited at different time.....	125
Fig. 8.10: Emission spectrum of $Y_2SiO_5:Ce^{3+}$ thin films at different deposition time.....	126
Fig. 8.11: Energy Level diagram of $Ce^{3+}$ .....	126
Fig. 9.1: $Y_2SiO_5: Ce^{3+}$ combustion synthesis flow chart .....	129

Fig.9.2: TEM images of (a) 0.014 M (b) 0.015 M .....	130
Fig.9.3: particle distribution as a function of diameter (nm).....	131
Fig.9.4: DTGA and TGA graphs of $Y_2SiO_5:Ce^{3+}$ phosphor powders at various TEOS concentrations.....	132
Fig. 9.5: excitation graph for the $Y_2SiO_5:Ce^{3+}$ phosphor powder .....	133
Fig. 9.6: Emission graph for the $Y_2SiO_5:Ce^{3+}$ phosphor powder .....	134
Fig. 9.7: TL glow curve of the powder synthesized at different TEOS concentrations .....	134

## List of Tables

Table.2.1 various types of luminescence and their mode of excitation.....	2
Table 2.2: electronic and oxidation state of trivalent Rare-earth elements .....	23
Table 2.3: letter of symbols assigned to each value .....	24
Table2.4: Allowed and forbidden electron transitions types (free ion scheme).....	26
Table 3.1: deposition categories of thin films .....	28
Table 5.1: Results of the fitted decay curves for a different deposition temperature of $Y_2SiO_5: Ce^{3+}$ thin films.....	76
Table 6.1: observed atomic percent of the elements in the thin films and the Powder .....	86
Table 6.2: Estimated kinetic and trapping parameters obtained using glow peak shape in UV-irradiated (10minutes) $Y_2SiO_5:Ce^{3+}$ nano crystalline thin film .....	94
Table 6.3: Calculation of trap parameters and order of kinetics for UV-irradiated $Y_2SiO_5:Ce^{3+}$ thin film phosphor.....	95
Table 7.1: EDS weight and atomic percentage of the elements of the compound material ( $Y_2SiO_5:Ce^{3+}$ ) .....	104
Table 7.2: roughness average (Ra) and mean square roughness (Rq) for different deposition pressures .....	108
Table 7.3: kinetic and trapping parameters of the UV- irradiated $Y_2SiO_5:Ce^{3+}$ nano crystalline thin films .....	113
Table 7.4: Trap parameters and order of kinetics for UV-irradiated $Y_2SiO_5:Ce^{3+}$ thin film phosphors.....	113
Table 8.1: atomic percentage of individual elements in the compound .....	122
Table 9.1: kinetic and trapping parameters of the UV- irradiated $Y_2SiO_5:Ce^{3+}$ nano crystalline phosphor powders.....	135
Table 9.2: Trap parameters and order of kinetics for UV-irradiated $Y_2SiO_5:Ce^{3+}$ phosphor powders.....	136

## Table of contents

Declaration .....	ii
Approval .....	iii
Dedication.....	iv
Acknowledgements .....	v
Abstract.....	vii
Keywords.....	ix
Abbreviations .....	ix
List of Figures .....	x
List of Tables.....	xiv
Table of contents .....	xv
<b>Chapter 1: Introduction.....</b>	<b>1</b>
1.1 Background of the study .....	1
1.2 Statement of the problem.....	3
1.3 Research objectives .....	4
1.4 Thesis Layout .....	5
<b>Chapter 2: Theoretical Aspect .....</b>	<b>1</b>
2.1 Basics of luminescence.....	1
2.2 Thermoluminescence.....	3
2.3 Photoluminescence .....	5
2.3.1 Forms of photoluminescence.....	6
2.3.1.1 Resonant radiation .....	6
2.3.1.2 Fluorescence .....	6
2.3.1.3 Phosphorescence.....	6
2.4 structural and electronic properties of phosphor materials.....	11
2.4.1 Definition and major application of phosphors .....	11
2.4.2 properties of $Y_2SiO_5:Ce^{3+}$ Phosphor material.....	13
2.5 Crystal field theory (CFT) .....	16
2.6 Electronic Transition in Rare-Earth Metal Ions .....	20

2.7 The RE Ions (4f-5d and Charge-Transfer Transitions) .....	21
2.8 Optical transition of Ce <sup>3+</sup> ions .....	22
2.9 selection Rules .....	24
<b>Chapter 3: Thin film deposition methods, Characterization and measurement techniques</b> .....	<b>27</b>
3.1 introduction to thin film deposition methods .....	27
3.1.1. Chemical Vapour Deposition (CVD) .....	28
3.1.2. Plasma Enhanced CVD (PECVD) Method .....	29
3.1.3. Atomic Layer Deposition (ALD) Method .....	29
3.1.4. Sol-Gel Method .....	30
3.1.5. Molecular Beam Epitaxy (MBE).....	30
3.1.6. Sputtering.....	31
3.1.7. Thermal Evaporation Method.....	31
3.1.8. Electrohydrodynamic Deposition .....	32
3.1.10. Pulsed Laser Deposition (PLD).....	32
3.1.10.1 Laser ablation of the target material and creation of a plasma .....	33
3.1.10.2 Dynamic of the plasma .....	34
3.1.10.3 Deposition of the ablation material on the substrate .....	34
3.1.10.4 Nucleation and growth of the film on the substrate surface .....	35
3.1.10.5. advantage of PLD method: .....	36
3.1.10.6. Disadvantage of PLD method: .....	36
3.2 Introduction to Characterization and measurement techniques.....	37
3.2.1 X-ray diffraction (XRD).....	37
3.2.1.1. Bragg's law .....	40
3.2.2 Photoluminescence spectroscopy (PL) .....	41
3.2.3 Ultraviolet-Visible (UV-VIS) Spectroscopy .....	43
3.2.4. Scanning Electron Microscope (SEM) .....	45
3.2.5 Atomic Force Microscope (AFM) .....	48
3.2.6 Energy Dispersive X-ray Spectroscopy (EDS) .....	50
3.3 Experimental procedures .....	51



<b>Chapter 4: Effect of target to substrate distance on the material properties of the <math>\text{Y}_2\text{SiO}_5:\text{Ce}^{3+}</math> thin film by pulsed laser deposition</b> .....	53
4.1. Introduction .....	53
4.2. Results and discussions .....	55
4.2.1 XRD analyses .....	55
4.2.2 SEM and EDS analysis.....	57
4.2.3 UV-VIS analysis.....	60
4.2.4 Photoluminescence analysis .....	61
4.4. Conclusions .....	65
<b>Chapter 5: Effect of substrate temperature on the material properties of the <math>\text{Y}_2\text{SiO}_5:\text{Ce}^{3+}</math> thin film by pulsed laser deposition (PLD) method</b> .....	67
5.1 Introduction .....	67
5.2 Results and discussions .....	68
5.2.1 XRD analyses .....	68
5.2.2 SEM and EDX analysis .....	70
5.2.3 UV-VIS analysis.....	73
5.2.4 Photoluminescence analysis .....	74
Conclusions .....	79
<b>Chapter 6: The influence of deposition gases on the material properties of <math>\text{Y}_2\text{SiO}_5:\text{Ce}^{3+}</math> thin films deposited by pulsed laser deposition (PLD) method</b> ....	80
6.1 Introduction .....	80
6.2 Results and discussion .....	82
6.2.1 XRD analysis.....	82
6.2.2 SEM and EDS analysis.....	83
6.2.3 UV-Vis Analysis.....	87
6.2.4 Photoluminescence Analysis .....	89
6.2.5 Thermoluminescence analysis .....	92
Conclusion.....	95

<b>Chapter 7: Influence of oxygen deposition pressure on the structural, morphological, photoluminescence and thermoluminescence properties of <math>Y_2SiO_5:Ce^{3+}</math> by pulsed laser deposition method</b> .....	97
7.1 Introduction .....	97
7.2 Result and discussion.....	99
7.2.1 Xrd analysis .....	99
7.2.2 Raman spectroscopy Analysis .....	101
7.2.3 SEM and EDS Analysis.....	102
7.2.4 AFM Analysis.....	106
7.2.5 UV-VIS analysis.....	108
7.2.6 Photoluminescence analysis .....	109
7.2.7 Thermoluminescence Analysis.....	111
Conclusion.....	113
<b>Chapter 8: The influence of deposition time on the structural, photoluminescence, morphological and optical properties of <math>Y_2SiO_5:Ce^{3+}</math> thin films deposited by Pulsed Laser</b> .....	115
8.1 Introduction .....	115
8.2 Result and discussion.....	116
8.2.1 Xrd analysis .....	116
8.2.2 Raman spectroscopy analysis .....	118
8.2.3 SEM and EDS Analysis.....	119
8.2.4 UV-VIS analysis.....	122
8.2.5 Photoluminescence analysis .....	124
Conclusion.....	127
<b>Chapter 9: Synthesis and characterization of <math>Y_2SiO_5:Ce^{3+}</math> phosphor powder by combustion method</b> .....	128
9.1 Introduction .....	128
9.2 Experimental analysis.....	129
9.3 Result and discussion.....	130
9.3.1 TEM analysis.....	130

9.3.2 Thermal analysis.....	131
9.3.3 PL analysis.....	132
9.3.4 TL analysis .....	134
Conclusion .....	136
<b>Chapter 10: conclusion, future work and Recommendation .....</b>	<b>137</b>
10.1: Conclusion.....	137
10.2: Future work and Recommendations .....	138
<b>Publications .....</b>	<b>139</b>
<b>Conferences and Workshops.....</b>	<b>139</b>
<b>References .....</b>	<b>140</b>

## Chapter 1: Introduction

### 1.1 Background of the study

The RE ion doped materials have a crucial advantage in the optoelectrical applications which are widely applicable in the solid-state lasers, solid state lightings and light emitting diodes. Recently, large number of RE ions doped material have been invented for different applications. These materials have been shown dramatic improvements upon their application from time to time. Therefore, it is very interesting and advantageous to develop new phosphor materials with high luminescence efficiency and color saturations by doping or co-doping them with RE ions like Ce, Eu and Tb activators. Inorganic luminescent material which are also known as phosphors have been widely investigated for different applications and are used as display materials and currently widely used in high definition television (HDTV), plasma display panels (PDP), cathode ray tubes (CRT) and field emission displays (FED)[1].

Currently, there is an increasing interest in the production and application of nanostructured phosphor materials doped with lanthanide ions and transition metal ions [2]. Where transition metals ions are defined as “an element whose atom has a partially filled d sub-shell, or which can give rise to cations with an incomplete d sub-shell where many scientists describes “transition metal” as an element in d block, which includes groups 3 to 12 in the periodic table[3]. In actual practice, the lanthanide and actinide series of f-block are also considered as transition metals and are called “inner transition metals”.

The phosphor materials doped with RE ions have various optical properties necessary for a wide range of applications in our day-to-day life, specifically in optoelectronic components as compared to the corresponding bulk materials. Transition ions and RE metals belongs to the class of multifunctional luminescent materials when bombarded with some energy source. They show the emission of radiation and have crucial applications in CRT, screens (from scintillators, X-ray to plasma screens), laser materials, printing inks for money security, fluorescent pigments, solar cells, etc[4, 5]. Most of these materials are produced by doping the RE ions into the mono-structure crystals, phosphors, and ceramics for practical applications. As a result, the RE doped materials are becoming one of the favourable compounds in the field of optoelectronics application[6, 7]. The luminescence properties of the material are determined by the structural properties of the host material. Therefore, selecting a suitable host material leads to improved luminescence efficiencies. In general, a host material must possess high chemical durability and thermal stability for high temperature processes and be more chemically stable giving to the potential application. It has been reported that oxide-based phosphors satisfy these properties[8]. In addition, to reduce the possibility

of non-radiative recombination, a phosphor with low phonon energy is required. It is reported that non-radiative recombination reduces luminescence efficiency. The control of the composition of the host matrix by chemical modification, for example, doping with metal ions, also influences the chemical environment of the host and, therefore, the resulting luminescence properties. The introduction of dopants (impurities/activators) in the host generates defects or surface states that impact the bandgap. Doping induces oxygen vacancies that form electron trap centres, which helps to delay the decay of charge carriers, improves the property of visible light absorption and decreases the recombination rate of electron holes[9]. By controlling the concentration of dopant, it is possible to modify the luminescence of RE elements. In addition, the luminescence properties of the materials are also strongly associated with geometric factors such as shape, dimensionality, size, etc[10].

A phosphor is a material that emits light as a result of it absorbing energy. Hundreds of thousands of phosphors have been synthesized, each one having its own characteristic color of emission and period of time during which light is emitted after excitation ceases [7]. In some applications, such as FED, thin film phosphor materials are more advantageous than powders to reduce degassing problems and have high resolution and contrast. Therefore, the study of thin film phosphor materials is as important as powder phosphor materials. In addition, the luminescence properties of the materials are generally improving after nanoscale reduction[11]. Most phosphor materials are composed of a transparent microcrystalline host (or a matrix) and an activator. Where activator is a small amount which is intentionally added impurity, atoms distributed in the host crystal. Therefore, the luminescence processes of a phosphor can be divided into two parts: the processes mainly related to the host, and those that occur around and within the activator. The effective characterization of these RE-doped materials with regard to their stability, luminosity, efficiency in industrial application and also in the application of field emission detectors are important points to consider in order to obtain better results in the area of industrial applications [12]. The band gap of  $Y_2SiO_5$  is about 7.4 eV, which is a good host because of its capacity to accommodate substantial amount of the doped materials (the RE ions), and is successfully used as a host material for different RE ions due to its chemical and thermal stabilities for the formation of photo-cathodes or scintillating phosphors [13]. The development of nanoscience and nanotechnology has so far been possible by the success in the production of nanomaterials. The preparation of nanomaterials involves the control of the size, shape and structure of the materials. In recent years, nanoparticles of ceramic materials have been produced in large quantities through the use of physical and chemical techniques. The significant improvements in the preparation of nanomaterials, such as incandescent, ceramic and semiconductor, are due to the discovery of new synthesis techniques such as co-precipitation, sol-gel, pulsed laser deposition method, combustion method, etc. Nevertheless, it is

reported that PLD has many advantages over other thin film deposition techniques. PLD is a highly flexible thin film growth technique that has been successfully applied to a wide range of materials [14]. PLD is a simple but versatile experimental method that is used as a means to model a very diverse range of materials in a wide areas of thin film deposition and multilayer research. Superficially, at least, the technique is conceptually simple, but this apparent simplicity hides a fascinating and still incomplete understanding in the chemical and physical aspect of the deposited material. This general description tracks our current physical and chemical understanding of the evolution of the material from the target ablation to the deposited film, addressing the initial laser-objective interactions by which the solid material enters the gas phase, the processing and the propagation of the material in the plume of the ejected material and the eventual accommodation of gas phase species on the substrate to be coated.

In this thesis we have studied the material properties of  $Y_2SiO_5:Ce^{3+}$  thin films deposited by PLD method with different deposition conditions for a possible application in the display technologies. The material has been studied with the following conditions: the effect of substrate distance from the target material in argon background gases, the effect of substrate temperature on the material properties of  $Y_2SiO_5:Ce^{3+}$ , the influence of deposition gases on the material properties of  $Y_2SiO_5:Ce^{3+}$ , the influence of oxygen pressure on the structural, morphological and photoluminescence properties of  $Y_2SiO_5:Ce^{3+}$ , the influence of deposition time on the morphological, synthesis and characterization of  $Y_2SiO_5:Ce^{3+}$  phosphor powder ,photoluminescence and thermoluminescence properties of  $Y_2SiO_5:Ce^{3+}$  thin films.

The phosphors thin films were characterized by a variety of techniques such as, X-ray diffraction (XRD), Grazing incidence X-ray diffraction (GIXRD), Scanning Electron Microscopy (SEM), Transmission electron microscopy (TEM), Energy Dispersive x-ray Spectroscopy (EDXS), Photoluminescence Spectroscopy (PL), Ultra Violet-Visible (UV-VIS) spectroscopy, Thermoluminescence (TL), and Atomic Force Microscopy (AFM), and thermogravimetry (TGA) techniques.

## **1.2 Statement of the problem**

Nowadays the inorganic phosphor materials are the focus of research topics for display applications which can be effectively used into solid-state lightings like phosphor lamps, light-emitting diodes (LEDs), and high-efficiency display devices like FEDS and plasma display panels (PDPs). Obtaining thin film phosphor materials with efficient luminescence and large area deposited thin film phosphor are some of the challenges in the research, manufacturing and application processes especially when the films are preferred to develop by pulsed laser deposition methods. Researchers

and scientists will have to come up with ways that would help and overcome these challenges and enhance the luminescence properties of thin-film phosphors with different scientific approaches. The luminescence of the pulsed laser deposited phosphor thin films depends on a different factor that needs due attention. Some of the factors that we have given attention are the optimum distance between the target and the substrate temperature, the background gases, the fluence, and the laser energy; generally, the chemical and thermodynamics of the plume should be optimized to get phosphor thin films with efficient luminescence. The powder  $\text{Y}_2\text{SiO}_5:\text{Ce}^{3+}$  has investigated extensively with different deposition routes, but there are limited literature reports of this material by a pulsed laser deposition method. Because of the potential luminescence applications of  $\text{Y}_2\text{SiO}_5:\text{Ce}^{3+}$  material, we need to understand the chemical, physical properties of the deposition parameters on the material properties of the thin films for possible display application and possible ways of enhancing the luminescence properties by increasing the deposition areas are some of our concerns that we have tried to deal with.

### 1.3 Research objectives

The main objective of this study is:

- To investigate the effect of target-substrate distance on the material properties of the  $\text{Y}_2\text{SiO}_5:\text{Ce}^{3+}$  thin films
- To investigate the effect of substrate temperature on the material properties of the  $\text{Y}_2\text{SiO}_5:\text{Ce}^{3+}$  thin films
- To investigate the influence of oxygen deposition pressure on the material properties of  $\text{Y}_2\text{SiO}_5:\text{Ce}^{3+}$  thin films
- To investigate the influence of variable deposition gases on the material properties of  $\text{Y}_2\text{SiO}_5:\text{Ce}^{3+}$  thin films
- To investigate the effect of deposition time on the material properties of  $\text{Y}_2\text{SiO}_5:\text{Ce}^{3+}$  thin films
- To investigate the effect of heating rate on the Thermoluminescence properties of the  $\text{Y}_2\text{SiO}_5:\text{Ce}^{3+}$  thin films
- To Synthesize  $\text{Y}_2\text{SiO}_5:\text{Ce}^{3+}$  phosphor powder and characterizing it with different analyses

## 1.4 Thesis Layout

This thesis presents the material characterization of  $\text{Y}_2\text{SiO}_5:\text{Ce}^{3+}$  for a possible display application. This thesis is organised in three basic categories. The first three chapters deals with the background of the study, literature review, application, characterization technique of the material. The next six chapters deals with the data collection with different conditions for each manuscript, and analysis of the results. The last chapter deals with summary and future works. some of the points embedded and discussed in the respective chapters are presented as follow.

Chapter 1 deals with the general and specific objective of the study. It also introduces the brief background of the study. The next chapter deals with the theoretical aspect of the material and its applications'. The basics of luminescence, thermoluminescence, photoluminescence, the types of photoluminescence are discussed in detail. Moreover, the structural and electronic properties of  $\text{Y}_2\text{SiO}_5:\text{Ce}^{3+}$ , the crystal field theory (CFT), electronic transitions in RE metal ions, optical transition of  $\text{Ce}^{3+}$  and the selection rules are roughly explained. Chapter 3 is related to thin film deposition techniques in comparison to the deposition technique we have employed (PLD). More over the measurement/characterization techniques we have used in this study and their basic theoretical aspects have discussed in detail. The next six chapter presents the material study of  $\text{Y}_2\text{SiO}_5:\text{Ce}^{3+}$  with different deposition and synthesis conditions. The conditions used to study the material properties of  $\text{Y}_2\text{SiO}_5:\text{Ce}^{3+}$  are pointed as below.

- Target to substrate distance
- Variable substrate temperature
- Variable deposition gases
- Variable oxygen pressure and
- Variable deposition time respectively.
- Synthesis and characterization with variable TEOS moles

Chapter ten deals with the summary of the study and future work.



## Chapter 2: Theoretical Aspect

This chapter presents an overview of the theoretical aspects that are relevant to this work. These aspects include basic concepts of luminescence, photoluminescence, phosphor, structural and electronic properties of phosphor materials, CFT, RE ions, properties of trivalent RE ions, dieke diagram and the optical properties of  $\text{Ce}^{3+}$  ions are briefly discussed.

### 2.1 Basics of luminescence

Luminescence is the spontaneous emission of light by a substance that does not result from heat; or “cold light.” Therefore, it is a form of cold-body radiation. It can be caused by chemical reactions, electrical energy, subatomic movements or stress in a crystal. This distinguishes luminescence from incandescence, which is the light emitted by a substance as a result of heating. Historically, radioactivity was thought to be a form of “radio-luminescence,” although today it is considered separate, since it involves more than electromagnetic radiation[15, 16]. The dials, hands, scales and aviation signs and navigation instruments and marks are often coated with luminescent materials in a process known as “luminescence”[17]. Luminescence is an emission of ultraviolet, visible or infrared photons of an electronically excited species. The word luminescence comes from the Latin word (lumen = light) which was introduced in to the literature for the first time by Wiedemann in 1888, to describe “all these phenomena of light which are not only conditioned by the increase in temperature “ as opposed to incandescence. Luminescence is a cold light while incandescent is a warm light [18]. The doped materials or the activators are responsible for the luminescence. A luminescent material, also called a phosphor, is a solid which converts certain types of energy into electromagnetic radiation [19]. When you heat a solid to a temperature in excess of about 600 °C, it emits infrared radiation. This is thermal radiation (not luminescence). The electromagnetic radiation emitted by a luminescent material is usually in the visible range, but can also be in other spectral regions, such as the ultraviolet or infrared[20]. Luminescence is a collective term for different phenomena where a substance emits light without being strongly heated, i.e., the emission is not simply thermal radiation. The emission of light that does not derive energy from the temperature of the emitting body, as in phosphorescence, fluorescence, and bioluminescence. Luminescence is caused by chemical, biochemical, or crystallographic changes in the matrix of the host material, the motions of subatomic particles, or radiation-induced excitation of an atomic system[21]. Luminescence is the phenomenon in which all or part of the absorbed energy is re-emitted in the form of electromagnetic radiation in the visible or almost visible region of the spectrum. The luminescence involves at least two steps, the excitation of the electronic system of the material and the subsequent emission of photons as shown in Fig.2.1. An example of luminescence is the light

or brightness emitted by a luminous clock. The luminescence contrasts with incandescence, which is the production of light by heated materials.

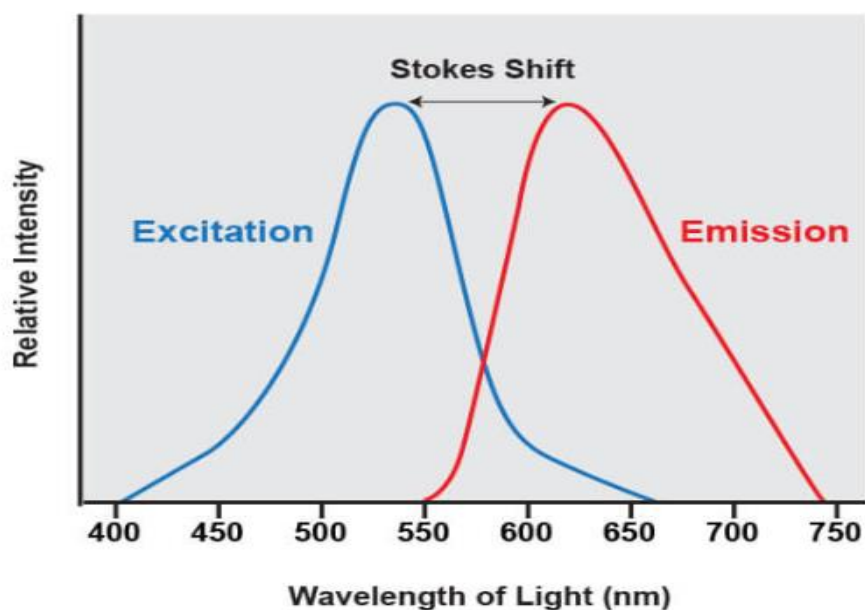


Fig 2.1: schematic diagram of excitation and emission characteristics

Luminescence can be excited by many types of energy. The various types of luminescence mechanisms and their corresponding mode of excitations is summarized in table 2.1

Table.2.1 various types of luminescence and their mode of excitation

Phenomenon	Mode of excitation
1. Photoluminescence (fluorescence, phosphorescence, delayed fluorescence)	Absorption of light (photons)
2. Radioluminescence	Ionizing radiation (X-rays, $\alpha$ , $\beta$ , $\gamma$ )
3. Cathodoluminescence	Cathode rays (electron beams)
4. Electroluminescence	Electric field
5. Thermoluminescence	Heating after prior storage of energy (e.g., radioactive irradiation)
6. Chemiluminescence	Chemical processes (e.g., oxidation)
7. Bioluminescence	Biochemical process
8. Triboluminescence	Frictional and electrostatic forces
9. Sonoluminescence	Ultrasounds

Stokes shift shown in Fig.2.1 is the difference (in energy, wavenumber or frequency units) between positions of the band maxima of the absorption and emission spectra (fluorescence and Raman being

two examples) of the same electronic transition[22]. When a system (either a molecule or an atom) absorbs a photon, it gains energy and enters an excited state. One way for the system to relax is to emit a photon, thus losing its energy (another method would be the loss of energy as heat). When the emitted photon has less energy than the absorbed photon, this difference in energy is the Stokes change. The Stokes shift is primarily the result of two phenomena: vibrational relaxation or dissipation and solvent reorganization.

## 2.2 Thermoluminescence

Thermoluminescence is a form of luminescence that is manifested by certain crystalline materials when energy previously absorbed by electromagnetic radiation or other ionizing radiation is re-emitted as light when the material is heated[23, 24]. The phenomenon is distinct from that of black body radiation. It is then a two-way street; it can either tell us how long a substance has been heated for the last time if we are making assumptions about the dosing rate, or it can tell us how much radiation has been captured in a given period. The “how long?” is useful to geologists and archaeologists; and the “how much” is important for physicians using radioactive treatment and for nuclear scientists and other personnel exposed to potentially dangerous radiation levels. The electron clouds that form around the crystal as a result of the interacting radiation cannot thermoluminescence by themselves. If the crystals were perfect, there would be no thermoluminescence. But the crystals have imperfections. They can have impurities in their system structures, just like the doping of “n” and “p” impurities in semiconductors. They may have mechanical structural defects. At higher temperatures, they can also present “statistical” defects, caused by thermal agitation. Some of these defects can capture a loose electron. These are called traps, and once an electron gets trapped, it is stuck there, at least for the time being. A trap that has caught an electron is called a filled trap. The greater the radiation dosage, the more electrons get knocked loose, and the greater the number of filled traps. Each trap can only supply so much holding energy to an electron. If we heat the material, the electrons can achieve enough additional thermal energy so that the trap releases the electron. Certain types of traps will also cause the electron to release its own excess energy in the form of light when the release temperature is reached. These traps produce thermoluminescence; they are also closely related to the mechanisms that determine the color of the substance. Once the electron has released its excess energy, it is free to once again get captured by an ion with a missing electron, removing the effect of the radiation dosage. Generally, energy from external radiation increases the energy of some internal electrons and breaks them loose, forming an electron cloud. Some of the electrons get trapped by crystal imperfections. Heating the crystal at a later time releases the extra kinetic energy stored in the trapped electrons and, for certain traps, the excess energy is liberated as light, thereby producing

thermoluminescence[25]. Some traps can very tenaciously hold onto an electron, while others can only retain one weakly. These are called high-energy and low-energy traps. There are usually many more low-energy traps. A slight temperature increase can empty a low-energy trap, while a large temperature increase is needed to empty a high-energy trap. When long, uniform dosage rates are being used, the equilibrium temperature is defined as that temperature at which thermal agitation is emptying the traps just as fast as incident radiation is filling them. In addition to dosimetric applications, thermoluminescence spectroscopy is a versatile tool for the study of defects in crystals and trapping phenomena at grain boundaries in nanostructures and soft materials. The glow curve TL represents the intensity of the light emitted as a function of the temperature; each light peak is associated with a recombination centre and linked to a specific trap. Activation energy and escape frequency factor are some of the parameters that can be calculated from the glow curve[26]. TL is an important technique for studying the nature and depth of traps in different types of solids[27, 28], and various methods can be used to calculate trap parameters according to the kinetic order of the glow peaks such as the initial rise method and the variable heating rates. A plot of thermoluminescence intensity versus temperature is known as a glow curve. Analysis of glow curves can provide quantitative information about trap levels. Most notably, one may use glow curve analysis to calculate the depth of the charge carrier traps. In a typical TL measurement, a sample is irradiated with high energy light for a period of time, which excites electrons from the valence band or dopant levels in the forbidden band toward the conduction band. The excited state is not stable, so after a certain time, the charge carriers recombine. A fraction of charge carriers can be trapped in a defect or impurity and cannot recombine with its counterpart. After the excitation is removed, the heater injects thermal energy into the system, providing trapped charge carriers with the energy necessary to escape from their traps. These released charge carriers can either recombine with their charge carrier counterpart in the luminescence centres, giving rise to TL emission, or be trapped in a deeper, higher energy trap. They have too much energy at this point to recover the same type of trap they just escaped or any shallower trap. The probability of trapping increases with increasing temperature. Fig. 2.2 presents a schematic diagram of the process of thermal stimulation and recombination of trapped charge carriers. TL emission intrinsically occurs at one or few luminescence centres. Thus, TL measurements provide a reliable method by which to record small luminescence intensities.

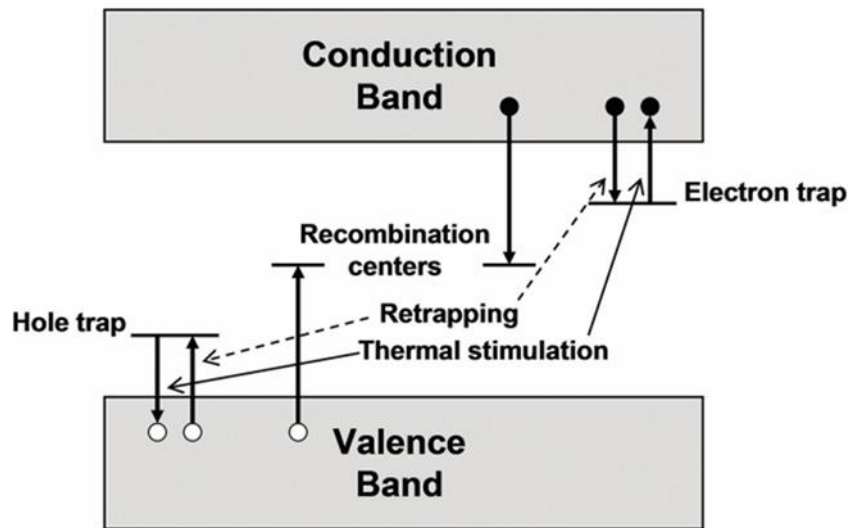


Fig. 2.2: Schematic diagram of the TL process after the thermal activation of trapped charge carriers [29].

### 2.3 Photoluminescence

Photoluminescence spectroscopy is a non-destructive characterization tool, most often used for the identification of shallow level, and sometimes deep level, impurities that produce radiative recombination. Photoluminescence spectroscopy is a non-contact and non-destructive method for probing the electronic structure of materials. The light is directed to a sample, where an excess of energy is absorbed and imparted to the material in a process called photoexcitation. One way in which energy can dissipate this excess energy is through the emission of light or luminescence. In the case of photoexcitation, this luminescence is called photoluminescence. Photoexcitation causes electrons within a material to move to permitted excited states. When these electrons return to their equilibrium states, excess energy is released and may include the emission of light (a radiative process) or not (a non-radioactive process). The energy of the emitted light (photoluminescence) is related to the difference in energy levels between the states of two electrons involved in the transition between the excited state and the equilibrium state. The amount of light emitted is related to the relative contribution of the radiative process [30]. The non-thermal luminescence of the radiative transitions of the electrically excited states (fluorescence and phosphorescence) can also be distinguished by the nature of the excited states. Fluorescence is produced from singlet excited states (S) and phosphorescence is produced from triple states (T) that have a different lifespan [31]. The type of excitation for luminescence determines the type of luminescence that takes place, for example, if the excitation comes from absorbed photons that result in radioactive recombination it is called photoluminescence and if it is obtained electronically through the p-n junction, it is a form of electroluminescence. When the photonic energy of the incident source is less than the difference

between two electronic states, these photons are not absorbed and the material is transparent to said radiation energy[32].

### **2.3.1 Forms of photoluminescence**

#### **2.3.1.1 Resonant radiation**

In resonant radiation, a photon of a particular wavelength is absorbed and an equivalent photon is immediately emitted, through which no significant internal energy transitions of the chemical substrate between absorption and emission are involved and the process is usually of an order of 10 nanoseconds. For an electron to make a transition from one energy level to a higher one, it needs to absorb a photon whose energy is equal to the difference in the energy levels involved. When jumping back down, it will emit a photon of that same energy. These discrete energy separations are characteristic of the atom involved, and it's what provides an atom with its fingerprint line spectrum[33].

#### **2.3.1.2 Fluorescence**

When the chemical substrate undergoes internal energy transitions before relaxing to its ground state by emitting photons, part of the absorbed energy is dissipated so that the emitted light photons are of lower energy than the absorbed ones. One of the most familiar phenomena is fluorescence, which has a short lifespan ( $10^{-8}$  to  $10^{-4}$  s). Fluorescence is the emission of light by a substance that has absorbed light or other electromagnetic radiation. It is a form of luminescence. In most cases, the emitted light has a longer wavelength and, therefore, a lower energy than the absorbed radiation. It is the emission of electromagnetic radiation, usually visible light, caused by the excitation of atoms in a material, which then emits again almost immediately (in about  $10^{-8}$  seconds). Initial excitation is usually caused by the absorption of energy from radiation or incident particles, such as X-rays or electrons[34].

#### **2.3.1.3 Phosphorescence**

Phosphorescence is a radiative transition, in which the absorbed energy experiences across between systems to a state with a different spin multiplicity. The lifespan of phosphorescence is usually  $10^{-4}$ - $10^{-2}$  s, much longer than that of fluorescence. Therefore, phosphorescence is even rarer than fluorescence, since a molecule in the triplet state has a good chance of undergoing a cross between systems to the fundamental state before phosphorescence can occur. The photoluminescence is divided into two categories: fluorescence and phosphorescence. A pair of electrons that occupy the same electronic ground state have opposite spins and are said to be in a singlet spin state as illustrated in Fig. 2.3 (a). After the absorption of an ultraviolet or visible photon, the valence electrons will be promoted from the fundamental state to an excited state. The electronic spin will

be preserved during this excitation process. But one of the electrons will go into an excited singlet state after the energy absorption of the incident photon as shown in Fig. 2.3 (b).

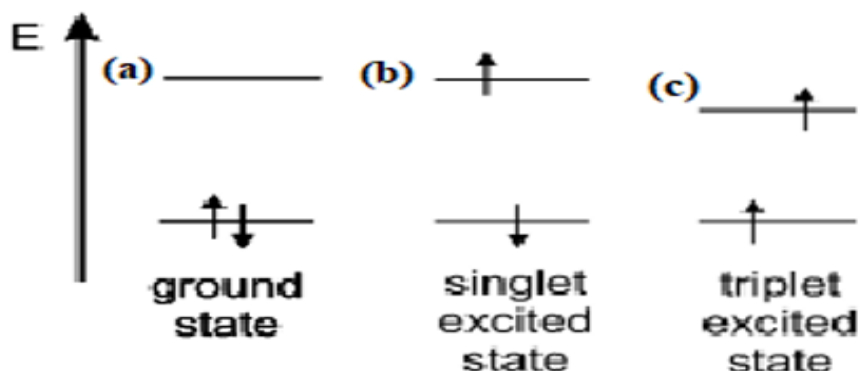


Fig. 2.3 (a),(b)and (c) shows the ground and excited states of a molecule [35].

In some cases, an electron in an excited singlet state is transformed into an excited triplet state as shown in Fig. 2.3 © in which its spin is no longer paired with the fundamental state. The emission between an excited triplet state and a fundamental singlet state or between two energy levels that differ in their respective spin states is called phosphorescence. Because the average lifespan of phosphorescence varies from  $10^{-4}$  to  $10^4$  s, phosphorescence may continue for some time after eliminating the source of excitation.

#### **Relation between absorption and emission spectra:**

Very diverse and fundamental knowledge about the nature of matter, such as the structure of atoms and molecules; the composition of distant stars; The identification of constituent atoms in a substance has been obtained from the analysis of the electromagnetic radiation emitted and absorbed by the substances. This information has often been obtained using spectroscopes or spectrometers. When light passes through a slit and a prism (or diffraction grating) it is divided into its component wavelengths as shown in Fig. 2.4. Each wavelength corresponds to a different color line.

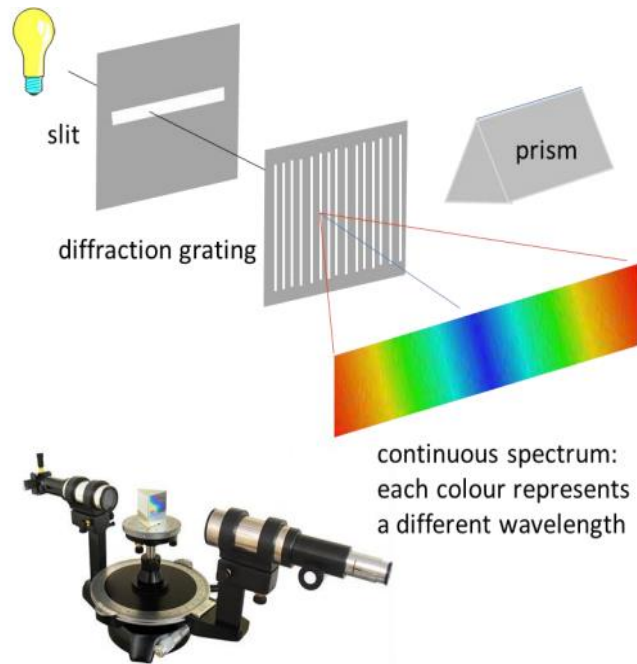


Fig. 2.4: A spectrometer can be used to display the spectrum of a light source on a screen.

The electrons surrounding the atomic nucleus are arranged in a series of levels of increasing energy. Each element has a unique number of electrons in a unique configuration. Therefore, each element has its own distinct set of energy levels. This arrangement of energy levels serves as the atom's unique fingerprint. In the early 1900s, scientists found that a liquid or solid heated to high temperatures would give off a broad range of colours of light. However, a gas heated to similar temperatures would emit light only at certain specific wavelengths (colours).

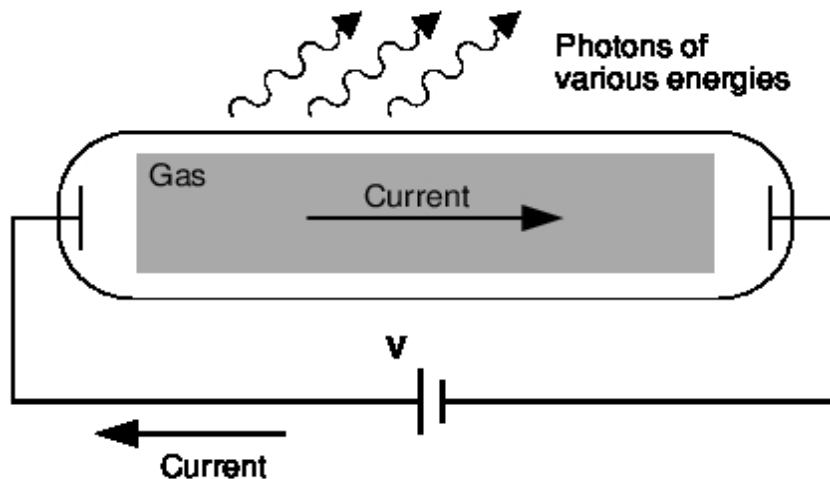


Fig. 2.5: Diagram of a discharge tube.

The tube is filled with a gas. When a high enough voltage is applied across the tube, the gas ionises and acts like a conductor, allowing a current to flow through the circuit. The current excites the atoms of the ionised gas. When the atoms fall back to their ground state, they emit photons to carry off the excess energy. A discharge tube (shown in Fig.2.5) is a glass tube filled with gas with a metal



plate on both ends. If a sufficiently large voltage difference is applied between the two metal plates, the gas atoms inside the tube will absorb enough energy to cause some of their electrons to release, that is, the gas atoms ionize. These electrons begin to move through the gas and create a current, which raises some electrons in other atoms to higher energy levels. Then, when the electrons in the atoms fall back, they emit electromagnetic radiation (light). The amount of light emitted at different wavelengths called the emission spectrum. When an electron in an atom falls from a higher energy level to a lower energy level, it emits a photon to carry extra energy. The energy of this photon is equal to the difference in energy between the two energy levels ( $\Delta E$ ).

$$\Delta E = E_f - E_i \dots\dots\dots 2.1$$

The frequency of a photon is related to its energy through the equation  $E = hf$ . Since a specific frequency of photons (or wavelength) gives us a specific color, we can see how each color line is associated with a specific transition.

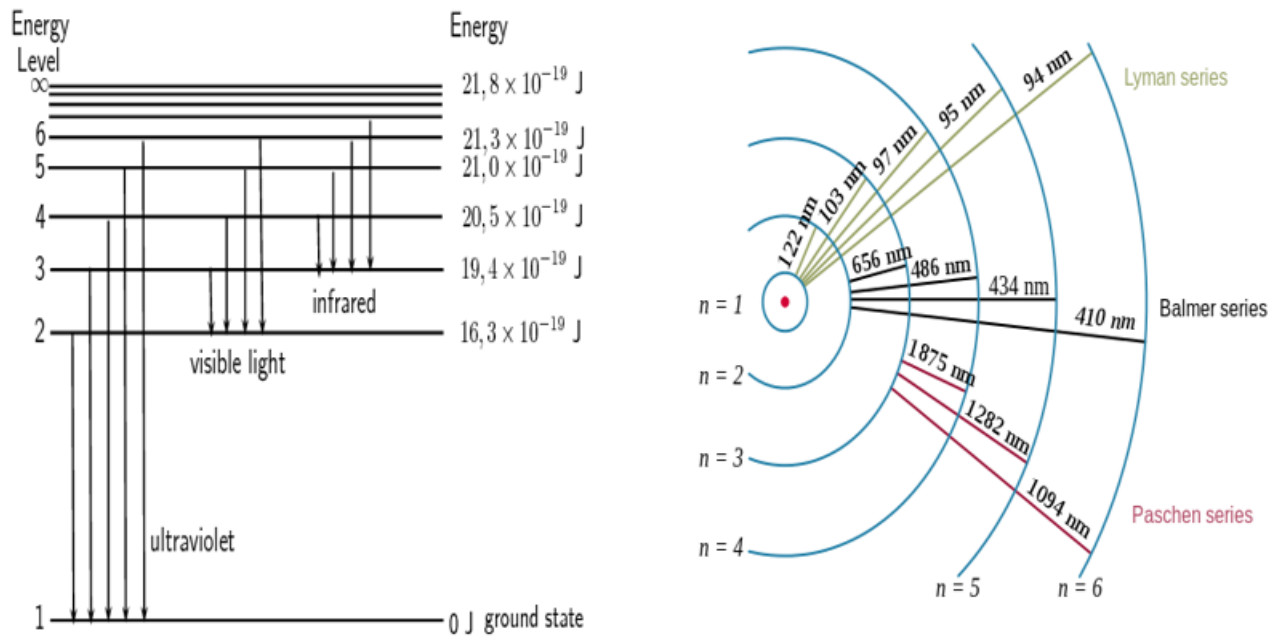


Fig. 2.6: Energy levels of hydrogen atom and various emission transitions [36].

The arrows in the diagram show the electron transitions from higher energy levels to lower energy levels. The energies of the emitted photons are the same as the energy difference between two energy levels. We can think of absorption as the opposite process. The arrows would point up and the electrons would jump to higher levels when they absorb a photon of the exact energy. The second representation, shows the wavelengths of the light that is emitted for the various transitions. Transitions are grouped into a series based on the lowest level involved in the transition. Visible light is not the only type of electromagnetic radiation emitted. More energetic or less energetic transitions can produce ultraviolet or infrared radiation. However, because each atom has its own

distinct set of energy levels (its fingerprint), Each atom has its own distinct emission spectrum. Atoms not only emit photons; They also absorb photons. If a photon hits an atom and the photon's energy is the same as the gap between two electron energy levels in the atom, then the electron at the lowest energy level can absorb the photon and jump to the highest energy level. If the photon's energy does not correspond to the difference between two energy levels, then the photon will not be absorbed (it can still be dispersed). If we have a photon source of various energies, we can obtain the absorption spectra for different materials. To obtain an absorption spectrum, just shine white light on a sample of the material that interests you. White light is formed by all the different wavelengths of visible light together. In the absorption spectrum, there will be gaps. The gaps correspond to energies (wavelengths) for which there is a corresponding difference in energy levels for the particular element. Absorbed photons appear as black lines because photons of these wavelengths have been absorbed and do not appear. Because of this, the absorption spectrum is the exact inverse of the emission spectrum[37]. The energy differences between levels in the Bohr model, and hence the wavelengths of emitted/absorbed photons, is given by the Rydberg formula[38].

$$\frac{1}{\lambda} = Z^2 R_{\infty} \left( \frac{1}{n_1^2} - \frac{1}{n_2^2} \right) \dots\dots\dots 2.2$$

Where Z is atomic number, n<sub>1</sub> and n<sub>2</sub> are the principal quantum number of the lower and upper energy level and R<sub>∞</sub> is the Rydberg constant (1.097\*10<sup>7</sup>m<sup>-1</sup>)[39]. Fluorescence and phosphorescence have a lower energy than absorption (excitation energy). As shown in Fig. 2.7, in absorption, the wavelength λ<sub>0</sub> corresponds to transition from the ground vibrational level of S<sub>0</sub> to the lowest vibrational level of S<sub>1</sub>. After absorption, the vibrating excited of S<sub>1</sub> molecule relaxes again at the lowest vibrational level of S<sub>1</sub> before emitting any radiation. The highest energy transition occurs at the λ<sub>0</sub> wavelength, with a series of peaks that follow a longer wavelength. The absorption and emission spectra will have an approximate mirror image ratio if the spaces between the vibrational levels are approximately equal and if the transition probabilities are similar. As we can see in Fig. 2.7, a molecule that absorbs radiation is initially in its electronic ground state, S<sub>0</sub>. Since the electronic transition is faster than the vibrational movement of atoms, when radiation is absorbed first, the excited molecule S<sub>1</sub> still has its S<sub>0</sub> geometry. Shortly after the excitation, the geometry changes to its most favourable values for the S<sub>1</sub> state. This rearrangement reduces the energy of the excited molecule. When the S<sub>1</sub> molecule fluoresces, it returns to the S<sub>0</sub> state with S<sub>1</sub> geometry. This unstable configuration must have greater energy than that of an S<sub>0</sub> molecule with S<sub>0</sub> geometry. The net effect in Fig. 2.7 is that the emission energy λ<sub>0</sub> is less than the excitation energy λ<sub>0</sub>.

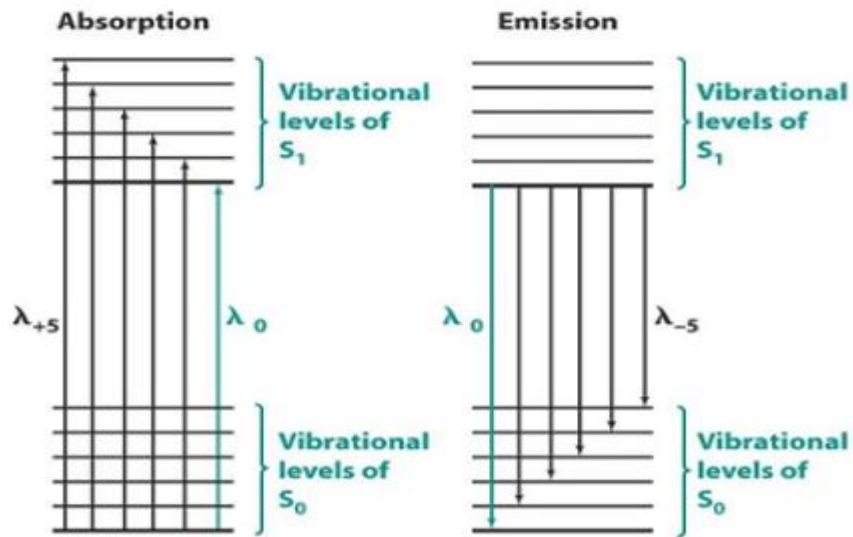


Fig. 2.7. Energy-level diagram of the mirror image of absorption and emission spectra [40].

The photoluminescence properties of a material are characterized both by the absorption (excitation) of the material by a source of primary excitation and by the emission of light by the material. A typical experimental arrangement for determining excitation and emission spectra is shown in Fig. 2.8. In this example, the source of excitation is the output of a monochromator that, like a prism, resolves the source of excitation light at its component wavelengths.

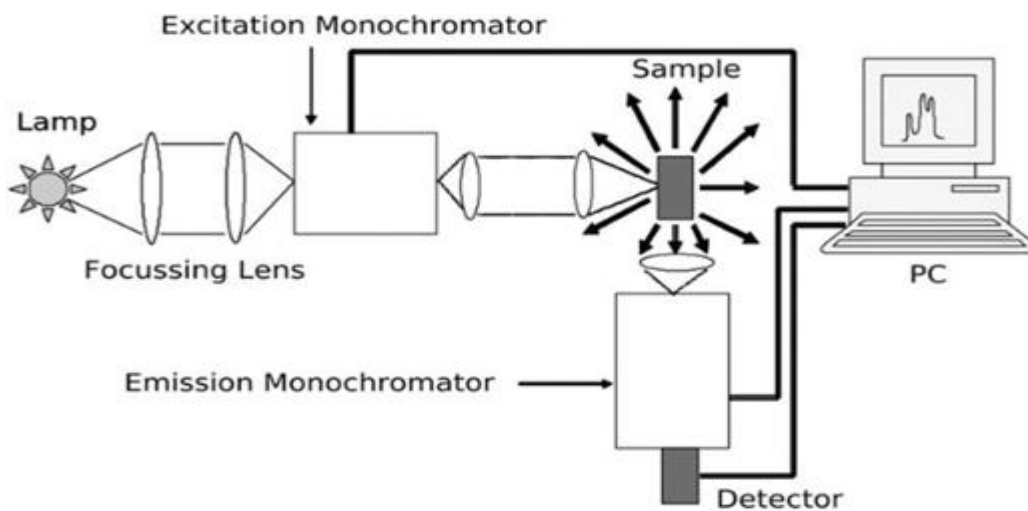


Fig. 2.8: Schematic diagram showing elements used to measure photoluminescence spectra [41].

## 2.4 structural and electronic properties of phosphor materials

### 2.4.1 Definition and major application of phosphors

The class of materials that emit characteristic luminescence are called phosphors. Phosphor consist of a host material that constitutes the bulk and intentional impurities introduced into the host. The characteristic luminescence properties are obtained directly from the host or activators/dopants

intentionally introduced into the host material. An activator is an impurity ion that incorporated into the host network results in a centre that can be excited for luminescence. If more than one activator is used, they are called co-activators or co-dopants. An activator (sensitizer) tends to absorb energy from the primary excitation and is transferred to the other activator to improve its luminescent intensity[42]. Fig. 2.9 shows a schematic diagram showing the role of an activator and sensitizer in the luminescence process of a phosphor. In Fig. 2.9 (a), the light emission is the result of direct excitation of the activating atom A (the absorber) surrounded by the lattice atoms of the host H, while Fig. 2.9 (b) shows the emission of light of A as a result of the excitation and transfer of energy from the co-activator atom (the sensitizer) S.

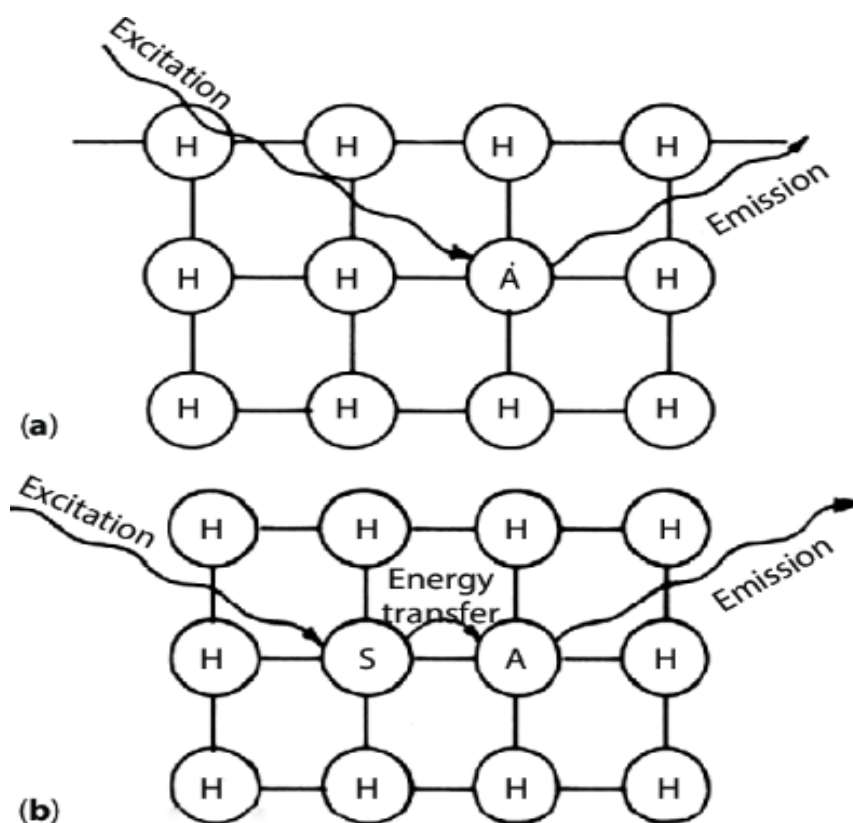


Fig. 2.9: Representation of luminescence process: (a) activator (A) in a host (H) and (b) sensitizer (S) and activator (A) in a host (H)[43].

Luminescent materials have been well known for a long time from traditional lighting and display applications, like cathode ray (television) tubes, fluorescent lamps, and also X-ray screens. Exploration of novel materials classes during the last years has enabled development of new applications, such as white LEDs, plasma display panels, bio-markers, and solar cells. Recent progress and future prospects show that luminescent materials remain not only interesting from a scientific point of view but also relevant from an application point of view. For many years to come, scientific challenges as well as societal needs in this research field can be addressed by chemists, physicists, and materials scientists [6]. The research on luminescent materials is stimulated by

various applications. Luminescent materials are widely applied today. In the last decades, a large number of luminescent materials based on RE ions or RE host lattices have been invented. In many cases, RE phosphors dramatically improved the performance of the devices in which they are applied.

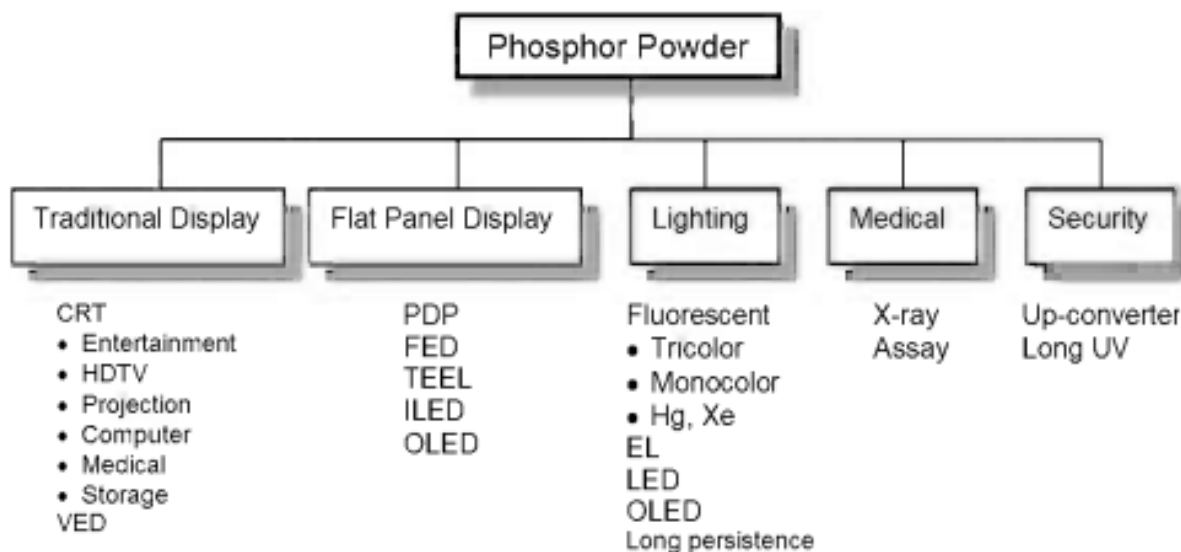


Fig. 2.10: Major application of phosphors [6]

A more specialized and important application is the use of X-ray intensifying screens for medical purposes [44]. Some X-ray detector systems are based on luminescent materials as well. Research on X-ray phosphors is mainly focused on photostimulable phosphors for digital imaging, the luminescence of which is obtained by optical excitation in an absorption band formed under X-ray irradiation[45]. Scintillator crystals convert the energy of ionizing radiations into UV or visible radiation. They are used for medical diagnostics, scientific experiments, and industrial control (e.g., inspection of baggage and containers, thickness control of metal sheets and paper, geophysical exploration).

#### 2.4.2 properties of $Y_2SiO_5:Ce^{3+}$ Phosphor material

RE-doped phosphors have the characteristics of long-time chemical stability, good illumination which can be applied in industrial processing of displays with a good efficiency and field emission display detector applications [46, 47]. Thin film phosphors are the best solution for the traditional phosphor powder cathode ray tubes. Thin film phosphor exhibits high contrast percentage, high ambient visibility, image resolution, and good heat resistance [48]. The most important parameter of thin film phosphors for the various deposition methods is the deposition at a low substrate temperature. This is due to the use of glass substrates and temperature sensitive phosphor materials. Yttrium silicate crystal is a well-known material for hosting RE ions such as cerium. Yttrium silicate has a wide band gap of 7.4 eV which can comprehend a large amount of RE ions. It has been used

successfully as a host matrix for RE ions due to its thermal and chemical stability, which contributes to the formation of phosphors or scintillating photocathodes. Energy structure of the bandgap of yttrium silicate ( $\text{Y}_2\text{SiO}_5$ ) activated with RE ions such as  $\text{Ce}^{3+}$  [49, 50],  $\text{Tb}^{3+}$  [49, 51] are widely investigated for different applications.  $\text{Y}_2\text{SiO}_5: \text{Ce}^{3+}$  has been studied by various experts for the purpose of scintillation [52, 53]. According to previous studies,  $\text{Y}_2\text{SiO}_5: \text{Ce}^{3+}$  phosphor is a blue light emitter and many studies have been conducted to investigate luminescence characteristics for lighting industries such as field emission screens (FEDS). The material structure of  $\text{Y}_2\text{SiO}_5$  belongs to orthosilicate crystalline structures of  $(\text{RE}_2\text{SiO}_5)$  [54]. This silicate material has two monoclinic crystalline phase structures which are classified by their synthesis temperatures. These are  $X_1$  phase which is synthesized at low temperature (below  $1190^\circ\text{C}$ ) and has lower Xrd-intensity with a space group of  $\text{P}2_1/\text{c}$  and  $X_2$  phases, synthesizing at high temperature (above  $1190^\circ\text{C}$ ) with a space group of  $\text{B}2/\text{c}$  [55]. There are two possible sites of  $\text{Y}^{3+}$  in each of these crystalline phases that can be attributed to the different number of coordination in these phases [55, 56]. Broadband light-emitting materials in the visible spectrum commonly used to sensitize the luminescence of RE ions and the transition of metal ions. Specifically,  $\text{Ce}^{3+}$  is a 4f-5d allowable transition that provides effective broadband luminescence. Furthermore, the emission and excitation spectra of  $\text{Ce}^{3+}$  ions are very sensitive to the crystallographic site of the host material.  $\text{Y}_2\text{SiO}_5: \text{Ce}^{3+}$  is a superb phosphorescent material emitting blue light. It is, therefore, crucial to study the optoelectrical and display applications of this material [57, 58]. In this compound, emission arises from electronic transitions in  $\text{Ce}^{3+}$  from the 5d ( $^2\text{D}_{3/2}$ ,  $^2\text{D}_{5/2}$ ) excited state to the 4f ( $^2\text{F}_{5/2}$ ,  $^2\text{F}_{7/2}$ ) ground state [44]. The change in bond lengths from  $\text{Ce}^{3+}$  ions to their  $\text{O}^{2-}$  and  $\text{F}^-$  ligands, the degree of distortion of the  $\text{Ce}(\text{O},\text{F})$  and  $\text{Ce}(\text{O},\text{F})$  polyhedral, and the change in lattice covalency dictated by the relative change in charged species all result in changes in the crystal field splitting of the  $\text{Ce}^{3+}$  5d levels [59]. The complex structure shown in Fig. 2.11(a) is composed of the building blocks of the tetrahedron ( $\text{SiO}_4$ ) and octahedron ( $\text{YO}_6$ ) structures as shown in Fig. 2.12 (a) and (b).



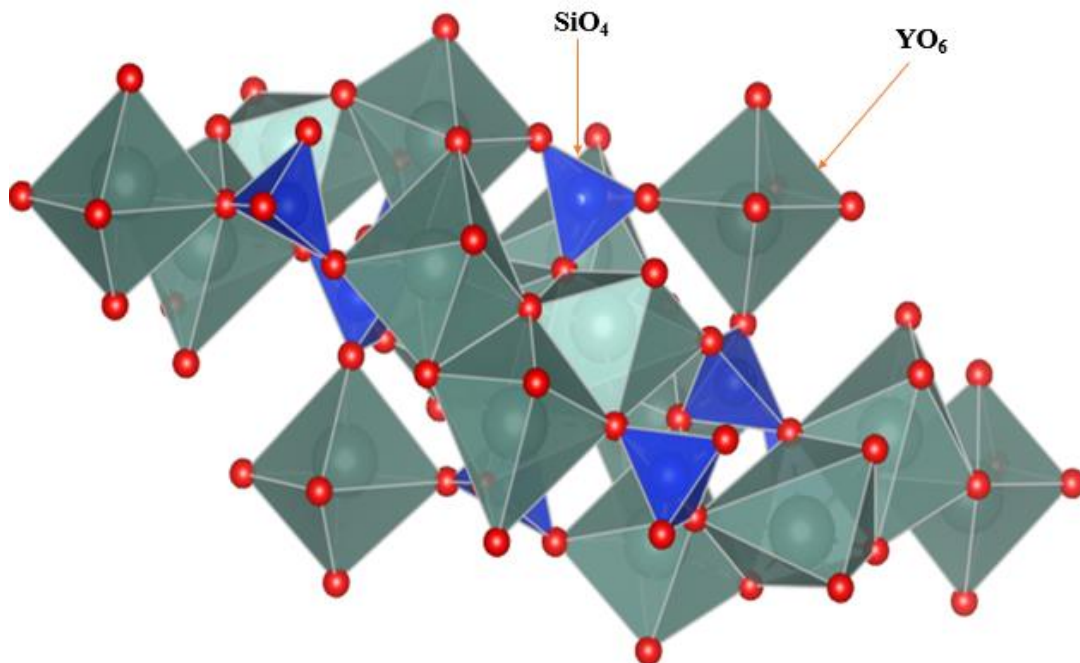


Fig. 2.11a: schematic crystal structure of Y<sub>2</sub>SiO<sub>5</sub>[60].

Two crystallographically distinct Y sites are present in the structure in Fig. 2.11(b) as a possible substitutional site for other +3 cations of Ce<sup>3+</sup>. One site, Y<sub>1</sub>, is characterized as a 6-coordinate polyhedron, while the other, Y<sub>2</sub>, is best described as a [6 + 1]-coordinate environment; each has symmetry C<sub>1</sub>. As seen from the representative formula Y<sub>2</sub>SiO<sub>4</sub>O, the structure also contains simple orthosilicate groups of SiO<sub>4</sub> and a unique O<sup>2-</sup> anion that is bound only to the Y<sup>3+</sup> cations. Each of the Y sites has two of the unique O<sup>2-</sup> anions in its coordination sphere. The coordination environments of the two Y sites are shown in Fig. 2.11(b).

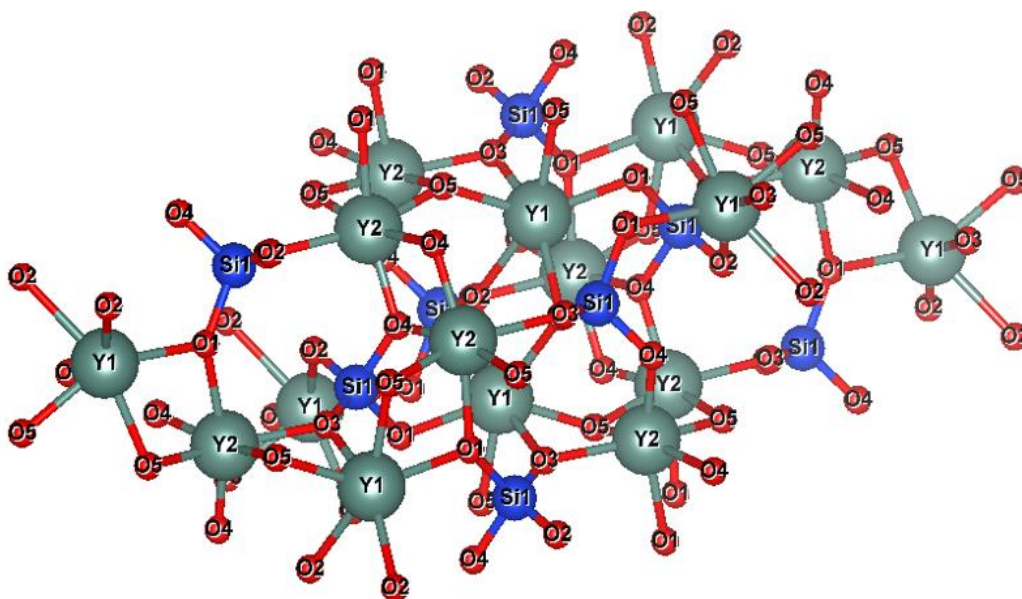


Fig. 2.11b: schematic diagram shows the sites of Y in the complex crystal structure of Y<sub>2</sub>SiO<sub>5</sub>

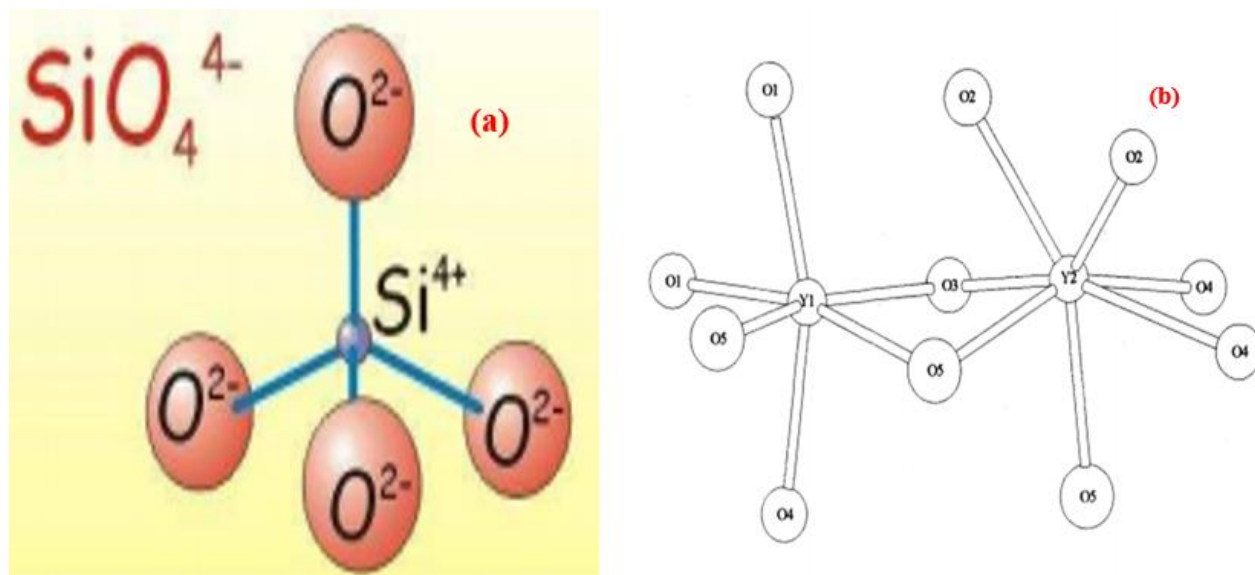


Fig. 2.12: Schematic illustration of (a)  $\text{SiO}_4$ -tetrahedron and (b)  $\text{Y}_1$  and  $\text{Y}_2$  centred polyhedron in the structures of  $\text{Y}_2\text{SiO}_5$  [61].

## 2.5 Crystal field theory (CFT)

Crystal field theory is one of several chemical bonding models and one that is applicable solely to the transition metal and lanthanide elements (La-Lu). The theory, which utilizes thermodynamic data obtained from absorption bands in the visible and near-infrared regions of the electromagnetic spectrum. It describes the breakdown of degenerations of the orbital states of electrons, usually d or f orbitals, due to a static electric field produced by a surrounding charge distribution (neighboring anions)[62]. This theory has been used to describe various spectroscopies of transition metal coordination complexes, in particular, optical spectra (colours). Crystal Field theory was developed to describe important properties of complexes (magnetism, absorption spectra, oxidation states, coordination,). The basis of the model is the interaction of the d-orbitals of a central atom with ligands, which are considered point charges. Atoms or molecules that surround a central atom or ion are known as ligands. The chemical properties of the transition metals as a group are more complex than those of other elements in the periodic table due to electrons being located in incompletely filled 3d atomic orbitals having different energy levels. Interaction with light causes electrons to be excited between the split 3d orbital energy levels, leading to absorption bands in the visible region and causing colour in chemical compounds and minerals containing cations of the first-series transition elements. The crystalline field theory can be seen as a special case of the ligand field theory. The crystalline field is defined as the electric field at the site of a particular ion under consideration due to the environment. As a result, the resulting orbital states of the d electrons (5d for RE ions and 3d for transition ions) will be divided. The luminescence properties of the phosphors are sensitive to this crystalline field. Some examples of this type which are found in the transitional



metals are  $\text{Cr}^{3+}$  and  $\text{Mn}^{2+}$  and the RE metal ions that show the 4f-5d transitions are  $\text{Ce}^{3+}$  and  $\text{Eu}^{2+}$ . According to CFT, the attraction between the central metal ion and the ligands in a complex is purely electrostatic. The theory is developed by considering the energy changes of the d orbitals of five degenerates (same quantum energy) surrounded by a series of point charges consisting of ligands. As a ligand approaches the metal ion, the ligand electrons will be closer to some of the d orbitals and further away from others, causing a loss of degeneration. The electrons in the d-orbitals and those of the ligand repel each other due to the repulsion between similar charges. Therefore, the d-electrons closest to the ligands will have more energy than those farther away, which results in energy splitting of d-orbitals.

This splitting is affected by the following factors:

- the nature of the metal ion
- The oxidation state of the central metal ion (a higher oxidation state leads to a greater division).
- the coordination number of the metal (i.e., tetrahedral, octahedral...)
- The nature of the ligands (the stronger the ligand, the greater the division).
- the arrangement of the ligands around the metal ion
- Size of d-orbitals (i.e., transition series).
- the geometry of the complex.

The five d-orbitals take the symbols  $d_{xy}$ ,  $d_{zx}$ ,  $d_{yz}$ ,  $d_{x^2-y^2}$  and  $d_{z^2}$ . In a complex, all are aligned differently in relation to the incoming charge. Depending on the geometry of the complex, some of the orbitals will point directly towards the ligands, while others will point between them. Those who target the ligands will experience more repulsion between their own electrons and those of the incoming ligands, than those who do not directly target them[63]. Therefore, the orbitals that target the ligands will be less stable and more energy efficient. Now all d-orbitals are no longer equivalent, giving rise to the phenomenon of orbital division, and the difference in energy between the more and less repelled orbitals is called the crystal field splitting parameter ( $\Delta$ ).

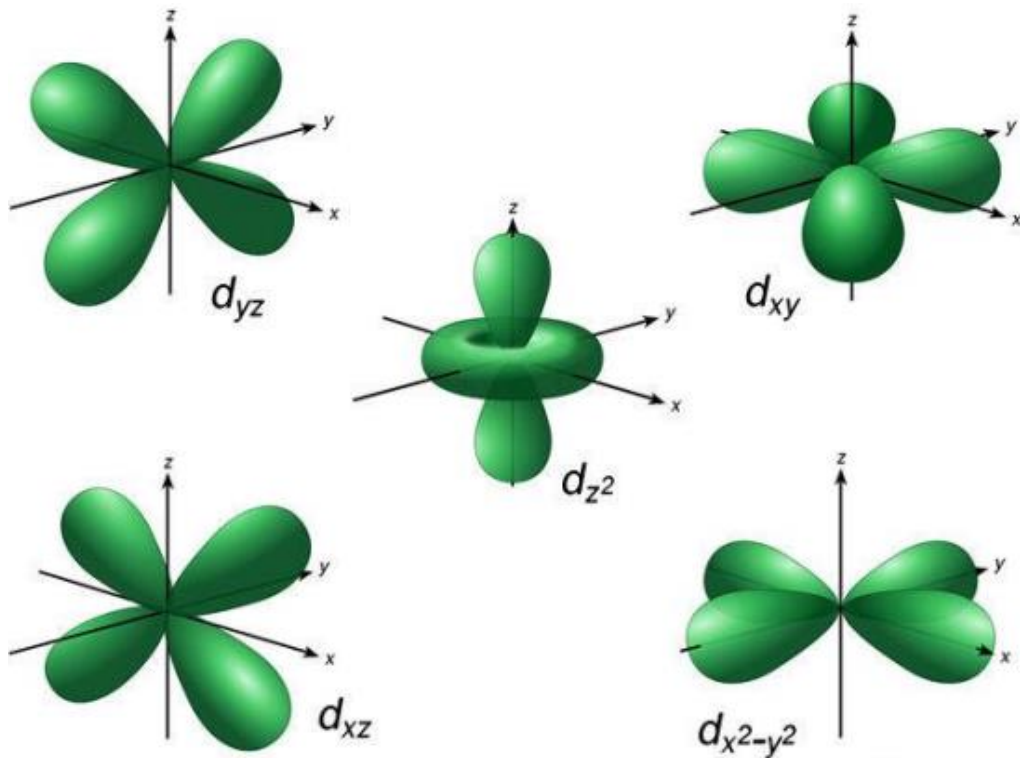


Fig. 2.13: Angular dependence functions of d-orbitals [64]

When the  $\text{Ce}^{3+}$  ion is placed in an octahedral field, as in a  $\text{Y}^{3+}$  site in  $\text{Y}_2\text{SiO}_5$ , the electron of the octahedral field will interact strongly with the  $\text{Ce}^{3+}$  ions found on the x, y, z axes (the  $d_{z^2}$  and  $d_{x^2-y^2}$  orbitals). These orbitals are called  **$e_g$**  orbitals and will be elevated in energy by the presence of an octahedral crystal field. On the other hand, the  $d_{xy}$ ,  $d_{xz}$ ,  $d_{yz}$  orbitals called  **$t_{2g}$**  orbitals will be repelled by the electrons and energy will be reduced more than energy without a crystalline field. This energy that is divided between  **$e_g$**  and  **$t_{2g}$**  orbitals is shown in Fig. 2.14. The electrons can go also into either a high spin or low spin arrangements depending on the magnitude of the crystal field splitting energy as shown in Fig. 2.15.

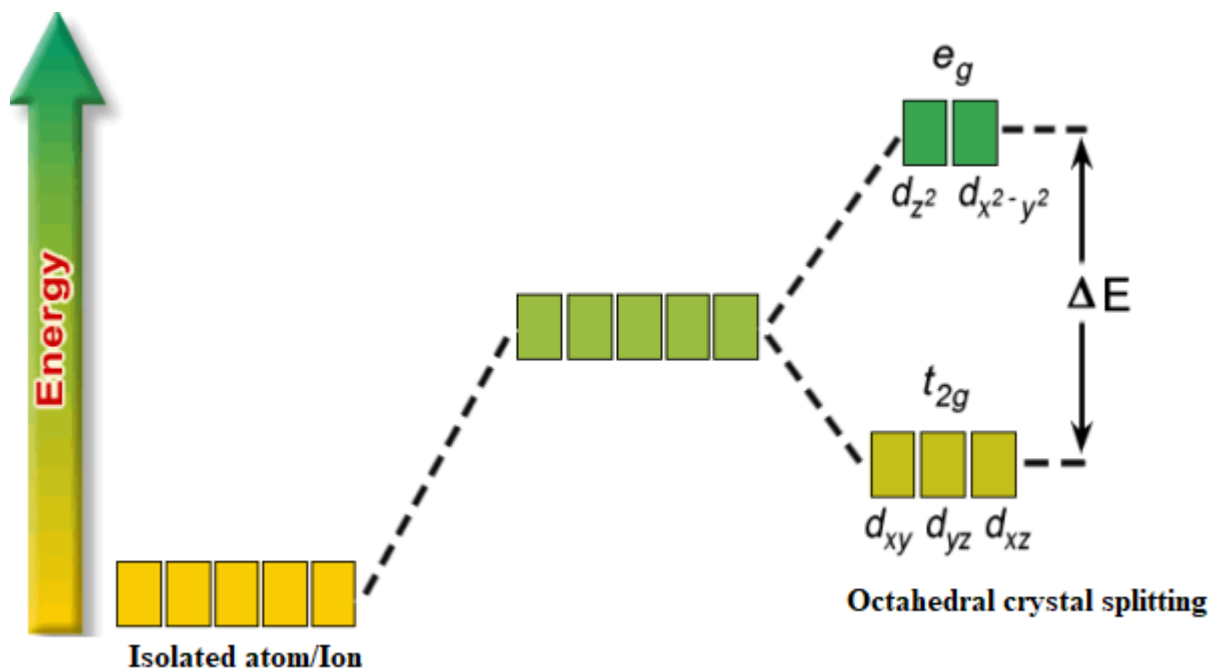


Fig. 2.14: Energy splitting of the five d orbitals for octahedral crystal field and the orbits of the free ion

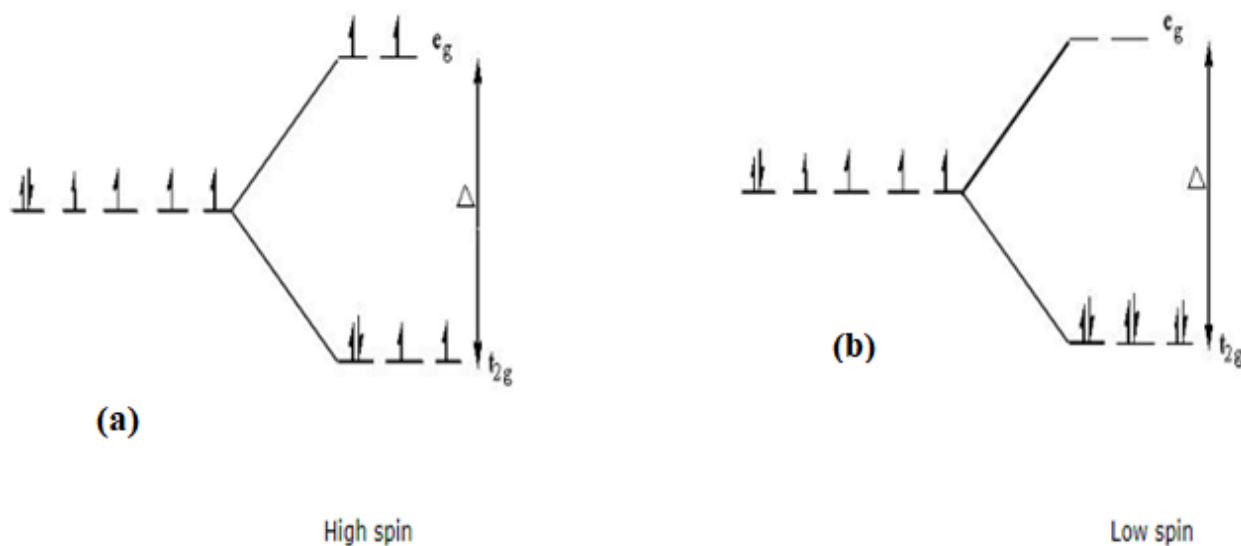


Fig. 2.15(a) and (b): Crystal field splitting diagrams for high and low spin orbit

The high and low spin is associated with the pairing and unpairing of electrons in the energy states. If we can see in Fig. 2.15 (a), there are four unpaired electrons and the electrons in Fig. 2.15 (b) are all paired. Therefore, the electrons in Fig. 2.15 (a) have a high spin, while the electrons in Fig. 2.15 (b) have low spins. The high spin configuration is considered to have a weakly field because unpaired electrons are weakly attracted to the external (paramagnetic) magnetic field, while the low spin configuration has a high strong field because it has zero unpaired electrons and It is weakly repelled by the external magnetic field (diamagnetic).

## 2.6 Electronic Transition in Rare-Earth Metal Ions

RE elements (REE) are a set of seventeen metallic elements. These include the fifteen lanthanides in the periodic table plus scandium and yttrium. Any of a group of chemically similar metal elements comprising the series of lanthanides and (generally) scandium and yttrium. They are not especially rare, but tend to occur together in nature and are difficult to separate from each other. RE elements (REE) are necessary components of more than 200 products in a wide range of applications, especially high-tech consumer products, such as cell phones, computer hard drives, electric and hybrid vehicles, and screen monitors flat and televisions. Major defense applications include electronic displays, guidance systems, lasers and radar and sonar systems. Although the amount of REE used in a product may not be a significant part of that product by weight, value or volume, REE may be necessary for the device to work. For example, magnets made of REE often represent only a small fraction of the total weight, but without them, the spindle motors and voice coils of desktop and laptop computers would not be possible. The U.S. Geological Survey news release "Going Critical" explains: explains that: In 1993, 38 percent of REE's world production was in China, 33 percent were in the United States, 12 percent were in Australia and five percent each was in Malaysia and India. Several other countries, including Brazil, Canada, South Africa, Sri Lanka and Thailand, made up the rest. However, in 2008, China accounted for more than 90 percent of global REE production, and in 2011, China accounted for 97 percent of world production. From 1990 and beyond, REE supplies became a problem as the Chinese Government began to change the amount of REE that allows them to be produced and exported. RE ions are characterized by an incompletely filled 4f shell. The 4f Orbital is inside the ion and is protected from the surroundings by the  $5S^2$  and  $5p^6$  filled orbitals. Therefore, the influence of the host network on optical transitions within the  $4f^n$  configuration is small (but essential). Fig. 2.16 shows a substantial part of the energy levels that originate from the  $4f^n$  configuration as a function of n for the trivalent ions. The width of the bars in Fig. 2.16 gives the order of magnitude of the crystal field division that looks very small compared to transition metal ions.



from the 4f to 5d shells of the ions ( $4f^n \rightarrow 4f^{n-1} 5d$ ), or charge-transfer (CT) transitions i.e. the promotion from the ligand atom to the unfilled 4f shell ( $4f^n L \rightarrow 4f^{n+1}$ ). There are a number of RE ions such as  $Ce^{3+}$ ,  $Pr^{3+}$ ,  $Tb^{3+}$ ,  $Er^{3+}$  and  $Eu^{2+}$  that can be excited directly from a state in the  $4f^n$  configuration to an excited state in the  $4f^{n-1}d^1$  configuration and emit either through an intraband  $4f \rightarrow 4f$  transition or a 5d-to-4f transition. Unlike the transitions via multiple states of a  $4f^n$  configuration that are strictly forbidden by the selection rule [66], the 4f-to-5d transitions are dipole allowed. However, unlike the 4f-state, the 5d states are diffuse and overlap with ligand orbitals. It is for this reason that the 4f-to-5d transitions are strongly dependent on the host, and vary over the spectral range from the deep UV to far-infrared region.

## 2.8 Optical transition of $Ce^{3+}$ ions

Like the other RE elements in the lanthanide group, Cerium (Ce) has an electronic configuration of  $[Xe] 4f^1 5d^1 6s^2$ . The  $4f^n$  energy levels are not affected by the host environment because they are completely protected by the  $5p^6$  and  $5s^2$  shells of the  $[Xe]$  configuration. The emission will change from the emission of the line in the UV radiation to the emission of the band in the visible region with the growing crystal field of the host. Therefore, it is very likely that one can find a host in which transitions from 4f to 5d can lead to absorption bands near the UV or blue region and the corresponding emission bands in the visible. The candidates for such transitions are the  $Ce^{3+}$  and  $Eu^{2+}$  ions. Not surprisingly, most phosphors for LED applications are based on  $Eu^{2+}$  and  $Ce^{3+}$  ions. The electronic configuration of  $Ce^{3+}$  is the simplest with an electron in 4f shell. This ion absorbs and emits through transitions from 4f to 5d. Therefore, after excitation at a level of  $4f^{n-1}5d^1$ , the ion normally does not relax to the fundamental state through transitions from 5d to 4f, but through energy levels associated with multiplet states of  $4f^n$  configuration. The  $4f^n$  electrons are, in fact, the valence electrons that are responsible for the optical transitions. A thorough literature search along with some exploratory studies of  $Ce^{3+}$  ions in hosts is not yet considered new based on crystalline structure data (for example, the Inorganic Crystal Structure Database, ICSD) could add potential candidates for  $Ce^{3+}$  activation [64]. The electronic structure the atom (M) and its ionized structure (M<sup>+</sup>) of the trivalent rare-earth elements are given in Table 2.2. It gives the number of valence electrons 4f for each trivalent RE ion of the lanthanide series. These valence electrons are protected by the 5s and 5p external electrons of the less energetic  $5s^2 5p^6$  configurations. Due to this protective effect, the valence electrons of the RE trivalent ions are weakly affected by the ligand ions in the crystals (a situation that corresponds to the case of a weak crystalline field). The  $5d \rightarrow 4f$  transitions of  $Ce^{3+}$  ion is electric-dipole allowed. Fig. 2.17 shows the energy level diagram of the  $4f \rightarrow 5d$  configuration of  $Ce^{3+}$  ion in a garnet structure.

Table 2.2: electronic and oxidation state of trivalent Rare-earth elements

Lanthanum Element	Symbol	Electronic structure of atoms (M)	Electronic structure of $M^{3+}$
Cerium	Ce	$[Xe]4f^15d^16s^2$	$[Xe]4f^1$
Praseodymium	Pr	$[Xe]4f^35d^06s^2$	$[Xe]4f^2$
Neodymium	Nd	$[Xe]4f^45d^06s^2$	$[Xe]4f^3$
Promethium	Pm	$[Xe]4f^55d^06s^2$	$[Xe]4f^4$
Samarium	Sm	$[Xe]4f^65d^06s^2$	$[Xe]4f^5$
Europium	Eu	$[Xe]4f^75d^06s^2$	$[Xe]4f^6$
Gadolinium	Gd	$[Xe]4f^75d^16s^2$	$[Xe]4f^7$
Terbium	Tb	$[Xe]4f^95d^06s^2$	$[Xe]4f^8$
Dysprosium	Dy	$[Xe]4f^{10}5d^06s^2$	$[Xe]4f^9$
Holmium	Ho	$[Xe]4f^{11}5d^06s^2$	$[Xe]4f^{10}$
Erbium	Er	$[Xe]4f^{12}5d^06s^2$	$[Xe]4f^{11}$
Thulium	Tm	$[Xe]4f^{13}5d^06s^2$	$[Xe]4f^{12}$
Ytterbium	Yb	$[Xe]4f^{14}5d^06s^2$	$[Xe]4f^{13}$
Lutetium	Lu	$[Xe]4f^{14}5d^16s^2$	$[Xe]4f^{14}$

Where [Xe] is the xenon noble gas with an electronic configuration of  $1s^22s^22p^63s^23p^63d^{10}4s^24p^64d^{10}5s^25p^6$  which can also written as [Kr]  $4d^{10}5s^25p^6$ .

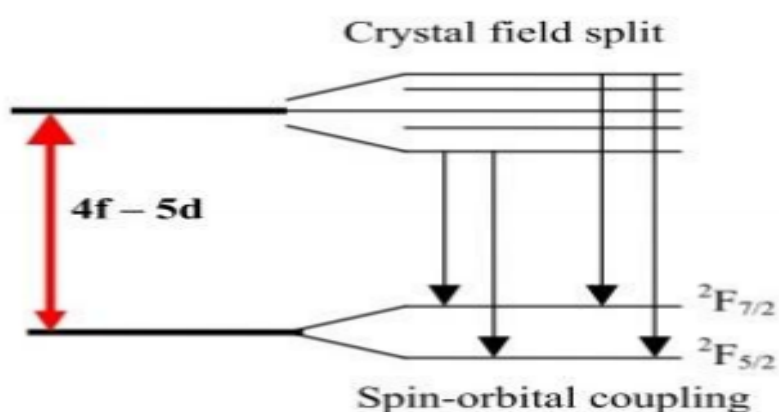


Fig.2.17: Scheme and crystal field splitting of the  $Ce^{3+}$  ion ( $4f^1$ )[\[67\]](#).

## 2.9 selection Rules

In physics and chemistry, a selection rule, or transition rule, formally restricts the possible transitions of a system from one quantum state to another. Selection rules have been derived for electromagnetic transitions in molecules, atoms, atomic nuclei, etc. The selection rules may differ according to the technique used to observe the transition. The selection rule also plays a role in chemical reactions, where some are formally prohibited reactions by centrifugation, that is, reactions in which the spin state changes at least once from reagents to products.

Every electron orbiting an atom can be assigned four unique quantum numbers, namely  $n$ ,  $l$ ,  $m_l$ , and  $m_s$ . Pauli's exclusion principle states that no two electrons orbiting a nucleus can have the same quantum numbers.  $n$ , is the principal quantum number which gives the number of the shells the electron is located in, and can be any positive integer number from 1 to infinity.  $l$ , the angular momentum quantum number, can be any positive integer from  $0 \leq l < n$ . For example, when  $n = 1$ ,  $l$  can only equal 0. When  $n = 2$ ,  $l = 0$  or 1. Thus, the number of atomic orbitals in each shell is determined by  $l$ . For each value of  $l$ , a symbol is assigned to distinguish the orbitals inside each shell, as shown in Table 2.3. Therefore, for  $n = 2$ ,  $l = 0$  or 1, there is ( $l = 0$ ) first orbital in the ( $n = 1$ ) first shell ( $l = 0, 1$ ) and  $2s$  and  $2p$  orbitals in the ( $n = 2$ ) second shell.  $m_l$ , the magnetic quantum number, represents the component of the angular momentum  $l$  along some reference axis ( $z$ ).  $m_l$  can have positive and negative integer values,  $-l \leq m_l \leq l$ . For example, for  $l = 2$ ,  $m_l = -2, -1, 0, 1$ , and 2.

Table 2.3: letter of symbols assigned to each value

l	0	1	2	3	4	5	6	7	8
Letter symbols	S	p	d	f	g	h	i	k	l

For atoms similar to hydrogen (atoms or ions with a single electron in a shell), the energy of the electron depends only on the principal quantum number  $n$ . However, when there is more than one electron in a shell, each electron still has a set of unique quantum numbers, but they repel each other through coulombic interactions. This leads to the division of the individual  $l$  orbitals, for example, making  $2p$  higher in energy than  $2s$ , etc. To take into account coulombic interactions, the total angular momentum of all electrons located on the closed shells in the atom is summed as:  $L = \sum_i l_i$  where  $L$  is term symbol. It is important to note here that  $L$  and  $l$  are not the same. Only when there is one electron located above a closed shell does  $L$  and  $l$  represent the same orbital. Because  $l$  is a vector quantity,  $L$  is determined by vector addition, and only those resultants that give integer values



give valid  $L$  values. Like  $L$ , the spins can be added giving the spin quantum number  $S$ , which is not a term symbol. The number of wave functions that can represent the electron interactions is called the multiplicity and is given by  $2S+1$ . Optical line spectra of RE arise from transitions between levels of the  $4f^N$  configuration. The positions of these levels arise from a combination of the Coulomb interaction between the electrons, the spin-orbit coupling and the crystalline electric field. The resultant splitting of the  $4f^N$  configuration are shown schematically in Fig. 2.18. The electrostatic interaction yields terms  $^{2S+1}L$  with separations of the order of  $10^4 \text{ cm}^{-1}$ . The spin-orbit interaction

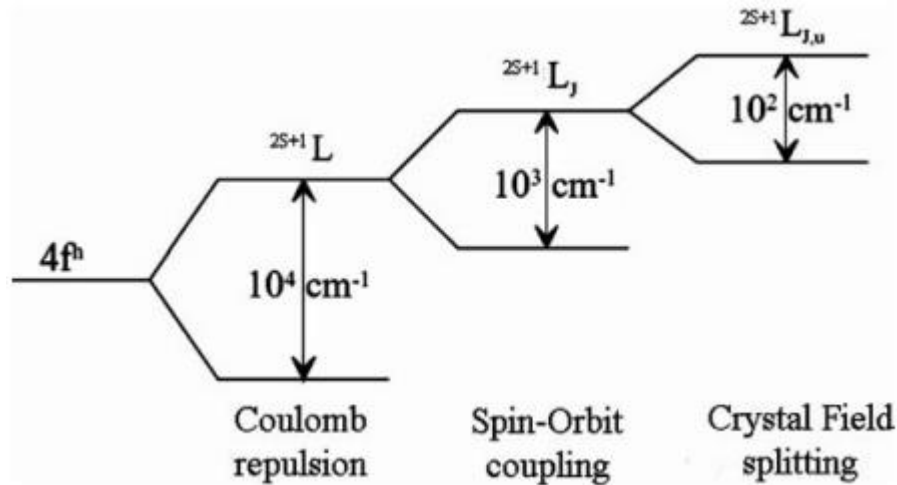


Fig. 2.18: Schematic diagram of the splitting of RE energy levels due to the electrostatic, spin-orbit and crystal field interactions[6].

The spin-orbit interaction then splits these terms into  $J$  states with typical splitting of  $10^3 \text{ cm}^{-1}$ . Finally, the  $J$  degeneracy of the free ion states is partially or fully removed by the crystalline Stark field, yielding a Stark manifold usually extending over several hundred  $\text{cm}^{-1}$ . When electrons occupy available energy levels, the electrons try to keep their spins the same, all  $+\frac{1}{2}$  or  $-\frac{1}{2}$ . This is known as Hund's rule, and it states that for equivalent electrons having the same  $n$  and  $l$  values, the lowest energy state occurs when all the electrons exhibit the same spin. This interaction arises from the magnetic coupling between the magnetic moments associated with the spin and orbital motion of the electrons. For one electron above a closed shell, this effect is taken into account by adding  $l$  and  $m_s$ , both vector quantities, to give the total angular momentum, denoted by the vector  $j$ :  $j = l + m_s$  or  $l - m_s$ , since the spin of the electron can have  $\pm\frac{1}{2}$  values. For more than one electron, the total spin angular momentum ( $S$ ) and the total orbital angular momentum ( $L$ ) couple to give a total angular momentum of the ion ( $J$ ), where  $J = |L + S|$ . The term symbol then can be written as  $^{2S+1}L_J$ . This is known as the  $L$ - $S$  or Russell-Saunders coupling scheme[68] and can better approximate the true energy states of the ion. The energy levels splitting due to the spin-orbit interaction is shown in Fig.2.16 and is labelled according the  $L$ - $S$  couple scheme and is less than the coulombic interaction.

Hund's rules dictate how to arrange the terms from the lowest to highest energy. The rules are as follows: (1) the term with the maximum multiplicity lies lowest in energy, (2) for a given multiplicity the term with the largest value of  $L$  lies lowest in energy, and (3) for atoms with less than half-filled shells the level with the lowest value of  $J$  lies lowest in energy, while for shells more than half full the highest  $J$  lies at the lowest energy[6]. For free ions, transitions are classified as either forbidden or allowed and generally only make transitions between adjacent states, as shown in Table 2.4. Transitions between states that have the same parity (wave functions with the same even ( $u$ ) or odd ( $g$ ) symmetry), i.e.,  $f \rightarrow f$ , are generally forbidden and if they occur, produce only very weak emission. This is known as Laporte's selection rule and basically means that electrons are not allowed to redistribute themselves within the same orbital and transitions only take place between even and odd wave functions. Allowed transitions are those that electrons transition between different orbitals or shells and the total angular momentum changes by 1, with the selection rules written as follows:  $\Delta n = \pm 1, \pm 2$ ,  $\Delta l = \pm 1$  and  $\Delta j = 0, \pm 1$ .

Table 2.4: Allowed and forbidden electron transitions types (free ion scheme)

Allowed Transitions	Forbidden transitions
<b>s↔p</b>	d↔d
<b>f↔d</b>	f↔f

When a photon is emitted by a transitioning electron, the total momentum of the system must be conserved. A photon has an angular momentum or "spin" of 1, so when this photon is ejected, the total momentum of the system must also change by 1. Electrons can make transitions that are termed electric dipole ( $E_1$ ), magnetic dipole ( $M_1$ ) and quadrupole ( $E_2$ ).  $E_1$  is allowed for the free ion while  $M_1$  and  $E_2$  are forbidden, and if they occur, are very weak. Each transition type is governed by certain selection rules. The selection rules in terms of the  $L$ - $S$  coupling scheme for allowed  $E_1$  is:  $\Delta S = 0$ ,  $\Delta L = 0, \pm 1$  (except  $0 \rightarrow 0$ ) That is, the spin moment does not change and the transition occurs between at least two adjacent states. For  $M_1$ , the rules are the same as  $E_1$  with the added rule  $\Delta J = 0, \pm 1$ . For  $E_2$ ,  $\Delta S = 0$ ,  $\Delta L = 0, \pm 1, \pm 2$ . When an activator ion is incorporated into a host lattice, the surrounding crystal field, or ligand field, can further split the energy levels of the activator ion. Each level can split into a number of sublevels, called the Stark effect. The number of sublevels can be at most  $(2J + 1)$  for  $J$  integer or  $(J + \frac{1}{2})$  for  $J$  half-integer. The number of sublevels is determined by the symmetry of the ligand field that surrounds the activator ion[6].

## **Chapter 3: Thin film deposition methods, Characterization and measurement techniques**

### **3.1 introduction to thin film deposition methods**

Any object with one of its physical dimensions (length, breadth and height) less than that of the other two is called a thin film. A thin film is a layer of material whose thickness varied from micrometre to nanometre [69]. Thin film deposition is the technology of applying a very thin film of material, between a few nanometres to approximately 100 micrometres, or the thickness of a few atoms, on a “substrate” surface to be coated, or on a coating previously deposited to form layers [70]. Nowadays, most of the technologies are used to minimize the materials in nano-size and nano thickness, which leads to the appearance of new and unique behaviours of said materials in optical, electrical, optoelectronic, dielectric applications, etc [71]. Therefore, a new branch of materials science/science is called thin films or coatings. The thin film can be defined as a thin layer of material, where the thickness varies from several nanometres to a few micrometres. Like all materials, the structure of thin films is divided into amorphous and polycrystalline structures, depending on the conditions of preparation and the nature of the material. Thin films comprise two parts: the layer and the substrate where the films are deposited on it. In addition, thin films may be composed of different layers, such as thin film solar cells, electrochromic cells, etc [72]. Thin film deposition is generally divided into two broad categories: Chemical deposition and Physical vapor deposition coating systems. In the Chemical deposition, a volatile fluid precursor produces a chemical change in a surface that leaves a chemically deposited coating. An example is the Chemical Vapor Deposition or CVD used to produce the highest purity and highest performance solid materials in the semiconductor industry today. Physical vapor deposition refers to a wide range of technologies in which the material is released from a source and deposited on a substrate by mechanical, electromechanical or thermodynamic processes.

Table 3.1: deposition categories of thin films

<b>Physical deposition</b>	<b>Chemical deposition</b>
<b>Laser beam evaporation</b>	Sol-gel technique
<b>Vacuum thermal evaporation</b>	Chemical bath deposition
<b>Electron beam evaporation</b>	Spray pyrolysis technique
<b>Molecular beam epitaxy</b>	Electro plating technique
<b>Ion plating epitaxy</b>	Chemical vapor deposition (CVD)
<b>Sputtering technique</b>	Low pressure chemical vapor deposition (LPCVD)

Physical evaporation is one of the oldest methods of depositing metal films. Aluminium, gold and other metals are heated to the point of vaporization, and then evaporate to form to a thin film covering the surface of the substrate. All film deposition takes place under vacuum or very carefully controlled atmosphere[73]. Thin films are formed by depositing material on a clean and suitable substrate for the thickness of the bulk material instead of thinning the bulk material[74].The mechanical strength of thin films is better than annealed, as well as bulk samples. The properties and versatility of the thin films can be obtained by selecting proper technique of film deposition. The difference between the chemical and physical thin film deposition methods depends upon the method of depositing thin film material on the substrate. In this study, we have applied a physical deposition method (pulsed laser deposition method), some of the other thin film deposition methods are also included for comparison and further studies.

### **3.1.1. Chemical Vapour Deposition (CVD)**

CVD is a vacuum deposition method used to produce high quality and high-performance solid materials. The process is often used in the semiconductor industry to produce thin films. In typical CVD, the wafer (substrate) is exposed to one or more volatile precursors, which react and/or decompose on the surface of the substrate to produce the desired deposit. Frequently, volatile by-products are also produced, which are removed by the flow of gas through the reaction chamber. Microfabrication processes use CVD extensively to deposit materials in various forms, including monocrystalline, polycrystalline, amorphous and epitaxial. These materials include silicon (dioxide,

carbide, nitride, oxynitride), carbon (fiber, nanofibers, nanotubes, diamond and graphene) [75]. The chemical reaction between the substrate and the precursor is continued at high temperature till the desired thickness of the film is obtained. CVD is commonly used to deposit compliant films and increase substrate surfaces in ways that more traditional surface modification techniques are unable to do. CVD is extremely useful in the process of deposition of the atomic layer by depositing extremely thin layers of material. There are a variety of applications for such films.

### **3.1.2. Plasma Enhanced CVD (PECVD) Method**

(PECVD) is a chemical vapor deposition process used to deposit thin films from a gaseous state (vapor) to a solid state in a substrate. Chemical reactions are involved in the process, which occurs after the creation of a plasma of the gases that react. Plasma is usually created by radiofrequency (RF) (alternating current (AC)) frequency or direct current (DC) discharge between two electrodes, space between which is filled with the gases that react. These atomic and molecular fragments interact with a substrate and this chemical reaction cause to develop a solid layer on the surface at the substrate [76]. In PECVD, lower temperatures (300→350 degrees centigrade) are used for thin film deposition while in CVD high temperatures (600→900 degrees centigrade) are used to develop thin films. Plasma deposition is often used in the manufacture of semiconductors to deposit films conformingly (covering the side walls) and in wafers containing metal layers or other temperature sensitive structures. PECVD also produces some of the fastest deposition rates while maintaining film quality (such as roughness, defects / voids), compared to cathodic spray deposition and thermal /electron beam evaporation, often at expense of uniformity.

### **3.1.3. Atomic Layer Deposition (ALD) Method**

(ALD) is a thin film deposition technique based on the sequential use of a gas phase chemical process; It is a subclass of chemical vapor deposition. Most ALD reactions use two chemicals called precursors (also called “reagents”). These precursors react with the surface of a material one at a time in a sequential and self-limited manner. Through repeated exposure to separate precursors, a thin film is slowly deposited. ALD is a key process in the manufacture of semiconductor devices, and part of the set of tools available for the synthesis of nanomaterials. The gaseous precursors are used to react with the substrate sequentially one at a time. The thin films obtained by this process are conformal [77]. The process of ALD is divided into two half reactions. These reactions include deposition of precursor and evacuation of the reaction chamber that run-in sequence and repeated for each precursor [78]. This chemical reaction occurs on the substrate resulting in the formation of desired film thickness. ALD is a stepwise procedure; therefore, it is slower one but can run even on

lower temperature. ALD is a useful process for the manufacture of microelectronics due to its ability to produce precise thicknesses and uniform surfaces, in addition to the production of high-quality films using different materials. In microelectronics, ALD is studied as a potential technique to deposit high  $\kappa$  gate oxides (high permittivity), high  $\kappa$  memory capacitors dielectrics, ferroelectric and metals and nitrides for electrodes and interconnections.

### **3.1.4. Sol-Gel Method**

In materials science, the sol-gel process is a method to produce solid materials from small molecules. The method is used for the production of metal oxides, especially silicon (Si) and titanium (Ti) oxides. The process involves the conversion of monomers into a colloidal solution (sol) that acts as the precursor of an integrated network (or gel) of discrete particles or network polymers. Typical precursors are metal alkoxides. In Sol-gel the deposition method, the precursor solutions are highly controlled for the deposition of the films [79]. The alkoxides involved in sol-gel, where the macromolecular oxide network is obtained first through the hydrolysis of the alkoxy group after these polycondensation reactions take place [80]. In this chemical process, a “sol” (a colloidal solution) is formed which then gradually evolves into the formation of a diphasic system similar to a gel that contains both a liquid phase and a solid phase whose morphologies vary from discrete particles to polymeric networks. In the case of the colloid, the fraction of particle volume (or particle density) may be so low that it may be necessary to initially remove a significant amount of liquid so that gel-like properties are recognized. This can be achieved in many ways. The simplest method is to allow time for sedimentation to occur and then pour the remaining liquid. Centrifugation can also be used to accelerate the phase separation process.

In physical deposition technique, mechanical or electromechanical methods are used to deposit the thin films on the substrate. Materials to be deposited on the substrate depend upon the temperature, pressure and other physical conditions. In these physical methods, the thin films formed are directional on nature because particles will follow a straight path from the target to the substrate.

### **3.1.5. Molecular Beam Epitaxy (MBE)**

(MBE) is an epitaxy method for thin film deposition of individual crystals. The MBE process was developed in the late 1970s at Bell Telephone Laboratories by J. R. Arthur and Alfred Y. Cho. MBE is widely used in the manufacture of semiconductor devices, including transistors, and is considered one of the fundamental tools for the development of nanotechnologies. MBE is used to manufacture diodes and MOSFET (MOS field effect transistors) at microwave frequencies, and to manufacture lasers used to read optical discs (such as CDs and DVDs). MBE combines advantages of both

chemical and physical methods for thin film deposition. Firstly, the target materials to be deposited are heated directly until they convert from solid to gaseous form. Then the gaseous elements are allowed to react chemically with the substrate to grow the thin film[81]. In MBE, target material is deposited in the form of layers but one layer at a time. MBE is a slow method but the degree of purity in this method is very high. Molecular beam epitaxy occurs in a high vacuum or in an ultra-high vacuum ( $10^{-8}$ – $10^{-12}$  Torr). The most important aspect of MBE is the deposition rate (typically less than 3,000 nm per hour) that allows films to grow epitaxially. These deposition rates require a proportionally better vacuum to achieve the same levels of impurities as other deposition techniques. The absence of carrier gases, as well as the ultra-high vacuum environment, result in the highest attainable purity of the grown films.

### **3.1.6. Sputtering**

In physics, sputtering is a phenomenon in which microscopic particles of solid material are ejected from their surface after the material is bombarded by plasma or gas energy particles[82]. It occurs naturally in outer space and can be an unwanted source of wear on precision components. However, the fact that it can be done to act on extremely thin layers of material is exploited in science and industry; there, it is used to make precise engraving, carry out analytical techniques and deposit thin film layers in the manufacture of optical coatings, semiconductor devices and nanotechnology products.

Sputtering is a physical thin film deposition method in which the atoms from a target material are released and come to rest on the substrate[83]. The target material is kept at low temperature. In this method, plasma of a noble gas such as argon is used as a target material. Noble gas does not allow any undesired chemical reactions therefore; it is a fast and an effective method to achieve the desired level of film thickness[77]. Sputtering only happens when the kinetic energy of the incoming particles is much higher than conventional thermal energies ( $\gg 1$  eV). When done with direct current (DC sputtering), voltages of 3-5 kV are used. When done with alternating current (RF sputtering), frequencies are around the 14MHz range.

### **3.1.7. Thermal Evaporation Method**

Thermal evaporation is the vaporization of a material by heating to a temperature such that the vapor pressure becomes appreciable and atoms or molecules are lost from the surface in a vacuum[84]. The material vapor finally condenses in form of thin film on the cold substrate surface and on the vacuum chamber walls. Usually low pressures are used, about  $10^{-6}$  or  $10^{-5}$  Torr, to avoid reaction between the vapor and atmosphere. The source material to be deposited is evaporated in a vacuum



by using an electron beam or resistive heating inside a high vacuum coating chamber. The vacuum allows the vapour particles to travel directly to the substrate where they condense back to a solid state to form a thin film[85].

### **3.1.8. Electrohydrodynamic Deposition**

Electrohydrodynamic deposition is also known as electro spraying deposition method [86]. In this method, stress is exerted on the liquid (mixture of nanoparticles to be deposited with the suitable solvent like methanol) which flow through the capillary nozzle by applying high electric field while the substrate is kept at ground potential. This stress results in the deposition of fine droplets of liquid on the substrate. The substrate is heated for complete evaporation of the solvent.

### **3.1.10. Pulsed Laser Deposition (PLD)**

The laser was first demonstrated in 1960. Since then, it has become a powerful tool in many applications. It is especially useful in the processing of materials [87]. The laser has many unique properties, such as narrow frequency bandwidth, consistency and high-power density. Often, the beam of light is intense enough to vaporize the hardest and heat resistant materials. In addition, due to its high precision, reliability and spatial resolution, it is widely used in the industry for thin film machining, material modification, material surface heat treatment, welding and micropatterning. In addition to these, poly- component materials can be removed and deposited on substrates to form stoichiometric thin films. This last laser application is called pulsed laser deposition (PLD). It is an ablation process. High power pulses of laser light are focused on the surface of the target material in a vacuum chamber[88] . This results in vaporization of the target material. The atoms ablated from the target material get deposited on the substrate. Pulsed laser deposition (PLD) is a physical vapor deposition (PVD) technique in which a high-power pulsed laser beam is focused inside a vacuum chamber to achieve a target of the material to be deposited. This material is vaporized from the target (in a plasma column) that deposits it as a thin film on a substrate (like a silicon wafer in front of the target). This process can occur in an ultra-high vacuum or in the presence of a background gas, such as oxygen that is commonly used when depositing oxides to completely oxygenate deposited films. While the basic configuration is simply relative to many other deposition techniques, the physical phenomena of laser-objective interaction and film growth are quite complex. When the target absorbs the laser pulse, the energy is first converted into electronic excitation and then thermal, chemical and mechanical energy, resulting in evaporation, ablation, plasma formation and even exfoliation[89]. The expelled species expand into the surrounding vacuum in the form of a plume that contains many energetic species, including atoms, molecules,



electrons, ions, groups, particles, and molten globules, before being deposited in the typically hot substrate. The PLD simple setup is presented in Fig. 3.1.

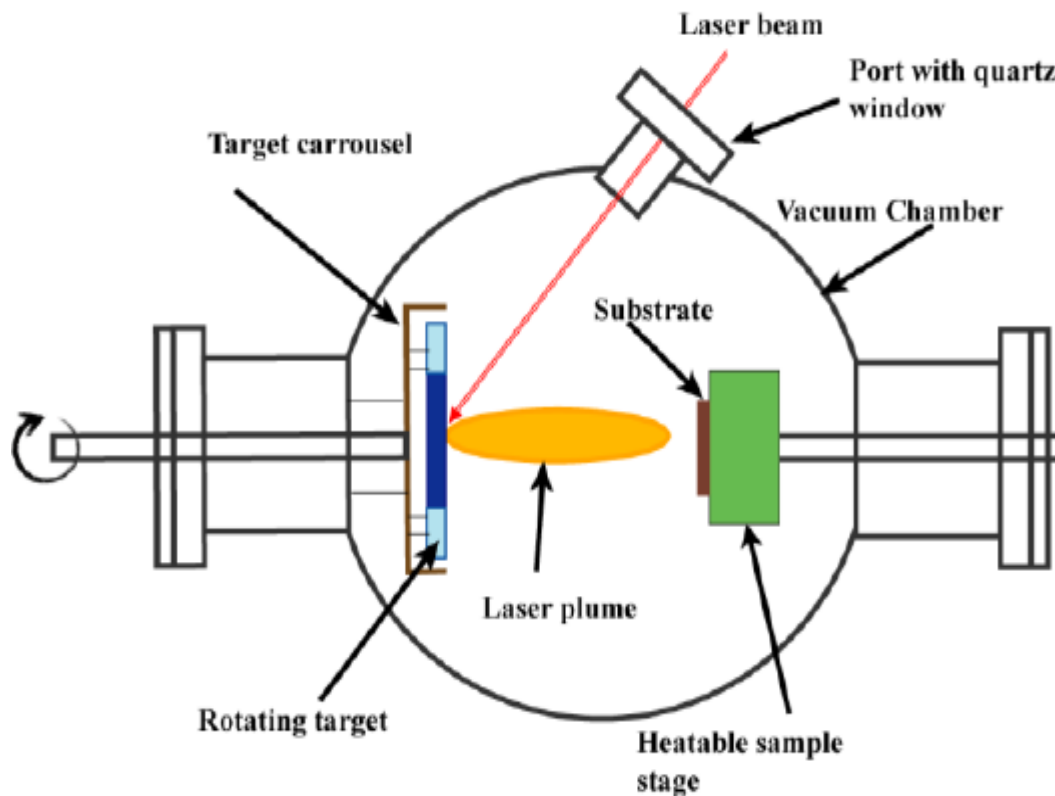


Fig. 3.1: possible configuration of a PLD deposition chamber.

The detailed mechanisms of PLD are very complex, including the process of ablation of the target material by laser irradiation, the development of a plasma plume with high energy, electron and neutral ions and the crystalline growth of the film on the heated substrate. The PLD process can generally be divided into four stages:

- Laser absorption on the target surface and laser ablation of the target material and creation of a plasma.
- Plasma dynamics.
- Deposition of the ablation material on the substrate.
- Nucleation and growth of the film on the surface of the substrate.

Each of these steps is crucial for the crystallinity, uniformity and stoichiometry of the resulting film.

### 3.1.10.1 Laser ablation of the target material and creation of a plasma

Ablation of the target material after laser irradiation and plasma creation are very complex processes. The removal of atoms from the bulk material is done by vaporizing the volume in the surface region in a non-equilibrium state. In this, the incident laser pulse penetrates the surface of the material within the penetration depth. This dimension depends on the wavelength of the laser

and the refractive index of the target material at the wavelength of the laser applied and, in general, is in the region of 10 nm for most materials. The strong electric field generated by the laser light is strong enough to remove the electrons from the bulk material from the penetrated volume. This process occurs within 10 ps of the pulse of a ns laser and is caused by non-linear processes such as the ionization of multiple photons that are reinforced by microscopic cracks on the surface, holes and nodules, which increase the electric field. Free electrons oscillate within the electromagnetic field of laser light and can collide with the atoms of the bulk material thus transferring part of their energy to the network of the target material within the region of the surface. The surface of the target is heated and the material vaporizes.

### **3.1.10.2 Dynamic of the plasma**

In the second stage, the material expands in a plasma parallel to the normal vector of the target surface towards the substrate due to the repulsion and recoil of Coulomb from the target surface. The spatial distribution of the plume depends on the background pressure inside the PLD chamber. The density of the plume can be described by a  $\cos^n(x)$  law with a shape similar to a Gaussian curve. The dependence on the shape of the plume with pressure can be described in three stages:

- The vacuum stage, where the plume is very narrow and directed forward; there is almost no dispersion with the background gases.
- The intermediate region where the division of high energy ions of less energetic species can be observed. Flight time data (TOF) can be adjusted to a shock wave model; However, other models may also be possible.
- A high-pressure region where we find an expansion more similar to the diffusion of the excised material. Naturally, this dispersion also depends on the mass of the background gas and can influence the stoichiometry of the deposited film.

The most important consequence of increasing the background pressure is the deceleration of high-energy species in the expanding plasma column. It has been shown that particles with kinetic energies of about 50 eV can re-spray the film already deposited on the substrate. This results in a lower deposition rate and can also result in a change in the stoichiometry of the film.

### **3.1.10.3 Deposition of the ablation material on the substrate**

The third stage is important to determine the quality of the deposited films. High-energy species ablated from the target are bombarding the surface of the substrate and can cause damage to the surface by scattering atoms from the surface but also by causing the formation of defects in the deposited film[90]. The scattered species of the substrate and the particles emitted from the target

form a collision region, which serves as a source for particle condensation. When the condensation rate is sufficiently high, a thermal equilibrium can be achieved and the film grows on the surface of the substrate at the expense of the direct flow of ablation particles and the thermal equilibrium obtained.

#### 3.1.10.4 Nucleation and growth of the film on the substrate surface

The nucleation process and the growth kinetics of the film depend on several growth parameters that include:

- **Laser parameters:** various factors such as laser fluence [Joule/cm<sup>2</sup>], laser energy and the degree of ionization of the material removed will affect film quality, stoichiometry [91] and deposition flow. In general, nucleation density increases as the deposition flow increases.
- **Surface temperature:** the surface temperature has a great effect on nucleation density. In general, nucleation density decreases as the temperature increases [92].
- **Substrate surface:** nucleation and growth can be affected by surface preparation (such as chemical etching [93], improper cutting of the substrate and roughness of the substrate).
- **Background pressure:** common in oxide deposition, an oxygen background is needed to ensure stoichiometric transfer from the target to the film. If, for example, the oxygen background is too low, the film will grow from stoichiometry, which will affect the nucleation density and the quality of the film [94].

In PLD, great supersaturation occurs in the substrate for the duration of the pulse. The pulse lasts about 10–40 microseconds depending on the laser parameters. This high supersaturation causes a very large nucleation density on the surface compared to molecular beam epitaxy or sputtering. This nucleation density increases the smoothness of the deposited film.

In PLD, [depending on the deposition parameters above] three growth modes are possible:

- **Step-flow growth** – All substrates have a miscut associated with the crystal. These miscut give rise to atomic steps on the surface. In step-flow growth, atoms land on the surface and diffuse to a step edge before they have a chance to nucleated a surface island. The growing surface is viewed as steps traveling across the surface. This growth mode is obtained by deposition on a high miscut substrate, or depositing at elevated temperatures [95].
- **Layer-by-layer growth** – In this growth mode, islands nucleate on the surface until a critical island density is reached. As more material is added, the islands continue to grow until the islands begin to run into each other. This is known as coalescence. Once coalescence is reached, the surface has a large density of pits. When additional material is added to the

surface the atoms diffuse into these pits to complete the layer. This process is repeated for each subsequent layer.

- **3D growth** – This mode is similar to the layer-by-layer growth, except that once an island is formed an additional island will nucleate on top of the 1<sup>st</sup> island. Therefore, the growth does not persist in a layer-by-layer fashion, and the surface roughens each time material is added.

There are many different arrangements to build a deposition chamber for PLD. The target material that is evaporated by the laser is usually found as a rotating disk attached to a support. However, it can also be sintered in a cylindrical bar with rotational movement and a translation movement up and down along its axis. This special configuration allows not only the use of a synchronized reactive gas pulse, but also of a multi-component target rod with which films of different multiple layers can be created.

Some factors that influence the deposition rate:

- Target material
- The energy of the laser pulse.
- The laser repetition rate
- The substrate temperature
- Distance from target to substrate
- Type of gas and chamber pressure (oxygen, argon, etc.)

#### **3.1.10.5. advantage of PLD method:**

- conceptually simple: a laser beam vaporizes a target surface, producing a film with the same composition as the target.
- versatile: many materials can be deposited in a wide variety of gases over a broad range of gas pressures.
- cost-effective: one laser can serve many vacuum systems.
- fast: high quality samples can be grown reliably in 10 or 15 minutes.
- scalable: as complex oxides move toward volume production.
- Compatible with oxygen and other reactive gases
- Deposition can occur in both inert and reactive background gasses.

#### **3.1.10.6. Disadvantage of PLD method:**

- Generation of Particulates in the deposition process.
- Composition and thickness depend on the deposition conditions.
- Difficult to scale-up to large wafers/deposition areas.

- The ablation plume cross section is generally small and this limits the sample size
- Variation in the thickness of the film

## 3.2 Introduction to Characterization and measurement techniques

This chapter includes the basic measurement techniques we have employed in this study. The structural, optical, morphological and luminescence properties of the thin films of  $\text{Y}_2\text{SiO}_5:\text{Ce}^{3+}$ , deposited by the pulsed laser deposition method (PLD) has been analysed with these measurement techniques. Several characterization techniques were used to analyse the PLD deposited thin films of  $\text{Y}_2\text{SiO}_5:\text{Ce}^{3+}$  which are developed under different deposition conditions. The structural properties of the samples were studied using a Bruker D8 Advance Germany X-ray powder diffraction (XRD) model equipped with Cu K-alpha radiation ( $\lambda = 1.5406\text{\AA}$ ), for a  $2\theta$  diffraction angle of  $10\text{-}800$  and the grazing incident X-ray diffraction (GIXRD) has been also used to measure the diffraction pattern at lower angles ( $0.05\text{-}1.50$ ). moreover, supportive measurement technique for the for the XRD i.e., the Raman spectroscopy measurements has been also employed. The optical properties have studied by UV-Vis absorbance spectra that have been recorded from  $200\text{-}800$  nm for thin films deposited on glass substrates. In addition, the luminescence properties have also been investigated by the photoluminescence spectrophotometer (PL) at room temperature. The morphology of the samples was studied using a high-resolution scanning electron microscope (SEM) and an atomic force microscope (AFM). The elemental composition was determined using energy dispersive X-ray spectroscopy. The most important characteristics of these characterization techniques are described in the following sections.

### 3.2.1 X-ray diffraction (XRD)

X-rays are electromagnetic radiation with typical photon energies in the range of  $100$  eV to  $100$  keV. For diffraction applications, only short wavelength X-rays on the order of a few angstroms are used. Because the wavelength of X-rays is comparable to the size of atoms, they are ideal for probing the structural arrangement of atoms and molecules in a wide range of materials. Energetic X-rays can penetrate deep into materials and provide information about the bulk structure[6]. X-rays are generally produced by X-ray tubes or by synchrotron radiation. In an X-ray tube, which is the main source of X-rays used in X-ray laboratory instruments, X-rays are generated when a focused electron beam accelerated through a high-voltage field bombards a stationary or rotating solid target as shown in Fig.4.2. When the electrons collide with the atoms of the target and slow down, a continuous spectrum of X-rays is emitted, called Bremsstrahlung radiation. High energy electrons also eject electrons from the inner shell in atoms through the ionization process. When a free

electron fills the shell, an X-ray photon with an energy characteristic of the target material is emitted. when the energy of the electrons accelerated towards the target becomes sufficiently high to dislocate the electrons of the k -shell, i.e., electrons of the L and M shells move to take the place of those dislocated. Each of these electronic transitions produces X-rays with a wavelength that depends on the exact structure of the bombed atom. A transition from L to K shell produces  $K\alpha$  X-ray, while the transition from M to K shell produces  $K\beta$  X-rays (see Fig. 4.3). These characteristic X-rays have a much higher intensity than those produced by continuous spectra,  $K\alpha$  X-rays having a higher intensity than  $K\beta$  X-rays. The important point here is that the wavelengths of these characteristic X-rays are different for each atom in the periodic table (of course, only the elements with higher atomic numbers have shell electrons L and M which can undergo transitions to produce X-rays). The energy  $E$  of an X-ray photon and its wavelength  $\lambda$  are related by the equation  $E = hc/\lambda$ , where  $h$  is Planck's constant and  $c$  the speed of light. The incident radiation on a crystal is diffused in various ways. When the wavelength of the radiation is similar to that of the spacing of the atoms in a crystal, scattering, which is called diffraction, gives rise to a set of well-defined beams arranged with a characteristic geometry, to form a diffraction pattern. The positions and intensities of the diffracted beams are a function of the arrangement of the atoms in space and certain other atomic properties, in particular, in the case of X-rays, the atomic number of the atoms. Thus, if the positions and intensities of the diffracted beams are recorded, it is possible to deduce the arrangement of the atoms in the crystal and their chemical nature[96]. X-ray diffraction (XRD) is one of the most vital analytical instruments in modern laboratory and is an effective non-destructive technique which is used to study the structural properties of crystalline and amorphous materials, phase identification, determination of grain size, evaluation of lattice constants and determination of the degree of crystallinity in a mixture of amorphous and crystalline substances[97]. Where Crystalline solids are solid materials which have regular ordered arrays of components held together by uniform intermolecular forces. Their characteristics are what we associate solids with. They are firm, hold a definite and fixed shape, are rigid and incompressible. They generally have geometric shapes and flat faces. To understand crystals, we need to understand their structure. The arrangement of the particles in a crystalline solid is very ordered. These items are arranged in a repeating pattern of a three-dimensional network. This network is known as the crystal network and the smallest unit of a crystal is a unit cell. Examples of crystalline materials are: sodium chloride, ice, metals, and diamonds,

Amorphous solids are rigid structures but they do not have a well-defined shape. They do not have a geometric shape. So, they are not crystalline. This is why they have no edges like crystals. The most common example of an amorphous solid is glass. Gels, plastics, various polymers, wax, thin films are also good examples of amorphous solids. This variation in the characteristics of solids

occurs due to the arrangement of their molecules. Here, the particles of matter do not form the three-dimensional network structure that we see in solids. Some natural amorphous solids have impurities that prevent such a structure from forming. So, they have short-lived arrangement of molecules. Amorphous solids break into uneven pieces with irregular edges. And they have no separate arrangement or shape of molecules. Therefore, they cannot be identified by their structure as crystals.

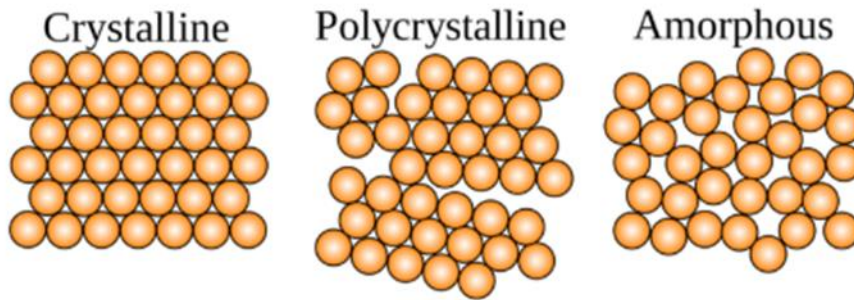


Fig. 3.2: Schematic diagram of crystalline and amorphous solids

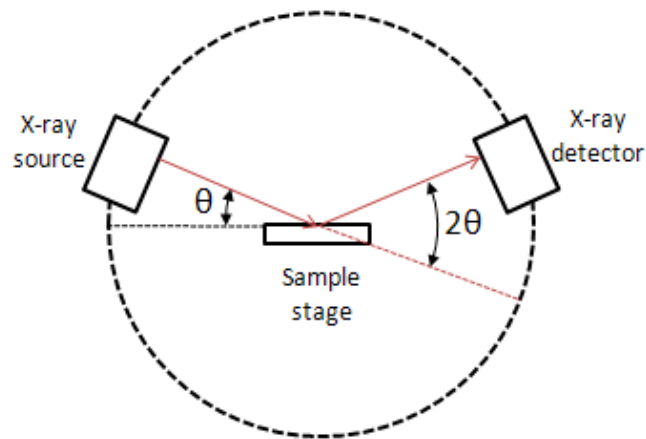


Fig. 3.3: Schematic diagram of the X-ray diffractometer[98].

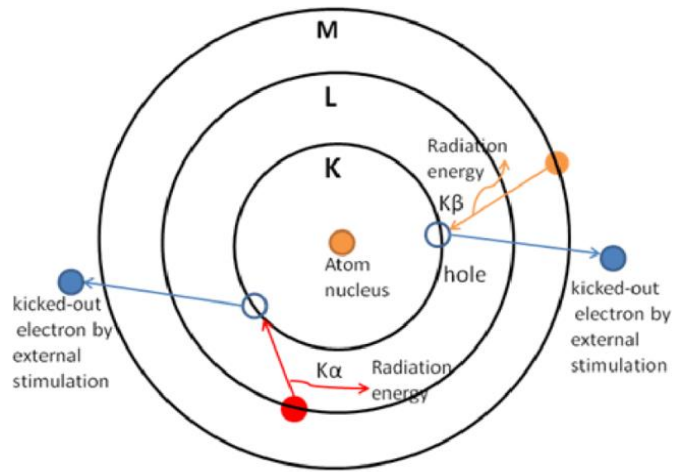


Fig. 3.4: Characteristic X-ray radiations[99].

### 3.2.1.1. Bragg's law

A beam of radiation will only be diffracted if it strikes a set of planes in a crystal, defined by Miller's indices (hkl), if the geometry of the situation meets very specific conditions, defined by Bragg's law:

$$n\lambda = 2d_{hkl}\sin\theta \dots\dots\dots 3.1$$

where n is an integer,  $\lambda$  is the wavelength of the radiation,  $d_{hkl}$  is the interplanar spacing (the perpendicular separation) of the (hkl) planes and is the diffraction angle or Bragg angle (Fig. 3.5). Note that the angle between the direction of the incident and diffracted beam is equal to  $2\theta$ . Bragg's law defines the conditions under which diffraction occurs, and gives the position of a diffracted beam, without any reference to its intensity.

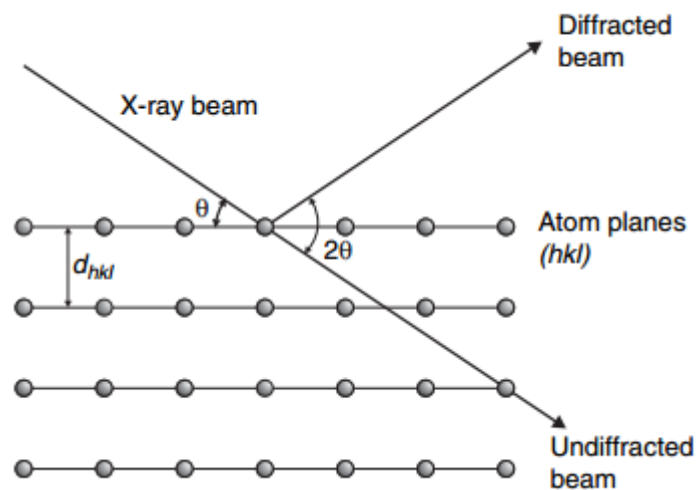


Fig. 3.5: The geometry of Bragg's law[96].

The d-spacing between the atomic planes is given by:



$$d_{hkl} = \frac{n\lambda}{2\sin\theta} \dots\dots\dots 3.2$$

The relationship between the lattice parameters and the d-spacing depends on the type of the unit cell. For a monoclinic structure of Y<sub>2</sub>SiO<sub>5</sub>; the perpendicular spacing (d spacing) between parallel planes (miller indices hkl) in relation to the lattice parameters, it can be calculated using equation 3.3.

$$\frac{1}{d_{hkl}^2} = \frac{1}{\sin^2\theta} \left( \frac{h^2}{a^2} + \frac{k^2\sin^2\theta}{b^2} + \frac{l^2}{c^2} - \frac{2hkl\cos\theta}{ac} \right) \dots\dots\dots 3.3$$

Where  $d_{hkl}$  is interplanar spacing, ( $a$ ,  $b$ , and  $c$ ) is the lattice parameter and  $h$ ,  $k$  and  $l$  are the reciprocal of the intercepts in three different dimensions (axes) respectively of a unit cell known as miller indices. The diffracted X-rays of a plane are then detected, processed and counted by scanning the sample through a range of angles  $2\theta$ , all possible directions of diffraction of the lattice must be obtained due to the random orientation of the sample. The conversion of diffraction peaks into d spacing allows the identification of materials because each material has a set of unique d spacing [100] Typically, this is achieved by comparing the d spacing with the reference files of the Joint Committee on Powder Diffraction and Standards (JCPDS). In this study, a Bruker D8 advanced X-ray diffractometer (XRD) equipped with monochromatic Cu-K $\alpha$  radiation = 1.5406Å and a resolution of 0.02° was used. The position of the diffraction peaks and the relative intensities can be modified by the existence of various types of defects such as a small number of dislocations in crystals of millimeter dimensions. The small size of the grain size can be considered as another type of defect and can modify the widths of the diffraction peaks. Very small crystals cause peak broadening. The size of the crystallites can be easily calculated using the full width at half maxima (FWHM), the position of the peak and the wavelength using Scherrer’s formula given in equation 3.4.

$$D = \frac{k\lambda}{\beta\cos\theta} \dots\dots\dots 3.4$$

Where D is the crystallite size of the particle, K is the shape factor (K = 0.9),  $\lambda$  is the wavelength of the incident X-ray;  $\theta$  is the Bragg’s diffraction angle; and  $\beta$  is the full width at half-maximum in radians.

### 3.2.2 Photoluminescence spectroscopy (PL)

Photoluminescence (PL) is the emission of light from any form of matter after absorption of photons (electromagnetic radiation). It is one of the many forms of luminescence (emission of light) and is initiated by photoexcitation (i.e. photons which excite electrons at a higher energy level in an atom)[101]. Photoluminescence spectroscopy is a non-contact, versatile, non-destructive and

powerful optical method for probing the electronic structure of materials. The light is directed onto a sample, where it is absorbed and transmits excess energy into the material in a process called photo-excitation[102]. Photoluminescence is the luminescence by which electromagnetic radiation (photons) is used to excite a material, usually using ultraviolet light. Excitation occurs when light is directed at a sample and it is absorbed and transmits excess energy to the material. This excess energy can be released by the sample through the emission of light [103], a process called luminescence. When luminescence is accompanied by photoexcitation, it is called photoluminescence. The photo-excitation causes the electrons in the material to move in allowed excited states. When these electrons return to their equilibrium state, excess energy is released and may include the emission of light (a radiative process) or not (a non-radiative process). The energy of the light emitted (photoluminescence) is linked to the difference in energy levels between the two-electron states involved in the transition between the excited state and the equilibrium state. The amount of light emitted is related to the relative contribution of the radiative process[6]. In PL measurement, the emission properties of materials are measured by using photons to induce excited electronic states in the material system and by analysing the optical emission when these states are relaxed. The sample is excited by light of certain wavelengths to create electron-hole pairs in the sample. The system is connected to a computer to display the excitation and emission spectra. Therefore, the excitation and emission spectra can be recorded separately. In the excitation spectra, the emission monochromator is fixed at any emission wavelength while the excitation wavelength is scanned within a certain spectral range. In the emission spectra, the excitation wavelength is fixed and the light intensity emitted is measured at different wavelengths by scanning the emission monochromator[104]. The apparatus for measuring the spectral characteristics of the phosphors is shown in Fig. 3.6. The excitation source consists of the light source and a monochromator, which selects a specific wavelength range in the incoming light. (The monochromator can be replaced by a filter). The light emitted by the sample is analysed by a monochromator equipped with a light detector. The light detector transforms photons into electrical signals. Once the signals are amplified, they are recorded, usually on a strip chart recorder. It is often convenient to collect all spectral data in the form of digitized electrical signals and to use a computer to further process the data.

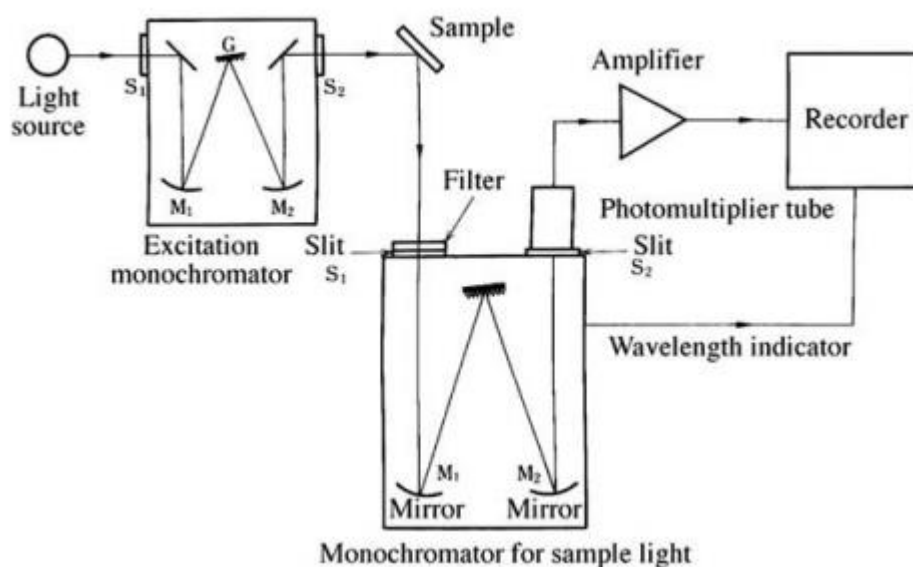


Fig. 3.6: Spectroscopic measurement apparatus[105].

In crystalline inorganic semiconductors where an electronic band structure is formed, secondary emission can be more complicated since events can contain both coherent contributions such as resonant Rayleigh scattering where a fixed phase relationship with the deriving light field is maintained (i.e. energetically elastic lossless processes) are involved), and incoherent contributions (or inelastic modes where certain energy channels in an auxiliary loss mode)[106]. In a typical PL experiment, a semiconductor is excited with a light source which supplies the photons with energy greater than the energy of the band gap. The incoming light excites a polarization which can be described with the semiconductor Bloch equations[107, 108]. Once the photons are absorbed, the electrons and the holes are formed with finite pulses  $\mathbf{K}$  in the conduction and valence bands, respectively. The excitations then undergo a relaxation of energy and momentum towards the minimum band gap. Typical mechanisms are Coulomb scattering and interaction with phonons. Finally, the electrons recombine with holes under the emission of photons. In this study, the excitation and emission spectra were measured at room temperature using a Cary Eclipse fluorescence spectrophotometer model: LS-55 with a built-in 150W xenon flash lamp.

### 3.2.3 Ultraviolet-Visible (UV-VIS) Spectroscopy

Ultraviolet-visible spectroscopy or ultraviolet-visible spectrophotometry (UV-Vis or UV/Vis) refers to absorption spectroscopy or reflectance spectroscopy in a part of the ultraviolet and of all adjacent visible spectral regions. This means that it uses light in the visible and adjacent ranges. The absorption or reflectance in the visible range directly affects the perceived color of the chemicals involved. In this region of the electromagnetic spectrum, atoms and molecules undergo electronic transitions. Absorption spectroscopy is complementary to fluorescence spectroscopy, in the sense

that fluorescence deals with transitions from the excited state to the ground state, while absorption measures the transitions from the ground state to the state excited[109]. UV spectroscopy is a type of absorption spectroscopy in which light from the ultraviolet region (200-400 nm) is absorbed by the molecule. The absorption of ultraviolet radiation causes the excitation of electrons from the ground state to a higher energy state. The energy of the absorbed ultraviolet radiation is equal to the energy difference between the ground state and the higher energy states ( $\Delta E = hf$ ). Ultraviolet (UV) and visible (VIS) spectrophotometry has become the method of choice in most laboratories concerned with the identification and quantification of organic and inorganic compounds in a wide range of products and processes. The electromagnetic spectrum goes from gamma radiation, with the shortest wavelength (1pm), to low frequency radiation, with the longest wavelength well beyond conventional radio waves (100 Mm or 100,000 km). Human beings can only directly detect a very small part of this spectrum, the thermal perception of radiant heat being sensitivity to infrared radiation (IR), and sight is limited to the VIS spectrum. UV-VIS spectrophotometry concerns the UV range covering 200-380 nm and the VIS range covering 380-770 nm. Many instruments will offer a slightly wider range from 190nm in the UV region to 1100nm in the near infrared (NIR) region[110]. When a beam of radiation hits an object, it can be absorbed, transmitted, scattered, reflected or it can excite fluorescence. The ultraviolet-visible spectrometer (UV-VIS) has become the most important analytical instrument in the modern laboratory. It is highly preferable in terms of simplicity, versatility, speed and precision. It measures the percentage of absorbance (% A), the percentage of reflectance (% R) and the percentage of transmittance (% T) in the visible ultraviolet spectral region. An absorbance versus wavelength graph measures the transitions from the ground state to an excited state (excitation). Obviously, it is the reverse of photoluminescence where the transition takes place from the excited state to the ground state[102].

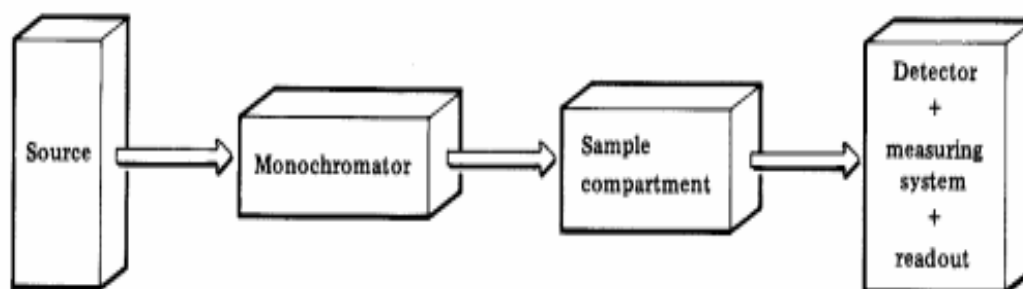


Fig. 3.7: Basic construction of spectrometer

The essential components of UV-visible spectrophotometer instrumentation shown in Fig.3.7 includes:

- A Stable radiant energy source.

- A dispersion device (monochromator), to break the polychromatic radiation into component wavelength (or) bands of wavelengths.
- Transport vessels (cuvettes), to hold the sample.

One or more detectors to measure the intensity of radiation For analytical purposes, two main propositions define the laws of light absorption:

**A. Lambert’s Law:** The proportion of incident light absorbed by a transparent medium is independent of the intensity of the light (provided that there is no other physical or chemical change to the medium). Therefore, successive layers of equal thickness will transmit an equal proportion of the incident energy.

Lambert’s law is expressed by:

$$T = \frac{I}{I_0} \dots\dots\dots 3.5$$

Where T is the transmittance, I is the intensity of the transmitted light and I<sub>0</sub> is the intensity of the incident light. The percentage of transmittance can also express as:

$$\%T = \frac{I_T}{I_0} * 100 \dots\dots\dots 3.6$$

**B. Beer’s Law:** The absorption of light is directly proportional to both the concentration of the absorbing medium and the thickness of the medium in the light path.

A combination of the two laws (known jointly as the Beer-Lambert Law) defines the relationship between absorbance (A) and transmittance (T).

$$A = \log \frac{I_0}{I} = \log \frac{100}{T} = \epsilon cb \dots\dots\dots 3.7$$

Where, where A is absorbance, ε is molar absorptivity, c is molar concentration and b is path length. It is important to note that ε is a function of wavelength and so the Beer-Lambert law is true only for light of a single wavelength, or monochromatic light.

In this work, a Perkin Elmer Scan-Lambda 950 UV-Vis spectrophotometer (LAMBDA™ 950) was used to record the absorbance characteristics of the samples.

### 3.2.4. Scanning Electron Microscope (SEM)

Electron microscopes use electrons for imaging, much like light microscopes use visible light. SEMs use a specific set of coils to scan the beam in a raster-like pattern and use electrons that are reflected or knocked from the region near the surface of a sample to form an image. Since the wavelength of

electrons is much smaller than the wavelength of light, the resolution of SEM is greater than that of an optical microscope[111].

There are two main types of electron microscopes:

1. The transmission electron microscope (TEM), which detects electrons that pass through a very thin specimen;
2. The scanning electron microscope (SEM), which uses the electrons that are reflected or knocked off the near-surface region of a sample to create an image.

We focus on SEM. A schematic representation of the SEM technology is illustrated in Fig. 3.8. In this type of electron microscope, the electron beam scans the sample according to a raster model. But first, the electrons are generated at the top of the column by the electron source. These are emitted when their thermal energy exceeds the working function of the source material. They are then accelerated and attracted by the positively charged anode. They are then accelerated and attracted by the positively charged anode.

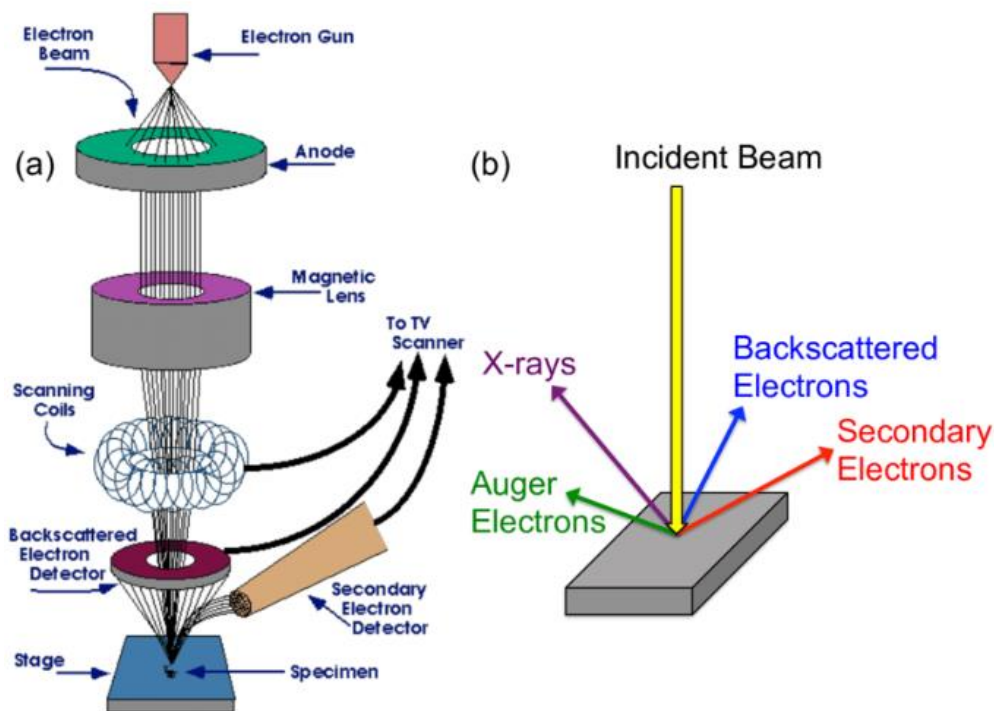


Fig. 3.8. Schematic representation of the basic SEM components[112].

Compared to an optical microscope, the electron microscope achieves a much higher resolution and magnification by taking advantage of the wave aspect of the electrons. The wavelength of an electron is generally 1/100,000 of that of visible light. Resolutions of 50pm and a magnification of 10 million X could be obtained, much better than the resolution of 200 mm and the magnification of 2000X of a laboratory optical microscope. The principle of imaging with an electron microscope is simple: the electron beam released by the electron gun will be accelerated due to the potential

difference. The accelerated electron beam will then be focused on the sample rather than the light, then the transmitted or reflected electrons will be amplified and synchronized to give enlarged useful images. The entire electron column must be under vacuum. Like all components of an electron microscope, the electron source is sealed inside a special chamber to preserve the vacuum and protect it from contamination, vibration or noise. Although the vacuum protects the electron source from contamination, it also allows the user to acquire a high-resolution image. In the absence of vacuum, other atoms and molecules may be present in the column. Their interaction with electrons deflects the electron beam and reduces the quality of the image. In addition, a high vacuum increases the efficiency of electron collection by the detectors in the column. Scanning electron microscopy (SEM) is used to study the topographic and morphological structures of samples at very high magnifications of up to more than 30,000 X. During SEM analysis, a well-defined electron beams energetically and highly focused is scanned through a sample. The electron beam is focused on a surface to create an image. The beam electrons interact with the sample, producing various signals which can be used to obtain information on the topography and composition of the surface. Similar to light microscopes, lenses are used to control the path of electrons. Because electrons cannot pass through glass, the lenses used here are electromagnetic. They simply consist of coils of wires inside metal pole pieces. When current flows through the coils, a magnetic field is generated. Since electrons are very sensitive to magnetic fields, their path inside the microscope column can be controlled by these electromagnetic lenses - simply by adjusting the current applied to them. Generally, two types of electromagnetic lenses are used (condenser and objective lenses). The condenser lens is the first lens that electrons meet when they move towards the sample. This lens converges the beam before the cone of the electron beam opens and is again converged by the objective lens before touching the sample. The condenser lens defines the size of the electron beam (which defines the resolution), while the main role of the objective lens is to focus the beam on the sample. The scanning electron microscope's lens system also contains the scanning coils, which are used to frame the beam on the sample. The interaction of electrons with a sample can lead to the generation of many different types of electrons, photons or irradiations. In the case of SEM, the two types of electrons used for imaging are backscattered (BSE) and secondary electrons (SE). The backscattered electrons belong to the primary electron beam and are reflected after the elastic interactions between the beam and the sample. On the other hand, the secondary electrons come from the atoms of the sample; they are the result of inelastic interactions between the electron beam and the sample.

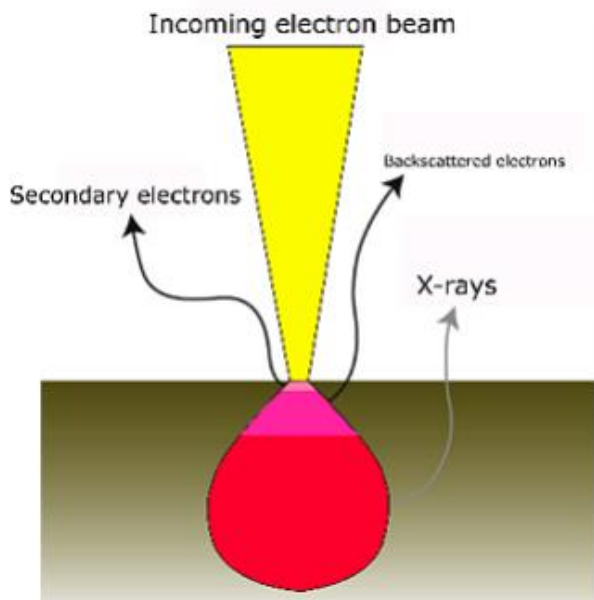


Fig. 3.9. Different types of signals used by a SEM and the area from which they originate[113].

BSE comes from deeper regions of the sample (Fig. 3.9), while SE comes from surface regions. Consequently, BSE and SE convey different types of information. BSE images show a high sensitivity to differences in atomic number: the higher the atomic number, the brighter the material appears in the image.

### 3.2.5 Atomic Force Microscope (AFM)

Atomic force microscopy (AFM) is a type of scanning probe microscopy (SPM), with a demonstrated resolution in the order of fractions of a nanometre, more than 1000 times better than the optical diffraction limit. Information is collected by “sensitivity” or “touching” the surface with a mechanical probe[114]. The AFM has three main capabilities: force measurement, topographic imaging’s, and manipulation. In force measurement, AFMs can be used to measure the forces between the probe and the sample based on their mutual separation. This can be applied to perform a force spectroscopy, to measure the mechanical properties of the sample, such as the Young’s modulus of the sample, a measure of stiffness. For imaging, the reaction of the probe to the forces that the sample imposes on it can be used to form an image of the three-dimensional shape (topography) of a sample surface at high resolution. This is achieved by raster scanning the position of the sample with respect to the tip and recording the height of the probe that corresponds to a constant probe-sample interaction. In manipulation, the forces between tip and sample can also be used to change the properties of the sample in a controlled way. Examples of this include atomic manipulation, scanning probe lithography and local stimulation of cells. The AFM uses a probe, silicon tip and cantilever spring, to record the surface topography of the measuring samples. While scanning, the force between the tip and the sample is measured by monitoring the deflection of the



cantilever. The deflection of the cantilever is controlled by the optical lever technique. A beam of a laser diode as shown in (Fig. 310) is focused on the end of the cantilever and the position of the reflected beam is controlled by a position sensitive detector[115]. The main difference between atomic force microscopy and competitive technologies, such as optical microscopy and electron microscopy, is that AFM does not use lenses or beam irradiation. Therefore, it does not suffer a limitation in spatial resolution due to diffraction and aberration, and it is not necessary to prepare a space to guide the beam (creating a vacuum) and stain the sample. The detector of AFM measures the deflection (displacement with respect to the equilibrium position) of the cantilever and converts it into an electrical signal. The intensity of this signal will be proportional to the displacement of the cantilever. In the current study the AFM images were collected by using the Shimadzu SPM - 9600 model.

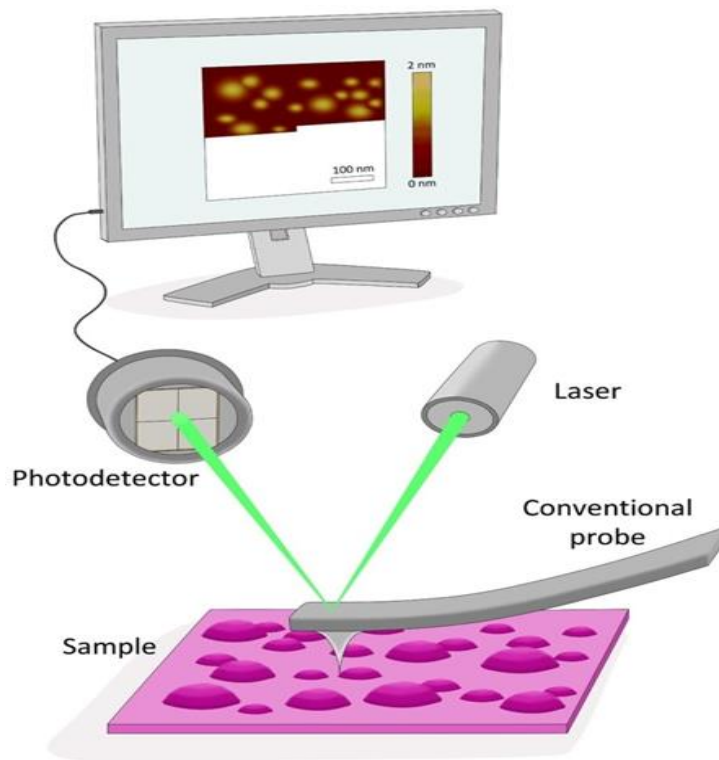


Fig. 3.10: schematic diagram of AFM setup[116].

The AFM can be operated in three modes namely, the contact, noncontact and tapping mode. In the contact mode, the tip is “dragged” across the surface of the sample and the contours of the surface are measured using the deflection of the cantilever directly or, more commonly, using the feedback signal required to keep the cantilever in a constant position[117]. In tapping/bypass mode, the cantilever moves to oscillate up and down at or near its resonance frequency[117]. This oscillation is commonly achieved with a small piezoelectric element in the cantilever support, but other possibilities include an AC magnetic field (with magnetic cantilever), piezoelectric cantilever or periodic heating with a modulated laser beam. In non-contact atomic force microscopy mode, the

tip of the cantilever does not make contact with the surface of the sample. The cantilever has oscillated in its resonant frequency (frequency modulation) or just above (amplitude modulation) where the amplitude of the oscillation is typically a few nanometres (<10 nm) to a few picometers[118].

### 3.2.6 Energy Dispersive X-ray Spectroscopy (EDS)

It is an analytical technique used for elemental analysis or chemical characterization of a sample. It is based on the interaction of some source of X-ray excitation and a sample. Its characterization capabilities are due in large part to the fundamental principle that each element has a unique atomic structure that allows a unique set of peaks in its electromagnetic emission spectrum[119] (which is the main principle of spectroscopy). Energy Dispersive X-Ray Spectroscopy (EDS or EDX) is a chemical microanalysis technique used in conjunction with scanning electron microscopy (SEM). The EDS technique detects x-rays emitted from the sample during bombardment by an electron beam to characterize the elemental composition of the analysed volume. When the sample is bombarded by the electron beam of the SEM, the electrons are ejected from the atoms that comprise the surface of the sample. The resulting electron vacancies are filled by electrons of a higher state, and an x-ray is emitted to balance the energy difference between the states of the two electrons. X-ray energy is characteristic of the element from which it was emitted. The EDS X-ray detector measures the relative abundance of X-rays emitted against its energy. The detector is typically a lithium-derived silicon solid state device. When an incident x-ray hits the detector, it creates a pulse of charge that is proportional to the energy of the x-ray. The charge pulse is converted into a voltage pulse (which remains proportional to the X-ray energy) by a load sensitive preamplifier. The signal is then sent to a multichannel analyser where the pulses are sorted by voltage. The energy, determined from the voltage measurement, for each incident x-ray is sent to a computer for display and subsequent evaluation of data. The X-ray energy spectrum versus counts is evaluated to determine the elemental composition of the sampled volume[119]. The number and energy of the X-rays emitted from a specimen can be measured by an energy-dispersive spectrometer. As the energies of the X-rays are characteristic of the difference in energy between the two shells and of the atomic structure of the emitting element, EDS allows the elemental composition of the specimen to be measured[119, 120].

EDS set up comprises four primary components:

- the excitation source (electron beam or x-ray beam)
- the X-ray detector
- the pulse processor
- the analyser.

The excess energy of the electron that migrates to an inner shell to fill the newly created hole can do more than emit an X-ray [121]. Often, instead of X-ray emission, the excess energy is transferred to a third electron from a further outer shell, prompting its ejection. This ejected species is called an Auger electron, and the method for its analysis is known as Auger electron spectroscopy (AES)[121]. X-ray photoelectron spectroscopy (XPS) is another close relative of EDS, utilizing ejected electrons in a manner similar to that of AES. Information on the quantity and kinetic energy of ejected electrons is used to determine the binding energy of these now-liberated electrons, which is element-specific and allows chemical characterization of a sample. EDS is often contrasted with its spectroscopic counterpart, WDS (wavelength dispersive X-ray spectroscopy). WDS differs from EDS in that it uses the diffraction of X-rays on special crystals to separate its raw data into spectral components (wavelengths). WDS has a much finer spectral resolution than EDS. WDS also avoids the problems associated with artifacts in EDS (false peaks, noise from the amplifiers, and microphonics).

### 3.3 Experimental procedures

Deposition of  $\text{Y}_2\text{SiO}_5:\text{Ce}^{3+}$  thin films with different deposition conditions were carried out using Neodymium-yttrium aluminium garnet (Nd –YAG) laser with a wavelength of 266 nm and energy of 4.67 eV, the pulse duration was 8 ns with a repetition rate of 10 Hz. The laser fluence was 10mJ/cm<sup>2</sup> in all the depositions. The background pressure was pumped to a base pressure of  $5.6 \times 10^{-5}$  mbar before introducing the deposition gas which were used for the deposition conditions. In the first manuscript, the thin films have grown at a different substrate to the target distances of 4.0, 4.5, 5, 5.5, and 6.0 cm on the silicon (100) substrate. Argon background gas was used in this deposition conditions. And the argon pressure and the substrate temperature were set at 350 °C. When the thin film deposition was carried out by varying the substrate temperature, keeping the other parameters constant as we did in chapter-4, the temperature was set at ambient temperature, 150, 250, 350, 450, and 600 °C. The deposition gas was maintained at 7.5 mT with a substrate distance fixing at 5 cm. To study the effect of deposition gases on the material properties of the deposited material, it was used Vacuum, Oxygen Argon and Nitrogen as depositing gases at a deposition pressure of 10mT. the effect of oxygen deposition pressure has also employed at a deposition pressure of 1.5, 20, 40, 60 and 100 mT by keeping the substrate temperature and substrate distance 250 °C and 5 cm respectively. More over the influence of deposition on the structural, morphological and thermoluminescence properties has studied at a deposition time of 30, 60, 90, 120 and 150 minutes keeping the substrate temperate and substrate distance at 450 °C and 4 cm with a deposition pressure of 10mT. A glass substrate was used alongside the silicon substrate to examine the optical properties of the deposited films for all deposition conditions in all the manuscripts. The silicon and the glass

substrate which are cut with an approximate area of  $2 \text{ cm}^2$  were cleaned with a soap and distilled water at first. It was then cleaned separately with ethanol and acetone after ultrasonically bathed for about 10 to 15 minutes. Finally, the substrates were rinsed with deionized water and dried with nitrogen gas. The mass of the substrates was measured by electronic micro balance before and after depositions to estimate the mass of the film, which helps us to calculate the thickness of the film deposited on the silicon substrates. A commercial powder of  $\text{Y}_2\text{SiO}_5:\text{Ce}^{3+}$  supplied by (Phosphor Technology Ltd, Norton Park, Norton Road, Stevenage, Hertfordshire, SG1 2BB, England) was used to prepare the pellet, a mass of 11g powder was used to make the pellet. It was mechanically pressed using hydraulic press at a pressure of 12.5 Torr. The pellet was annealed at  $850^\circ \text{C}$  for 8 hours to remove any moisture present on the surface of the pellet.

X-ray diffractometer using a Bruker D8 advance operating at a voltage of 40 kV and a current of 40 mA using  $\text{Cu K}\alpha = 0.15406 \text{ nm}$  was used to study the crystalline structure of the thin films. SEM and EDS were used to analyse the morphology and the elemental composition of the deposited films, respectively. Photoluminescence measurement which was operating at room temperature using the Cary Eclipse fluorescence spectrometer (Model: LS-55) with an integrated 150W Xenon lamp was used to measure the electronic emission and excitations. The UV-VIS spectrometer was also used to study the optical property in the wavelength range of 200 to 800 nm. Grazing incidence X-ray diffractometer (GIXRD) was performed using the Rigaku Smart lab X-ray Diffractometer (Rigaku Corporation, USA). Raman spectroscopy measurement was also used to see the finger print of the material and to analyse the vibrational modes of the molecules. Atomic force microscopy (AFM) with tapping mode was used to study the topography of the thin films. The chromaticity coordinate values of the thin phosphor films were estimated from the 1931 Commission International de l'éclairage (CIE) system using the excitation wavelength wavelengths.

## Chapter 4: Effect of target to substrate distance on the material properties of the $\text{Y}_2\text{SiO}_5:\text{Ce}^{3+}$ thin film by pulsed laser deposition

### 4.1. Introduction

Many deposition techniques have been applied to prepare thin film phosphors of different composition, like chemical deposition [122], electron beam and thermal evaporation [123] and magnetron sputtering [124]. For any functional techniques, depositing a quality thin film at low temperature is the favorite and cost-effective method to apply for deposition techniques. It is for the fulfillment of temperature sensitive phosphor materials in the application wise. Pulsed laser deposition (PLD) is an effective deposition technique in the field of production of superconductors alongside with the evaporation method of the target material [125]. It is fascinating to study PLD as a technique for making new kinds of thin phosphor films and for examining their luminescent and other related properties [126]. PLD is a deposition method for ablation of a material by focusing the pulsed laser on the target material in a vacuum chamber. Beyond a threshold power density, molecules or particles removed from the target and ejected, the plume of material partially ionized due to the interaction between the eliminated molecules and the background gas.

The power density is responsible for the creation of the plasma plume. Depending on the absorption properties of the target material, the wavelength of the laser for ablation and the duration of the pulse can be adjusted. The removed molecules lead towards the substrate and condense to form a thin film on the surface of the substrate [127]. In other words, the evaporated plume condenses on the surface of the substrate to form a thin film. Material flow, repetition rate, growth temperature, substrate type and pressure of background gas, the position of the target from the substrate are some of the important parameters for the thin film growth kinetics and characterization [128]. Doping with RE ions ( $\text{RE}^{3+}$ ) influence the morphological, the size of the particle and the band configuration of the nanocrystals [56]. Doping also performs a crucial role in the quality of luminescence and in the point of the emission bands, which induces practical influences in their applications.

The efficient energy transfer from the semiconductor host to RE ions achieves the enhanced luminescence of  $\text{RE}^{3+}$  ions [19]. RE doped inorganic compounds are a vital class of phosphors due to superb chemical stability, excellent luminescence quality and emission spectrums with various activators [19, 58]. The phosphor materials have useful applications, in the area of lamp industries, radiation dosimetry, cathode ray tubes, photodiodes, lamps, biosensors, X-ray detectors and color screens [129-133]. Yttrium silicate phosphor activated by RE ions shows some interesting practical applications such as long-lasting phosphorescence, plasma display panel (PDP), lasers, X-ray

images, flat screens displays and environmental control, are some of the important applications in which many researchers are recently attracted and given attention to this area [134-136].

The RE ions in which their electronic configuration is in the level of  $4f^n$  gives emission because of the shift in energy between the ground and excited states. Since the  $5s^2$  and  $5p^6$  electrons shelter the  $4f$  electrons, the host material do not have a significant effect on the energy levels of the rare-ions and radiative emission with a spectral width of  $5 - 20 \text{ cm}^{-1}$  looks like those of the free ions in the crystalline host [137]. Thin films have significant benefits over powders, which has good substrate adhesion and reduced gas emissions [138]. Thus, studying thin film phosphors is as important as powder phosphors. Growth mechanisms of rough surface films with less absorbent substrates and optimization of parameters during deposition can increase luminescence capacity of thin films [139].

The host material has two monoclinic crystalline structures. These are phase  $X_1$  at low temperature with space group  $P2_1/c$ , and  $X_2$  with a phase group of  $B2/c$ , which is a high-temperature phase. The transformation temperature between the two phases is approximately  $1190 \text{ }^\circ\text{C}$ . Structural studies show that  $X_1$  and  $X_2$  phases contain tetrahedral oxygen and silicon-free  $\text{SiO}_4$ , and structures  $X_1$  and  $X_2$  have two different  $\text{Y}^{3+}$  sites, with a coordination number of 7 and 9 for phase  $X_1$ , 6 and 7 for phase  $X_2$  [140, 141]. From the Gaussian fitted emission (Fig. 5.8) graph, a broadband that elongates from 400 to 600 nm shows maximum emission points peaked at 438 and 476 nm, which is completely in the blue region that is also in a good agreement with the CIE graph (Fig. 5.10). This can be ascribed to the  $5d \rightarrow 4f$  ( $2F_{5/2}$  and  $2F_{7/2}$ ) transitions of  $\text{Ce}^{3+}$  from low excited state or the donor state to the ground state. The excitation spectrum shows three excitation bands, at 267, 303 and 356 nm, all of which can be attributed to ground state transitions of  $4f^1$  ( $2F_{5/2}$ ) to different components of the excited state of  $5d$  crystal field. Similar results have also reported by references [53, 142-144]. From our literature review study, no study has been conducted on our title and condition used to study the material properties.

In this work,  $\text{Y}_2\text{SiO}_5:\text{Ce}^{3+}$  thin film phosphor materials are deposited to study the effect of substrate to distance on the luminescence, structure and morphology of the thin films.  $\text{Y}_2\text{SiO}_5:\text{Ce}^{3+}$  is an effective luminescent material when irradiated with cathode rays and X-rays. The purpose of this study is to find the optimized condition of the substrate to target distance and studying the corresponding characteristics, which is structurally better from the morphological point of view that can be considered for possible future applications in display technologies.

## 4.2. Results and discussions

### 4.2.1 XRD analyses

The XRD spectra of  $\text{Y}_2\text{SiO}_5:\text{Ce}^{3+}$  thin films deposited at a constant deposition pressure of 0.01 mbar and temperature of  $350^\circ\text{C}$  is shown in Fig. 4.1. The miller indexes are shown for the prominent peaks. The thin film is crystallized in a monoclinic structure of  $\text{Y}_2\text{SiO}_5$  with the value of lattice constants  $a = 10.41 \text{ \AA}$ ,  $b = 6.73 \text{ \AA}$  and  $c = 12.46 \text{ \AA}$  and cell volume  $852.25 \text{ \AA}^3$  and an angle of  $102.5^\circ$  which corresponds to the JCPDS card # 211458.

The average crystallites size was calculated from the most intense peaks (022) using the Scherer equation. Given by equation 3.4. It was found that the average crystallite size was approximately 37 nm. As the target distance increases, the crystallite size gradually decreases with small intervals which can be attributed to the size of the full width at half maximum. Relatively, the film deposited at a distance of the substrate  $d = 5.0 \text{ cm}$  has the highest diffraction peak; this implies that, films of good crystalline quality were obtained at this deposition distance. The temperature of the substrate and the separation distance between the target material and the substrate plays an important role in the development of the thin film. Since the temperature of the substrate is set at  $350^\circ\text{C}$ , its impact is constant to all deposition conditions. The kinetic energy of the species removed from the target material depends on the path between the target and the substrate. As the distance increases, the species is more likely to collide or interact with the plasma plume; as a result, not all the required materials from the target will reach the substrate to form the expected thin film material because of the lost in kinetic energy. The crystallinity of the material can be also ensured from Fig. 5.2 by the position dependent of FWHM. A relative increase in FWHM is observed at  $d = 4.0 \text{ cm}$  and  $d = 5.5$  to  $d = 6.0 \text{ cm}$  compared to  $d = 5.0 \text{ cm}$ . The crystallinity of the material in these positions decreases especially in the larger distances. The reason is that, as the distance increases, the collision of the species with the plasma plume lasts a long time, which leads to the decrease in the kinetic energy of the ejected species from the target material.

The measurement of the thickness of the film is necessary to know the effectively deposited film on the silicon substrate. By taking the mass difference before and after deposition using sensitive mass measuring devices in our case, sensitive electronic microbalance, we estimated the mass of the deposited film.  $X = (m_2 - m_1) / \rho A$  was used for estimating the thickness of the thin film. Where  $m_1$  and  $m_2$  are the mass before and after deposition in grams respectively,  $\rho$  is the density of the material in  $\text{g/cm}^3$  and  $A$  is the area covered by the film in  $\text{cm}^2$ . The estimated film thickness is  $X = 32.0, 70.9, 78.3, 12.0$  and  $10.15 \text{ nm}$  for the corresponding distances of  $d = 4.0, 4.5, 5.0, 5.5$  and  $6.0 \text{ cm}$ , respectively. A slight increase in thickness was observed when the distances increased from 4.0 to

5.0 cm (in this case, the plasma plume did not decrease the energy of the ejected species because of interaction since the mean free path is short and interaction lasts for short time as compared to the distance beyond 5 cm). Moreover, the thickness has decreased as the distance is increased, which can be attributed to the decrease in the deposition rate (When the substrate and target distance is increasing, the time of collision/interaction between the ejected/ablated species and the plasma plume takes long time, which can decrease the kinetic energy of the species. As a result, the deposition rate on the surface of the substrate reduces. The reduction of the deposition definitely leads to decrement of the film thickness). In addition to this as the distance to the substrate increases beyond 5.0 cm, the expansion of the plume increases hemispherically, during which not all particles removed from the target reach the surface of the substrate. This can minimize the deposit rate [145]. This is supported by the EDS results given in Fig. 4.4. The weight composition of the elements increases when the substrate distance increases from 4.0 cm to 5.0 cm and decreases from 5.0 to 6.0 cm.

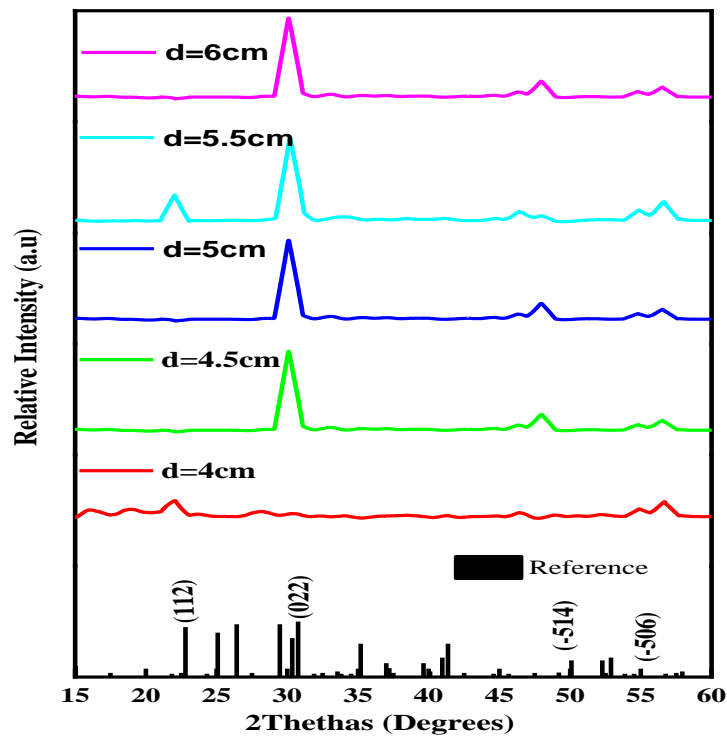


Fig. 4.1: XRD pattern for phosphor thin film of  $Y_2SiO_5:Ce^{3+}$



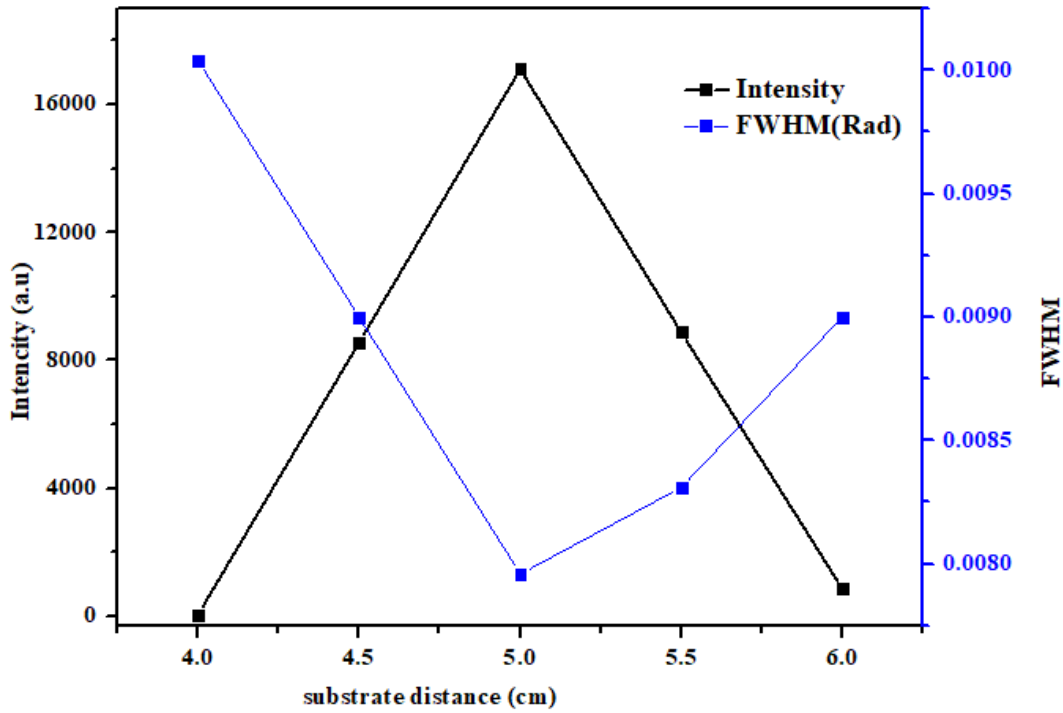


Fig. 4.2: Intensity and FWHM of the intense peak (022) as a function of substrate distance

#### 4.2.2 SEM and EDS analysis

Fig 4.3 shows micrographs of scanning electron micrograph (SEM) for the thin films of  $Y_2SiO_5:Ce^{3+}$  deposited by PLD at lower, medium and higher substrate to target distances (4.0, 5.0 and 6.0 cm), respectively. The micrographs clearly show the morphological variation of the films and the variation nanoparticle size. All thin films have clear and well-defined nanoparticles of different sizes and morphologies. Fig. 4.3a shows a mixture of nanoparticles with different sizes and looks uniformly distributed over the deposition areas. However, in Fig. 4. 3b, the size of the nanoparticles has increased compared to the nanoparticle size shown in Fig's 4.3a and 4.3c, and their distribution is uniform regardless of some aggregated areas, which might be due to the formation of spitting out particles by high-speed ablation.

At a larger distance ( $d = 6.0$  cm), the particles size and corresponding distribution are reduced, which can be attributed to kinetic energy loss of the ablated particles due to the hemispherical expansion of the plume as a result of increasing target to substrate separation distance. The hemispherical expansion of the plume, which might be partially out of the deposition areas, can be the possible reason for the decrement of the deposition rate. Fig.4. 4 shows that all the atomic composition of the phosphor compound material ( $Y_2SiO_5:Ce^{3+}$ ) which exists with a reduced weight of the doping material (Ce) for the lower and maximum distances ( $d = 4.0$  and  $6.0$  cm respectively). However, for the medium distance ( $d = 5.0$  cm), the composition of the dopant increases.

From Fig.4. 4,  $d= 5.0$  cm is relatively the optimal distance to get morphologically good thin film in depositing this material. The change in morphology and crystal size as a function of the change in substrate distance from  $d= 4.0$  to  $d= 6.0$  cm shows the growth rate of the thin film is sensitive to the substrate-target distance. Therefore, in addition to other control conditions, substrate-target distance also plays a crucial role in the deposition of a thin film using PLD for display applications.

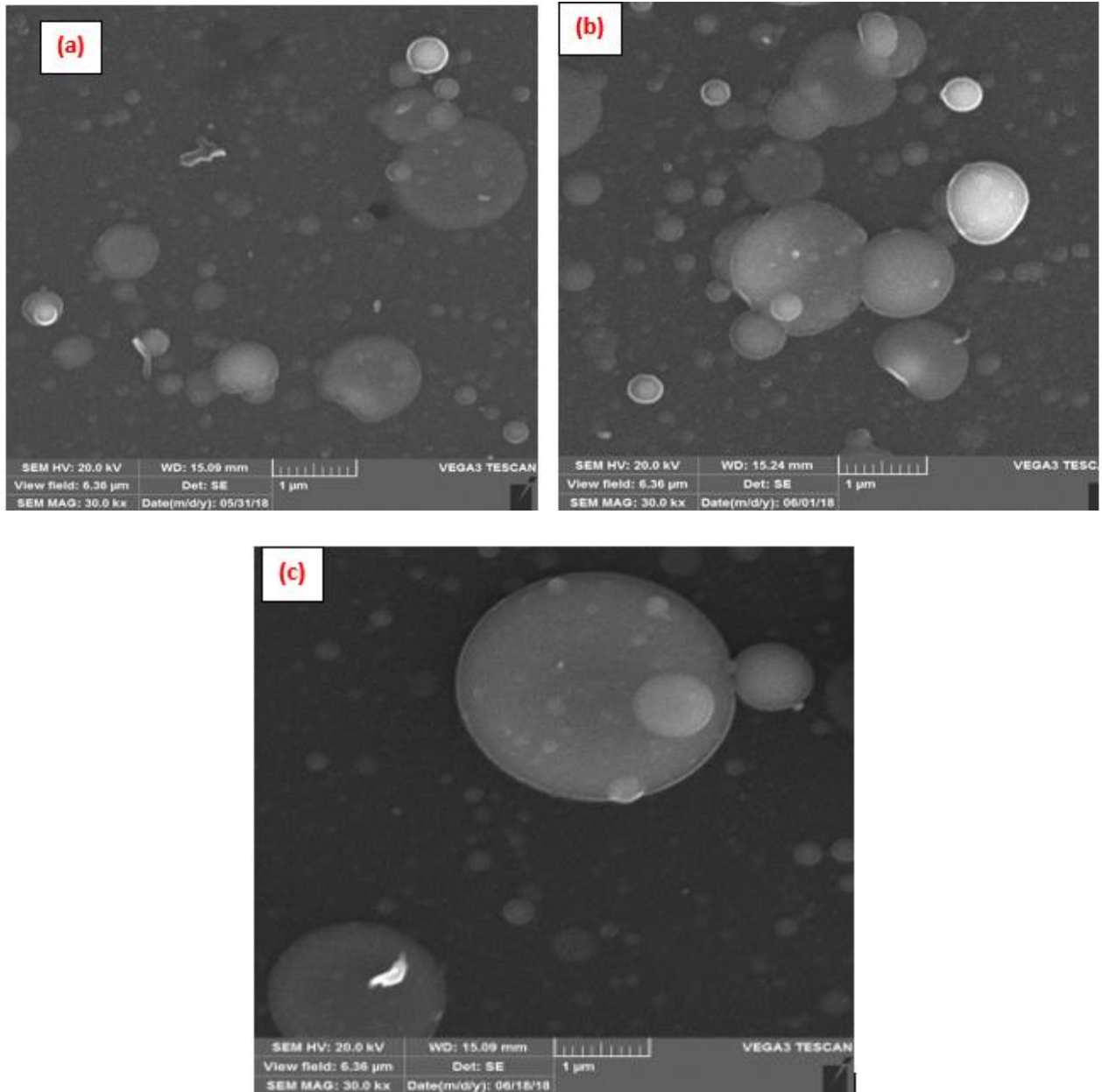


Fig. 4.3: SEM micrograph of (a)  $d= 4.0$  cm (b)  $d= 5.0$  cm and (c)  $d= 6.0$  cm respectively

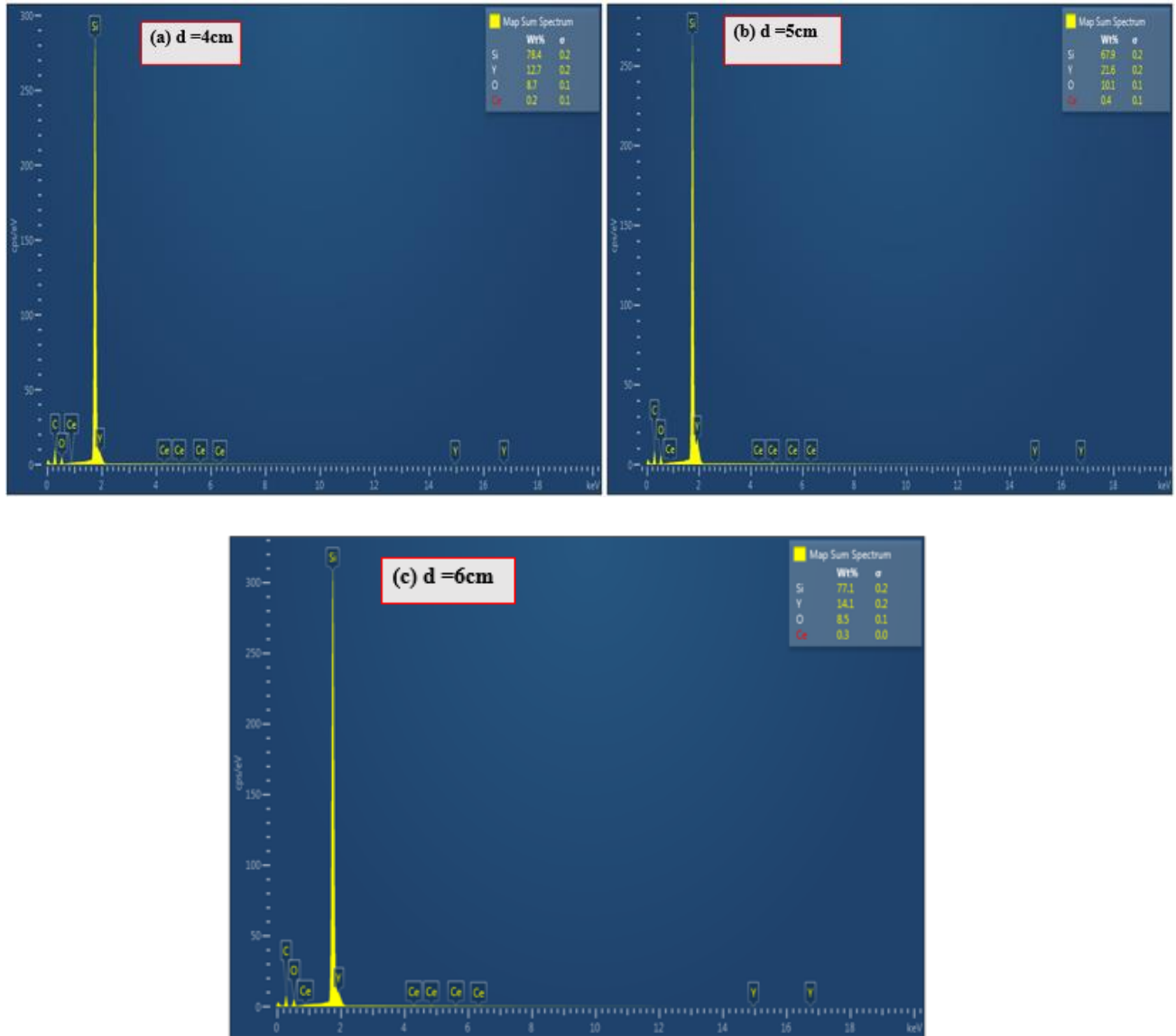


Fig. 4.4: EDS spectrum for (a)  $d = 4.0$  cm (b)  $d = 5.0$  cm and (c)  $d = 6.0$  cm

As observed in Fig. 4.5, when the distance of the substrate-target increases, the average roughness (Ra) and the root mean square (Rq) increase proportionally until  $d = 5.0$  cm and begin to decrease linearly thereafter. The increase in roughness can be attributed to the good deposition rate of the incoming particles in the substrate. By further increasing the distance of the substrate beyond 5.0 cm, the plume expands in a hemispherical manner, which may be outside the deposition zone of the substrate, resulting in a decrease of the deposition rate, average roughness and mean square value of the root.

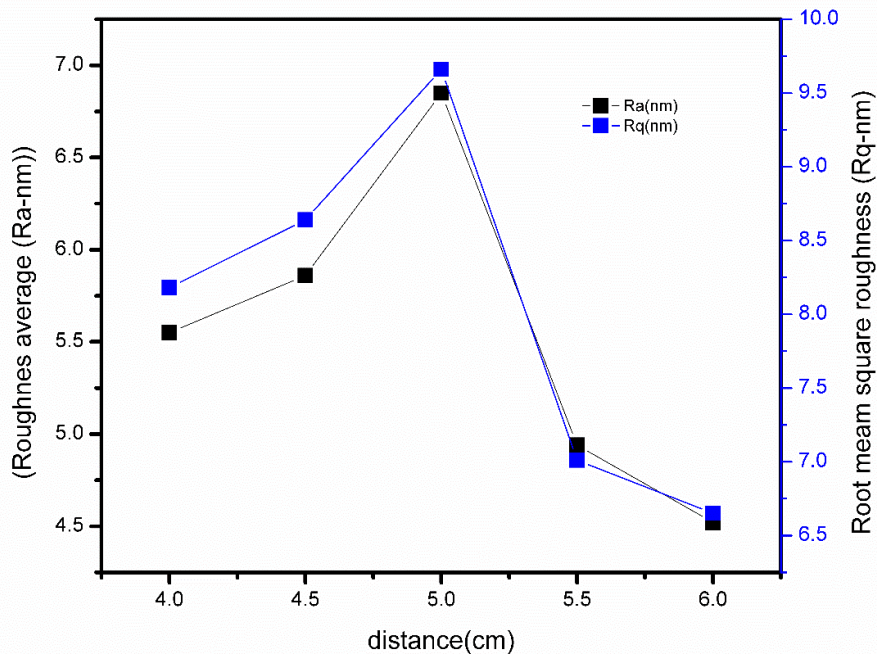


Fig. 4.5: The average roughness and Root mean square of the thin films measured by Gwyddion2.50 software [146].

#### 4.2.3 UV-VIS analysis

The UV-VIS technique was employed for measuring the optical properties of the material ( $\text{Y}_2\text{SiO}_5:\text{Ce}^{3+}$ ). In the graph of absorbance versus the wavelength of the incoming photons (Fig.4.6), the absorption edge is around 356 nm, which is in good agreement with the excitation wavelength used to excite the material. The maximum and minimum absorbance was observed for the substrate-target distance of 4.0 and 6.0 cm, respectively. The decrease in absorbance as the substrate-target distance increases can be ascribed to the decrease of the thickness of the deposited thin film. The bandgap of the host material ( $\text{Y}_2\text{SiO}_5$ ) is 7.4 eV, which corresponds to the wavelength of 168 nm, as a result, the lower absorption spectrum of the host was not observed since the UV-VIS measurement is taken place from 200-800 nm. This confirms that the absorbance is definitely from the dopant ( $\text{Ce}^{3+}$ ) ion.

As observed from the UV-Vis graph, the highest absorption is observed for  $d=4.0$ . The reason for the lower absorbance of the 5.0 cm than the 4.0 cm may be due to the position of the glass substrate. Since the silicon substrate and the glass substrate have been placed side by side during deposition, the glass may not have been placed in the appropriate position as the silicon substrate when deposited at  $d=5.0$  cm; as a result, the deposition should be lower in the glass. In pulsed laser depositions, the ablated particles deposits on a small area, it cannot expand to the areas of the silicon widely and uniformly unless the positions are perfectly in the right way, which is the disadvantage

of the PLD. This can be the main reason for the low absorption for the substrate distance of 5.0 cm as compared to that of 4.0 cm.

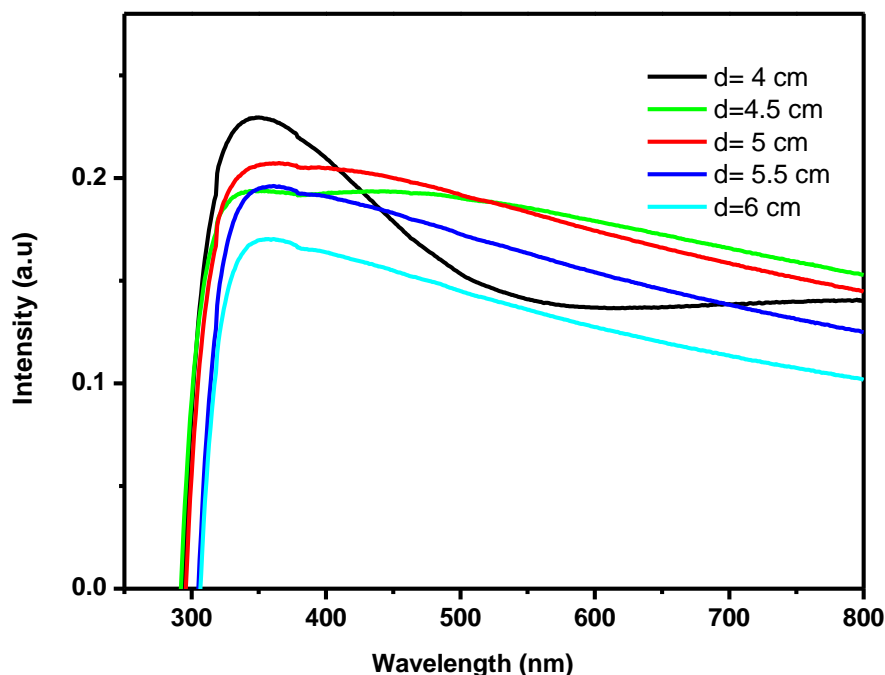


Fig. 4.6: UV-VIS absorbance of  $\text{Y}_2\text{SiO}_5:\text{Ce}^{3+}$  thin film

#### 4.2.4 Photoluminescence analysis

The PL spectra of  $\text{Y}_2\text{SiO}_5:\text{Ce}^{3+}$  thin films show three excitation peaks at 267, 303 and 356 nm. The corresponding emission graph shows a blue emission band positioned at 438 with the excitation wavelength of 356 nm. The blue emission band of  $\text{Y}_2\text{SiO}_5:\text{Ce}^{3+}$  can be ascribed to the electronic transition of  $5d \rightarrow 4f$  of  $\text{Ce}^{3+}$  (from the excited state of 5d energy level to the ground state of 4f) [147]. From the atomic configurations of cerium  $4f^2 5s^2 5p^6 6s^2$ , the  $\text{Ce}^{3+}$  has only 4f electrons, which describes the two ground state energy levels ( $^2F_{7/2}$  and  $^2F_{5/2}$ ). The spinning electron around its axis and orbiting around the nucleus has a doublet character that is observed because of the splitting of the ground state (parallel to  $^2F_{7/2}$  and antiparallel to  $^2F_{5/2}$ ). Wang et al [56] studied the “influence of RE elements (Sc, La, Gd and Lu) on the luminescent properties of blue phosphorus powder of  $\text{X}_2\text{-Y}_2\text{SiO}_5:\text{Ce}$ ”. They have shown that 270, 300 and 360 nm are the excitation peaks for the material, which is very similar to our result that can be attributed to the ground state transitions of  $4f^1$  ( $^2F_{5/2}$ ) to various sections of the excited 5d crystal fields of  $\text{Ce}^{3+}$  ion as shown in Fig. 4.9. The energy levels of 4f and 5d created due to the electrostatic interactions between the ions and the atoms on the crystal field of the host on the expense of the surrounding charges. This could results into a decrease of the center of the mass of the 5d structure, particularly in conditions containing oxygen, to a value of 4.3 eV [148] which corresponds to the excitation wavelength of 276 and 303. The 5d level is the first excited state in the energy level of the  $\text{Ce}^{3+}$  ion with two close states of  $^2D_{3/2}$

and  $^2D_{5/2}$ . The interaction between the electronic transition orbitals (the ground and excited state) of the trivalent cerium ion and the host material is the most probable reason for d-splitting. In this energy level, the energy difference between 5d and 4f is about 6.3 eV. Many studies have been reported on the luminescence properties of  $Y_2SiO_5$  but no complete explanation could be given for the division of 5d energy level. The electronic transitions of the  $Ce^{3+}$  ion from  $5d \rightarrow 4f$  are allowed by electric dipole moment, by the principle of selection rules, which is the measure of the polarity of charges. Therefore, the emission level has a short lifespan, which is a common property in some phosphor materials like  $CeP_5O_{14}$ , as reported by D.Bimberg et al [149].

Another interesting point of the cerium-based phosphor is that the excited 5d energy level of  $Ce^{3+}$  depends on the host materials. The 4f electrons of  $Ce^{3+}$  ion is hardly affected by the crystal lattice, due to the interaction with the electrons of the outer layer. The use of  $Ce^{3+}$  in various host materials as an activator can help us to produce UV and green emission spectra [150]. Because of the interaction, the 5d state is at low energy levels due to the shifts of its energy levels, and as a result, emission can simply happen by a means of energy transition from higher state to lower state. The host material ( $Y_2SiO_5$ ) has a complex crystalline structure, so the emissions of all the neighboring, which are differently oriented  $Ce^{3+}$  ions, could produce transitions with energies slightly lower or higher than near ions.

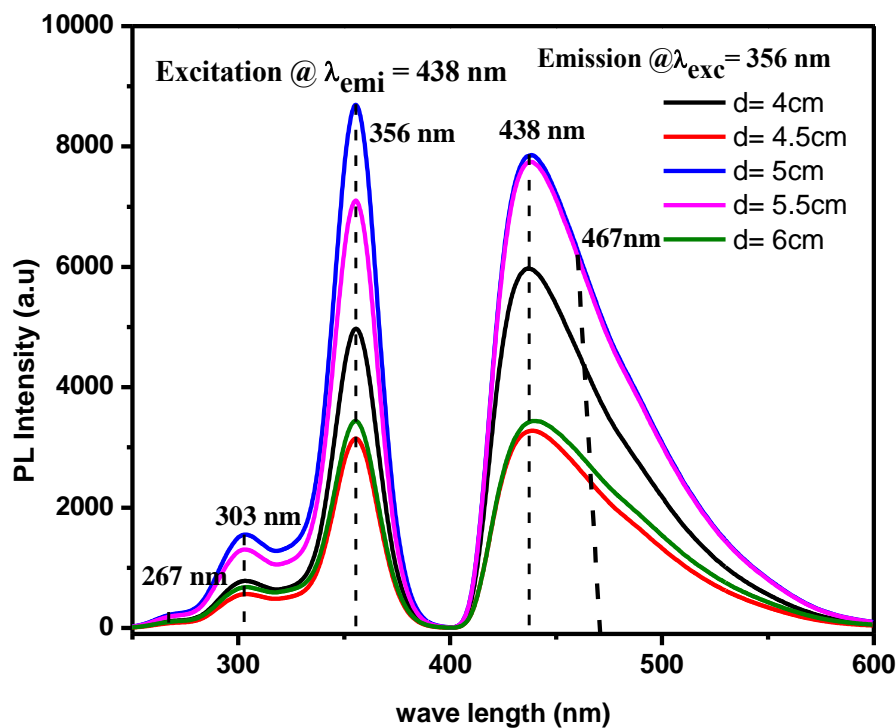


Fig.4.7: Excitation and emission bands of  $Y_2SiO_5:Ce^{3+}$  thin film at 438 nm and 356 nm respectively

From Fig. 4.5 the distance from the substrate to the target increases from 4.0 to 5.0 cm, the surface roughness, which has a maximum value at 5.0 cm, also increases, which can be attributed to a good

deposition rate. In addition, it begins to decrease beyond 5.0 cm. Fig 4.5 shows that on the roughest surface ( $d = 5.0$  cm), the PL graph has the maximum emission and excitation. When the surface is rough, its absorbance of photons is maximum, the electrons are excited to a higher energy states, and then they radiate to a lower energy state with emission, as shown in Fig. 4. 7.

The  $Ce^{3+}$  ion has different coordination numbers; accordingly, it has two distinct seats in the lattice positions of the host material. However, due to the broad emission of  $Ce^{3+}$  several emissions could be hiding on the broad emission as shown in Fig. 4. 7. This broad emission can be de-convoluted into constituent emission peaks as shown in Fig. 4.8. Therefore, the main emission peaks of  $Ce^{3+}$  are at 438 and 467 nm.

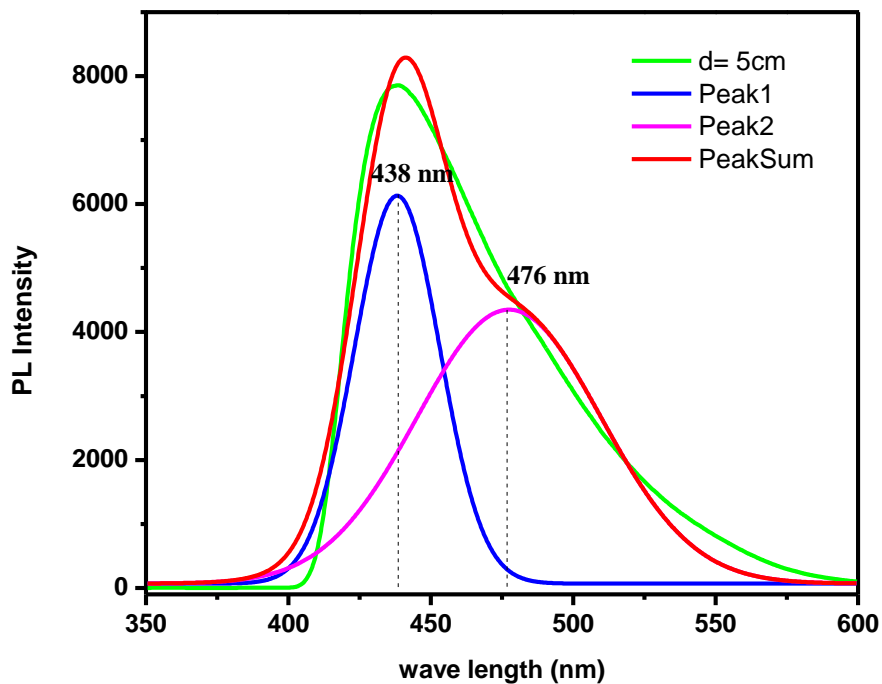


Fig. 4.8: Deconvoluted emission of  $Y_2SiO_5:Ce^{3+}$  thin film at  $d=5.0$  cm



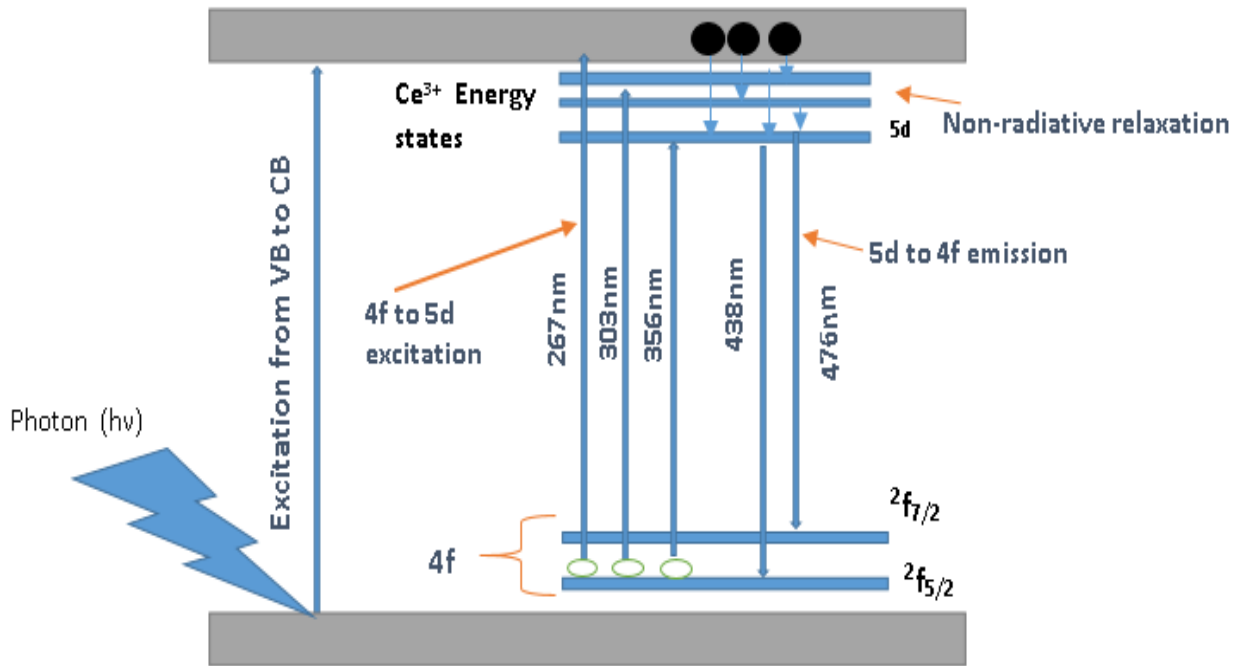


Fig. 4.9: Energy diagram for the  $\text{Y}_2\text{SiO}_5:\text{Ce}^{3+}$  thin film for the excitation and emission spectra's

When a photon with energy ( $h\nu$ ) is applied to excite an electron from valance band of the host material, the electrons get enough energy to escape from their position and excited to the conduction band as shown in Fig. 4.9. When electrons are excited from the valence band, it provides holes in the valence band, which may later make recombination reaction with the relaxed electrons. The electrons excited from the ground state of the 4f energy level of the  $\text{Ce}^{3+}$  reaches in a different excited level of the  $\text{Ce}^{3+}$  ion depending upon their energy as shown in the above diagram. The electrons from the conduction band relax non-radiatively in to the excited state of the  $\text{Ce}^{3+}$  ions from the 5d low excited state of the  $\text{Ce}^{3+}$  ion to the 4f ground state ( $^2f_{7/2}$  and  $^2f_{5/2}$ ).

All the possibilities mentioned above must be considered to explain the luminescent properties of  $\text{Y}_2\text{SiO}_5:\text{Ce}^{3+}$  for the evaluation of the luminescence properties and its efficiency. Preparation condition of the thin film can also strongly be responsible for the oxygen vacancies and deficiencies, which can affect the alignment of crystal structures on the crystal field. As can be seen from the emission graph of Fig. 4.7, the excitation and emission intensity are maximum for the substrate to target distance of 5.0 cm, which can be ascribed for the good crystallite quality of the material for the possible applications in display technologies. From the commission international de'Eclairage (CIE), the chromaticity coordinates of the color spectrum were calculated for the emission wavelength of 438 nm excited at 356 nm as shown in Fig. 4.10(a). The position of the chromaticity coordinate is found at  $x = 0.152$  and  $y = 0.124$ . The corresponding spectrum is in the blue region. This shows us, the  $\text{Y}_2\text{SiO}_5:\text{Ce}^{3+}$  phosphorescent material is a good blue emitter that can be used for particular blue display technologies when excited at 356 nm. The relationship between the excitation



wavelengths used to excite the thin films and their corresponding maximum intensities is illustrated in Fig. 4.10(b). For all excitation wavelengths, the target substrate distance of 5.0 cm has a maximum intensity relative to the others.

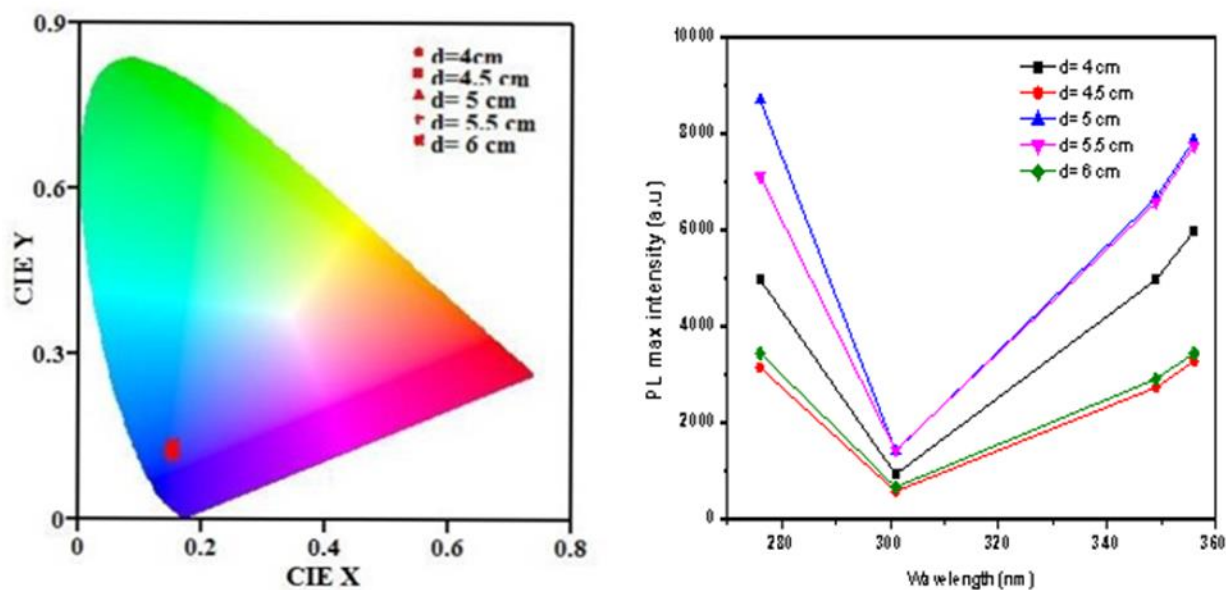


Fig.4.10: (a) CIE coordination graph for all samples emitted at excitation wavelength of 356 nm (b) max PL emission for the corresponding excitation wavelengths.

#### 4.4. Conclusions

Cerium-doped yttrium silicate ( $\text{Y}_2\text{SiO}_5:\text{Ce}^{3+}$ ) thin films were successfully deposited by PLD from a commercial phosphor. The average crystallite size is 37 nm with monoclinic structures. A slight increase in the thickness of the thin film is observed as the substrate–target distance increases from 4.0 to 5.0 cm and begins to decrease thereafter which is supported by the EDS results. The percentage weight of the elemental composition increases as the substrate–target distance increases from 4.0 to 5.0 cm. 267, 303 and 368 nm are the excitation wavelength and 438 nm are the corresponding emission wavelength for all the excitations, which is attributed to the blue emission. The 4f-electrons of the  $\text{Ce}^{3+}$  ion have ground-state levels of  $^2f_{5/2}$  and  $^2f_{7/2}$  and first excited state of 5d level. The interaction of the two states with the host material is the main probable reason for the division of the energy level 5d into sub-states  $^2D_{3/2}$  and  $^2D_{5/2}$ . The energy levels of the 4f and 5d are also created by the electrostatic interaction between the ions and the crystalline field of the host at the expense of the surrounding charges. The highest excitation and emission wavelength were observed at  $d= 5.0$  cm. The CIE was evaluated at the emission wavelength of 438 nm and the corresponding color spectrum is in the blue region. The maximum UV–Vis absorbance was observed around 356 nm, which is used for excitation of all the thin films. From the SEM

micrographs, when the distance increased (beyond  $d = 5.0$  cm), the size and uniformity distribution of the particles decreases. The corresponding EDS micrographs show reduction in composition of the atomic weights for the distances ( $d = 4.0$  and  $6.0$  cm). However, at  $d = 5.0$  cm, the composition of the dopant and other constituents increases. The Ra and Rq also increase from  $4.0$  to  $5.0$  cm and begin to decrease afterward.

## Chapter 5: Effect of substrate temperature on the material properties of the $\text{Y}_2\text{SiO}_5: \text{Ce}^{3+}$ thin film by pulsed laser deposition (PLD) method

### 5.1 Introduction

Currently, there is increasing interest in the production and application of nanostructured phosphor materials doped with lanthanide ions and transition metal ions [2]. These materials most likely have various optical properties necessary for a wide range of applications in our day-to-day life, specifically in optoelectronic components as compared to the corresponding bulk materials. Transition ions and RE metals belong to the class of multifunctional luminescent materials when bombarded with some energy source. They show the emission of radiation and have crucial applications in cathode ray tubes, screens (from scintillators, X-ray screens to plasma screens), laser materials, printing inks for money security, fluorescent pigments, solar cells, etc. [4, 5]. Most of these materials are produced by doping the rare-earth ions into the mono-structure crystals, phosphors, and ceramics for practical applications [6]. As a result, the rare-earth doped materials are becoming one of the favorable compounds in the field of optoelectronics application [6, 125, 151]. The effective characterization of these rare-earth-doped materials with regard to their stability, luminosity, efficiency in industrial application and also in the application of emission field detectors are important points to consider in order to obtain better results in the area of industrial application [12]. The band gap of  $\text{Y}_2\text{SiO}_5$  is about 7.4 eV, which is a good host because of its capacity to accommodate substantial amount of the doped materials (the rare-earth ions), and is successfully used as a host material for different rare-earth ions due to its chemical and thermal stabilities for the formation of photo-cathodes or scintillating phosphors [13].  $\text{Y}_2\text{SiO}_5: \text{Ce}^{3+}$  phosphors have been studied by various researchers and it has been proved to be a blue emitting phosphor material. This blue phosphor material is applicable in lighting industry like field emission screens. The phosphor crystallizes in a rare-earth oxy-orthosilicate ( $\text{RE}_2\text{SiO}_5$ ) structure [54]. Previous studies indicate that the material has two distinct crystalline structures, which are mainly classified by their synthesis temperature and the coordination number of the compound. The high-temperature structure, synthesized above  $1190^\circ\text{C}$ , which has space group of  $\text{P}21/\text{c}$ , and low temperature synthesized below  $1190^\circ\text{C}$  with a space group of  $\text{B}2/\text{c}$ , are the two classifications of the silicate material [55]. In the described phases of the compound, there are two sites of  $\text{Y}^{3+}$  in the  $\text{Y}_2\text{SiO}_5$  compound matrix.  $\text{Y}_2\text{SiO}_5: \text{Ce}^{3+}$  is an efficient luminescent material under the UV, cathode ray, as well as X-ray excitations.

The  $\text{Y}^{3+}$  two sites are mainly attributed to the difference in coordination number. During the formation of the  $\text{Y}_2\text{SiO}_5: \text{Ce}^{3+}$  thin films, since the ionic radius of  $\text{Ce}^{3+}$  (0.106 nm) is similar to  $\text{Y}^{3+}$

(0.093 nm), it has a high probability of substituting the position of  $Y^{3+}$  sites. The coordination number of phases  $X_1$  is 7 and 9, and the coordination number for phase  $X_2$  is 6 and 7. In phase  $X_1$  of the composite matrix, the coordination number of 9 is linked to the bonding of the 8 atoms of the oxygen to the atoms of yttrium and silicon and the rest is bonded only to yttrium [56, 57, 152-154]. The pulsed laser deposition method is the deposition mechanism used in the preparation of the  $Y_2SiO_5: Ce^{3+}$  thin film. This deposition method is an advantageous and versatile technique for the growth of thin films. It is used to deposit materials with a wide temperature range with different background gases. Where the background gas and temperature are among the important parameters which plays a substantial role in the development of the thin film during the deposition time [155-157]. It also plays a significant role in the formation of the thin film as well as the amorphous character and crystallinity of the produced thin films. In many research areas, PLD has been used for the development of thin film phosphor materials like ZnS, SrS, ZnO, YAGG, and  $Y_2O_3: Eu$  [150, 158, 159]. Because of their better chemical stability than phosphors of sulfur materials under electronic interaction, the phosphorus materials of the silicate oxide require special attention. Electroluminescence devices are also composed of silicates [160]. Rare-earth doped silicate phosphors are a complex compound, which can be composed of four and more than four elements. Since the host material has good thermal, chemical stability and the space for accommodating the dopants, the rare-earth doped silicate materials are suitable for PLD studies. In this study, commercial  $Y_2SiO_5: Ce^{3+}$  powder was used to deposit thin film phosphors using PLD. To the best of our knowledge, no similar research work has been reported under conditions similar to our current work. Therefore, in current work it has reported on the effect of the substrate temperature on the material properties of the  $Y_2SiO_5: Ce^{3+}$  thin film by pulsed laser deposition mechanism, at different temperatures (ambient temperature, 150, 250, 350, 450 and 600 °C) keeping the other parameters constant. The purpose of this study is to identify the optimum substrate temperature of the material which is structurally, morphologically and luminescently good which can be used for potential applications in the future display technologies.

## 5.2 Results and discussions

### 5.2.1 XRD analyses

Fig. 5.1 illustrates the XRD pattern of the phosphor  $Y_2SiO_5: Ce^{3+}$  material prepared at different substrate temperatures. The diffraction spectrum is a pure phase of the phosphor material ( $Y_2SiO_5: Ce^{3+}$ ) with small impurities. The structure of the phase shown is monoclinic with lattice constants  $a = 9.012 \text{ \AA}$ ,  $b = 6.979 \text{ \AA}$  and  $c = 6.630 \text{ \AA}$  with a cell volume of  $399.40 \text{ \AA}^3$  in accordance with the JCPDS card # 410004. We have noticed three diffraction peaks at  $2\theta = 29.2, 22.4, \text{ and } 16.14^\circ$  corresponding to (021), (111) and (110) diffraction planes. The prominent diffraction peaks are

mainly oriented in the (021) plane, which shows that the grains are grown in the position perpendicular to the 'b' and 'c'-axis'. The average crystallite size was calculated using the Scherrer relations given in equation 3.4, from the most prominent peak (021) and it is approximately 1.66 nm; The physical deposition of the thin film on the silicon substrate was assured by measuring the mass of the substrates before and after deposition by sensitive microbalance mass measurements. The thickness of the deposited thin film was estimated by the mathematical relations given by  $X = (m_2 - m_1) / \rho A$  [161, 162]. Where  $m_1$  and  $m_2$  are the mass of the substrates before and after depositions respectively,  $\rho$  ( $\text{g}/\text{cm}^3$ ) is the density of substrate before deposition which is constant and  $A$  ( $\text{cm}^2$ ) is the area where the film is deposited. A slight increment in film thickness was observed as the substrate temperature is increased from vacuum to  $450^\circ\text{C}$  but further increase in temperature from  $450$  to  $600^\circ\text{C}$  led to a decrease in film thickness. The film thickness we obtained for room temperature,  $150$ ,  $250$ ,  $350$ ,  $450$  and  $600^\circ\text{C}$  are:  $X = 23.7$ ,  $35.4$ ,  $42.8$ ,  $51.3$ ,  $60.9$  and  $57.2$  nm respectively. The reason for decreasing the thickness of the thin films for a substrate temperature above  $450^\circ\text{C}$  is; the thermal energy overcomes the adhesion energy and the bonding energy of deposited atoms on the substrate will break down and will be re-evaporated. For this reason, these atoms absorbed on the surface of the substrate, the thickness of the films decrease with further increasing of substrate temperature. All the films have the highest intensity for the diffraction peak at  $29.2^\circ$ .

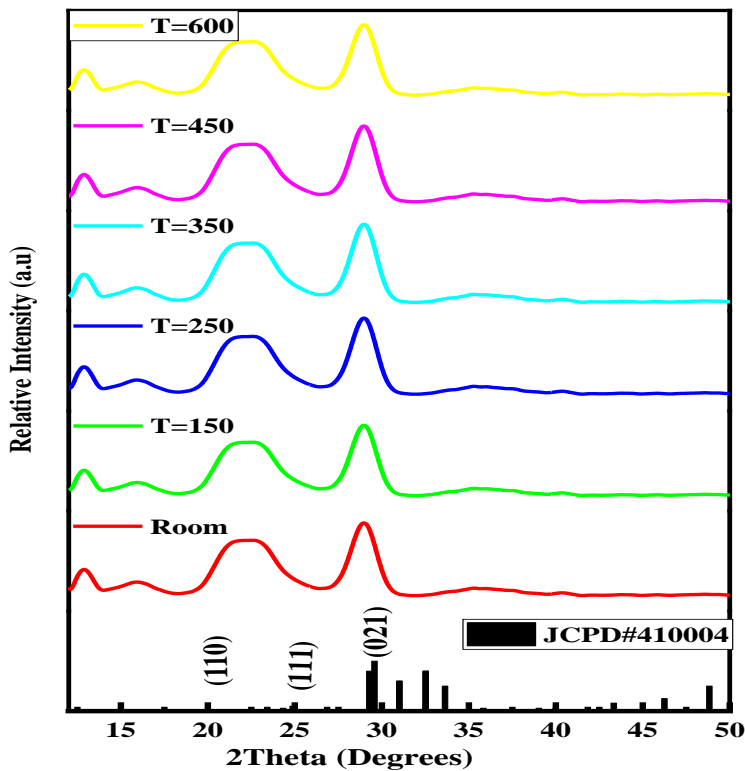


Fig. 5.1: XRD pattern of the  $\text{Y}_2\text{SiO}_5: \text{Ce}^{3+}$  phosphor thin films

### 5.2.2 SEM and EDX analysis

SEM microscopy of the thin film phosphors deposited at different substrate temperatures is shown in Fig. 5.2. The micrographs of the deposited films were taken at lower, middle and maximum temperatures (150, 450 and 600 °C), respectively, to compare and find out morphologically better thin film for potential applications in the field of display technology. It is clearly seen from Fig. 5.2 (a)-(c) that the surface morphologies of all the thin films are different. At a substrate temperature of 150 °C, the distribution of the grains seems uniform regardless of agglomeration in some areas. When the substrate temperature increases to 450 °C the agglomeration also increased, the possible reason for the agglomeration may be due to the spitting out of the small particles into the large sized particles. In addition to this, it is realistic to say that ionized particle (s) or ions do attract each other on solid surfaces to form ionic bond or cluster or agglomerate. The change in thermal energy of the substrate and the adhesion and the bonding energy has also a significant effect on the density and agglomeration of the particles. When the thermal energy is less than the adhesion energy of the particles, it has a high probability of being clustered at a particular area. However, as the substrate temperature is further increasing to 600 °C, the distribution of the particles seems relatively uniform and the agglomeration significantly decreased, and the density of the thin film on the surface decreases, which may be ascribed to diffusion of the particles as result of the high substrate temperature. In this case, the thermal energy of the substrate is greater than the adhesion and bonding energy of the particles, in which the adatoms has high freedom of finding an appropriate place to seat. When the deposition temperature is increased, the composition of the constituent particles deposited on the silicon substrate gradually decreases, which is confirmed by the EDS micrograph shown in Fig. 5.3 (a)-(c). The atomic composition of the phosphor material is observed to contain a decreasing amount of the cerium ion ( $Ce^{3+}$ ) as the deposition temperature is further increased from room to 600 °C. This is in a good agreement with the PL and SEM measurements. The lattice crystallinity and surface smoothness are the parameters, which determines the quality of the deposited thin film. In the PLD method, the generation of particulates are the key issues, which affects the smoothness of the resultant thin film [163]. The crystallinity of thin films is associated with the mobility of atoms on the surface of the substrate, which can be improved by increasing the temperature of the substrate (in our case, it ends at 450 °C). At low deposition temperatures, the vapor species have relatively low surface mobility, which promotes their settlement in different positions of the substrate. However, when the temperature of the substrate is high enough that the arriving adatoms can leave them at high thermal energy, their mobility increases. Thermal energy can help particles form an amalgam to form a nucleation centre by improving the quality of thin films.

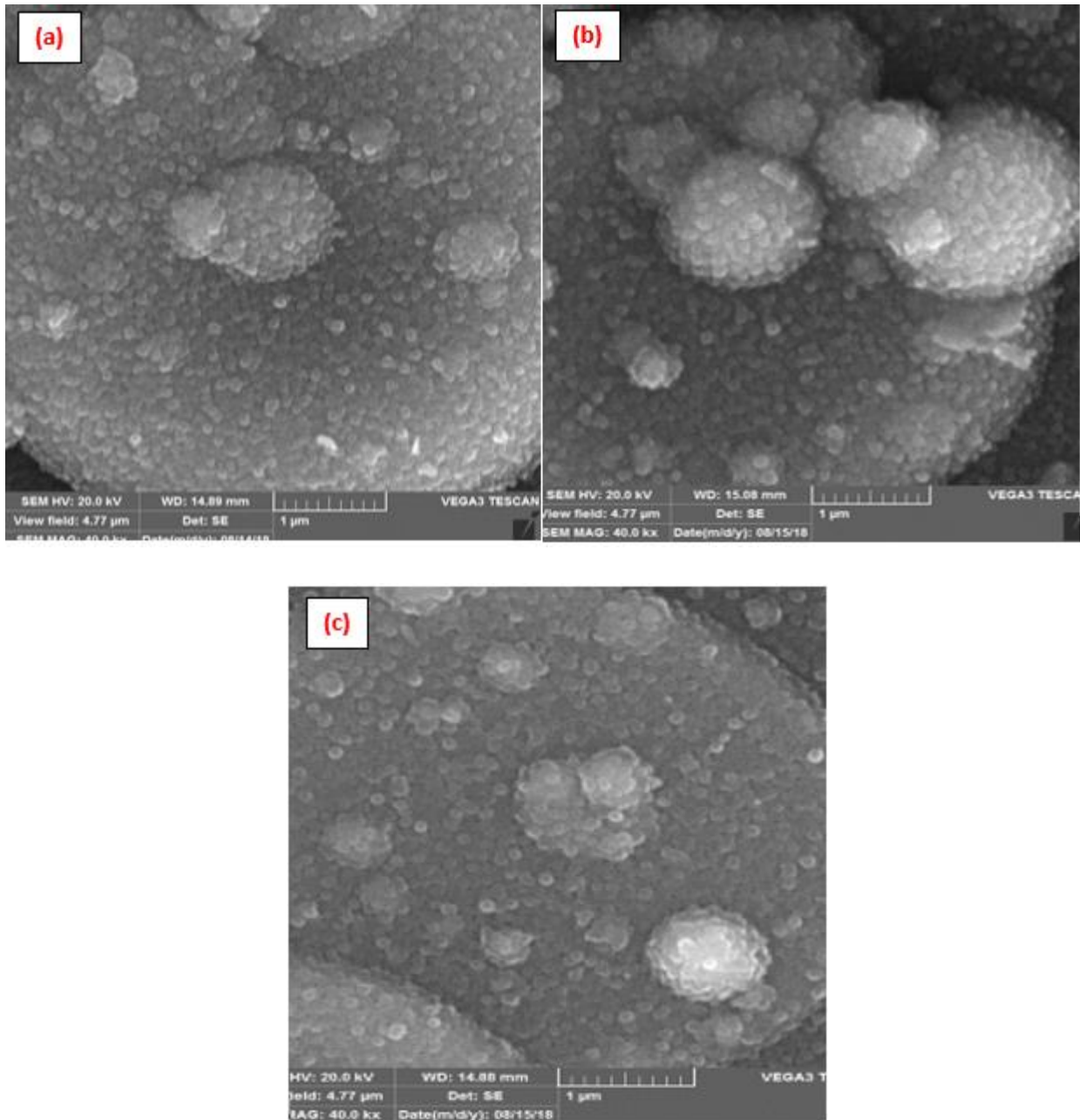


Fig. 5.2: SEM graphs of thin film phosphor at a substrate temperature of (a) 150<sup>0</sup> C (b) 450<sup>0</sup>C and (c) 600<sup>0</sup> C

The EDS micrograph in Fig. 5.3 shows the presence of all elements with their respective atomic weight ratios. It is shown that as the temperature increases to a higher value, the corresponding atomic weight of the elements decreases, particularly the yttrium, oxygen, and cerium atoms which might to be due to the re-evaporation because of the thermal energy of the substrate. However, the silicon atom has increased, which may be from the atoms of the substrate (silicon). When the temperature of the substrate is higher, the probability of re-evaporation of the atoms on the substrate is high, resulting in a decrease in the composition of the atoms, as shown in Fig. 5.3.



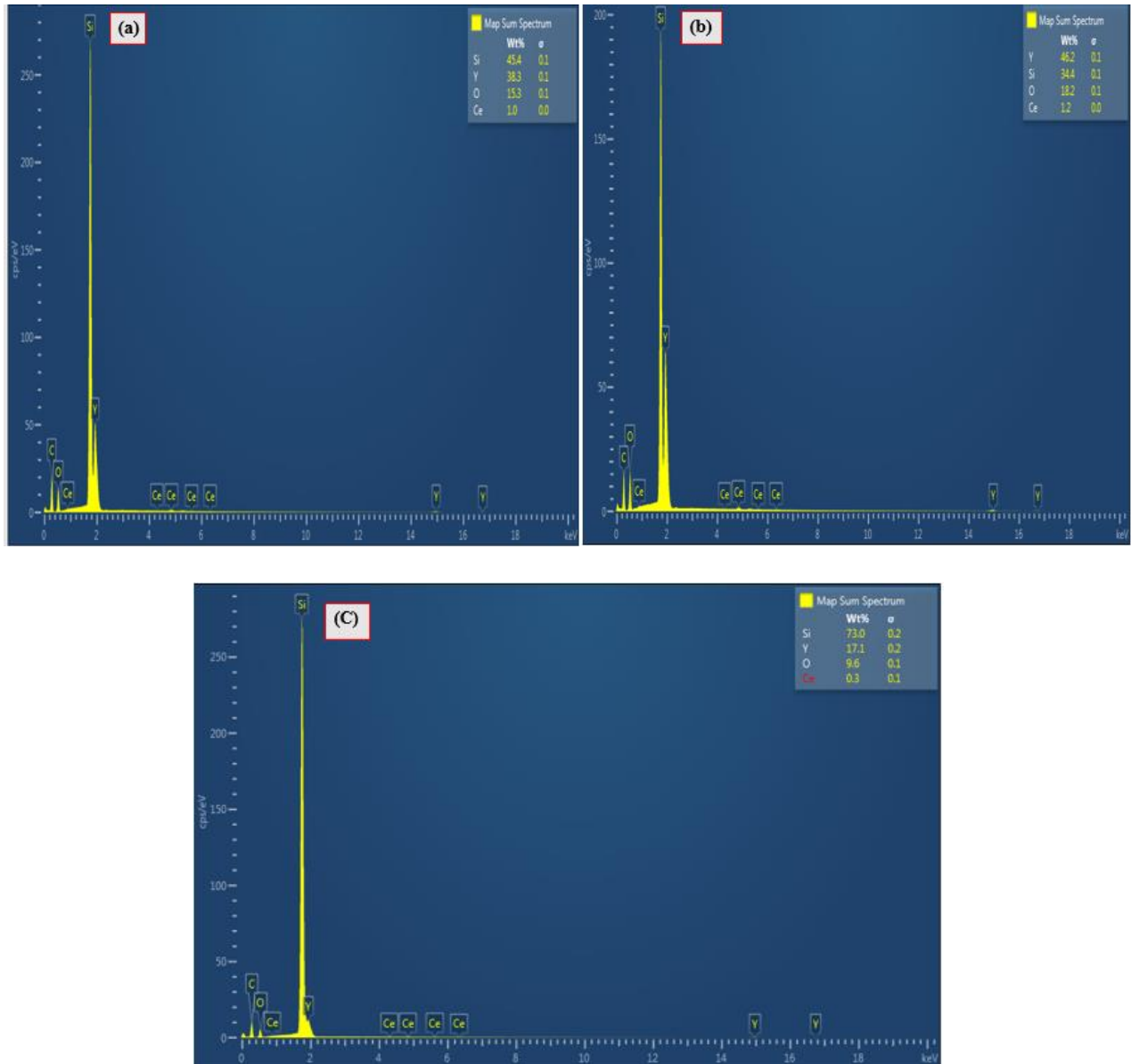


Fig. 5.3: EDS micrographs the thin film phosphor at a substrate temperature of (a) 150 °C (b) 450 °C and (c) 600 °C

Fig. 5.4 shows the elemental mapping of  $Y_2SiO_5: Ce^{3+}$  thin film phosphor materials at a deposition temperature of 150 °C, 450 °C and 600 °C, respectively. At a deposition temperature of 150 °C, the distribution of elements is dominated by silicon and yttrium. When the temperature reaches 450 °C, the distribution of yttrium decreases and the silicon looks more. When the deposition temperature is increased to 600 °C, silicon elements is mainly detected. Other atoms may re-evaporate due to the high substrate temperature. This result is similar to the results of the EDS micrographs presented in Fig. 5.3.



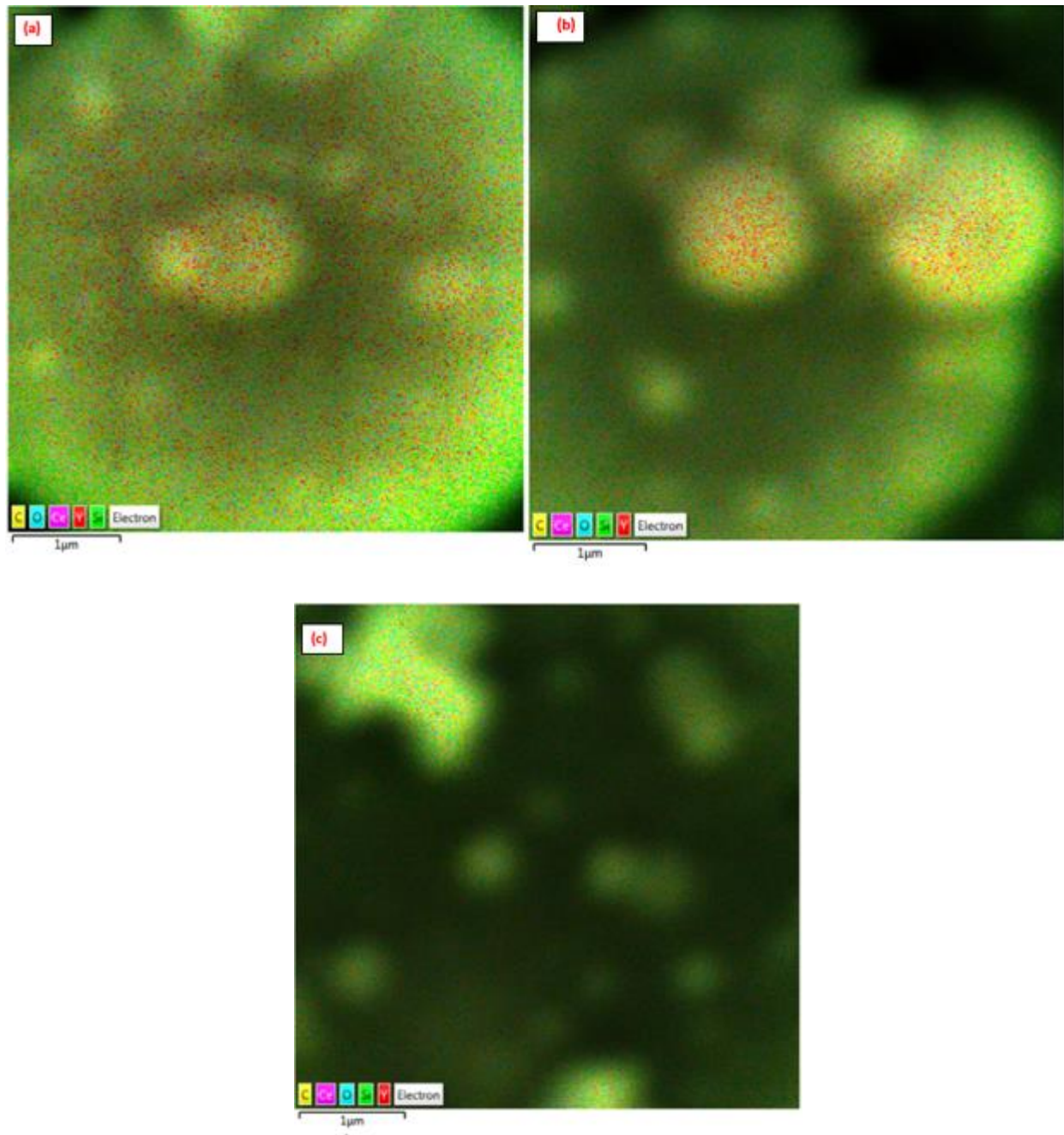


Fig. 5.4: Elemental maps of the thin film phosphors at a substrate temperature of (a) 150 °C (b) 450 °C and (c) 600 °C

### 5.2.3 UV-VIS analysis

The UV-VIS measurement has a significant advantage to understand the optical properties like the band gap, absorption, transmission and reflection of the materials in consideration. Fig. 5.5 shows the optical absorption spectra of  $\text{Y}_2\text{SiO}_5:\text{C}^{3+}$  thin film phosphor material prepared at different deposition temperatures. The maximum absorption peak is at around 337 nm. This is in a good agreement with the excitation wavelength that was used to probe the emission spectra of the  $\text{Y}_2\text{SiO}_5:\text{C}^{3+}$  thin film phosphor material. As observed in Fig. 5.5 the deposition temperature of 450

$^{\circ}\text{C}$  and room temperature are the deposition conditions corresponding to the maximum and minimum absorptions, respectively. The absorbance increases as the deposition temperature increase from room temperature to  $450^{\circ}\text{C}$ . However, when the deposition temperature increases further to  $600^{\circ}\text{C}$ , the absorbance decreases; this is ascribed to the decrease in thickness of the thin film. The band gap of the host ( $\text{Y}_2\text{SiO}_5$ ) is  $7.4\text{ eV}$ , which corresponds to an absorption wavelength of  $168\text{ nm}$ . Our UV-Vis measurement was employed between  $200\text{-}800\text{ nm}$  in which the absorption wavelength of the host is out of this range. Therefore, the absorption observed in our measurement is definitely from the dopant cerium ion ( $\text{Ce}^{3+}$ ).

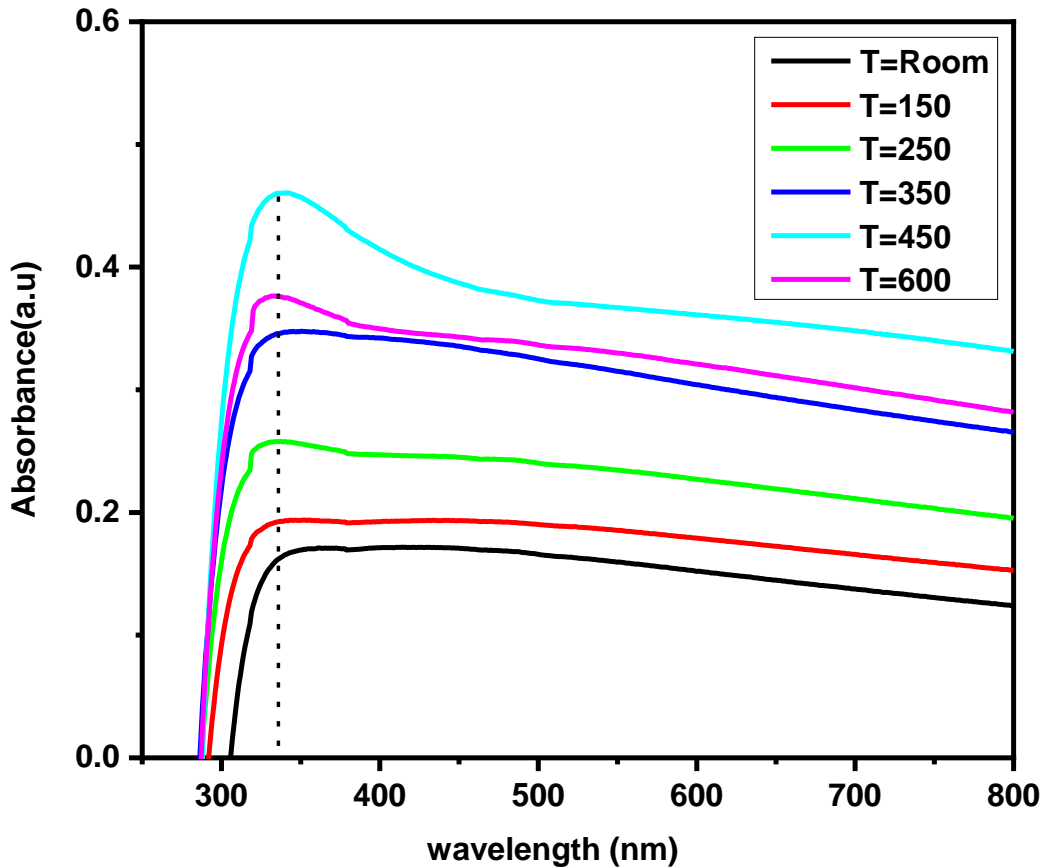


Fig. 5.5: Absorption graph of UV-Vis for the  $\text{Y}_2\text{SiO}_5:\text{C}^{3+}$  thin film phosphors

#### 5.2.4 Photoluminescence analysis

Fig. 5.6 shows the excitation spectra of the  $\text{Y}_2\text{SiO}_5:\text{C}^{3+}$  phosphor thin-films deposited at various substrate temperatures. These spectra were accomplished when phosphor materials were probed using the PL emission at a wavelength of  $465\text{ nm}$ . The main excitation band was observed at  $337\text{ nm}$  and a low and broad one observed at  $285\text{ nm}$ . It observed that the thin film of  $\text{Y}_2\text{SiO}_5:\text{Ce}^{3+}$  deposited at a temperature of  $450^{\circ}\text{C}$  has the highest intensity, which can be attributed to the presence of a good crystalline quality of the crystal at this particular deposition conditions. Both peaks could result from two different energy levels. This may be due to the band gap of the host material or the excited energy level of the  $5d^1$  configuration of the  $\text{Ce}^{3+}$  ion in the host band gap and

the doping ion ( $Ce^{3+}$ ) [164]. The excitation peak of 337 nm could result from the charge transfer of electrons from the 2p of  $O^{2-}$  into the 4f orbitals of  $Ce^{3+}$  and the other peak is due to the 5d splitting. As can be seen in Fig. 5.7, the maximum emission intensity is observed at a substrate temperature of 450 °C. The corresponding emission graph shows a blue emission band positioned at 465 nm with an excitation wavelength of 337 nm. This emission wavelength corresponds to the blue light in the electromagnetic spectrum as shown in Fig. 5.9. This emission band can be attributed to the 5d  $\rightarrow$  4f electron transition of the  $Ce^{3+}$  ion [147]. It can be realized that the excitation band controlled at 465 nm, composed of the strong and weak bands at 337 and 285 nm respectively, corresponds to the transition of an electron from the ground state ( $^2F_{5/2}$ ) to the excited state (5d) of  $Ce^{3+}$ . In addition, the emission band of  $Ce^{3+}$  monitored at 337 nm shows a single band at 465 nm, which can be attributed to the allowed parity of the transition from the lower excited state of 5d to the ground state of  $Ce^{3+}$  (to the  $^2F_{5/2}$  and  $^2F_{7/2}$  manifold split by spin-orbit coupling) [165]. The broadness of emission shown in Fig. 5.7 can be ascribed to the emission from more than one energy levels.

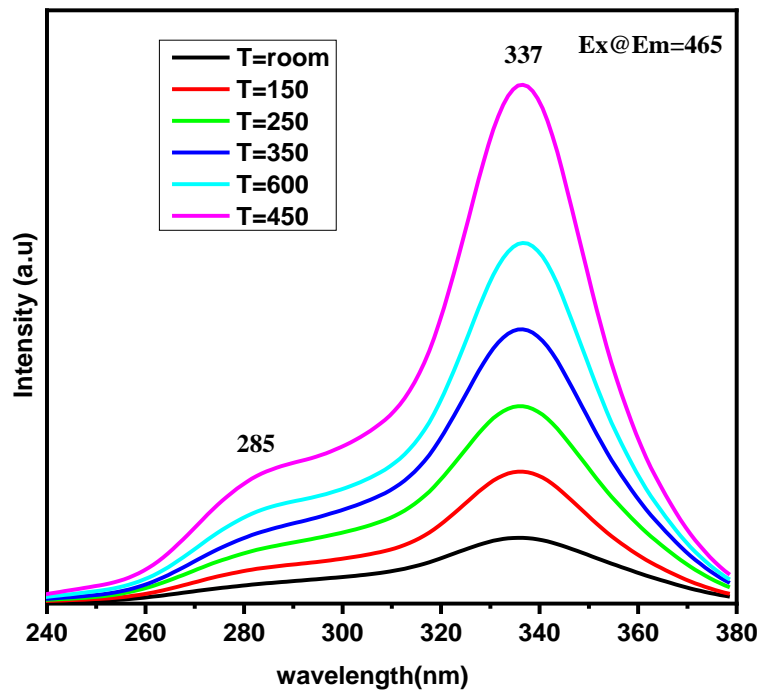


Fig. 5.6: PL excitation graph probed with the emission peak at 465 nm

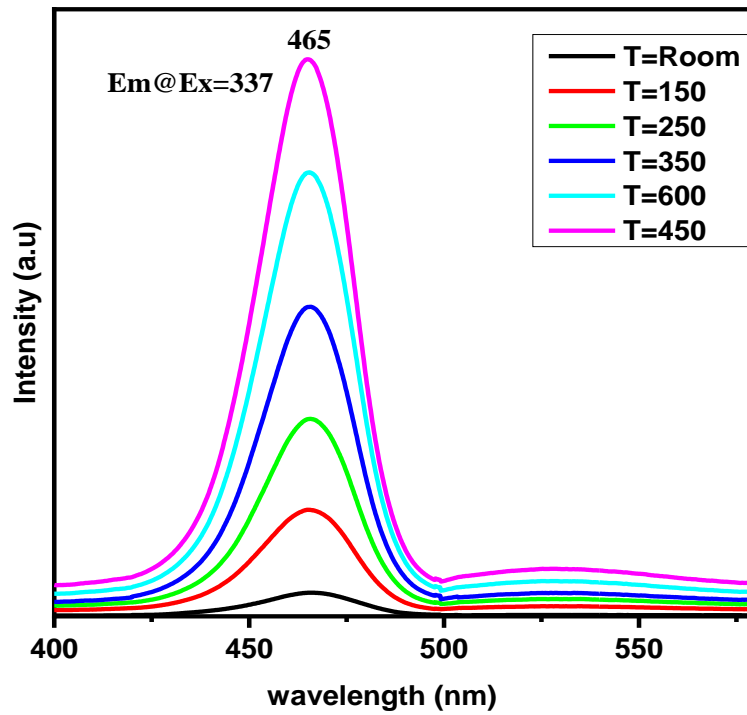


Fig. 5.7: PL emission spectra at an excitation of 337 nm

Table 5.1: Results of the fitted decay curves for a different deposition temperature of  $Y_2SiO_5: Ce^{3+}$  thin films.

Deposition Temperature ( $^{\circ}C$ )	Fitting parameters				
	$A_1$	$\tau_1(ms)$	$A_2$	$\tau_2(ms)$	$\langle\tau\rangle(ms)$
600	47.28	0.68	45.31	4.98	4.44
450	49.49	5.32	37.92	0.63	4.92
350	45.93	0.67	46.09	4.78	4.27
250	31.04	5.36	38.67	1.01	4.54
150	31.04	5.36	38.67	1.00	4.54

A measure of the decay time of  $Y_2SiO_5: Ce^{3+}$  thin films are summarized in table 5.1 and its corresponding graph is shown in Fig. 6.8 for different deposition temperatures. The decay curve was fitted using the second-order exponential functions as shown in equation (5.1).

$$I(t) = I_0 + A_1 e^{-\frac{t}{\tau_1}} + A_2 e^{-\frac{t}{\tau_2}} \dots\dots\dots (5.1)$$

Where  $I$  is the intensity of the phosphorescence at the time of  $t$  (ms);  $I_0$ ,  $A_1$  and  $A_2$  are constants,  $\tau_1$  and  $\tau_2$  are also decay times in milliseconds (ms). The analytic fit subjects to the least square fit for the sum of at most two exponential terms. The decay patterns provide us information about the thermal nature and emission mechanisms of the luminescent material [166, 167]. The average decay time has deployed using the general second order mathematical formula given in equation (5.2) [168] which is written as below.

$$\langle \tau \rangle = \sum_{i=1}^n \frac{A_i \tau_i^2}{A_i \tau_i} \dots \dots \dots (5.2)$$

Where  $n$  is the frequency of decay times. Therefore, from equation (5.2), the average decay time was calculated by equation (5.3) and the corresponding results are given in table 5.1.

$$\langle \tau \rangle = \frac{A_1 \tau_1^2 + A_2 \tau_2^2}{A_1 \tau_1 + A_2 \tau_2} \dots \dots \dots (5.3)$$

The lifetime of the phosphorescent decay was measured from the decay profiles of the emission wavelength of 465 nm for all thin films and with an excitation wavelength of 337 nm. As can be seen in table 5.1, the average decay time of all the thin films is different, indicating that the deposition temperature has a great influence on the phosphorescence property of the  $Y_2SiO_5: Ce^{3+}$  thin films. The average decay time has a maximum value at a deposition temperature of 450 ° C; the life of the phosphor becomes relatively longer and begins to decrease when the deposition temperature reaches 600 ° C.

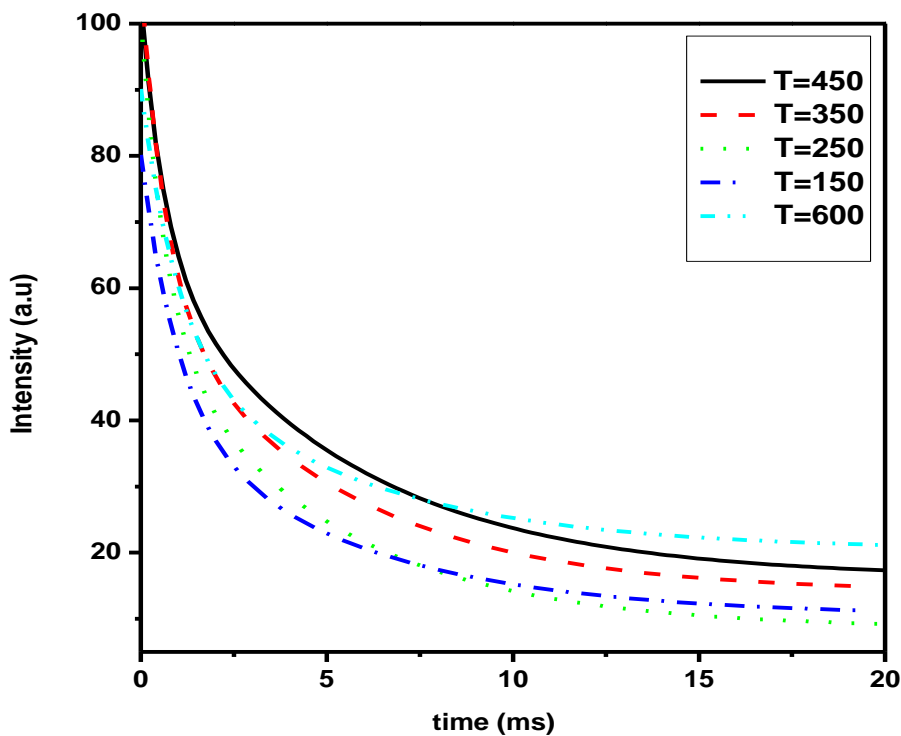


Fig. 5.8: decay curve for the  $Y_2SiO_5: Ce^{3+}$  thin films

The chromaticity coordinates of  $\text{Ce}^{3+}$  doped  $\text{Y}_2\text{SiO}_5$  phosphors were calculated using the excitation wavelength of 337 nm as shown in Fig. 5.9 and the corresponding values are in the blue region. This clearly shows that  $\text{Y}_2\text{SiO}_5:\text{Ce}^{3+}$  can be used for applications emitting blue light. Its mean chromaticity coordinate is  $(x, y) = (0.172, 0.126)$ . The results indicate that the phosphors  $\text{Y}_2\text{SiO}_5:\text{Ce}^{3+}$  ( $T = 450^\circ\text{C}$ ) can be selected as a potential candidate for blue light display applications

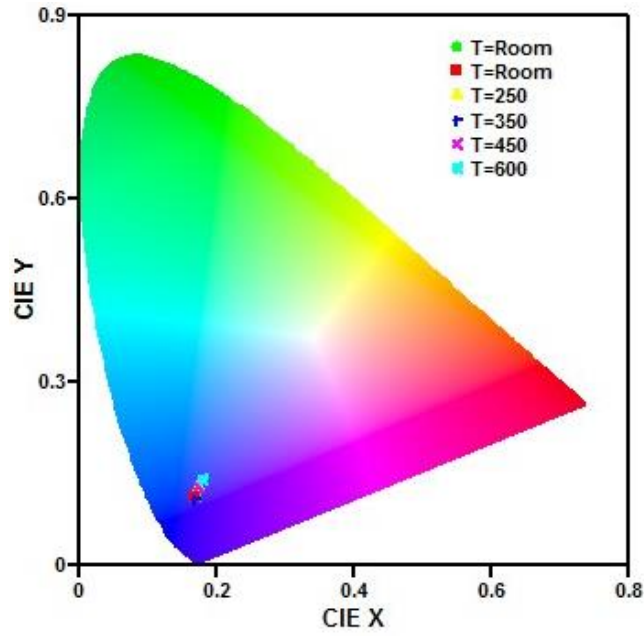


Fig. 5.9: CIE of the  $\text{Y}_2\text{SiO}_5:\text{Ce}^{3+}$  thin film phosphor

## Conclusions

The effect of substrate temperature on the material properties of  $\text{Y}_2\text{SiO}_5:\text{Ce}^{3+}$  thin film studied by the pulsed laser deposition method. From the XRD measurements, the material is monoclinic in structure, the diffraction peaks are observed at  $29.2^\circ$ ,  $22.4^\circ$  and  $16.14^\circ$  and the most prominent diffraction peaks are oriented in the (021) plane. An increment in surface thickness was observed from a deposition temperature of  $150^\circ\text{C}$  to  $450^\circ\text{C}$  and began to decrease from  $450^\circ\text{C}$  to  $600^\circ\text{C}$ . The average crystallite size was  $1.66\text{ nm}$ . The morphology of the thin layers is different. At lower deposition temperatures, particle distribution appears uniform regardless of agglomeration in some areas. When the temperature increases to  $450^\circ\text{C}$ , the density of the particles and the agglomeration increase which may be because of the spitting out of small particles into the cluster. When the temperature further increases to  $600^\circ\text{C}$ , the density of particles slightly decreases, which may be ascribed to the decrease in the deposition rate. The EDS measurement shows all the constituent elements of the compound exists. The percentage atomic weight of the constituent elements decreases as deposition temperature increases, which ascribes to the re-evaporation of the deposited particles from the substrate. The elemental maps support the EDS result; when the substrate temperature is increased, the surface is dominated by silicon (which may be also from the substrate). From the UV-Vis measurement, maximum and minimum absorption spectra observed for the thin films deposited at  $T=450^\circ\text{C}$  and room temperature respectively. The absorbance peak is at  $337\text{ nm}$ . The PL measurement shows excitation and emission wavelength of  $337$  and  $465\text{ nm}$ , respectively. The emission wavelength ascribes to a  $5d-4f$  electronic transition of  $\text{Ce}^{3+}$ . The excitation wavelength of  $337\text{ nm}$  ascribes to the transition of an electron from the ground state ( $^2F_{5/2}$ ) to the excited state ( $5d$ ) of  $\text{Ce}^{3+}$ . The maximum decay time observed at  $T = 450^\circ\text{C}$ . From the CIE evaluation, the color of the material lies in the blue region.

## Chapter 6: The influence of deposition gases on the material properties of $\text{Y}_2\text{SiO}_5: \text{Ce}^{3+}$ thin films deposited by pulsed laser deposition (PLD) method

### 6.1 Introduction

The luminescent materials that emit optical radiation (infrared, visible, or ultraviolet light) are sometimes called solid phosphors. The phosphors are widely used in fluorescent lamps, cathode ray tubes (CRT) and X-ray intensifiers [169, 170]. It converts parts of the absorbed energy into electromagnetic radiation that is greater than thermal radiation. When a solid is heated to a temperature of above  $600^\circ \text{C}$ , it emits infrared radiation. This condition is observed due to the thermal radiation, not a luminescence phenomenon [171]. Now a days, many researches are concerted on nano-structural phosphors doped with lanthanide ions and transition metal ions. These materials have various optical properties with a range of applications in optoelectrical devices. These compounds can be easily established by doping the RE (RE) elements into the single crystal, semiconductor, ceramic or polymer matrix [172]. These RE-doped compounds are the most favourable compounds in the field of optoelectronic and display applications [6, 125, 151]. RE-doped phosphors have the characteristics of long-time chemical stability, good illumination which can be applied in industrial processing of displays with a good efficiency and field emission display detector applications [46, 47]. Thin film phosphors are the best solution for the traditional phosphor powder cathode ray tubes. Thin film phosphor exhibits high contrast percentage, high ambient visibility, image resolution, and good heat resistance [48]. Sputtering, thermal evaporation and chemical bath deposition, sanochemical deposition [173] methods are some of the other methods used to deposit thin films of phosphor materials alongside the PLD. The most important parameter of thin film phosphors for the various deposition methods is the deposition at a low substrate temperature. This is due to the use of glass substrates and temperature sensitive phosphor materials. The pulsed laser deposition (PLD) method has been used to deposit thin films with stoichiometrically unique evaporation of target materials, such as complex superconducting oxides [174]. Therefore, thin film phosphor deposition using PLD is useful to investigate the luminescence and other properties of the phosphor material as we did in our previous papers [175]. Yttrium silicate crystal is a well-known material for hosting RE ions such as cerium. Yttrium silicate has a wide band gap of 7.4 eV which can comprehend a large amount of RE ions. It has been used successfully as a host matrix for RE ions due to its thermal and chemical stability, which contributes to the formation of phosphors or scintillating photocathodes. Energy structure of the bandgap of yttrium silicate ( $\text{Y}_2\text{SiO}_5$ ) activated with RE ions such as  $\text{Ce}^{3+}$  [49, 50],  $\text{Tb}^{3+}$  [49, 51] are widely investigated



for different applications.  $\text{Y}_2\text{SiO}_5: \text{Ce}^{3+}$  has been studied by various researchers for the purpose of scintillation [52, 53]. According to previous studies [49, 176],  $\text{Y}_2\text{SiO}_5: \text{Ce}^{3+}$  phosphor is a blue light emitter and many studies have been conducted to investigate luminescence characteristics for lighting industries such as field emission screens (FEDS). However, as far as our knowledge this material has not been studied in the thin film form with PLD deposition with the deposition condition we have used. The structure of  $\text{Y}_2\text{SiO}_5$  belongs to orthosilicate crystalline structures of  $(\text{RE}_2\text{SiO}_5)$  [54]. This silicate material has two monoclinic crystalline phase structures which are classified by their synthesis temperatures. These are  $X_1$  phase which is synthesized at low temperature (below  $1190^\circ\text{C}$ ) and has lower XRD-intensity with a space group of  $\text{P}2_1/\text{c}$  and  $X_2$  phases, synthesizing at high temperature (above  $1190^\circ\text{C}$ ) with a space group of  $\text{B}2/\text{c}$  [55]. There are two possible sites of  $\text{Y}^{3+}$  in each of these crystalline phases that can be attributed to the different number of coordinations in these phases [55, 56]. Broadband light-emitting materials in the visible spectrum commonly used to sensitize the luminescence of RE ions and the transition of metal ions. Specifically,  $\text{Ce}^{3+}$  is a 4f-5d allowable transition that provides effective broadband luminescence. Furthermore, the emission and excitation spectra of  $\text{Ce}^{3+}$  ions are very sensitive to the crystallographic site of the host material.  $\text{Y}_2\text{SiO}_5: \text{Ce}^{3+}$  is a superb phosphorescent material emitting blue light. It is, therefore, crucial to study the optoelectrical and display applications of this material [57, 58].

Measurement of thermoluminescence (TL) is a common technique for determining ionizing radiation that is known as thermoluminescence. TL is also known as thermally stimulated luminescence (TSL) which is a phenomenon related to the release of photonic energy following exposure to external thermal energy from low to high temperature, and this type is called delayed phosphorescence. In the TL measurement, heat is not the only source of energy for the luminescence to occur. This only causes the release of energy that originally came from another source. TL occurs following heating, when radiative transition (trapping and de-trapping) of the electrons from their metastable state occurs. TL is then resulted by the release of the trapped and de-trapped electrons and holes (charge carriers) and their combination [177]. If the trapping sites are emptied, the ionized radiation transfers the charges to the pre-existed sites. Consequently, the passage of the charges to the recombination region generates luminescence. The emission observed from the sample during heating up on the interaction of the radiation with matter gives information about the defect levels caused by the interaction of the ionized radiation with the sample [178, 179].

The present study describes the effect of different deposition gases on the luminescent, thermoluminescence, structural, optical and morphological properties of the PLD deposited  $\text{Y}_2\text{SiO}_5: \text{Ce}^{3+}$  thin-film phosphors. To the best of our knowledge, no research papers have been reported or

is under consideration for publication with the deposition condition we have used for the material under investigation for a possible display application.

## 6.2 Results and discussion

### 6.2.1 XRD analysis

Fig. 6.1 shows the XRD diffraction pattern of the thin film deposited at different deposition gases. The diffraction pattern has been observed at  $15.7^\circ$ ,  $19.9^\circ$ ,  $25.06^\circ$  and  $28.65^\circ$ . All the thin films have the strongest diffraction peak at  $15.7^\circ$  with a Bragg reflection plane of (110). The structures of these thin films formed on the silicon substrate are monoclinic in agreement with the JCPDS data Card No. 742158. The full width at half maximum (FWHM) of the main peak were  $0.37^\circ$ ,  $0.43^\circ$ ,  $0.45^\circ$  and  $0.6^\circ$  for the deposition gases of oxygen, argon, nitrogen and vacuum, respectively. The corresponding crystallite sizes, calculated using the Scherer's equation [180] given in equation (3.4), varies between 14.07 and 22.4 nm.

The highest diffraction peak pattern was observed under oxygen deposition atmosphere. This can imply that a good crystalline thin film is formed in this deposition conditions as compared to the other deposition conditions. The temperature, distance of the substrate from the target has also considerable influence on the development of the thin films by pulsed laser deposition [181]. However, since these parameters are kept fixed; the only significant impact on the growth of the thin film is from the deposition gases. The effect of deposition gases on the crystallite size and FWHM of the deposited thin films are shown in Fig. 6.2. From Fig. 6.2, the oxygen deposition gas has least value of FWHM and larger crystallite size as compared to the other deposition gases. This can be ascribed to the crystallinity of the thin films at the respective deposition conditions. In the oxygen deposition, oxygen vacancies are small because of the substitution of the background gas (oxygen) in the stoichiometric formation of the resultant compound, which could be a possible reason for the good crystallinity of the thin film in this deposition condition. In the vacuum deposition condition, the minor peaks are reduced which might be due to the variation of oxygen vacancies. In the vacuum deposition condition, there is high concentration of oxygen vacancies, when the X-ray photons are interacted with the oxygen vacancies, the photons will be trapped which in turn the diffraction intensity will be very small which can be simply dominated by the relative diffraction peaks from another area of interaction. From the Xrd diffraction peaks, it is possible to calculate the average crystallite size, macrostrain, volume of unit cell, dislocation density, stacking fault probability, and texture coefficient [182] which we can consider it in our future works.

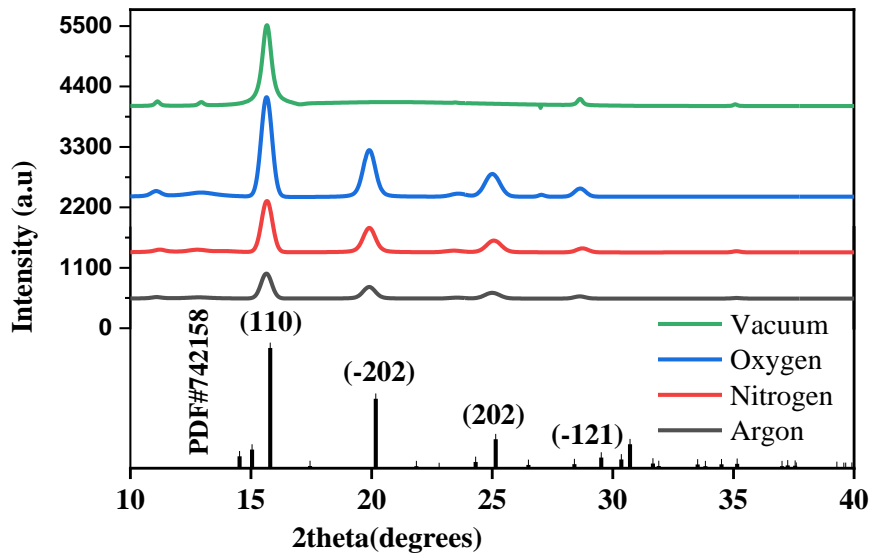


Fig. 6. 1: XRD diffraction patterns for the  $Y_2SiO_5: Ce^{3+}$  thin films deposited at different gases

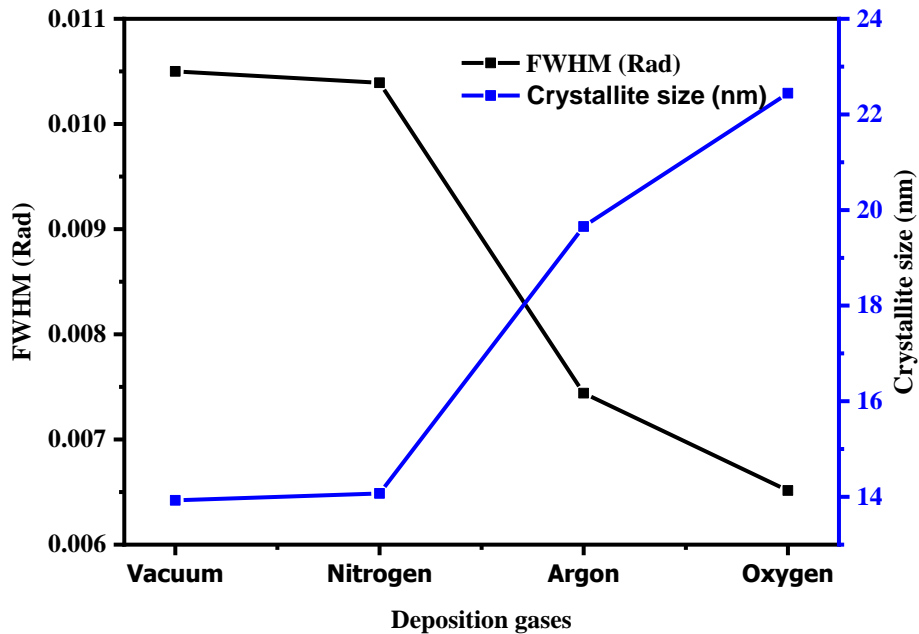
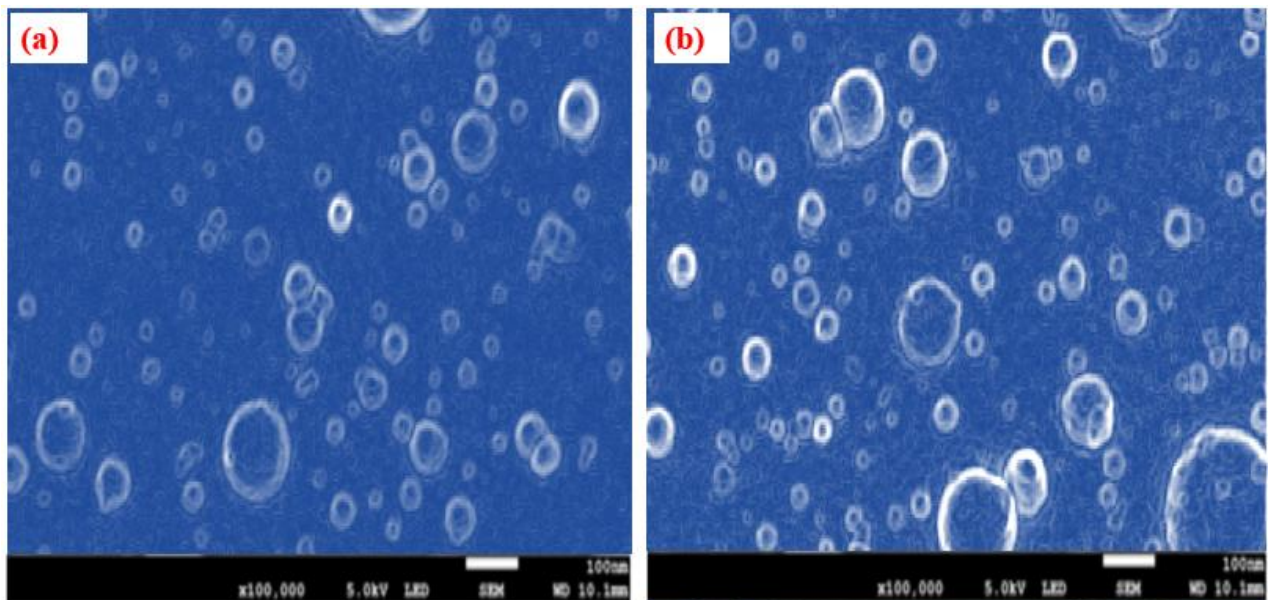


Fig. 6.2: Effect of deposition gases on the crystallite size and FWHM of the  $Y_2SiO_5: Ce^{3+}$  thin films

### 6.2.2 SEM and EDS analysis

Fig. 6.3 shows the SEM micrographs for thin films deposited under different deposition gases. As clearly seen from the micrographs, the morphology and size of the particle's changes with varying deposition conditions. The deposition parameters have a large influence on the plasma plume produced during laser ablation in which the propagating energy and mobility can be controlled by modifying deposition parameters like background gases [183]. When the background gases interact with the plasma plume the kinetic energy, the spatial distribution and the stoichiometry of the ablated particles from the target material changes. As a result, the thin films will have different

deposition rate and morphologies for the altered deposition gases as shown in Fig. 6.3. The collision of the atomic species of the deposition gases with the plume can also increase the vibrational energy of the ablated molecular species which can introduce variation of surface composition on the resulting thin films because of the variation in deposition rate [184]. SEM images of thin films with a magnification of x100,000 are shown in Fig. 6.3. In all images, particle distribution appears uniform, except for some agglomerations in a particular area. Under the vacuum atmosphere, the particles look small in size as compared to other deposition gases, the distribution of particles over the surface of the substrate appears uniform and smooth regardless of some rarely distributed large particulates (which might be clusters of particles). Under the nitrogen deposition gas, the particle size shows small increment, and clusters of particles are observed similar to the samples deposited under the vacuum condition. Mixtures of small and large sized particles are observed in all deposition conditions. However, under the argon and oxygen deposition conditions the agglomeration of particles is significantly decreased. The possible reason for the increase in agglomeration in vacuum and nitrogen deposition gases atmosphere and the roughness of the films in these background gases is due to the formation of particulates in the plume, which is a distinctive behavior of high pressure laser ablations [185]. The other reason for agglomeration is the condensation of the small clusters of particles removed from the target material in the background gases due to the formation of shock wave in the ablation process, resulting in the formation of large groups and agglomerations on the surface of the thin film.



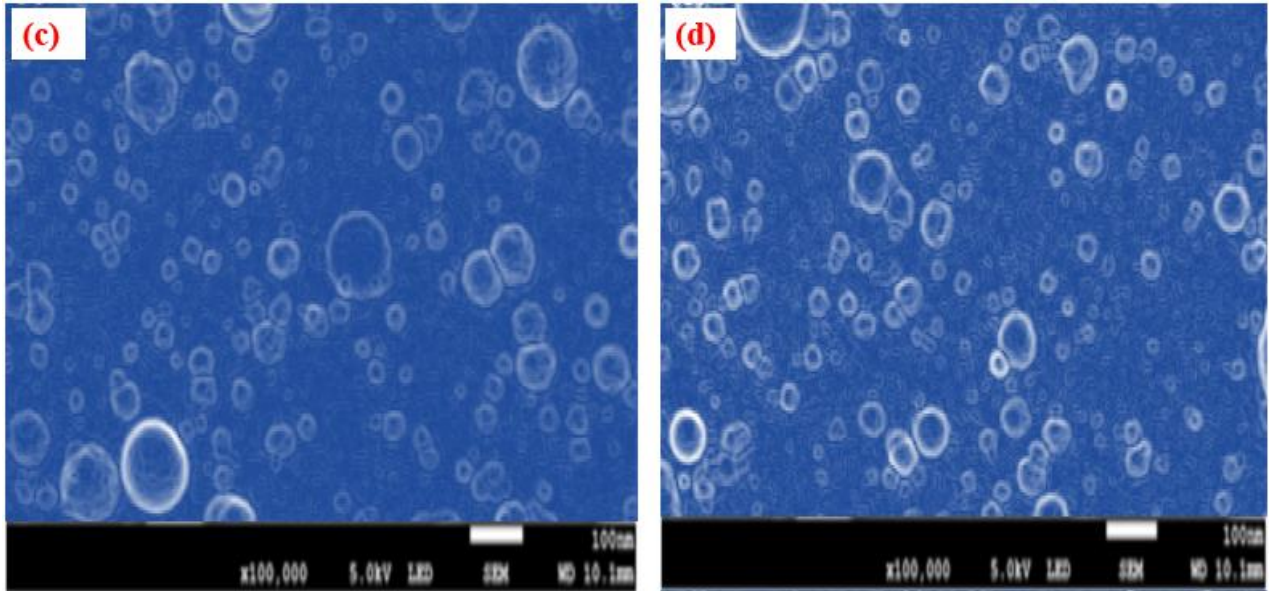


Fig. 6.3: SEM micrographs of  $Y_2SiO_5:Ce^{3+}$  thin films deposited at different gases: (a) vacuum (b) nitrogen (c) argon and (d) oxygen

A histogram which shows the distribution of nanoparticles in all deposition condition is shown in Fig. 6.4 with their respective diameters. The average nanoparticle size ( $X_c$ ) is 26.66, 26.69, 29.95 and 29.105 nm for vacuum, nitrogen, argon and Oxygen respectively. The average nano particle size of all deposition gases is 28.1 nm. The average polydispersity in diameter of the nanoparticles is calculated by equation (6.1). The calculated average polydispersity of the nanoparticles is 31.6.

$$PD = \left( \frac{\sigma_{av}}{X_{av}} \right) * 100 \% \dots\dots\dots (6.1)$$

Where  $\sigma_{av}$  is the average deviation and  $X_{av}$  is the average size of nanoparticles.

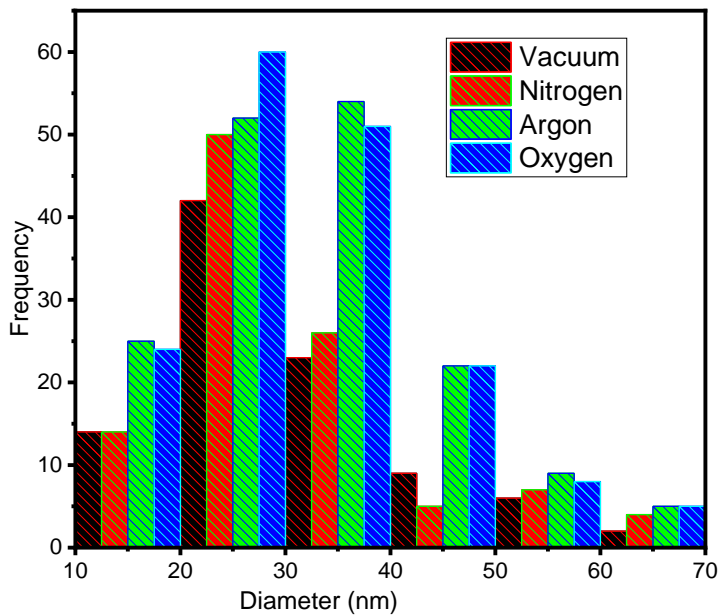


Fig. 6.4: Distribution of nanoparticles

Table 6.1: observed atomic percent of the elements in the thin films and the Powder

Elements	Observed At%			Standard at%
	Nitrogen	Argon	Oxygen	Powder
<b>Si</b>	58.55	64.93	53.93	12.73
<b>Y</b>	11.29	9.73	12.58	26.3
<b>O</b>	29.98	24.96	33.03	60.52
<b>Ce</b>	0.18	0.38	0.46	0.45

Table 6.1 shows the atomic percentages of the elements for the respective deposition conditions and the powder used to make the pellet for ablation. The cerium (dopant) element has high concentration in the oxygen and argon deposition conditions respectively and lower in the Nitrogen gas deposition condition. The atomic percentage of Si is observed to be high in the thin films which might be due to the silicon substrate used to deposit the films. As a result, the atomic percentage of the elements in the thin film and in the powder have significant difference except Ce. Fig.6.5 shows the energy dispersive spectroscopy (EDS) for the samples deposited under different deposition conditions and the powder used to make the pellet. All the elemental components of the phosphor were detected with their respective weight percent. The plasma plume created during the laser ablation process is strongly directed forward. Consequently, the thickness of the material formed on a substrate could not be uniform and the stoichiometric composition or ratio may vary among deposition conditions. The variation of the weight percentage and atomic percentage of the constituents of the crystalline compound can be observed from Fig. 6.5 and table 6.1. When the material is deposited in Nitrogen, the weight and the atomic percentages of the dopant (Ce) reduces considerably. However, the atomic concentration of  $Ce^{3+}$  ions increase in the argon and oxygen gas atmospheres.



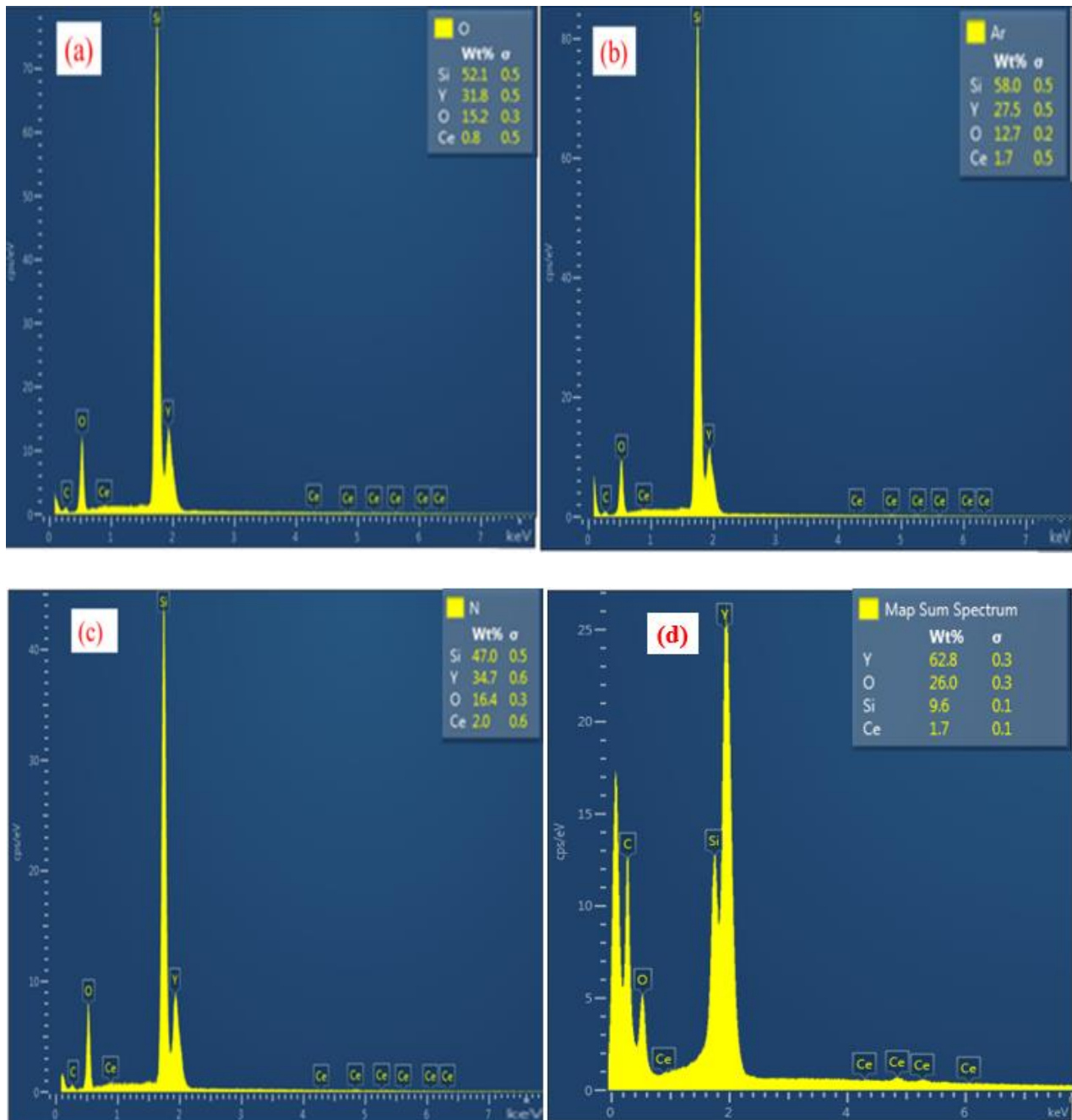


Fig. 6.5: EDS spectra of the  $\text{Y}_2\text{SiO}_5: \text{Ce}^{3+}$  thin films deposited at different background gases (a) Oxygen (b) Argon and (c) Nitrogen (d) powder

### 6.2.3 UV-Vis Analysis

UV-VIS spectroscopic measurement was taken to determine the optical properties of the thin film materials. Fig. 6.6 represents the absorbance of  $\text{Y}_2\text{SiO}_5: \text{Ce}^{3+}$  thin films as a function of the UV-wavelength. The maximum absorbance spectrum was observed for films grown under the Argon and oxygen deposition atmospheres respectively, this can be ascribed to the thickness of the thin films. The optical absorption under the oxygen deposition gas could be due to the increase in roughness and thickness of the surface of the thin film. The minimum optical absorption was observed in vacuum deposition conditions. The thickness of the film deposited on the silicon

substrate was calculated by measuring the mass of the substrate before and after deposition respectively, taking the mass difference between the two measurements and plugging in to the mathematical relationship given in equation (6.2), thin films deposited with argon and vacuum background gas showed maximum and minimum thickness, respectively. The decrease of the absorption value under vacuum deposition conditions could be attributed to the decrease in thickness of the film deposited on the substrate. The optical absorption leaning for the thin film deposited in different deposition gases shows a uniform decrease from the oxygen absorption edge to the vacuum absorption edge as shown in Fig. 6. 6. The thickness of the thin films has been calculated by equation (7.3)[186].

$$X = \frac{(m_2 - m_1)}{\rho A} \dots\dots\dots (6.2)$$

Where X is the thickness, m<sub>1</sub> and m<sub>2</sub> are the mass of the substrate before and after deposition in grams, ρ is the density of the silicon in g•cm<sup>-3</sup>. A is the deposition area in cm<sup>2</sup>. The estimated thickness of the thin film deposited on the substrate is, X = 62, 94, 125 and 134 nm for the thin films deposited in vacuum, nitrogen, oxygen and argon, respectively.

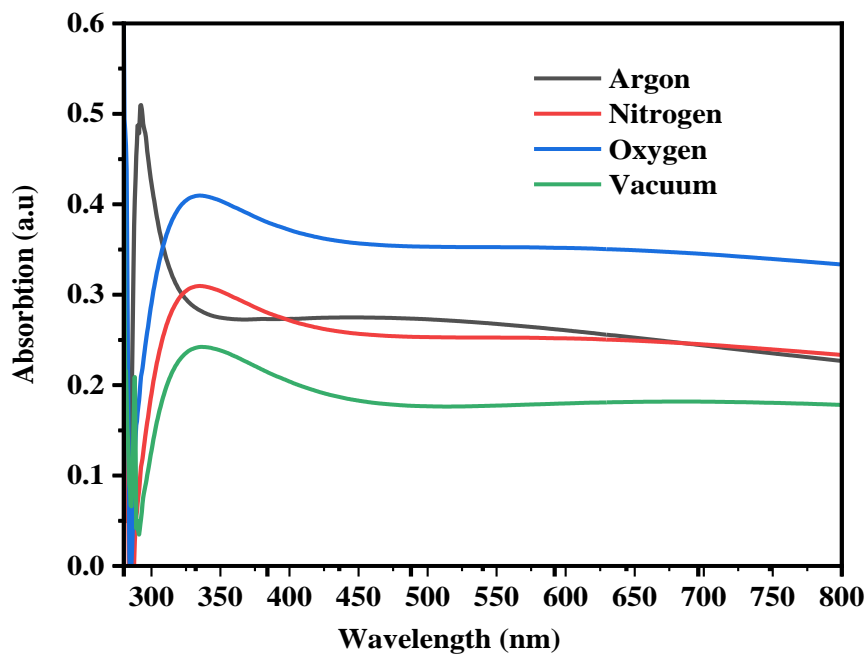


Fig. 6.6: Absorbance graphs of Y<sub>2</sub>SiO<sub>5</sub>: Ce<sup>3+</sup> thin films deposited at different deposition gases

The energy band gap is calculated using Tauc relation [187] which is given by:

$$(\alpha h\nu)^2 = K(h\nu - E_g) \dots\dots\dots (6.3)$$

where h is the plank’s constant, ν is the frequency of the incident wave, K is energy independent constant, α is absorption coefficient and E<sub>g</sub> is the optical band gap. The optical band gap of the material deposited at different gases which was obtained by extrapolating the (αhν)<sup>2</sup> Vs the hν plots



to the energy axis. As we can see from Fig. 6.7: the energy band gap varies between 3.14 and 4.33 eV. The thin films deposited at oxygen gas and the Argon has the minimum and maximum bandgap, respectively. The optical band gap decreases from Argon to oxygen deposition conditions. The decrease in optical band gap can be attributed to the improvement in crystalline quality [188].

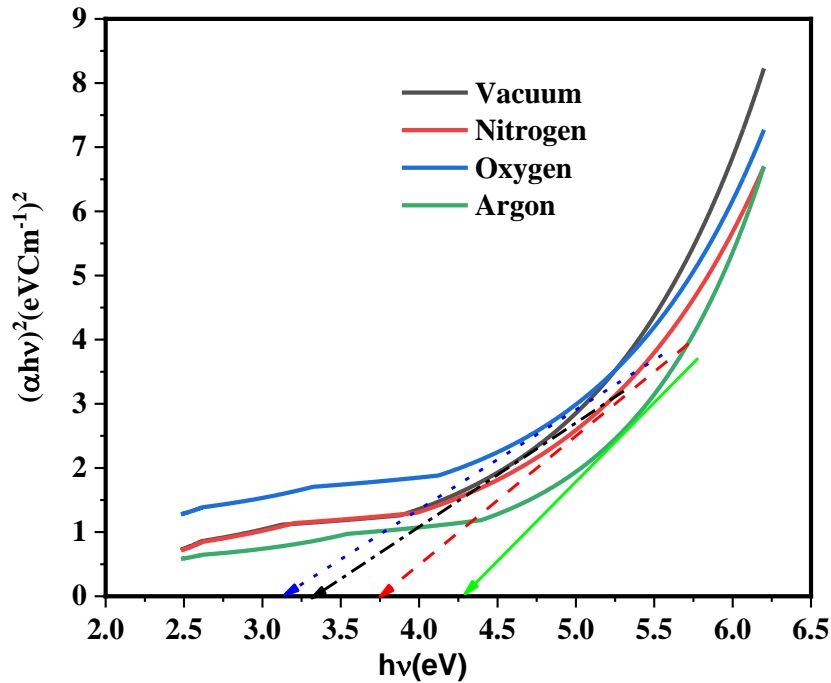


Fig. 6.7: Dependence of  $(\alpha hv)^2$  on the photon energy ( $h\nu$ ) for  $Y_2SiO_5:Ce^{3+}$  thin films deposited at different deposition gases.

#### 6.2.4 Photoluminescence Analysis

The PL emission and excitation of the  $Y_2SiO_5:Ce^{3+}$  thin films deposited at different background gases are shown in Fig. 6.8. All the thin films were excited at an excitation wavelength of 370 nm. The PL emission spectrum was observed at 423 nm, this is comparable to the emission wavelength reported in [176, 189]. However,  $Ce^{3+}$  ion has different coordination numbers when it occupies two separate lattice sites in the crystalline field of the host material ( $Y^{3+}$ ), therefore several emission peaks are hidden under the broadband of  $Ce^{3+}$  emission spectrum. The broadband emission can be decomposed into the constituent emission bands using the Gaussian peak fitting method as shown in Fig. 6.9. So, the main PL emission peaks are positioned at 420 and 457 nm which corresponds for the electronic transition of  $5d \rightarrow 4f^1(^2F_{7/2})$  and  $5d \rightarrow 4f^1(^2F_{5/2})$  respectively. The excitation spectrum which was probed at 423 nm shows two peaks at 370 and 332 nm which corresponds to the electronic transition from the valence band to the conduction band ( $4f \rightarrow 5d$ ). The electron that revolves around its axis and orbiting around the nucleus has a doublet character that is observed due to the division of the ground state of  $Ce^{3+}$  into  $^2F_{7/2}$  and  $^2F_{5/2}$ . The emission bands positioned at 420 and 457 nm corresponds to the blue color. This emission could be attribute to the electron transition

of the  $\text{Ce}^{3+}$  ion from 5d to 4f states. The electronic configuration of cerium ( $\text{Ce}^{3+}$ ), consists of one electron in the 4f energy state; When the 4f<sup>1</sup> configuration of  $\text{Ce}^{3+}$  is irradiated with UV radiation, the 4f electron is excited and transferred into the 5d orbit leaving the 4f shell empty. Therefore, the excitation spectrum of the cerium ion gives information on the crystal division of the 5d orbitals, which is the reason for the PL emission centers of 420 and 457 nm. Due to the spin-orbit interactions, the ground state 4f splits into  $^2f_{5/2}$  and  $^2f_{7/2}$  energy sub-levels. When the 4f and 5d states interact, the electron is excited to the 5d state. The electronic transition from 4f to 5d is parity and spin allowed [190]. The interaction between the dopant ions (Ce) and the atoms in the crystalline field of the host material through the surrounding charges is the possible reason for the creation of 4f and 5d energy levels at the positions of the valence and conduction band, respectively. The creation of the energy levels of 4f and 5d could decrease the center of mass of the 5d structures due to the electrostatic interaction [148] that corresponds to the excitation wavelength of 332 nm. The entry of the  $\text{Ce}^{3+}$  ion into a specific lattice site causes the 5d state to be divided into different sub-states according to the symmetry of the site [191]. If the 5d state is in more than one lattice site, it is very likely to split into several sub-levels [190]. The division of the ground state energy of  $\text{Ce}^{3+}$  ion into  $^2F_{7/2}$  (parallel) and  $^2F_{5/2}$  (antiparallel) is the possible cause for the doublet characters (rotation of electrons around its axis and orbiting the nucleus). Deposition gases play a very important role in the growth of thin films during PLD ablation. During the ablation process, the phenomena that can take place are: the reflection of ions or atoms on the surface of the film, scattering of the incoming atoms from the deposited atoms and the establishment of the arriving particles [192]. High emission and excitation were observed under the oxygen background gas. Since oxygen gas has effective chemical reaction and conversion capabilities when interacting with the ablated particles, molecules and groups are more abundant in the oxygen gas background than other deposition gases [193] which can be attributed to the suppression of oxygen vacancies.

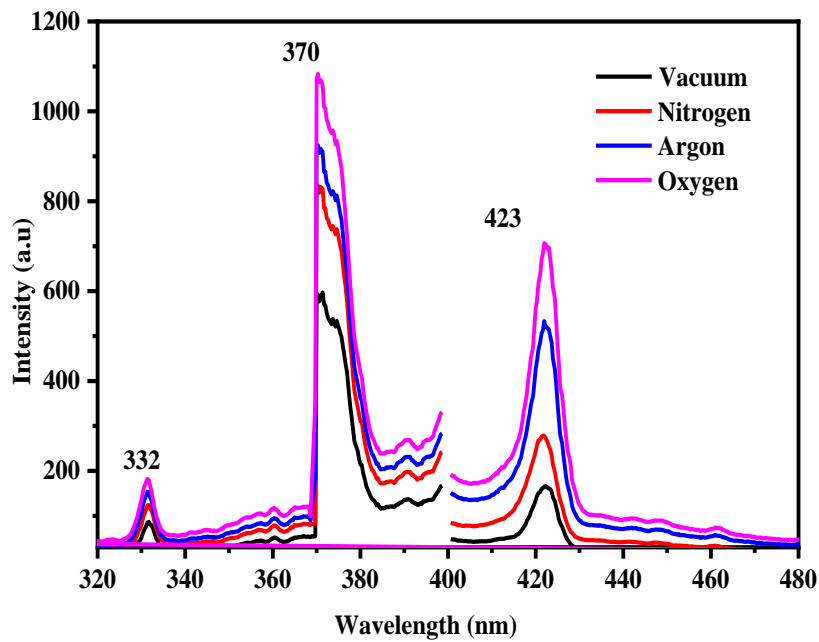


Fig. 6.8: Excitation and emission spectra of Y<sub>2</sub>SiO<sub>5</sub>: Ce<sup>3+</sup> thin films

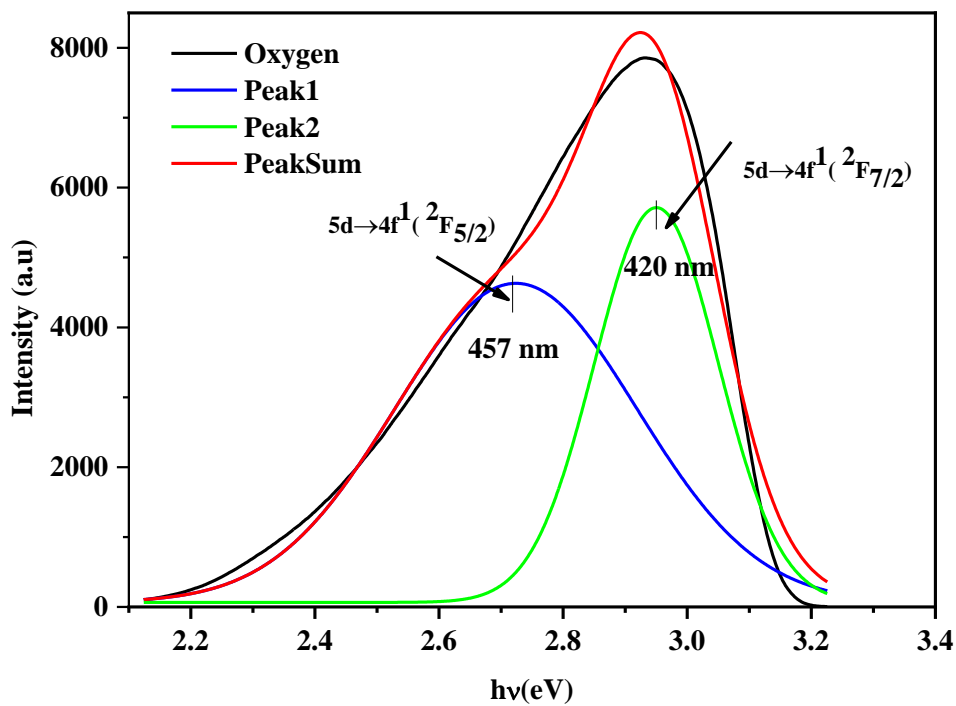


Fig. 6.9: Deconvoluted emission peak of Y<sub>2</sub>SiO<sub>5</sub>: Ce<sup>3+</sup> thin film for oxygen deposition

Therefore, the emission spectrum of the Ce<sup>3+</sup> ion is positioned at 420 and 457 nm, which are completely in the blue range. The chromaticity coordinates of the Ce<sup>3+</sup> doped Y<sub>2</sub>SiO<sub>5</sub> phosphor were calculated using the 423 nm emission wavelength, as shown in Fig. 6.10 and the corresponding values are in the blue region. This clearly shows that Y<sub>2</sub>SiO<sub>5</sub>: Ce<sup>3+</sup> can be used for blue light emitting applications. Its average chromaticity coordinate is (x, y) = (0.178, 0.136). The results indicated that

the corresponding color for all the thin films rests in the blue color region, which are a good candidate for blue light display applications. Nevertheless, the thin films deposited at the oxygen background gas has relatively better emission as shown from the PL graph.

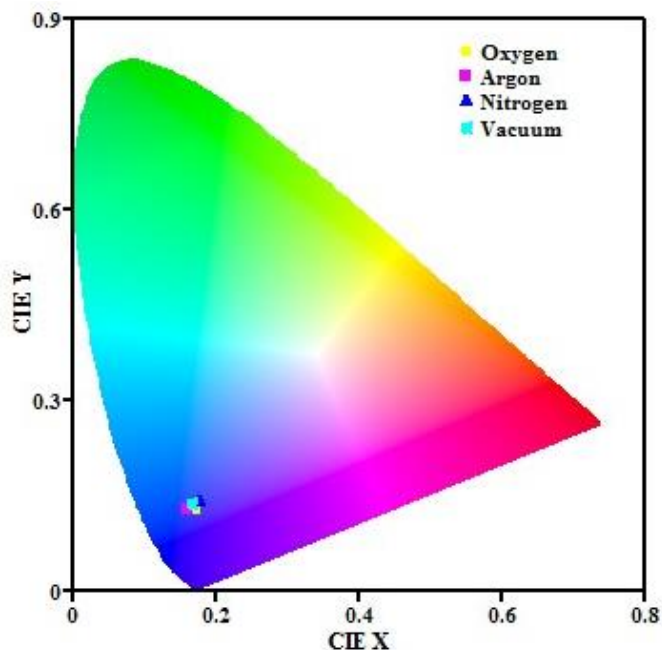


Fig. 6.10: The CIE chromaticity diagram for the  $Y_2SiO_5:Ce^{3+}$  thin films excited at 370 nm

### 6.2.5 Thermoluminescence analysis

TL is the stimulated emission of light resulting from the absorption of radiation. The absorbed radiation causes the electrons to move through the crystal lattice. When the sample is heated, the trapped electron returns to its normal position which exists at low energy levels by releasing energy in the process of return. This measurement is effective for biological applications (age determination), dosimetry, geology, analysis of the structure of solid-state defects etc. The main objective of the TL measurement is to exploit the data from the experimental glow curve to calculate the associated parameters (activation energy, frequency factor, kinetic order and form factor) in the energy space related to the luminescence process. The trapping parameters shown in table 6.2, are related to the TL glow curve which seats in different depth in the band gap (between the conduction and valence bands of the material) [194]. The activation energy gives us information about the depth of the trap and measure their energy levels in the band gap. The order of kinetics (b) is mainly related to the mechanism of recombination of the trapping charges with their counterparts. The frequency factor (s) represents the product of the number of times (frequency) the electron heats the potential wall (trap) and the reflection coefficient of the wall as a result of interaction. TL is a very sensitive measurement method that is used to estimate the concentration of luminescent centers in the solid. The TL emission also reveals the levels of defects (traps) created in solids irradiated by a certain energy [195]. The TL glow curves of UV irradiated  $Y_2SiO_5:Ce^{3+}$  thin film grown by different

deposition gases are shown in Fig. 6.11 and the estimated kinetic and the trapping parameters which are obtained from the glow peak shape are given in table 6.2 and 6.3. The TL glow curve for nitrogen deposition gas was not plotted because the intensity was very small as compared to the other deposition gases which can be ascribed to shallower defect level. We have applied Chen's peak shape equation [195] to find the activation energies from the corresponding parameters ( $\tau$ ,  $\delta$  and  $\omega$ ) that are obtained from the glow curve of the experimental data (Fig.6.11). The value of the parameters is as follow:

$$\tau = T_m - T_1, \delta = T_2 - T_m, \omega = T_2 - T_1 \text{ and } \mu_g = \delta/\omega \dots\dots\dots (6.4)$$

Where;  $T_M$  = peak temperature at the maximum TL intensity,

$T_1, T_2$  = temperatures on either side of  $T_M$ , corresponding to the half-maximum intensity and  $\mu_g$  is the geometrical shape factor or symmetry factor.

The most appropriate chen's equation to calculate the activation energy is given in equation (6.5).

$$E_\alpha = C_\alpha \left( K \frac{T_m^2}{\alpha} \right) - b_\alpha (2KT_m) \dots\dots\dots (6.5)$$

Where  $\alpha$  stands for  $\tau, \delta$  or  $\omega$ .

The value of  $C_\alpha$  and  $b_\alpha$  is summarized below:

$$\begin{aligned} C_\tau &= 1.51 + 3(\mu_g - 0.42) ; b_\tau = 1.58 + 4.2(\mu_g - 0.42) \\ C_\delta &= 0.976 + 7.3(\mu_g - 0.42); b_\delta = 0 \\ C_\omega &= 2.52 + 10(\mu_g - 0.42); b_\omega = 1 \end{aligned}$$

Theoretically, the system factor ( $\mu_g$ ) ranges between 0.42 and 0.52. when the system is closing to 0.42, it is first order kinetics and if the system factor is closing to 0.52, it is second order kinetics. The system factor ( $\mu_g$ ) is practically independent of the activation energy (E) but it strongly depends on the order of the kinetics (b) [196]. When E and b are known, S can be evaluated by Chen and Kirsh relation [197].

$$\frac{\beta E}{KT_m^2} = S. \exp \left[ \frac{-E}{KT_m} \right] [1 + (b - 1)\Delta m] \dots\dots\dots (6.6)$$

Where  $\beta$  is the linear heating rate, b is the order of kinetics and  $\Delta m = \frac{2KT_m}{E}$ . Shenker and Chen [198] and Kivits and Hagebeuk [199] tested the accuracy of these methods of calculating E. They concluded that the methods give trap depths at 5% close to the real value. Using equation (6.5) and (6.6), the corresponding activation energy and the frequency factor are summarized in table 6.3. As can be seen from table 6.2 and 6.3 the value of the kinetic factor approaches that of the first order

kinetics (0.42), as a result, the value of  $C_\alpha$  and  $b_\alpha$  ( $\alpha = \tau, \delta$  and  $\omega$ ) have been used to calculate the corresponding activation energies.

Table 6.2: Estimated kinetic and trapping parameters obtained using glow peak shape in UV-irradiated (10minutes)  $Y_2SiO_5:Ce^{3+}$  nano crystalline thin film

Deposition condition	$T_1(^{\circ}C)$	$T_m(^{\circ}C)$	$T_2(^{\circ}C)$	$\omega$	$\tau$	$\delta$	$\mu_g = \delta/\omega$
Argon	50.238	120.15	164.26	114.022	69.912	44.11	0.38686
Oxygen	41.101	115.4	162.59	121.489	74.299	47.19	0.38843
Vacuum	57.23	134.4	180.088	122.858	77.17	45.69	0.37188

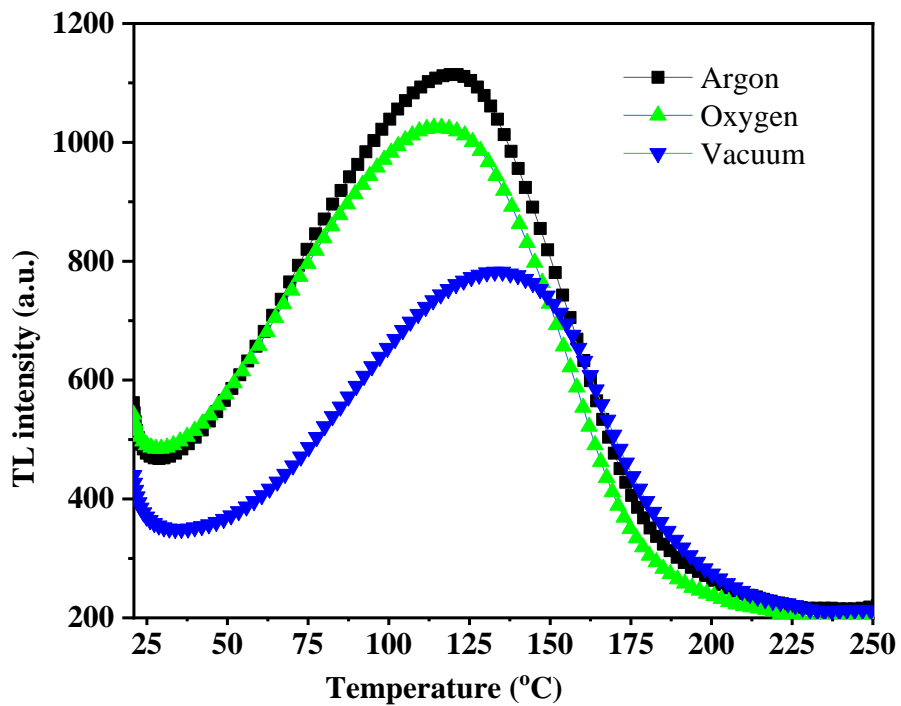


Fig. 6.11: Effect of deposition gases on TL intensities of  $Y_2SiO_5:Ce^{3+}$  thin film phosphors

Table 6.3: Calculation of trap parameters and order of kinetics for UV-irradiated  $Y_2SiO_5:Ce^{3+}$  thin film phosphor.

Deposition condition	$T_m(K)$	Order of kinetics $\mu_g(b)$	Activation energy (eV)				Frequency factor ( $S^{-1}$ )
			$E_\tau$	$E_\delta$	$E_\omega$	$E_{av}$	
Argon	393.15	0.38686	0.1727	0.2212	0.1875	0.1938	$1.16 \times 10^3$
Oxygen	388.4	0.38843	0.1522	0.2050	0.1686	0.1752	$6.56 \times 10^2$
Vacuum	407.4	0.37188	0.1579	0.1952	0.1668	0.1733	$4.30 \times 10^2$

The average activation energy ranges between 0.1733 and 0.1938 eV. Maximum activation energy was obtained under the argon deposition gas. This can be ascribed to the existence of maximum defect level on the argon deposited thin film as compared to the other thin films deposited at different gases.

## Conclusion

The  $Y_2SiO_5:Ce^{3+}$  thin films have been deposited at different background gases to characterize their luminescence, thermoluminescence, optical, morphological and structural properties. The material is structurally monoclinic with a prominent diffraction peak of  $15.7^\circ$ . Relatively, good crystalline thin film has been obtained at oxygen deposition gas, which can be due to the suppression of oxygen deficiency by the background gas. From the SEM measurements, the thin films have different textures and topographies. The collision of the deposition gas with the plume increases the vibrational energy of the eliminated molecular species and induces a variation of the composition during the formation of the thin films. The crystallite size of the particles has increased from vacuum to oxygen deposition condition. Agglomeration was observed due to the condensation of the shock wave formation introduced at the surface of the thin film. The average diameter of the nanoparticles is 28.1nm. From the EDS measurements, all constituent elements were detected with their respective atomic weight. Maximum and minimum UV absorbance was noticed at argon and vacuum respectively. Thickness and roughness of thin films play an important role in increasing and decreasing the absorbance value of thin films. All the thin films were probed at an excitation wave length of 370 nm. The corresponding emission spectrum was observed at 420 and 457 nm by deconvoluting the broad PL emission into its constituents. Due to the spin-orbit interactions, the ground state 4f alienated into  $^2f_{5/2}$  and  $^2f_{7/2}$  sub-energy levels. From the CIE measurement, all the color coordinates of the thin films are in the region blue. Maximum TL emission was observed at

393.15, 388.4 and 407.4 K for Argon, Oxygen and vacuum respectively. The activation energy ranges between 0.1733 and 0.1938 eV.



## **Chapter 7: Influence of oxygen deposition pressure on the structural, morphological, photoluminescence and thermoluminescence properties of $\text{Y}_2\text{SiO}_5:\text{Ce}^{3+}$ by pulsed laser deposition method**

### **7.1 Introduction**

The transforming capacity of phosphor materials from the excited states of the UV-light, electrons or X-rays in to visible radiation makes them simple to apply for lights, displays and communication application fields [200, 201]. Phosphors are used as a host lattice for the incorporations of RE ion or transitional metals for different display applications. Due to their interesting brightness, chemical stability and extensive industrial applications, many research developments are aimed in optimizing the characteristics of RE doped phosphor materials for various applications such as display panels and field emission display detectors by improving the efficiency of its luminescence [202]. In the visible range, broadband light emitter materials are typically sensitizing transition metal ions and luminescence of RE ions. Specifically, the cerium ion ( $\text{Ce}^{3+}$  which is 4f-5d parity and spin allowed transitions) exhibits effective broadband luminescence. In addition to this, the excitation and emission of  $\text{Ce}^{3+}$  is very sensitive to the crystallographic site of the host material.  $\text{Y}_2\text{SiO}_5:\text{Ce}^{3+}$  is a good blue-emitting phosphor material, it is vital for optoelectrical applications like telecommunication laser, fiber optic, LED traffic light, photodiode and solar cell which are preferably used in solid state lamps and lasers [52, 58]. Common optoelectronic devices are LEDs, laser diodes, photodiodes, and solar cells. The band gap of yttrium silicate is wide, it can accommodate the doped ion which a result emits an effective blue light, it can also apply in different applications of the field of emission displays (FED). where FED is a flat panel technology that uses large field electron emission sources to provide electrons that hit the color phosphor to produce a color image [142, 175]. In the wideband gap materials (insulators and semiconductors), the presence of defects in the bandgap will affect the electrical and optical properties of the material. Identifying and characterizing the defect levels which are literally acting as electron and hole traps is very crucial in understanding the dynamics of the charge carriers and excitons which can ultimately control the optical and electrical properties of the insulator or semiconductor materials. Thermoluminescence (TL) can measure traps and their depth in the band gap. It is commonly used for dosimetry and has also been used for defect and radiation damage studies. The material property measured as function of temperature is called thermally stimulated process. When the sample is exposed to ionizing radiation, by increasing the temperature it becomes thermally stimulated back to equilibrium by releasing accumulated energy in the form of light emission[25]. The presence of thermoluminescence in a crystal depends on the existence of defect levels in the interaction zone

which is capable of absorbing the irradiations and does not cause an emission of light until after heating of the sample [23, 24, 203]. Gamma rays, beta rays, x-rays and UV radiation are the possible irradiation sources used to irradiate (excite) during the TL measurement. The absorbed energy during irradiation time is known as radiation dose, which is equivalent to the product of dose rate and exposure time (dose rate x exposure time), which makes the TL measurement effective in the application of radiation dosimetry. Alongside the dosimetric applications, TL measurement is useful tool in studying the defect level and the trapping parameters in the nanomaterials. In the TL measurement, the temperature versus intensity graph, as shown in Fig. 8.12, represents the TL glow curve. Each peak represents the corresponding recombination centre's/traps. The activation energy and the escape frequency can be calculated from the glow curves [26].

Based on the synthesis conditions, yttrium silicate can exist in two monoclinic structural phases i.e. the low temperature phase ( $X_1\text{-Y}_2\text{SiO}_5$ ) where the synthesis temperature is less than 1190 °C and the high temperature phase ( $X_2\text{-Y}_2\text{SiO}_5$ ) where the corresponding temperature is above 1190 °C. In these two structures the  $\text{Y}^{3+}$  can occupy the low symmetry sites, which can be distinct by their coordination numbers.  $X_1\text{-Y}_2\text{SiO}_5$  phase has a coordination number of 7 and 9 and  $X_2\text{-Y}_2\text{SiO}_5$  has a coordination number of 6 and 7 [204, 205]. In literature, the high temperature phase is suitable for high intensity emissions than the low temperature phase. So, the high temperature phase is the main focus for investigations [206]. PLD method has been used for the deposition of various materials like polymers, semiconductor materials, ferroelectrics, and non-crystalline materials. The plasma which is introduced by the laser ablation is energetic in which its mobility can be controlled by the processing parameters. Hence the PLD deposition method has been used for practical applications by producing high-quality thin films. The stoichiometry [207], texture [208], microstructure [209] and other properties of the deposited thin films can be affected by the background gas during deposition processes. Moreover, the dielectric or electrical performance of the thin films are also affected [210]. The preferred orientation of the crystallites could be changed (orientation might change from “a” to “c” axis) due to the increase in oxygen pressure. The suppression of the oxygen vacancy could improve the quality of the thin films. On the other hand, the increasing oxygen pressure could also deteriorate the film as a result of more droplets that could be formed on the surface of the film. The increase in oxygen pressure could also introduce rougher surfaces. Many research work has been reported on this material, synthesized using combustion method in investigating its luminescence [49, 211], thermal [212], thermoluminescence properties [177]. However, to the best of our knowledge, no research paper has been reported or is being considered for publication on the deposition method and deposition conditions that have been employed to grow  $\text{Y}_2\text{SiO}_5\text{:Ce}^{3+}$  thin films. The purpose of this work is to investigate the influence of oxygen

deposition pressure on the structural, morphological and photoluminescence properties of  $\text{Y}_2\text{SiO}_5:\text{Ce}^{3+}$  by pulsed laser deposition method

## 7.2 Result and discussion

### 7.2.1 Xrd analysis

Fig. 7.1 shows the GIXRD pattern of  $\text{Y}_2\text{SiO}_5:\text{Ce}^{3+}$  thin film phosphor material deposited at different oxygen pressures (1.5, 20, 40, 60 and 100 mT). The diffraction pattern of the thin films shows a diffraction peak at  $2\theta$  of 28.9, 32.2 and 52.6 degrees. A prominent diffraction peak has been observed at a diffraction position of  $28.9^\circ$  as seen in all deposition conditions, which could be the most preferred orientations especially at higher oxygen pressures ( $> 1.5$  mT). Small shift of the prominent diffraction peak to the higher angle has been observed as the deposition pressure increases to 60 mT. This can be ascribed to the impurities created by the dopant material (variation in ionic radius), lattice shrinkage or internal stress which could be introduced by irradiation. The Xrd of the powder material is included to observe the shifts in crystal orientation and structure. The diffraction pattern has compared and fitted with the JCPDS#410004 which has a monoclinic structure of the  $\text{Y}_2\text{SiO}_5$  material with space group of  $\text{P}2_1/\text{c}$  (14) and cell parameters of  $a=9.012$ ,  $b=6.979$  and  $c=6.63\text{\AA}$ . Maximum diffraction intensity has been observed at the maximum deposition pressure (100 mT) with a prominent miller index of  $(12\bar{1})$ . It is known that the kinetic energy of atoms can affect the crystallization of thin film materials on the substrate[183]. When laser energy and substrate temperature are controlled, the kinetic energy of atoms is derived from the oxygen partial pressures. When the oxygen pressure is high enough, the surface ad-atoms move quickly to reach the site with low energy and form a low energy structure that can improve the crystallinity of thin films. As a result, high diffraction intensity for the deposition pressure of 100 mT has been observed, which can ascribe to the occurrence of better crystalline thin film at this deposition pressure.

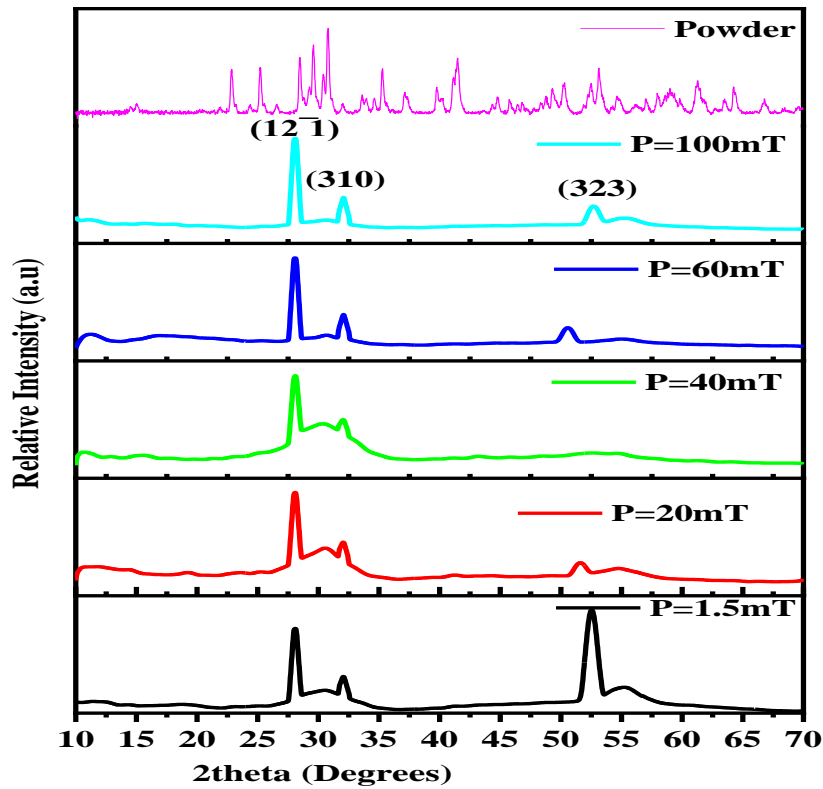


Fig. 7.1: GIXRD pattern of  $Y_2SiO_5:Ce^{3+}$  thin films deposited at different oxygen Pressure

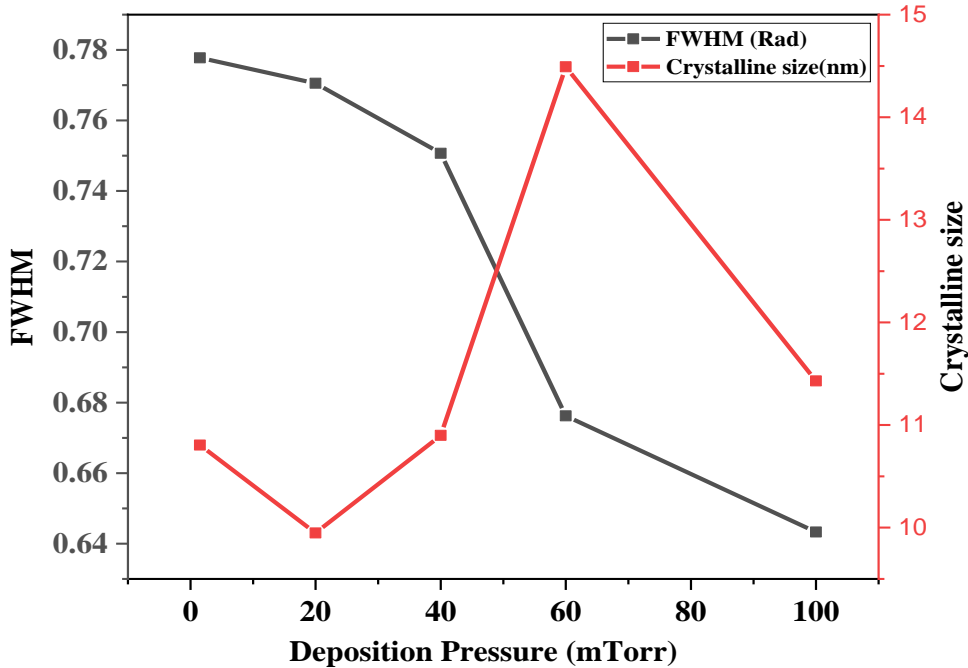


Fig.7.2 Effect of oxygen deposition pressure on the crystal size of the thin films

When laser energy and substrate temperature are controlled, the kinetic energy of atoms is derived from the oxygen partial pressures. When the oxygen pressure is high enough, the surface ad-atoms move quickly to reach the site with low energy and form a low energy structure that can improve the crystallinity of thin films. As a result, high diffraction intensity for the deposition pressure of

100 mT has been observed, which can ascribe to the occurrence of better crystalline thin film at this deposition pressure. The dependence of Full width at half maximum and crystalline size is shown in fig .7.2.

The GIXRD diffraction peaks has been used to determine the crystalline size using sheerer equation [213]. The full width at half maximum of the prominent peak has been used to calculate the crystalline size of the nanoparticles developed in the silicon substrate using equation (3.4). Maximum crystalline size has been obtained at oxygen deposition pressure at 60 mT and starts decreasing when the deposition pressure is further increased to 100 mT. The increase in crystalline size can be ascribed to better crystallization of the deposited material at moderate oxygen deposition pressures.

### **7.2.2 Raman spectroscopy Analysis**

The Raman spectra of the thin films deposited at different oxygen deposition pressures are shown in Fig.7.3. This measurement is compatible with GIXRD measurements which enables us to see the formation of crystalline, non-crystalline or amorphous films by looking at the frequency mode in the materials system. Where the Raman spectra are acquired by irradiating the sample with a monochromatic laser source in the range of visible or IR spectral regions[214]. The lower frequency emission of Raman spectrum observed at a wavenumber of around  $8\text{ cm}^{-1}$  refers to the stokes scattering and the higher emission spectrum observed at a wavenumber of  $533\text{ cm}^{-1}$  refers to anti-stokes scattering. Raman scattering is an inelastic scattering where the incoming photon energy is not conserved in contrast to elastic scattering. The emitting energy is either increasing or decreasing which can be limited by the energy exchange between the interacting particles and the photon. After the interaction has taken place with the sample, the frequency of the photon shifts towards either red or blue. A red shift is observed in the stokes scattering where the energy of the incoming photon is transferred in to the matter during interaction, where as in the anti-stokes scattering where the energy of the interacting matter is transferred to the photon, blue shift observed at wave number of  $533\text{ cm}^{-1}$ , maximum emission intensity is measured. There is no significant shift in wavenumber for all deposition pressures. The highest intensity peak indicates the formation of crystalline thin film at a position of emission point which is in a good agreement with the GIXRD diffraction peak shown in fig.7. 1 where the intense diffraction peak was observed around  $28.9^\circ$ .

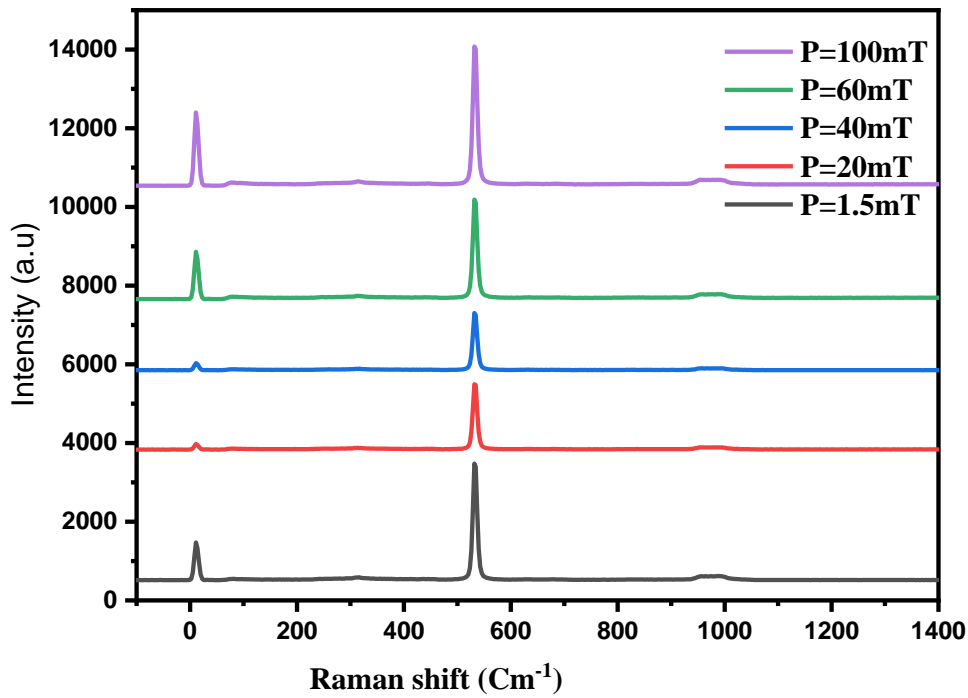


Fig. 7.3: Raman spectra of  $Y_2SiO_5:Ce^{3+}$  thin films deposited at different oxygen pressure

### 7.2.3 SEM and EDS Analysis

The SEM analysis were used to study the surface morphology and microstructural characteristics of  $Y_2SiO_5:Ce^{3+}$  thin films. Scanning electron microscope (SEM) micrographs of the samples deposited at different oxygen deposition gas are shown in fig. 7.4. As clearly observed in fig. 7. 4, the topography and surface roughness of the depositions show significant variation. This is also confirmed by the AFM micrographs measurement presented in fig. 7.8. The grains are spherical in shape and uniformly distributed over the silicon substrate apart from some small agglomerations observed in all deposition conditions. This can be attributed to the decrease in slow arrival speed of the particles in the plume on to the deposition areas due to the reduced deposition rate. Hence the ablated particles in the plume allow a better nucleation on the substrate during the ablation process. Deposition gas is one of the most vital parameters for thin film depositions using the pulsed laser method, particularly for  $Y_2SiO_5: Ce^{3+}$ . The high deposition pressure can maintain the crystalline quality of thin films by controlling the atomic kinetic energy in the plume during collision with oxygen particles. When the collisions between the oxygen atoms and the plasma plume are weak, the surface ad-atoms will have high kinetic energy. This energy could re-evaporate the ad-atoms that are formed on the surface. At high oxygen pressure, the ad-atoms can obtain enough energy by dispersing the oxygen atoms and accelerating the ad-atoms to reach the appropriate (thermodynamically stable) sites through surface repositioning. The observed cracks in both measurements can be ascribed to the surface damage induced by the electron beam during image formation. The grains observed in these depositions are spherical in shape and have almost similar



size. At the highest oxygen pressure, the mobility of the ad-atoms on the surface decreases due to the flow of lined oxygen fluxes. As a result, structural defects and crystalline degradation could be observed. The size of the nanoparticles on the SEM measurements distributed on the substrate for the deposition pressures of 1.5, 20, 60 and 100 mTorr respectively is given in the histogram (fig.7.5). The average diameter of the distributed nanoparticle is 0.54, 0.49, 0.39 and 0.55 $\mu\text{m}$  respectively. The relative Gaussian distribution of the nanoparticles (NPs) is given in fig. 7.6. As we can see from fig.7.6 the nanoparticles are evenly distributed over the substrate.

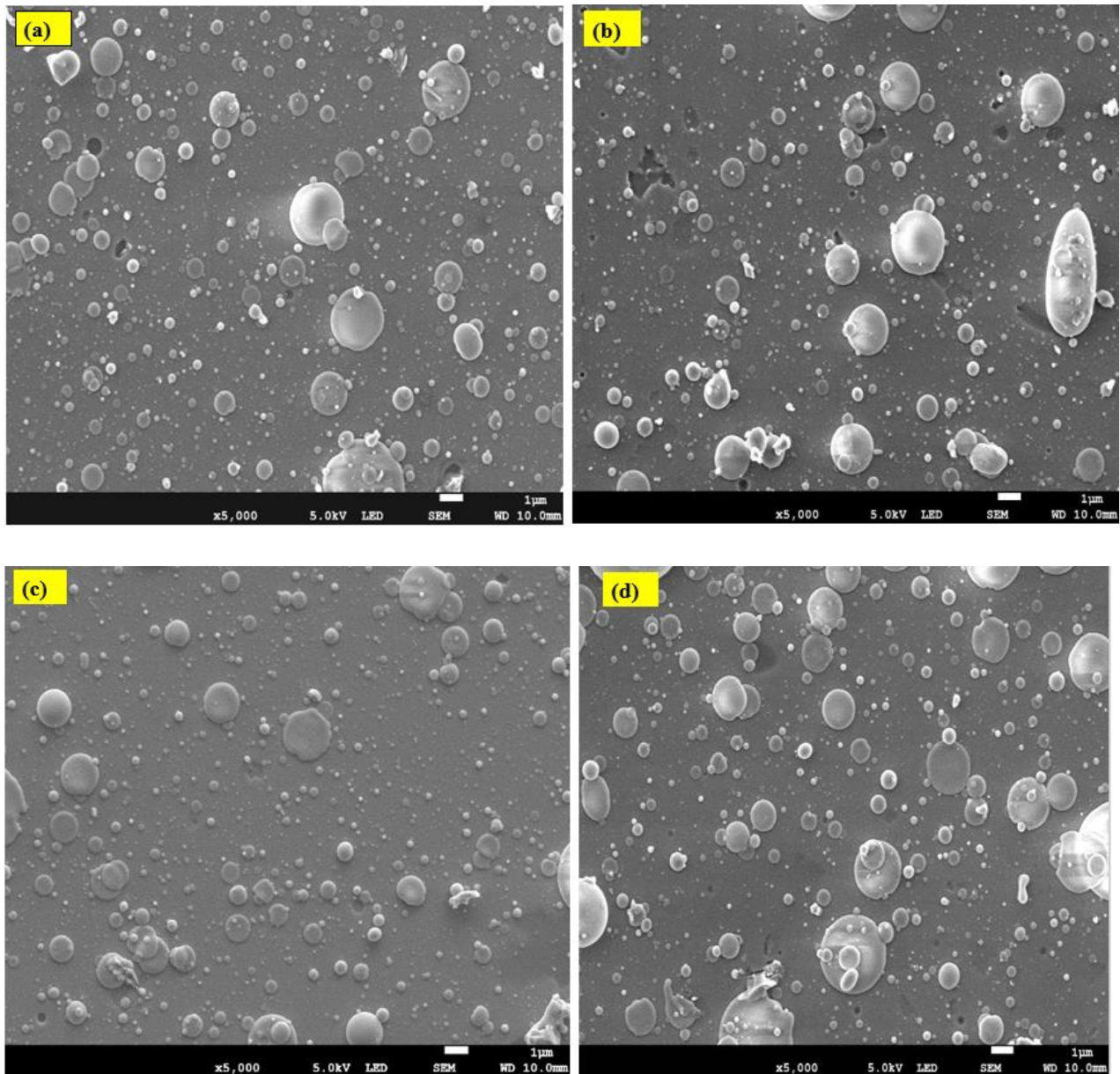


Fig. 7.4: SEM graphs of  $\text{Y}_2\text{SiO}_5:\text{Ce}^{3+}$  thin films for different oxygen deposition pressure: (a) 1.5mT, (b) 20 mT (c) 60 mT and (d)100 mT

EDS measurement has been taken to confirm the quantitative formation of the elements in the thin films as shown in fig. 7.7, all elements were detected with their respective weight percentage. The weight percentage of the cerium atom increases progressively with increasing deposition pressure

up to 20 mTorr and begins to decrease as the deposition pressure further increases. Depending on the incident energy of the electron beam, emission lines are generated from each element. The incident electron removes an electron from the K-layer of the atom then there is a cascade of electrons from the outer shells of the atom to fill this vacancy. The transition from one energetic state to another will emit a characteristic X-ray with a proportional energy and the detector will measure this energy. The composition and structure of the thin film materials can vary depending on the magnitude of the deposition pressure of oxygen, the substrate type and the thickness of the film. The O, Si are K-series elements while Y, Ce are L-line elements. As observed in fig. 7.7, the presence of dominant Si spectrum is because of the silicon substrate (wafer) used to deposit the films.

The percentage weight is given in the micrographs and the corresponding atomic percent of the elements are given in table 7.1. Max atomic percentage of Y and Ce have observed at a deposition pressure of 20mT.

Table 7.1: EDS weight and atomic percentage of the elements of the compound material ( $Y_2SiO_5:Ce^{3+}$ )

Deposition pressure (mTorr)	Yttrium	Silicon	Oxygen	Cerium
<b>1.5</b>	<b>At. %</b>	<b>At. %</b>	<b>At. %</b>	<b>At. %</b>
	11.32	58.81	29.67	0.20
<b>20</b>	12.39	58.37	28.96	0.28
<b>60</b>	8.72	64.49	26.59	0.20
<b>100</b>	7.54	68.56	23.77	0.13



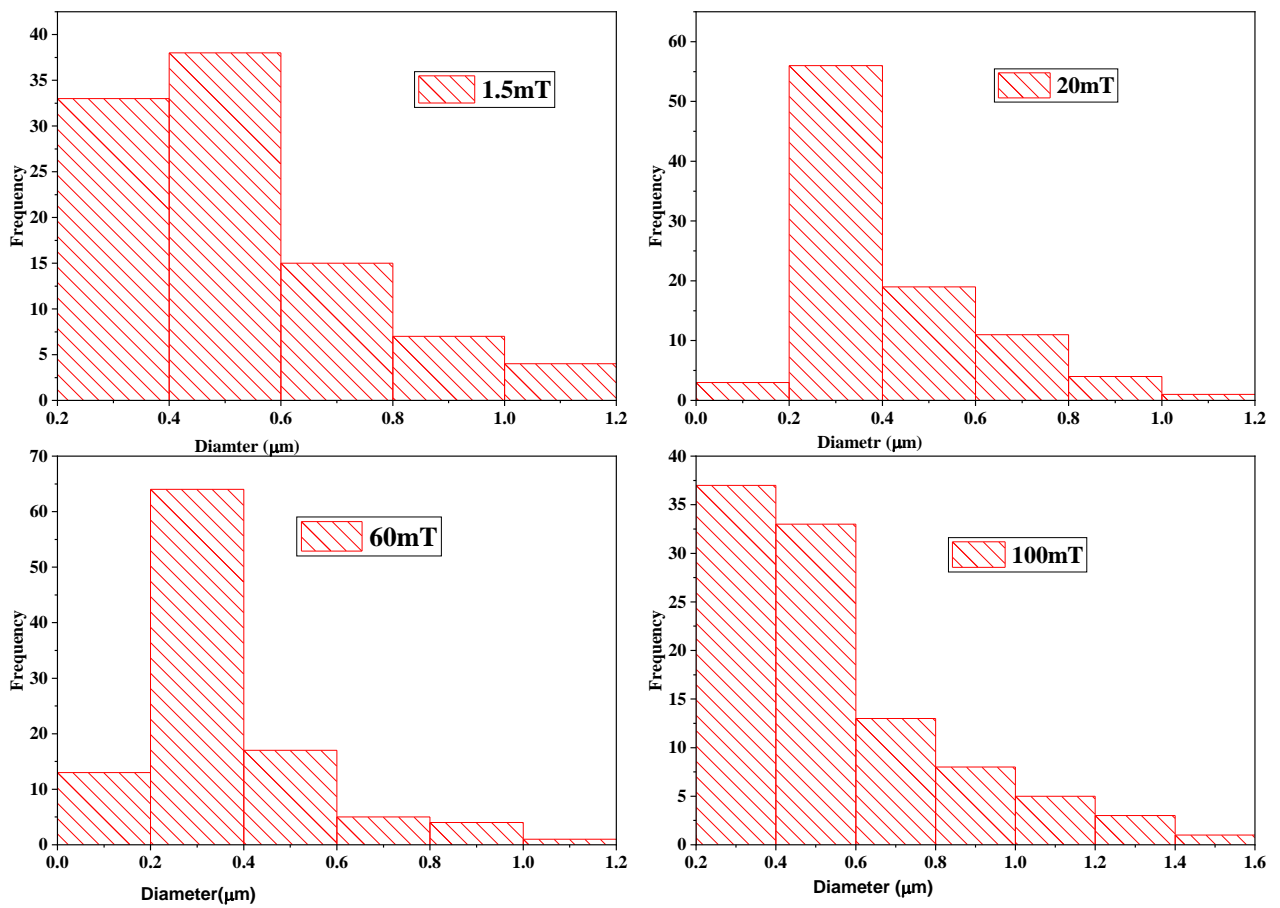


Fig. 7.5: Distribution of nanoparticles (NPs) in diameter (nm)

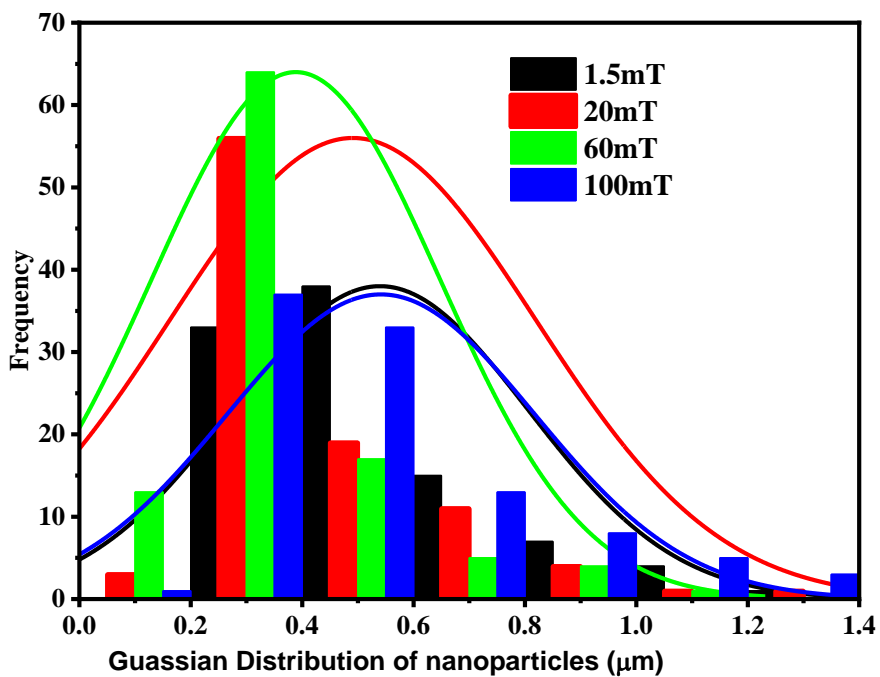


Fig. 7.6: Gaussian distribution of nanoparticles on the substrate

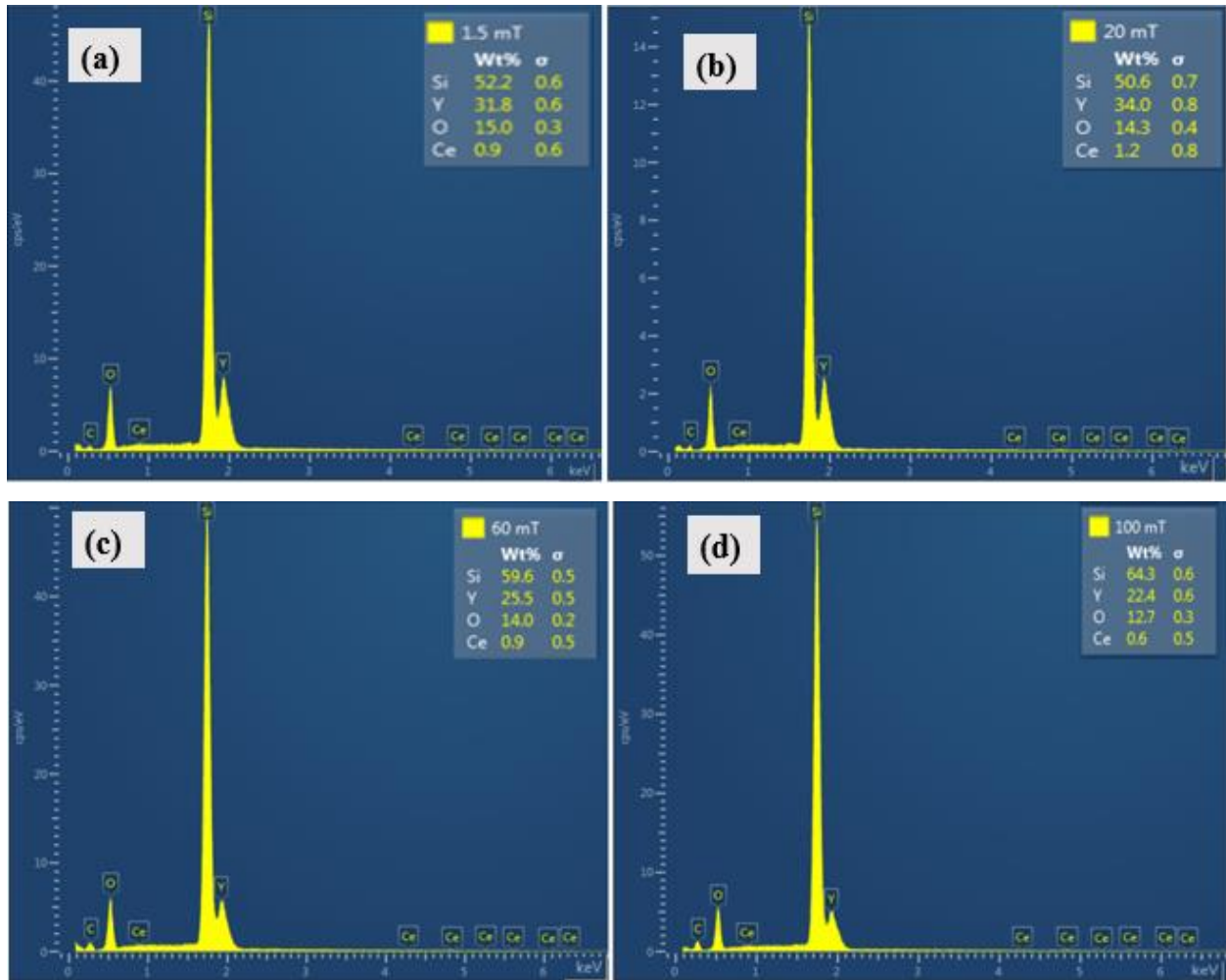
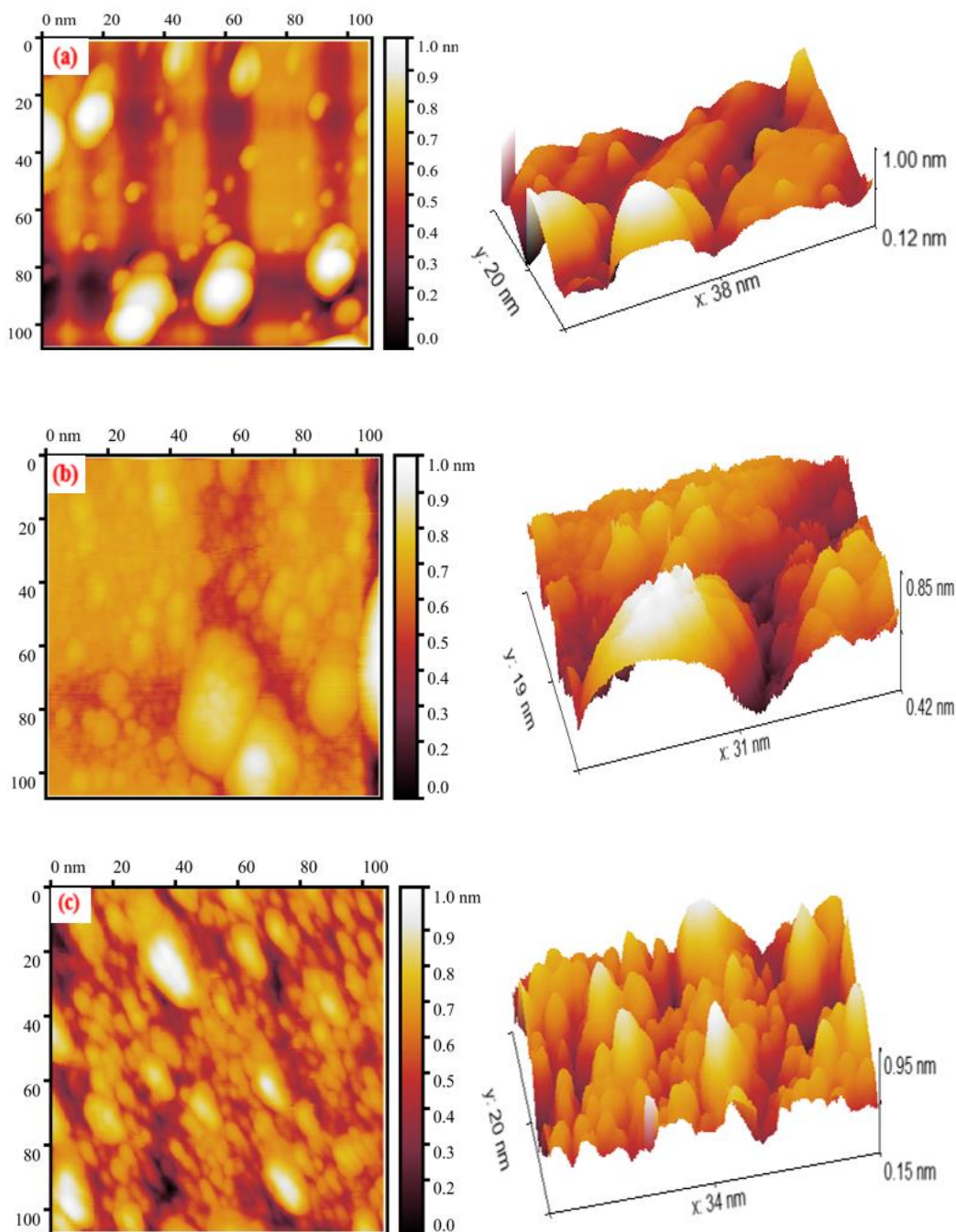


Fig. 7.7: EDS spectrum of  $Y_2SiO_5:Ce^{3+}$  thin films for different oxygen deposition pressure: (a) 1.5mT, (b) 20mT (c) 60mT and (d) 100mT

### 7.2.4 AFM Analysis

Fig. 7.8(a-d) shows the 2D and 3D-AFM images of  $Y_2SiO_5:Ce^{3+}$  thin films deposited at different oxygen pressure gas (1.5, 20, 60 and 100 mTorr respectively). The average roughness and root mean square roughness of the thin films are presented in table 7.2. The thin films deposited at a deposition pressure of 60 mTorr has higher RMS values of 31.12 nm. The RMS value increases with increasing deposition pressure from 13.08 to 31.12 nm and starts decreasing when the deposition pressure increases further to 100 mTorr. As observed in table 7.2, the maximum surface average roughness (Ra) and the root mean square roughness (Rq) is observed at 60 mTorr and starts decreasing when the deposition pressure is increased to 100mTorr. At a higher deposition pressure of 100 mTorr, the collision between the deposition gas and the plume is weak due to the scattering away of the plume particles by the oxygen molecules, this affects the arrival rate of the ablated species on the substrate[215]. As a result, the ad-atoms which are previously deposited have high kinetic energy, which leads to a re-evaporation from their lattice position and the surface reduces its roughness. At

lower deposition pressure (1.5 mTorr) the ad-atoms diffuse with lower kinetic energy on the surface of the substrate. As a result, the ad-atoms would have enough time to reside and nucleate on the surface of the substrate which leads to indistinct boundaries and coarse surface [216, 217]. At a lower deposition pressure (1.5 and 20 mTorr), the distribution of the nanoparticles is not uniform, particularly at a deposition pressure of 1.5 mTorr. The surface of 3D micrographs displays porous regions attributed to the dislocation of nanoparticles or defects. More over the reason for the agglomeration of the nanoparticles on the surface of the silicon substrate is due the adhesion of the agglomerated particles with a weak force producing micron sized entities. When deposition pressure is increased to higher values (60 and 100 mTorr), compacted and aggregated surface has been observed.



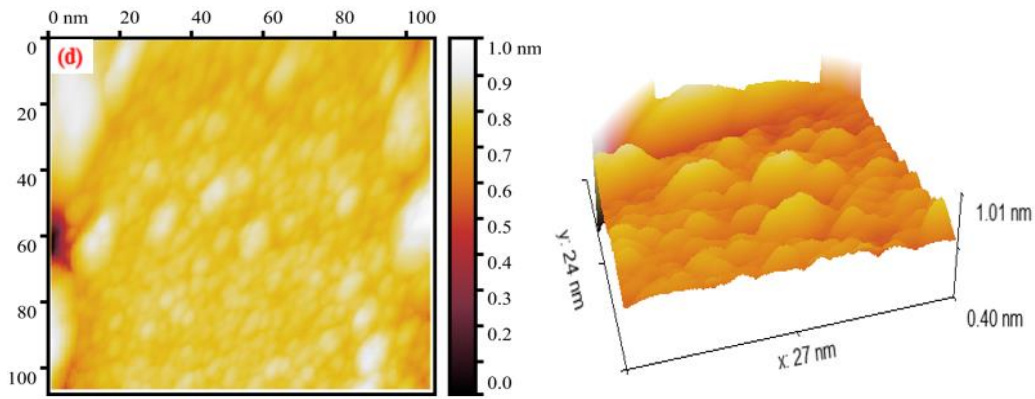


Fig. 7.8: 2D and 3D AFM images of  $Y_2SiO_5:Ce^{3+}$  thin films for different oxygen deposition pressures (a)1.5mT, (b) 20mT (c) 60mT and (d) 100mT

Table 7.2: roughness average (Ra) and mean square roughness (Rq) for different deposition pressures

Deposition pressure in mTorr	Roughness average (Ra) in nm	Root mean square roughness (Rq) in nm
1.5	13.08	21.18
20	25.98	44.66
60	31.12	47.33
100	10.75	17.35

### 7.2.5 UV-VIS analysis

Studying the optical properties of the deposited thin film is important as far as optoelectronic device application is concerned. Fig. 7.9 shows the UV-VIS absorption graph with strong absorption peak, which varies with the cerium (Ce) to yttrium (Y) ratios in the complex matrix. The absorption band edges at wavelength of around 260 nm were observed for thin films deposited at 1.5, 20, 40, 60 and 100 mTorr. The absorption value is similar to the excitation wavelength used to excite the samples in the PL measurement. Optical absorption gives information about the band to band electron transition and the band structure of the material [218]. When the incoming photon is absorbed an electron from the lower energy level is excited to higher energy state with discrete energy, possible electronic transition could be observed as a result of change in the transmitted radiation [219]. The absorption band peaked around 260 nm is in the ultraviolet region. This absorption band is from the  $Ce^{3+}$  in the  $Y_2SiO_5$  host material from the 4f to 5d transitions [220]. The ground state energy of 4f

splits in to  $^2F_{5/2}$  and  $^2F_{7/2}$  where the 5d states splits in to five sub energy levels. The deposited film has the highest absorption peak and absorbance value around 0.4 when deposited at 60 mT that can be ascribed to the film thickness and reduced absorption peak was observed at 100 mT which might be due to the scattering of the interacting light with the sample because of particulates and also occurrence of surface cracks.

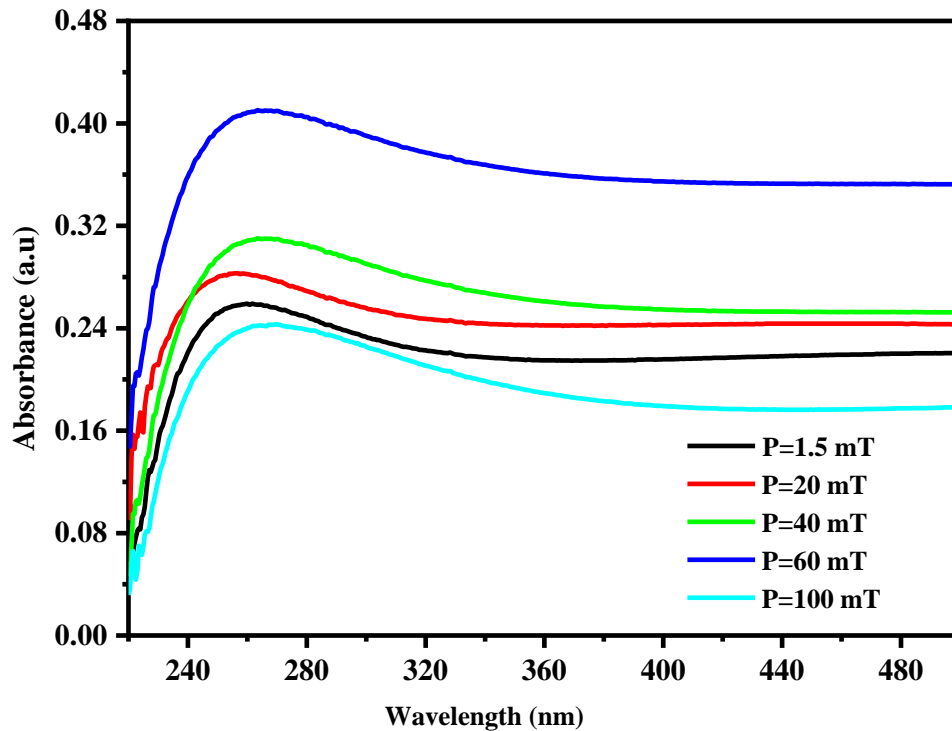


Fig. 7.9: UV-VIS for  $Y_2SiO_5:Ce^{3+}$  thin films deposited at different oxygen pressure

### 7.2.6 Photoluminescence analysis

Fig. 7.10 and Fig. 7.11 shows the excitation and emission spectrum of the thin films deposited at different oxygen deposition pressures. It shows enhancement in both the excitation and emission intensities as a function of increasing in deposition pressures. The improvements in intensity are due to the surface roughness and increase in recombination probabilities of the electron and hole recombination. When the surface is rough, the internal reflections are reduced, which could be the main reason for the intensity to increases [221]. However, when the deposition pressure is increased further to a deposition pressure of 100 mTorr, the excitation and emission spectrum show weak intensity, which implies that there is dominance of the non-radiative transition over the radiative one. The collision of the atoms with the plasma column will definitely decrease the atomic kinetic energy, which may reduce the prospect of the ad-atoms obtaining the lowest energy site to form a low energy structure. On the other hand, the collision between the ambient gas and the atoms forms the thinnest films, as a result, the quality of the films decreases in terms of thickness. Therefore, the optimal oxygen pressure selected for the experiment plays an important role in the crystalline quality

of thin films. The emission peak observed in Fig. 7.11 could be attributed to the electronic transition of  $Ce^{3+}$  ion from 5d to 4f energy state [222]. The 4f electron of  $Ce^{3+}$  has two states of energy in the ground level in which the orbital moment and rotation are parallel and antiparallel to  $^2F_{7/2}$  and  $^2F_{5/2}$  respectively. The division of the energy level of the ground state leads to a doublet character.

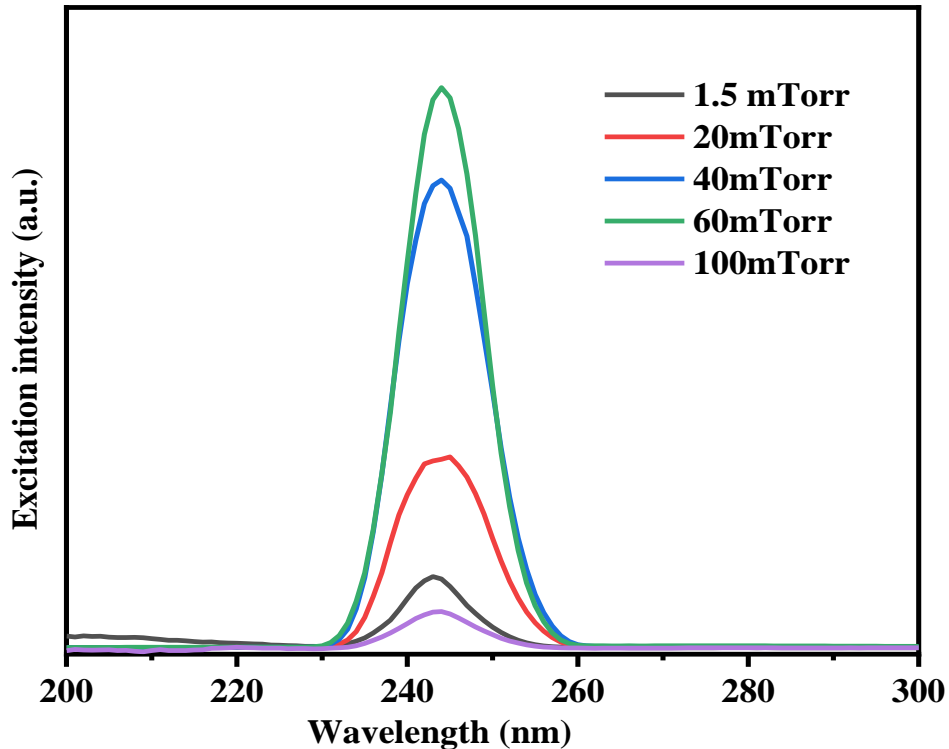


Fig. 7.10: Excitation spectrum of  $Y_2SiO_5:Ce^{3+}$  thin films for different Oxygen deposition pressures

The transition of electron from 5d to 4f levels is allowed by an electric dipole. As a result, the emission level has a short lifespan. The emission of  $ce^{3+}$  is generally observed in the UV or blue spectral region [223]. As a result of explorations for a fast-emitting phosphor in a green and red band, the  $Ce^{3+}$  ion was found to emit longer wavelengths. At low energy level or strong nephelauxetic effect and high crystal field, the 5d energy centre is responsible for the emission to happen in this region of emission. Where the nephelauxetic effect stands for a decrease in the Racah (electrostatic interaction of the electrons) interelectronic repulsion parameter, which occurs when the free transition ion forms complex with the ligands. The excitation and emission wavelengths were observed at 244 and 470 nm respectively. Similar excitation and emission wavelengths has reported in [224] which lies in the UV and blue spectral region of the electromagnetic spectrum respectively. In a cerium doped phosphor material, since the electron in the outer layer is screening the electron in 4f, the level of the excited energy (5d) depends on the host material. Subsequently, the 4f electron is hardly affected by the crystalline lattice of the host material. The energy levels of the electron in the outer shell in the 5d state is also affected by the crystalline lattice field.



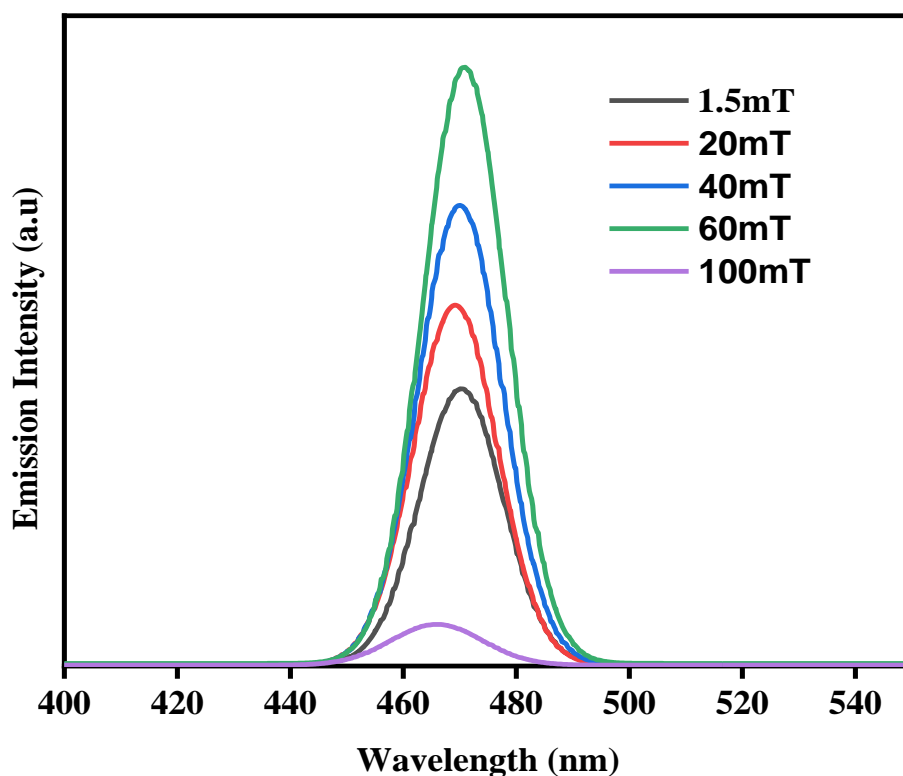


Fig. 7.11: Emission spectrum of  $Y_2SiO_5:Ce^{3+}$  thin films grown at different Oxygen deposition pressures.

### 7.2.7 Thermoluminescence Analysis

Thermoluminescence (TL) is the release of light in the crystalline material as a result of heating at a constant rate. The light is proportional to the dose of nuclear radiation that the material has received. Once the light is produced, the previous radiation history of the material is erased as the thermal cycle performs a destructive reading of the sample history. When the irradiation energy increases, the internal energy of the electrons breaks and makes an electron cloud where some of them are trapped by the crystal imperfection of the material. Upon heating the crystal, the excess kinetic energy stored in the electrons, which were trapped in the crystal traps starts liberating in the form of light by producing thermoluminescence. The TL intensity is corresponding to the concentration of the luminescence centres in the solid material. In addition, the TL emission gives us information on the nature of the defect centres and its energy level [195]. The TL graph (glow curve) of the samples deposited at a deposition pressure of 1.5, 40, 60 and 100 mT are shown in Fig. 7.12. The plot shows that the samples deposited at higher deposition pressure (60 and 100 mT) have high TL intensities, which can be ascribed to the existence of high defect levels. Comparatively the samples deposited at low deposition pressures (1.5 and 40mT) show low TL intensities which suggests the existence of less defect levels compared to the samples deposited at high deposition pressures. The shifts of the peaks to the higher temperature significantly suggests that there is a

change in activation energy [225]. The maximum intensity of thermoluminescence emission observed at a deposition pressure of 60 mT can be ascribed to the de-trapping of the maximum charge carriers.

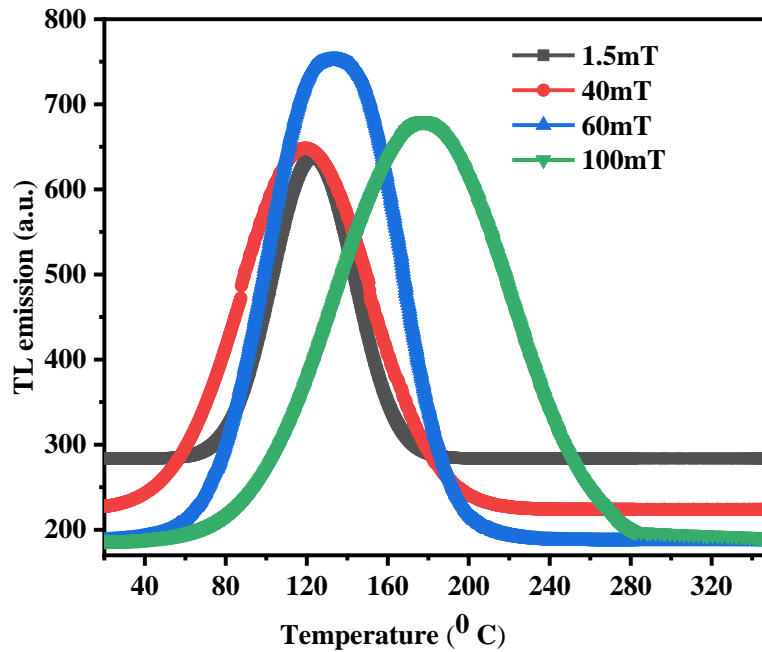


Fig. 7.12: UV-irradiated TL glow curve of  $Y_2SiO_5:Ce^{3+}$  thin films deposited at different oxygen pressures.

The estimated kinetic and trapping parameters calculated from the glow peak shape (Fig. 7.12) are given in table 7.3 and 7.4. The Chene's peak shape equation [226] was employed to calculate the activation energy from the kinetic parameters ( $\tau$ ,  $\delta$  and  $\omega$ ). Where the parameters are defined in equation (6.4). The activation energy can be calculated using equation (6.5).

The theoretical value of  $\mu_g$  is between 0.42 and 0.52. The system is first or second order if the value of the system factor is around 0.42 and 0.52, respectively.

The geometrical factor ( $\mu_g$ ) is independent of the activation energy (E) but it depends on the order of the kinetics (b) [196]. When E and b are known, S can be evaluated by Chen and Kirsh relation [197] given in equation (6.6).



Table 7.3: kinetic and trapping parameters of the UV- irradiated  $Y_2SiO_5:Ce^{3+}$  nano crystalline thin films

Deposition pressure(mT)	$T_1$ (k)	$T_m$ (k)	$T_2$ (k)	$\omega$	$\tau$	$\delta$
1.5	353	439	397	86	44	42
40	339	446	392	107	53	54
60	375	476	428	101	53	48
100	391	508	451	117	60	57

Table 7.4: Trap parameters and order of kinetics for UV-irradiated  $Y_2SiO_5:Ce^{3+}$  thin film phosphors.

Deposition pressure (mT)	$T_m(K)$	Order of kinetics $\mu_g(b)$	Activation energy (eV)				Frequency factor ( $S^{-1}$ )
			$E_\tau$	$E_\delta$	$E_\omega$	$E_{av}$	
1.5	439	0.48837	0.401	0.476	0.437	0.438	$3.3 \times 10^6$
40	446	0.50467	0.309	0.390	0.348	0.349	$2.3 \times 10^5$
60	476	0.47525	0.365	0.453	0.406	0.408	$4.5 \times 10^5$
100	508	0.48718	0.355	0.450	0.400	0.401	$2.0 \times 10^5$

Maximum activation energy has been calculated at the minimum deposition pressure (1.5 mT) which can be related to the trap depth existed at this deposition pressure.

## Conclusion

$Y_2SiO_5:Ce^{3+}$  thin films have been grown by PLD at different oxygen deposition pressures. The material deposited on the substrate is structurally monoclinic with a prominent diffraction peak at  $28.9^\circ$ . The crystallinity of the thin films was characterized by the Raman spectroscopy measurements. Morphological and structural variations of the thin films were observed both in the SEM, and AFM measurements. The grains are spherical in shape and some agglomerated areas has been observed in all deposition conditions which could be ascribed to the decrease in arrival speed of nanoparticles into the deposition areas. The deposition pressure can maintain the crystalline quality of thin films by controlling the kinetic energy in the plume during collision with oxygen

particles. The average diameter of the nanoparticles was 0.54, 0.49, 0.39, 0.55  $\mu\text{m}$  at a deposition pressure of 1.5, 20, 60 and 100 mTorr, respectively. From the quantitative measurement, all the constituent elements have been observed with varying atomic percentages. Higher average surface roughness and root mean square roughness was observed at a deposition pressure of 60 mTorr. UV-VIS absorption band was observed at 260 nm with a maximum absorbance value of 0.4. Maximum and minimum absorption value was measured at a deposition pressure of 60 and 100 mTorr, respectively which can be ascribed to the surface thickness of the film. Photoluminescence emission has been observed at 470 nm, which could be ascribed to the electronic transition of  $\text{Ce}^{3+}$  ion from the 5d to 4f energy states. Maximum and minimum emission intensity has been observed at 60 and 100 mTorr respectively. Enhancement both in excitation and emission intensities were observed from low to high deposition pressure, which could be attributed to the surface roughness and increase in recombination probabilities of the electron and hole. Maximum TL intensity was observed at 60 and 100 mTorr, which could be ascribed to high defect levels. Emission shifts was shown between the lower and higher depositions due to change in activation energy. The average activation energy varies between 0.349 and 0.438 eV. Maximum and minimum activation energy was obtained at a deposition pressure of 1.5 and 40 mTorr, respectively. The observance of higher activation could be due to the maximum trap depth.

## Chapter 8: The influence of deposition time on the structural, photoluminescence, morphological and optical properties of $\text{Y}_2\text{SiO}_5:\text{Ce}^{3+}$ thin films deposited by Pulsed Laser

### 8.1 Introduction

The material we have characterized ( $\text{Y}_2\text{SiO}_5:\text{Ce}^{3+}$ ) is a blue emitting phosphor which has been studied by many researchers to characterize the luminescence properties in the field of optoelectrical applications [52, 58]. The effective luminescence of cerium-doped yttrium silicate phosphor which excites at UV (~ 350 nm) excitation due to the electron transition of  $\text{Ce}^{3+}$  ions between 5d and 4f energy levels. Phosphor materials are materials that can emit radiation when it is exposed to UV, electron bombardment, X-rays, or some other form of excitation, this form of emission is known as luminescence [222]. This compound has two distinct monoclinic structures that varies based on their synthesis temperatures. The two phases are categorized as low temperature phase ( $\text{X}_1\text{-Y}_2\text{SiO}_5$ ) and high temperature phase ( $\text{X}_2\text{-Y}_2\text{SiO}_5$ ), the turning point of the synthesis temperature for the two phases is around 1200 °C [205]. According to literatures, the  $\text{X}_2\text{-Y}_2\text{SiO}_5$  phase is more suitable to produce than the  $\text{X}_1\text{-Y}_2\text{SiO}_5$  phase for optoelectrical applications because of the challenge of finding a single pure phase of  $\text{X}_1\text{-Y}_2\text{SiO}_5$  for the possibility appearing various coordination of yttrium atoms which is supposed to be substituted by the RE element (Ce) [227]. Different deposition routes has been used to develop the phosphor thin film by: combustion [228], hydrothermal processes [229], sol-gel techniques [230], pyrolysis [231], solid-state reaction [232] and PLD [175, 233] where each deposition technique has its own advantages and disadvantages. Nowadays, the rare-earth doped nanostructure compounds are a major source of concern for phosphor production. These materials have many applications in optoelectronic devices when the RE ion is doped into the single crystal or the ceramic of the host material. In addition, these compounds doped with RE ions are the most promising materials in the field of optoelectronics [6, 7]. These have generated interest in the development of rare-earth-doped phosphor materials with good chemical stability, luminosity and industrial process characteristics for potential panel and field emission applications with enhanced efficiencies [202]. Yttrium silicate is well known for hosting rare-earth ions because of its wide band gap (7.4 eV) which can simply accommodate the doped ions. This material has been used as host lattice for RE ions due to the chemical and thermal stabilities in the development of luminous phosphors. The visible light emitters are served as sensitizers for the transitional metal ions and luminous RE ions.  $\text{Ce}^{3+}$  ion is 4f→5d spin allowed transitions which emits broad band luminescence. Furthermore, the emission and excitation position of the luminescent centre of  $\text{Ce}^{3+}$  is very sensitive to the crystallographic site of the host material. The blue emitting  $\text{Y}_2\text{SiO}_5:\text{Ce}^{3+}$

phosphor material is crucial in optoelectrical applications and it can be also used in solid state lightings and solid-state lasers [52, 234]. So, this material demands more investigation and characterizations with various characterization and deposition methods. As far as our knowledge, this research paper has not reported or considered for publication with the conditions we have used to investigate its properties for possible applications.

## 8.2 Result and discussion

### 8.2.1 Xrd analysis

Fig. 8.1, Shows the GIXRD graph for the thin films deposited at different deposition time of 30, 60, 90, 120 and 150 minutes for a  $2\theta$  scans starting from  $10^\circ$  to  $65^\circ$ . The GIXRD patterns seems amorphous from glances view but the diffraction patterns observed at a diffraction angle of  $15.01^\circ$ ,  $24.16^\circ$ ,  $30.6^\circ$ ,  $42.27^\circ$ ,  $50.96^\circ$  and  $54.78^\circ$ , are similar with the reference which is structurally end centered monoclinic structure of  $Y_2SiO_5$  PDF#361476. The diffraction peak observed at diffraction angle of  $30.6^\circ$  is very wide in width which shows that there is less crystallinity of particles at that plane. But sharp diffraction pattern has been observed at  $52^\circ$  especially at the thin films deposited at a deposition time of 120 and 60 minute respectively. This could be ascribed to the existence of crystallized surfaces at this plane. It is known that the crystallinity of the deposited film will be affected by the substrate temperature [235]. However, since the substrate temperature and other parameters were fixed, the only Significant parameter that could induce change in the crystallinity of the deposited material is the deposition time. The effect of deposition time can be clearly seen on the width and position of the diffraction peaks. The variation in width of the diffraction patterns is ascribed to the crystallinity of the thin films. The dominant diffraction peak of the thin films in all deposition time in comparing to the standard was observed at  $30.6^\circ$  which corresponds to the miller index of  $(\bar{4}02)$  which is also associated with lower intensity and high broadening which can be ascribed to the poor crystallinity of the film. Better crystallized film with a sharp diffraction peak has been observed at diffraction pattern of  $52^\circ$  with a miller index of  $(233)$  which dominantly observed at a deposition time of 60 and 120 minutes respectively.

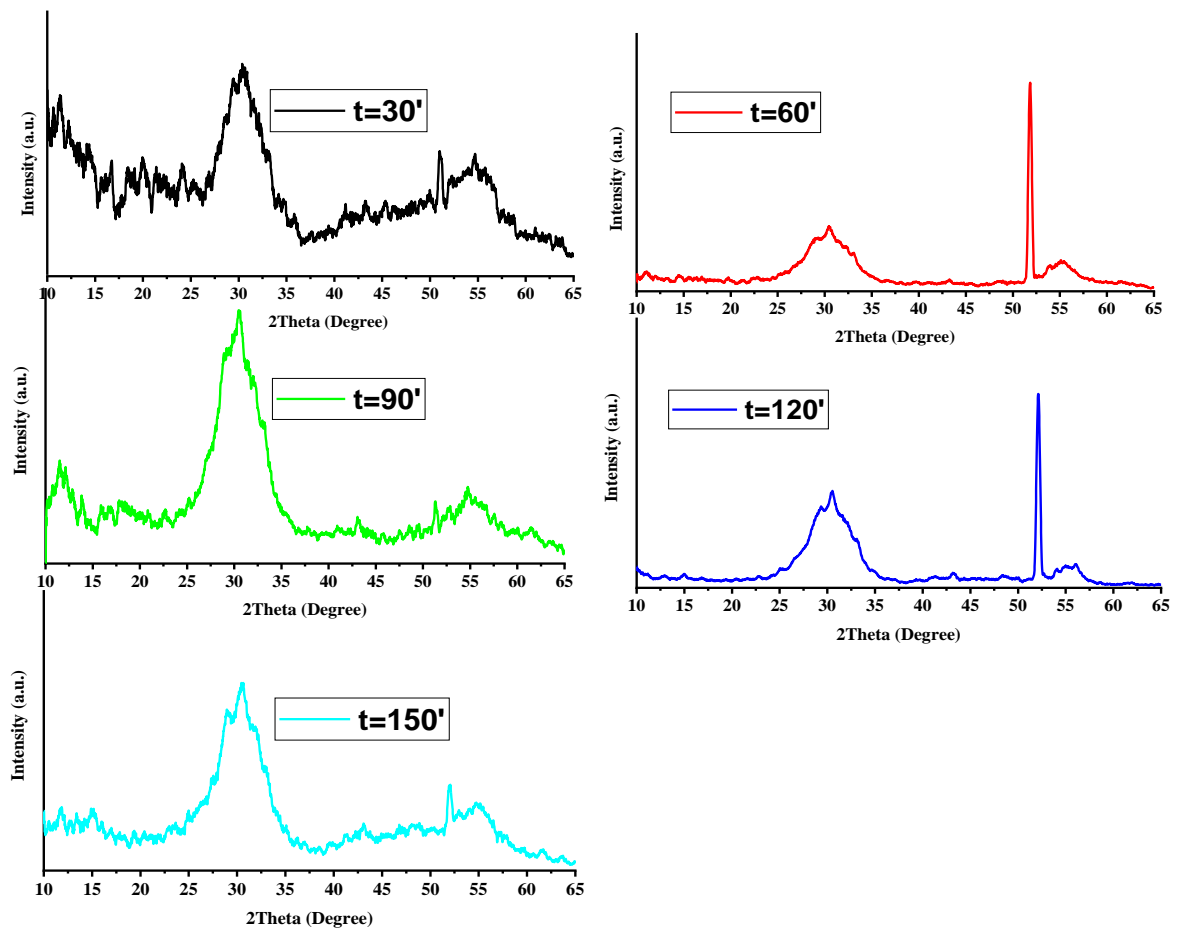


Fig. 8.1: GIXRD diffraction pattern of  $Y_2SiO_5:Ce^{3+}$  thin films at different deposition time

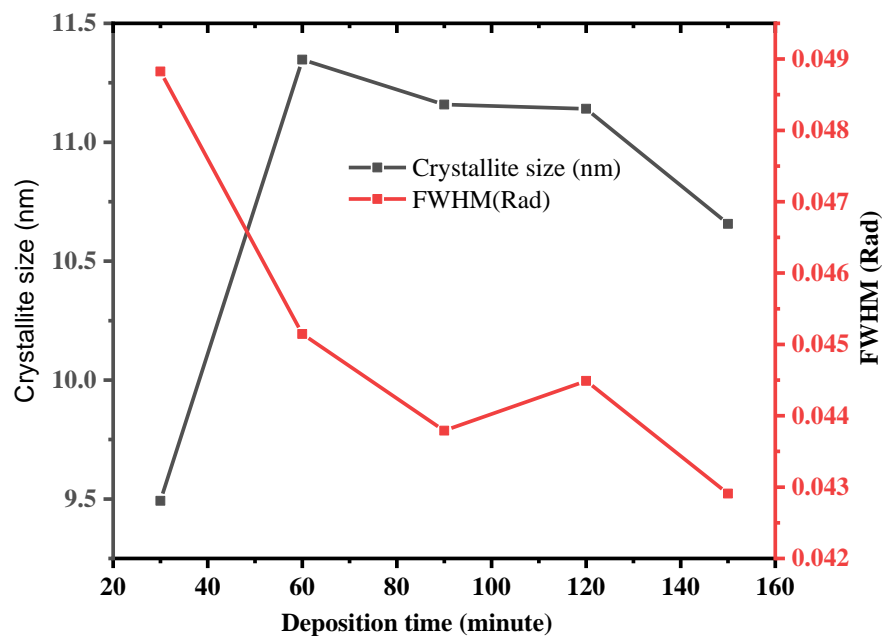


Fig. 8.2: effect of deposition time on FWHM and crystallinity size

The crystallite size of the thin film phosphor  $Y_2SiO_5:Ce^{3+}$  has been calculated from the full width at half maximum of different peaks using the Scherrer equation[236] given in equation (3.4)

A maximum crystallite size has been observed at a deposition time of 60 and 90 minutes, respectively. Where a small crystalline size has been observed at a deposition time of 30 and 150 minutes respectively.

### 8.2.2 Raman spectroscopy analysis

Fig. 8.3 shows the Raman spectroscopy spectrum for thin films deposited at different deposition times. Raman spectroscopy measurement has been used to analyse qualitative and quantitative samples from inorganic, organic and biological samples [237]. Raman studies are very important to identify information related to the composition, structure and stability of the coordinated compounds in the sample. In Raman measurement, three probable scenarios could be observed (Rayleigh scattering, stokes and anti-stokes). When the samples interact with the intense monochromatic radiation beam, the molecule excites and returns to the ground by emitting light in all directions, that is, Rayleigh scattering. The Scattered light should contain some lines that may be more frequent or less frequent than the incident lines. From Fig.8.3, the very intense peak lines observed at approximately  $536\text{ cm}^{-1}$  correspond to Rayleigh scattering and the observed peak line at approximately  $6.9$  and  $980\text{ cm}^{-1}$  respectively are stokes and anti- stokes scattering spectra. In the Rayleigh scattering both the incident and emitted energy are the same whereas the stokes scattering is a lower frequency emission and the anti-stokes scattering is a higher frequency emission. A highly intense peak line has been observed at the samples deposited at a deposition time of 120 minutes which could ascribe to the relative crystallinity of the film.

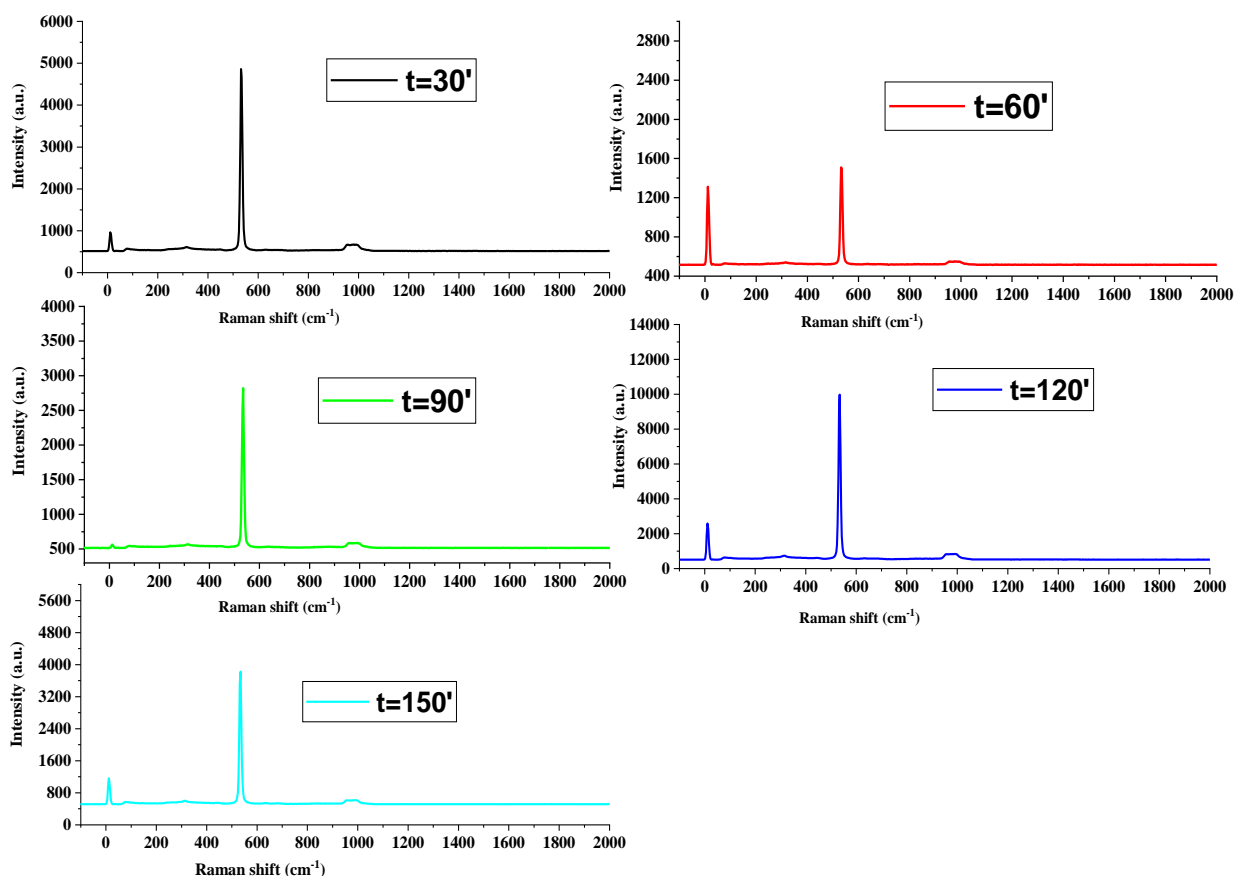


Fig. 8.3: Raman spectroscopy of  $\text{Y}_2\text{SiO}_5:\text{Ce}^{3+}$  thin films deposited at different time

### 8.2.3 SEM and EDS Analysis

The morphological images of the samples deposited at different deposition times of 30, 60, 90 and 150 minutes are shown in Fig. 8.4. It is shown that at all deposition times the nanoparticles are distributed uniformly with an almost circular shape. The density of the nanoparticles distributed in the deposition areas increases as the deposition time increases. A much denser area of nanoparticles has been observed in the longest deposition time. In a deposition time of 30 minutes, the nanoparticles are distributed less densely, which could be due to a shorter deposition time and the plume produced by the laser has a high probability of decreasing and stopping the speed of the ejected nanoparticles due to a collision or interaction. As a result, they have less arrival fate to reach the substrate, however, when the deposition time is further increased to 60 minutes, aggregation increases. In a deposition time of 150 minutes, highly dense and aggregated nanoparticles have been observed, which can be attributed to long-term deposition. When deposition time increases, ablated species have enough time to find a suitable and thermodynamically stable place to sit for a long time. We have considered approximately 200 nanoparticles (NP) from each micro image and the average distribution of the nanoparticles is shown in Fig. 9.4. As we can clearly see in Fig. 8.4,

particles with a size of 0.2 to 0.4  $\mu\text{m}$  with high frequency. The average nanoparticle size is 0.31, 0.32, 0.34 and 0.38  $\mu\text{m}$  for the deposition time of 30, 60, 90 and 150 minutes respectively.

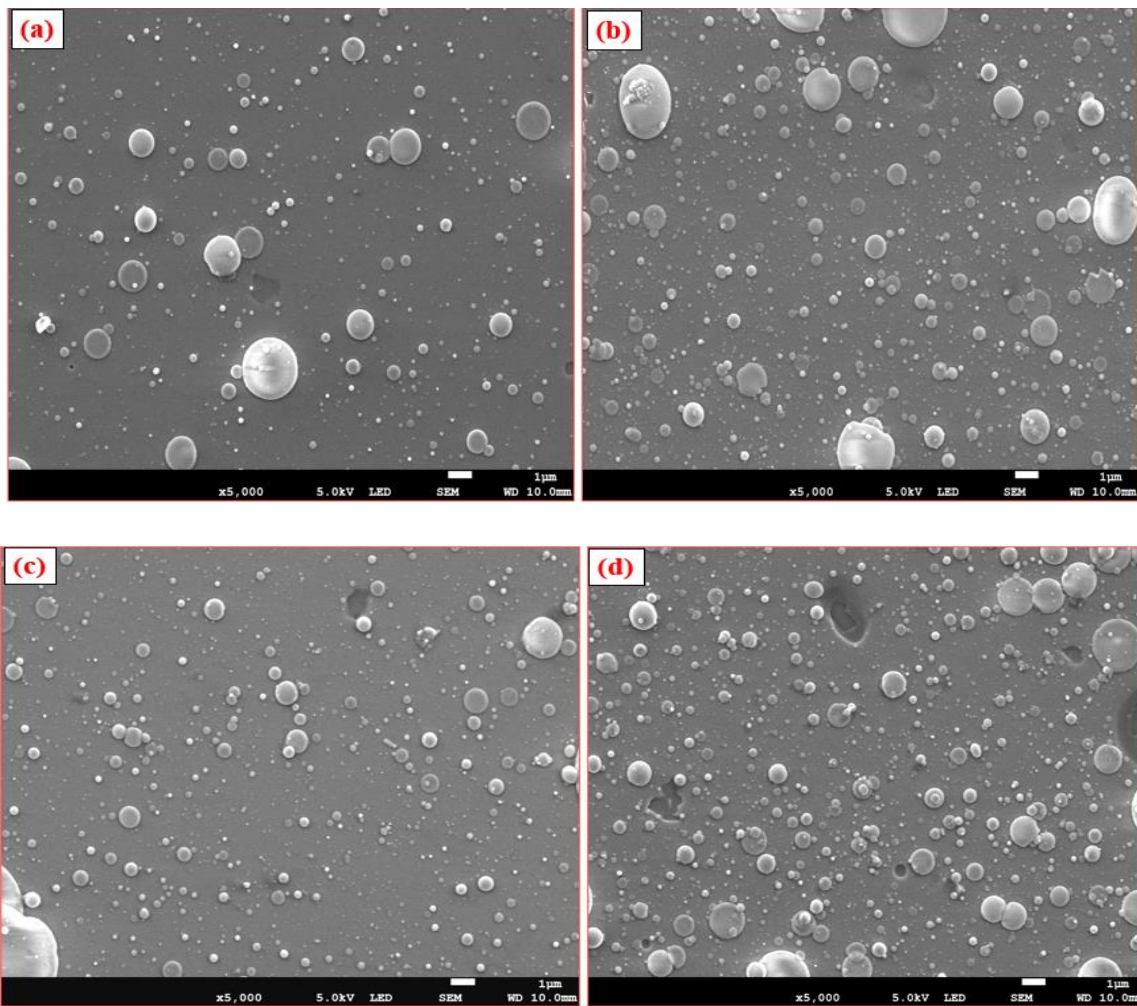


Fig. 8.4: SEM micro images for: (a) 30 minute (b) 60 minute (c) 90 minute and (d) 150 minutes

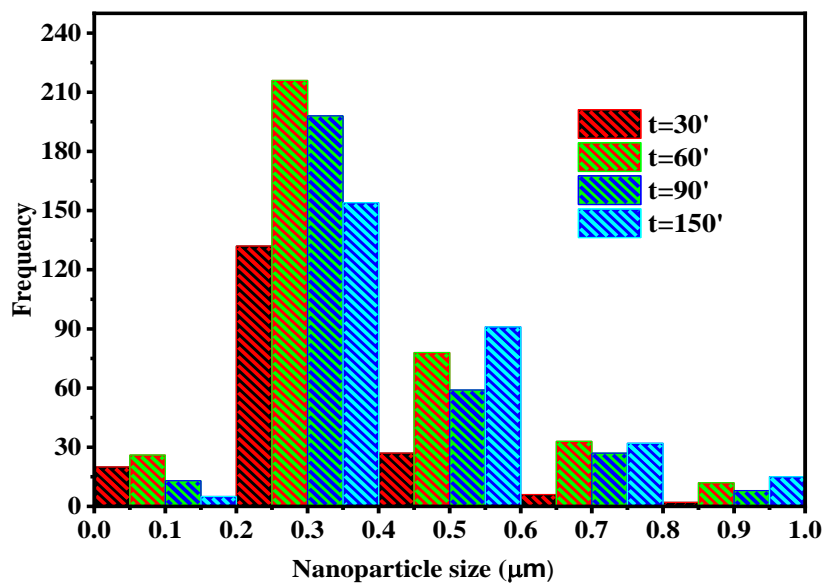


Fig. 8.5: Nano particles' distribution of  $\text{Y}_2\text{SiO}_5:\text{Ce}^{3+}$  thin films in the mentioned deposition



The EDS measurement has been used in conjunction with the SEM measurement and has been used to analyse the quantitative chemical composition of the compound formed in the substrate after taking the deposition. EDS measurements have been used to confirm the formation of YSO: Ce in the newly formed compound with respective percentage weights as shown in Fig. 8.6 (a) to (b). It also helps us to know if all the constituent chemical elements of the precursor compound have occurred in the new compound formed in the substrate. In addition to quantifying the amount of each element in the compound, homogeneity and elemental distribution can be determined in the composite structure of the thin films. From Fig. 8.6, we can see the progressive change in percentage weight of each element. The percentage weight of the dopant (Ce) shows an increase from Fig. 8.6 (b) to Fig. 8.6 (d). When the deposition time is increased, the doping element has a long time to migrate and sit in a suitable place replacing the Y position to form the compound phosphor material and gives emission as a result of change in energy level. where Ce is responsible for luminescence due to recombination of the electron from 5d to ground state (4f). The return of the electron from the excited state to the energy level of the ground results in emission.

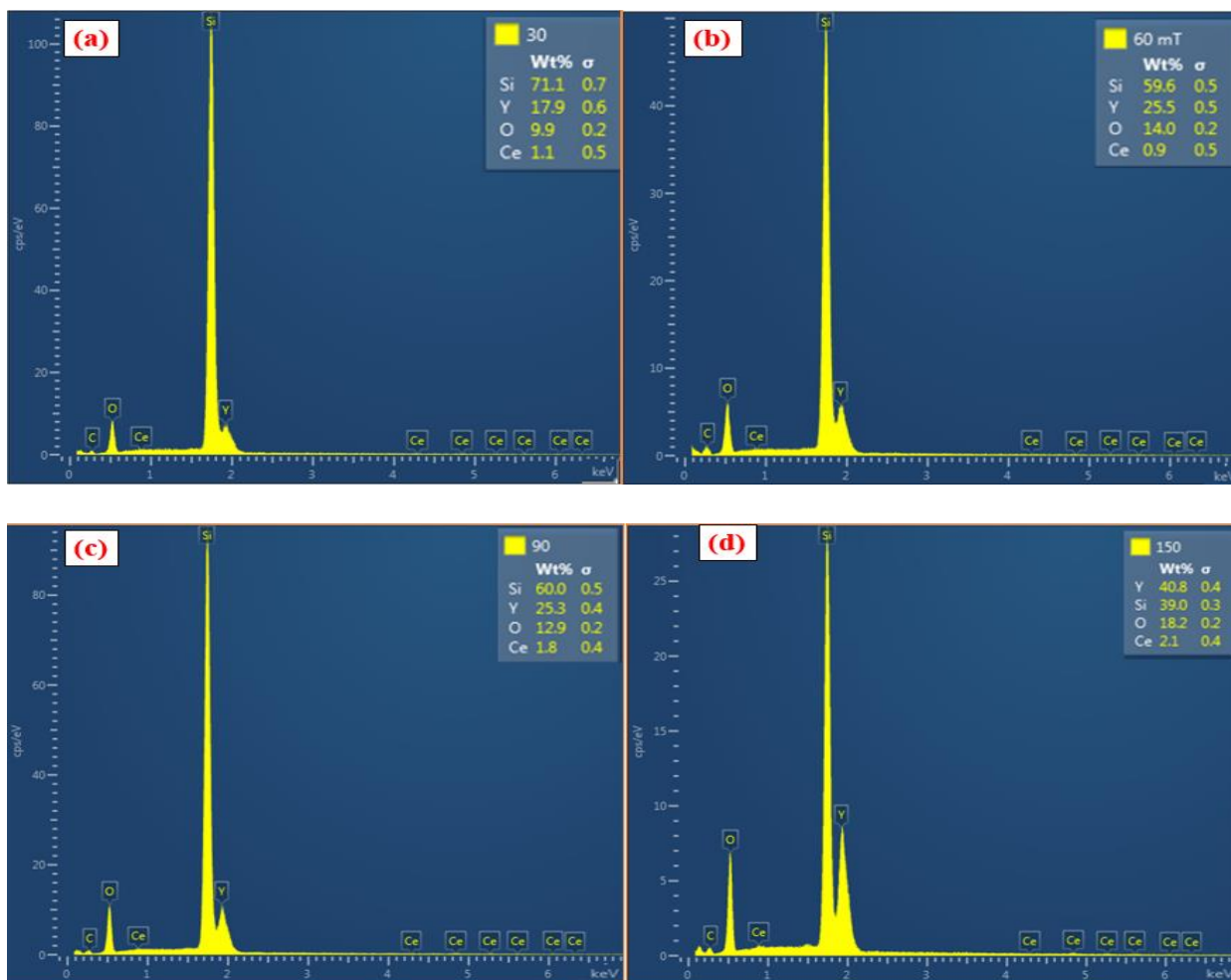


Fig. 8.6: EDS spectrum for: (a) 30 minute (b) 60 minute (c) 90 minute and (d) 150 minutes

Table 8.1 presents the atomic percentage of individual elements in the compound  $Y_2SiO_5: Ce^{3+}$ . The atomic percentage is the measure of the percentage of atomic presence of individual elements compared to the other elements that are present in the compound. As we can see from Table 8.1, silicon (Si) is the most dominant element in percentage in the compound. The reason is that, in addition to the presence of silicon in the compound phosphor, the substrate used to deposit the film has also contributed to the presence of a more percentage of silicon. Cerium ion is the main one responsible in changing the property of luminescence and structure of the material. Where Ce is supposed to replace the lattice position of Y and emit when Ce's outermost electron transitions from 4f to 5d energy levels as shown in Fig. 8.11. The two elements have a comparable ionic radius (Y = 0.93 and Ce = 1.01 Angstrom) where the large difference in ionic radius can induce the expansion or contraction of the lattice positions.

Table 8.1: atomic percentage of individual elements in the compound

Deposition time (minute)	Atomic percentage (%)			
	Y	Si	O	Ce
<b>30</b>	5.99	75.35	18.42	0.23
<b>60</b>	8.72	64.49	26.59	0.20
<b>90</b>	8.78	65.94	24.88	0.40
<b>150</b>	15.30	46.29	37.92	0.50

#### 8.2.4 UV-VIS analysis

Fig. 8.7 shows the UV/Vis spectrum of the  $Y_2SiO_5:Ce^{3+}$  thin films deposited at different time on a glass substrate. The spectroscopy shown is related to the attenuation of light after it interacts with the sample. The incoming radiation interacts with the compound formed in the glass substrate and excites the free electrons to a higher anti-bonding orbital. Maximum absorption has been absorbed at a deposition time of 120 minute. The absorption wavelength has been used to excite the samples for the PL excitation measurement. As we can see from Fig. 8.7, it has been observed maximum and minimum absorptions at a deposition time of 120 and 30 minutes respectively. The absorbance value ascribes to the thickness of the film. When the film is thick enough, the interacting radiation has high probability of attenuation.

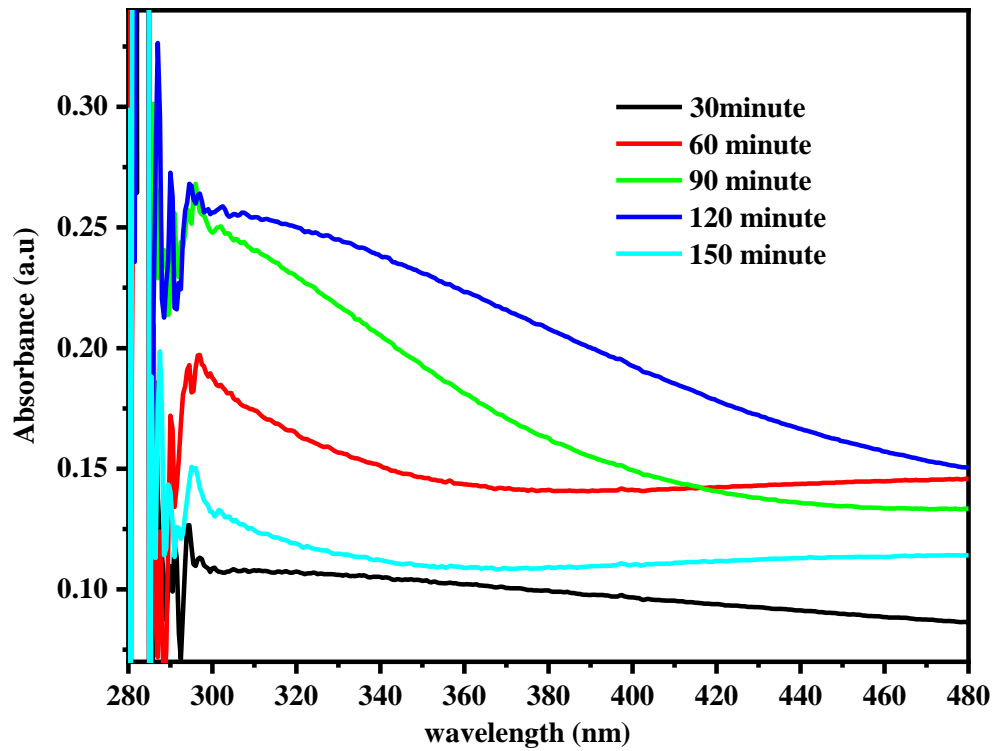


Fig. 8.7: UV-VIS absorption of thin films deposited at different time deposition

The bandgap of the thin films deposited at a deposition time of 90 and 120 minutes has been calculated using the Tauc relation given by equation (6.3). Where bandgap is the electronic separation between the valence and conduction bands, which is also the minimum energy required to excite electrons from the valence band to the conduction band. The optical bandgap of thin films has been obtained by extrapolating  $(\alpha h\nu)^2$  Vs  $h\nu$  graphs to the horizontal axis. The energy band interval of the thin films deposited at a deposition time of 90 and 120 minutes has been obtained 2.49 and 1.76 eV respectively. Bandgap determines the conductivity of materials; The increase in bandgap and the arrangement of the electronic levels in the material are attributed to the decrease in particle size and decrease in conductivity of the material. When a bandgap is larger, it requires more energy to excite electrons from the valence band to the conduction band where higher frequency, lower energy radiation would be absorbed.

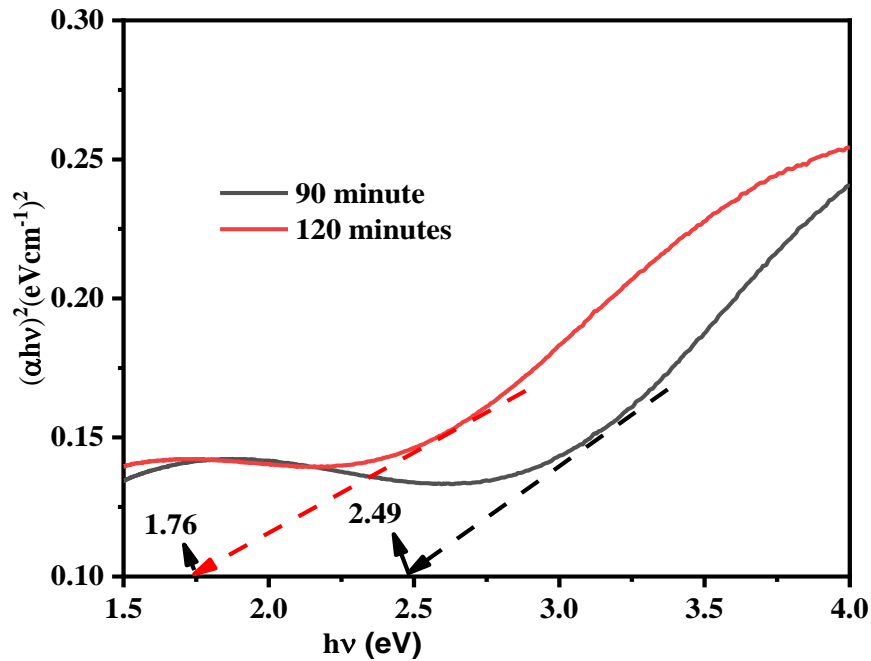


Fig. 8.8: Band gap of thin films deposited at a deposition time of 90 and 120 minutes

### 8.2.5 Photoluminescence analysis

Fig. 8.9 shows an absorption spectrum of all samples deposited at different deposition times. The maximum absorption of the  $4f \rightarrow 5d$  transition has been observed at around 282 and 269 nm respectively. Studies of Ce-doped orthosilicate materials showed that the two  $\text{Ce}^{3+}$  emission bands are related to the two  $\text{Ce}^{3+}$  crystallographic sites in the matrix [238]. Where the crystallographic site of  $\text{Ce}^{3+}$  has studied in detail in the EPR study of  $\text{Lu}_2\text{Si}_2\text{O}_7$  and  $\text{Lu}_2\text{SiO}_5$  [239] the two sites can be classified as Ce1 that has seven oxygen ligands and its probability of occurrence is 95% and Ce2 that could exist with six oxygen ligands and probability of occurrence of 5%. The excitation peak observed at 269 nm is due to host absorption, while the excitation peak observed at 282 nm is attributed to the  $4f \rightarrow 5d$  electronic transitions of  $\text{Ce}^{3+}$  ions. This transition is parity allowed, as a result it could give great oscillator force. Similar excitation wavelengths have been observed in [238, 239]. Furthermore, the emission spectra shown in Fig. 8.10 shows a maximum emission peak at 473 nm with a shoulder at 448 nm. This emission is attributed to the probability of recombination of the excited  $\text{Ce}^{3+}$  electron from 5d state to 4f ground state with a sub-energy level of  $4f_{7/2}$  and  $4f_{5/2}$ , respectively, as shown in Fig. 8.11. The broadband emission of  $\text{Y}_2\text{SiO}_5:\text{Ce}^{3+}$  is attributed to the electronic transition of  $\text{Ce}^{3+}$  ions that occupy the  $\text{Y}^{3+}$  crystallographic site in the host structure.

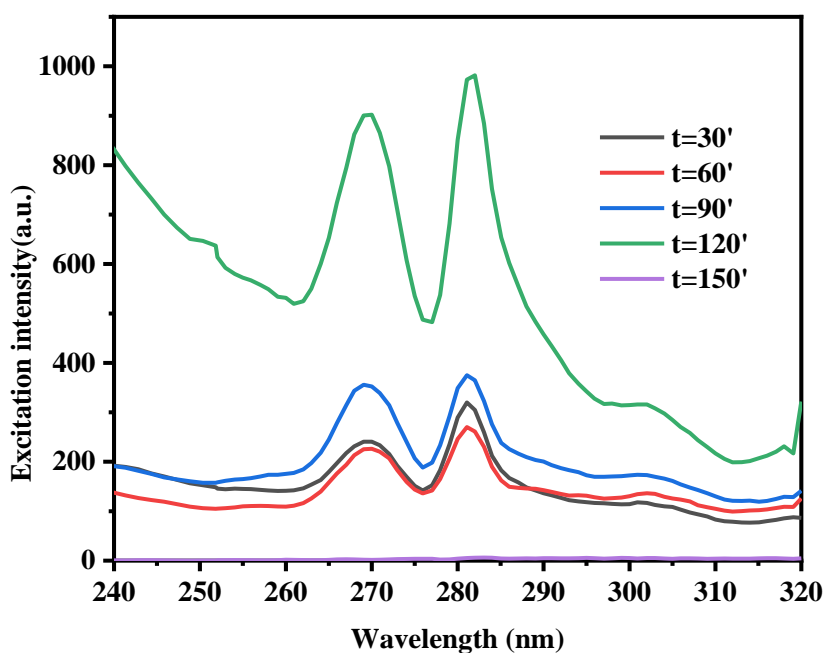


Fig. 8.9: Excitation spectrum of  $\text{Y}_2\text{SiO}_5:\text{Ce}^{3+}$  thin films deposited at different time

In the preparation of  $\text{Y}_2\text{SiO}_5:\text{Ce}^{3+}$ , it is expected probabilistic creation of defects in the lattice site which is also common for other phosphor materials during their preparation mostly oxygen vacancy. Comparing to  $\text{O}^{2-}$  site, the created vacancies are positive and electrostatically attracts nearby electrons and forms neutral centres. In  $\text{Y}_2\text{SiO}_5:\text{Ce}^{3+}$ , the only source of electron is  $\text{Ce}^{3+}$ , the charge imbalance is therefore stabilizing by electron transformation from  $\text{Ce}^{3+}$  and forming  $\text{Ce}^{4+}$  centres. The oxygen vacancies and the  $\text{Ce}^{4+}$  centres are electrostatically closely placed with some variation. The variation observed could give us some luminescent bands which can be different from the standard luminescent centre of the material in consideration [57]. Yttrium silicate ( $\text{Y}_2\text{SiO}_5$ ) has a band gap of 7.4 eV which has enough space to accommodate any doping element like  $\text{Ce}^{3+}$  to make electronic transitions from the valence band to the conduction band by giving characteristic emissions[49]. Under the excitation of cathode ray, X-ray and UV,  $\text{Y}_2\text{SiO}_5:\text{Ce}^{3+}$  is an efficient blue emitter. As we can see from Fig. 8.10 the emission spectra from the thin films deposited at a deposition time of 30 and 150 minute have suppressed by the other emissions due to reduced intensity. Fig. 8.11 also shows the Cerium ion energy diagram that is configured between 4f ground state and 5d excited states. The incoming UV interacts with the material, the electrons from the 4f energy level of Ce ion excites to the 5d energy level and begins to emit at different wavelengths corresponding to different energies.

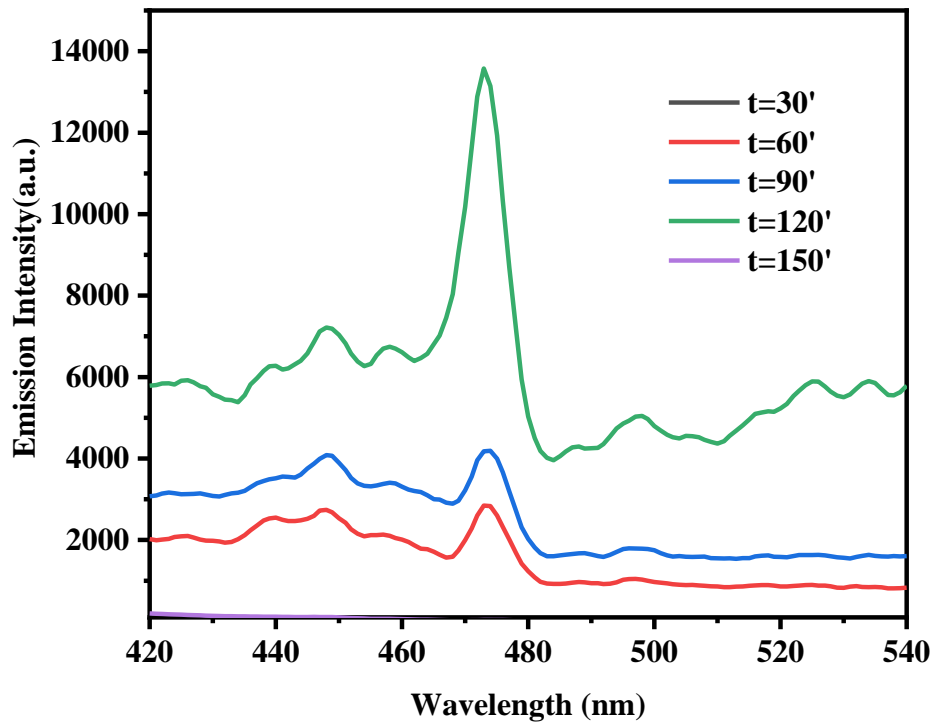


Fig. 8.10: Emission spectrum of  $Y_2SiO_5:Ce^{3+}$  thin films at different deposition time

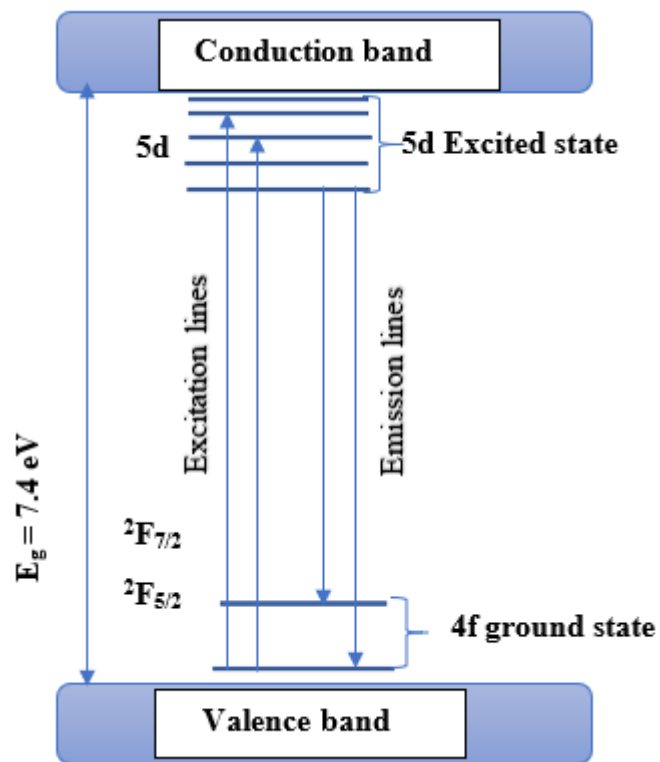


Fig. 8.11: Energy Level diagram of  $Ce^{3+}$

## Conclusion

Cerium doped yttrium silicate has been successfully deposited by pulsed laser. The deposited thin films are structurally end centered monoclinic. The prominent diffraction peak has been observed at a diffraction angle of  $30.6^\circ$  without any significant shift in all deposition conditions. Maximum and minimum crystallite size has been observed at a deposition time of 60 and 30 respectively. In the Raman spectroscopy measurement, the Rayleigh scattering was observed at  $536\text{ cm}^{-1}$  and the Stokes and anti-Stokes scattering were observed at a wave number of  $6.9$  and  $980\text{ cm}^{-1}$  respectively. In Rayleigh scattering the excitation and emission energy is the same. Whereas in the Stokes and anti-Stokes scattering the two energies are different. Very intense peak has been observed at a deposition time of 120 minute which can be ascribed to good crystallinity. The particles are uniformly distributed on the deposition area are nearly circular shape. Highly dense and aggregated nanoparticles have been observed at high deposition time. The nanoparticle size was in the micron size which varies between  $0.2$  and  $0.4\text{ }\mu\text{m}$ . Maximum nanoparticle size was observed at 150 and 30 minutes respectively. As it can confirm from the EDXS measurement, all the constituent elements have been detected with their respective atomic ratio. More atomic percentage of silicon were observed and the atomic percentage of cerium increase as the deposition time increases. Maximum and minimum absorbance were observed at the deposition time of 120 and 30 minutes respectively which can be ascribed to the thickness of the film. The bandgap calculated from the thin films deposited at 90 and 120 minutes were  $2.49$  and  $1.79\text{ eV}$  respectively. Where the bandgap is related to the size between valence and conduction bands. The PL excitation wavelength were observed at  $269$  and  $282\text{ nm}$  which ascribes to the two crystallographic sites of  $\text{Ce}^{3+}$ . Excitations of  $269\text{ nm}$  is due to the host and  $282\text{ nm}$  is due to  $4f \rightarrow 5d$  electronic transition of  $\text{Ce}^{3+}$  ion. Maximum emission was observed at  $473\text{ nm}$  with a shoulder of  $448\text{ nm}$ . The emission is ascribed to the probability of recombination of excited  $\text{Ce}^{3+}$  electron from  $5d \rightarrow 4f$  energy states with sub energy level of  $4f_{7/2}$  and  $4f_{5/2}$  respectively.

## Chapter 9: Synthesis and characterization of $\text{Y}_2\text{SiO}_5:\text{Ce}^{3+}$ phosphor powder by combustion method

### 9.1 Introduction

In recent decades, luminescence materials like yttrium silicate doped with trivalent RE ions have attracted to different studies for a possible applications in the area of optical technology such as phosphor materials, fiber amplifiers[240, 241], high density optical storage [241] lasers and electroluminescent display devices [242]. Due to the promising application in a flat display panels (FPDS), trivalent RE ions ( $\text{RE}^{3+}$ ) have attracted due attention. Nevertheless, the progressive development and efficiency of these materials needs further study and improvement. On the other side the Sulphides or selenides are also efficient phosphor materials in the current display technologies especially in the cathode ray tube (CRT) technologies which is effective at high voltages of 5 to 10 KeV [243]. Even though some wonderful studies have been done on the sulphide-based luminescent phosphor materials, there are still some limitations to be improved on the degradation life of the display material for advanced applications, there is also a problem in the chemical stability and charge build ups[243]. Oxide-based phosphors such as yttrium silicate have shown excellent advancement over sulphide-based phosphors due to their transparency, chemical and thermal stability, and luminescence performance[242, 244]. As a result, phosphorescent materials doped with trivalent REs become a promising material for possible application in optoelectrical fields[1, 6]. The recent plasma, field emission displays (flat electroluminescence) developments in industrial applications have increased demands for material characterizations for better brightness, chemical and temperature stability and industrial processing capacities[129, 245]. Due to their visible transparency, chemical and temperature stability, low thermal expansion and high conductivity silicate families are interesting materials in a wide range of applications. The yttrium orthosilicate (YSO or  $\text{Y}_2\text{SiO}_5$ ) are among the silicate families which are used to be host materials for the RE ions which displays exciting applications in the field of long-lasting phosphors, lasers, X-ray imaging, displays (PDP, FDP), environmental monitoring, good laser host, and promising candidate for coherent time domain optical memory. The powder has been synthesised by the combustion route. This route gives effective, easy and low-cost processes for several powders for various advanced applications and it is the best synthesis method to prepare variety of materials at the nanoscale level [246]. The combustion principle generates fire with the help of oxidizer, fuel, and suitable temperatures to remove unnecessary gases in the exothermic redox reactions that take place between the fuel and the oxidant. It was characterized by a low heating temperature of  $500^\circ\text{C}$ , which is a short duration reaction and high heating rates.



## 9.2 Experimental analysis

After synthesizing the phosphorus powder with different concentrations of TEOS and obtaining the pure phase of  $Y_2SiO_5: Ce^{3+}$ . The aim/objective of this experiment is to produce pure phase of  $Y_2SiO_5: Ce^{3+}$  and further doping with different concentrations of cerium and another RE ions for further luminescence characterizations. This material has been synthesised by Combustion route which involves a highly exothermic reaction between metal nitrates and an organic fuel, which produces high temperatures in excess of  $1500^{\circ}C$ , and sustains these high temperatures long enough for the crystallization of the product and growth. All the chemical reagents used in the synthesis of the material were commercial with analytical grade, and used directly without further purification for the synthesis. The reagent materials were Yttrium (III) nitrate hexahydrate [ $Y(NO_3)_3 \cdot 6H_2O$  (Sigma-Aldrich 99.99%)], Cerium (III) nitrate hexahydrate [ $Ce(NO_3)_3 \cdot 6H_2O$  (Sigma-Aldrich 99.99%)], Urea [ $CO(NH_2)_2$ ], and Tetramethyl orthosilicate (TEOS) [ $C_4H_{12}O_4Si$ ]. In synthesising this product, we have varied the silicate source ( $Si(CH_3O)_4$ ) by keeping the other precursors constant.  $Y(NO_3)_3 \cdot 6H_2O$  were kept at 2.81mL,  $CH_4N_2O$  at 5.2735mL,  $Ce(NO_3)_3 \cdot 6H_2O$  were kept at 0.233mL and the deionized water which were used as a solvent has been fixed at a volume of 15 mL for all synthesising conditions. The silicate source was varying with a molar of 0.007, 0.011, 0.014, 0.015 and 0.021 M. The synthesising procedure is schematically shown in Fig. 9.1. The powder samples were analysed by TEM, DTGA, TL and PL characterizing machines. The sample preparation for the TL exposure were a 20 g of  $Y_2SiO_5: Ce^{3+}$  powder, with the UV exposure time of 20 minutes and heating rate of  $2^{\circ}C/s$ .

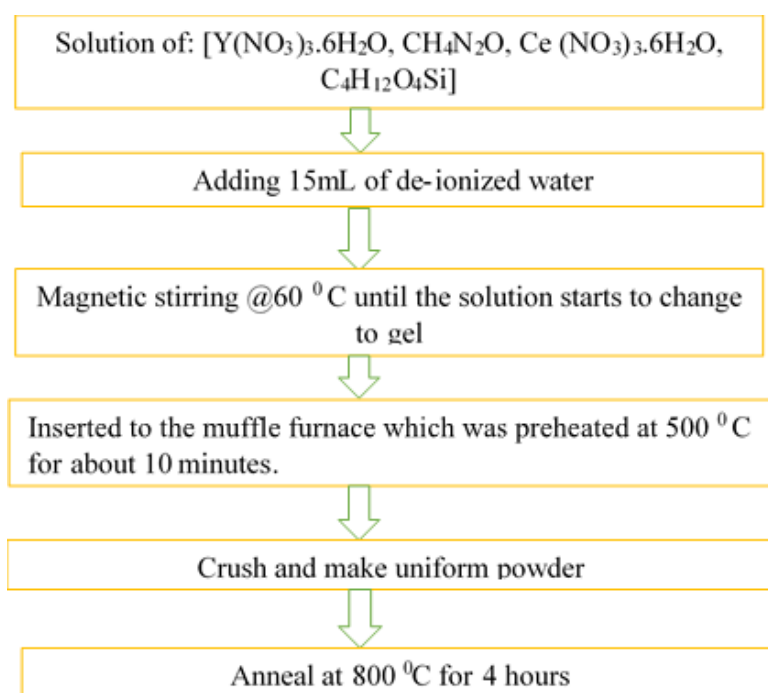


Fig. 9.1:  $Y_2SiO_5: Ce^{3+}$  combustion synthesis flow chart

## 9.3 Result and discussion

### 9.3.1 TEM analysis

TEM measurement gives us detailed information about particle size, grain size, lattice type, morphological information and crystallographic details of nanoparticles. The TEM images of the phosphor powder deposited with at TEOS concentration of 0.014 and 0.015 M respectively are shown in Fig.9.2. The phosphor powder synthesised at a concentration of 0.014 M shows small cracks and agglomerations compare to the phosphor powder synthesised at molar concentration of 0.015 M. The nanoparticles are uniformly distributed at a molar concentration of 0.015 M with small agglomeration in some portion of the images. The nanoparticle distribution is given in Fig.9.3. The average nanoparticle size is found to be 13.8 nm.

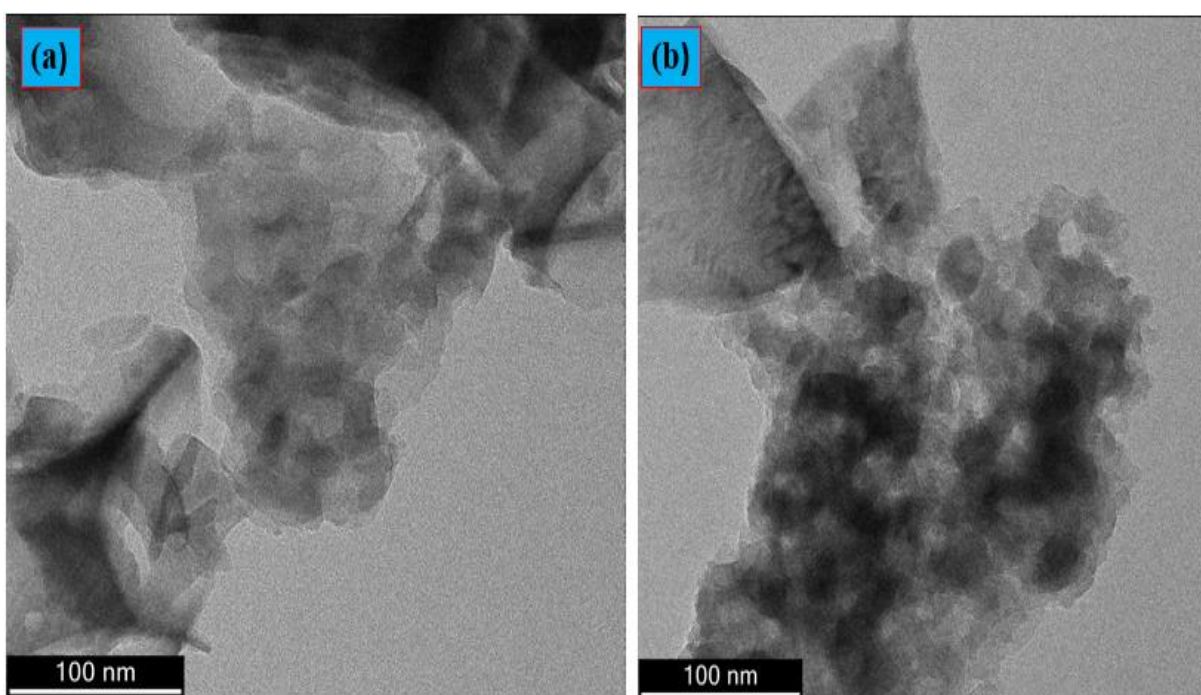


Fig.9.2: TEM images of (a) 0.014 M (b) 0.015 M

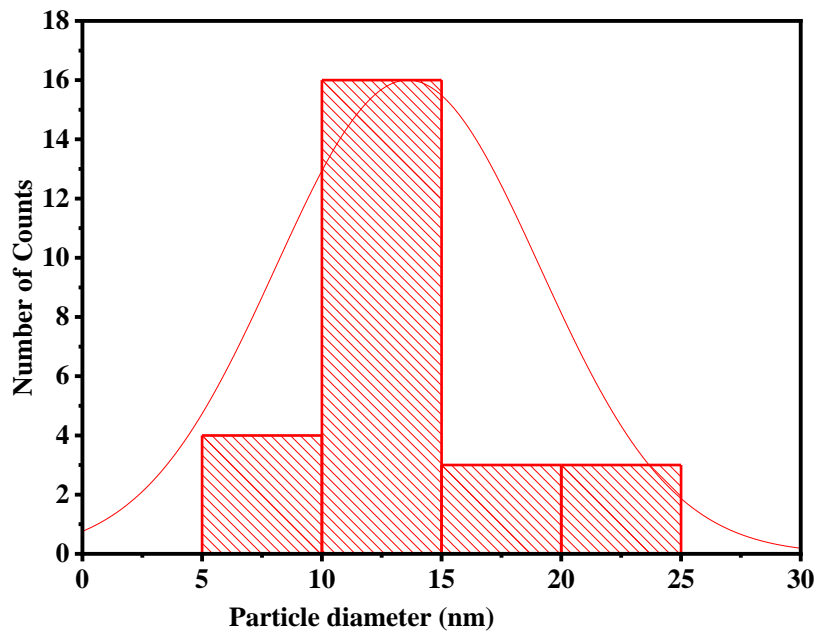


Fig.9.3: particle distribution as a function of diameter (nm)

### 9.3.2 Thermal analysis

This analysis describes the performance of thermogravimetry (TGA) and differential scanning calorimetry (DTGA) synchronously on the same sample that was used to measure both. The physical and chemical properties of the material are controlled by thermal analysis when exposed to multiple temperatures. The assessment conditions of TGA and DTGA keeps same when the temperature is varied. As a result, both the amount and the rate of change in mass are measured. Fig. 9.4 shows the TGA and DTGA graphs of the as-prepared  $Y_2SiO_5:Ce^{3+}$  powder phosphor grown at various Tetramethyl orthosilicate (TEOS) concentrations in the precursor solution. The phosphor nanomaterial  $Y_2SiO_5:Ce^{3+}$  prepared at 0.015 M of TEOS concentration appears relatively stable than samples prepared at 0.014 M concentration of TEOS. As we can see in Fig. 9.4, the slope at 0.015 M shows a gradual decrement while the graph at 0.014 M shows sharp slopes which indicate a rapid rate of weight loss of the samples as we can clearly see the percentage of weight loss from the TGA graph of the two samples, a high percentage of weight loss was observed at TEOS concentration of 0.014 than 0.015 M. Further from the DTGA plots, a sharp peak was observed at a concentration of 0.014 especially at a temperature of around 95 °C. This can show that more weight loss of the sample on 0.014 than 0.015 M at this temperature. As we can see from the DTGA graphs two downward peaks related to the main weight loss were observed at around 95 °C and 600 °C. De-ionized water was used as a solvent for the solution. The weight loss at temperature around 95 °C can be ascribed to the evaporated deionized water and the weight loss at around 600 °C could be ascribed to the residual organic materials.

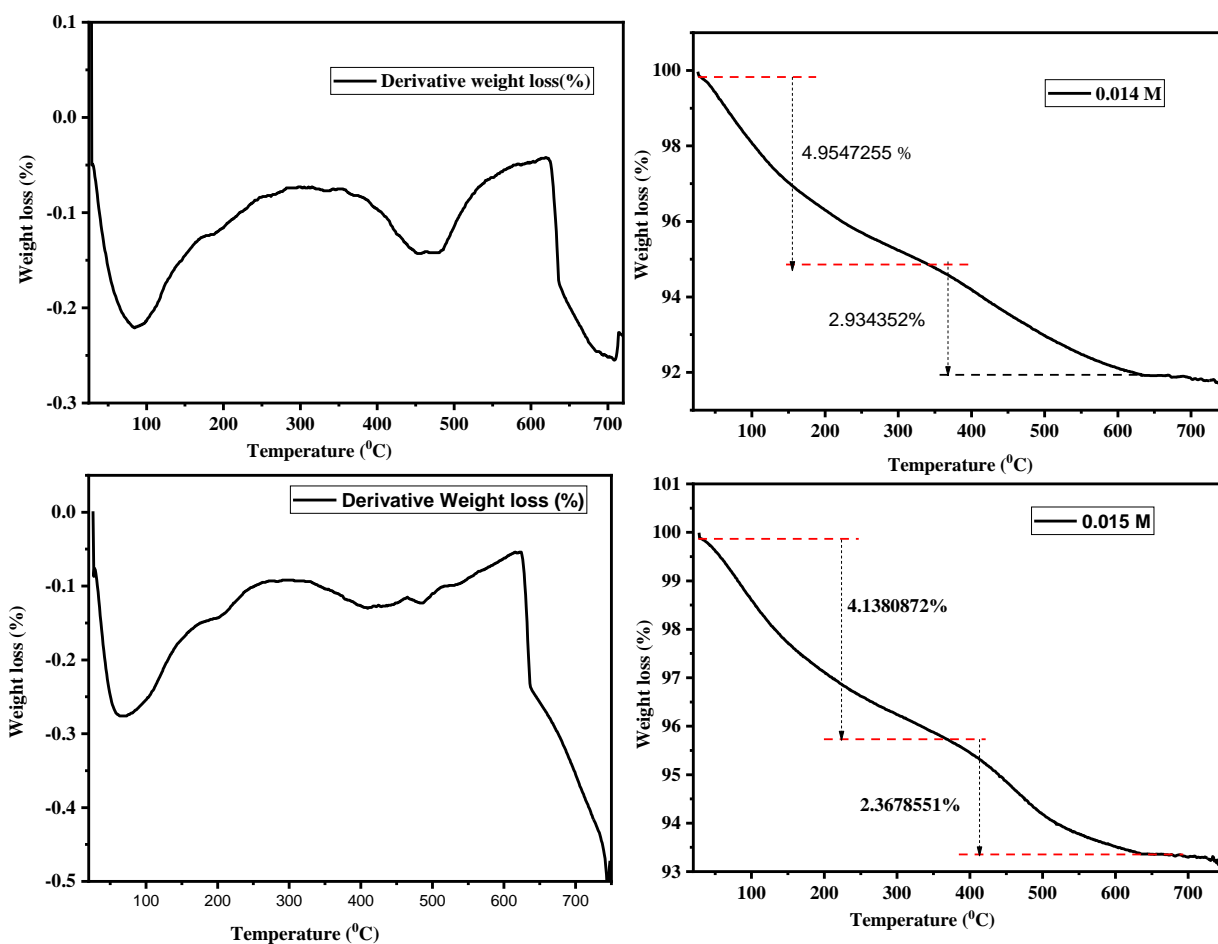


Fig.9.4: DTGA and TGA graphs of  $Y_2SiO_5:Ce^{3+}$  phosphor powders at various TEOS concentrations.

### 9.3.3 PL analysis

The photoluminescence excitation and emission spectra are given in Fig. 9.5 and Fig. 9.6 respectively. Where excitation is the wavelength absorbed by the material which is able to emit a specific wavelength as a result of absorption and the de-exciting electron from the 5d excited state to the 4f ground state of the Ce ion energy levels. From Fig. 9.5 three excitation wavelengths were observed at around 220, 308 and 340 nm which can be ascribed to the transition of electrons from the ground state of  $^2F_{5/2} (4F^1)$  to the crystal field splitting of the 5d states of  $Ce^{3+}$ . From similar studies on  $Y_2SiO_5: Ce$  [153], maximum excitation wavelengths have been observed at 356 nm which could probably resulted from the transition of 2P electrons of  $O^{2-}$  to the 4f empty orbitals of  $Ce^{3+}$  ions and the other two peaks are due to the excited 5d splitting in to sub energies. The  $Ce^{3+}$  ion usually emits two emission spectra which could be resulted from the spin-orbit interactions of the ground state where its emission position is extremely related to the crystal structure of the host material [247]. The  $Ce^{3+}$  has different coordination numbers. it has two separate sites on the lattice position of the host. However, in our emission spectra one broad emission spectra at around 483 nm has been observed. The other emission peak might be dominated hidden in the broad emission peaks as shown in Fig. 9.6. The emission spectra are positioned at the blue range with an excitation

wavelength of 340 nm. This emission can be ascribed to the electronic transition of 5d→4f energy level of the  $Ce^{3+}$  ion [13]. The  $Ce^{3+}$  ion has two ground state energy levels at  $^2f_{5/2}$  and  $^2f_{7/2}$ . The splitting of the 4f energy level for  $Ce^{3+}$  ion into sub energy levels is due to the doublet character of the electrons i.e., the spinning of the electron around its axis and rotation of the electron around the nucleus are the possible scenarios to the creation of the two sub energy levels. The excitation wavelengths observed at 220, 308 and 340 nm could be attributed to the electron transition from the ground state of  $4f^1$  ( $^2f_{5/2}$ ) into different sections of the 5d excited state. The electrostatic interaction between the ions and the atoms of the crystal field of the host materials are the main reason for the creation of the 4f and 5d energy levels. As the precursor concentration increasing, the excitation wavelength becomes broader from a precursor concentration of 0.021 to 0.011M. The broadness of the excitation might be probably due to the increase of distortion. It is known that the narrow bands in the luminescent spectrum of  $Ce^{3+}$  are sensitive to the crystallographic site symmetry occupied by  $Ce^{3+}$  ions.

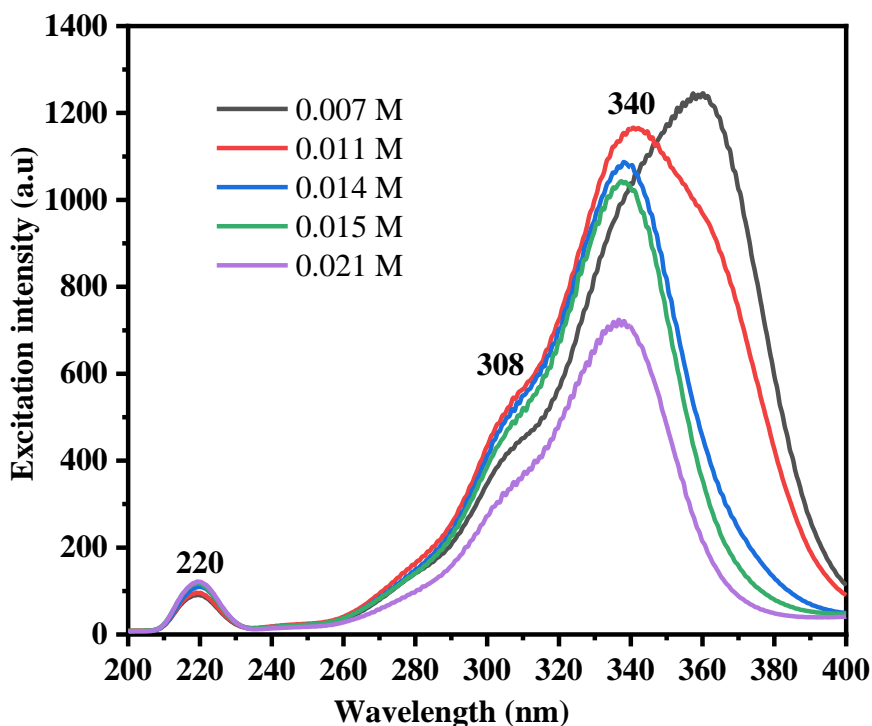


Fig. 9.5: excitation graph for the  $Y_2SiO_5:Ce^{3+}$  phosphor powder

As we can see from fig.9.6, when the precursor concentration is increased from 0.007 to 0.021M, the luminescent intensity increases. This can be due to the strength of the absorption energy and also increase in the crystallite sizes.

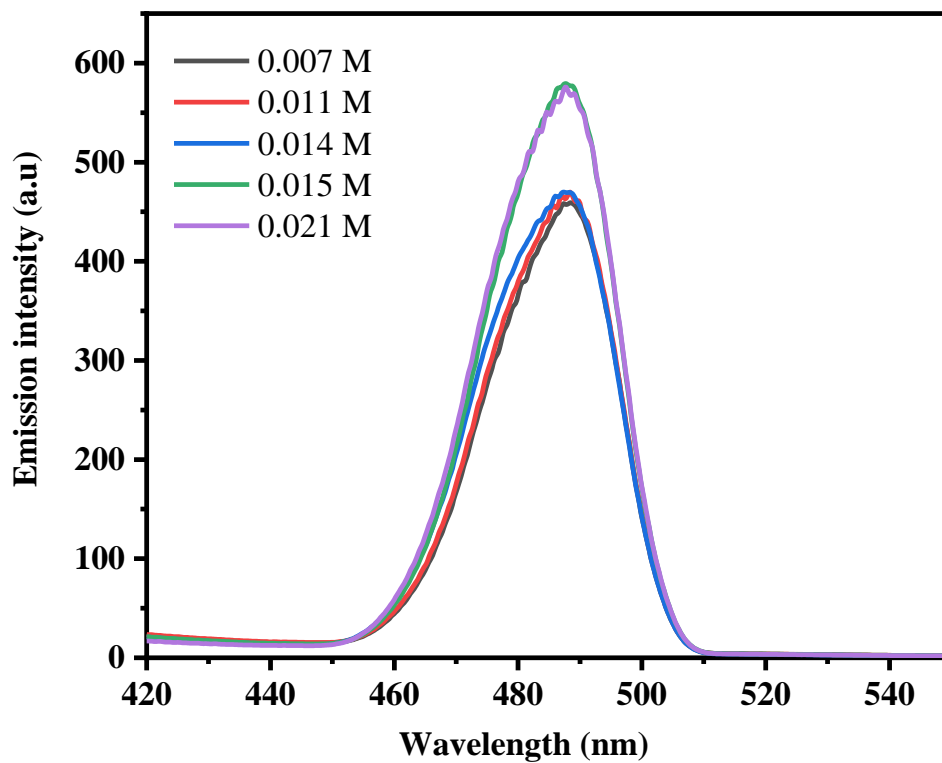


Fig. 9.6: Emission graph for the Y<sub>2</sub>SiO<sub>5</sub>:Ce<sup>3+</sup> phosphor powder

### 9.3.4 TL analysis

Fig .9.7 represents the TL glow curve for the material synthesized at different TEOS concentrations.

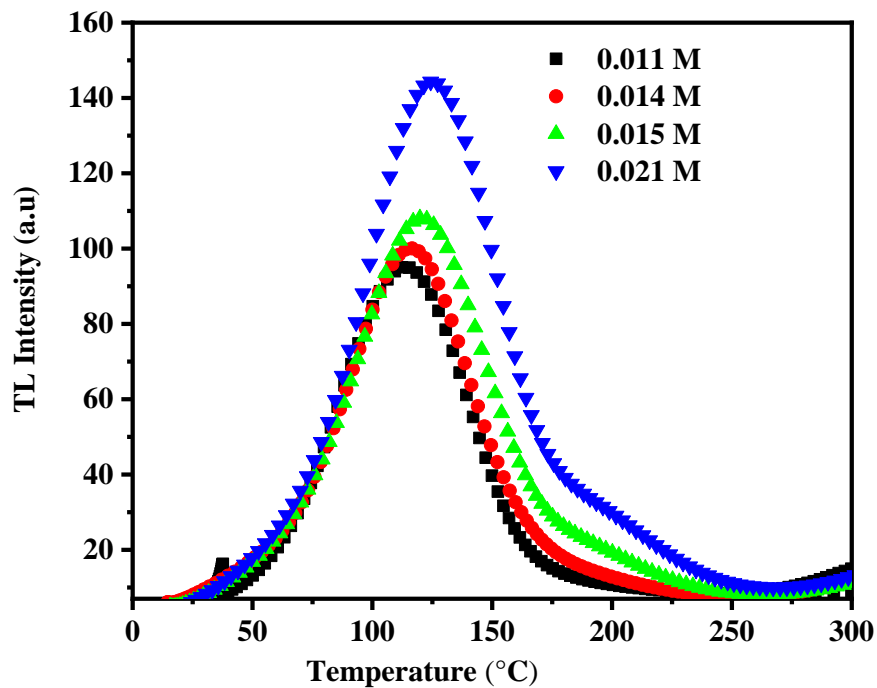


Fig. 9.7: TL glow curve of the powder synthesized at different TEOS concentrations

When the crystal in the sample is heated up to its maximum limit, the excess energy stored in the electrons or holes which were previously trapped starts thermally luminating. The luminescence

intensity corresponds to the concentration of luminescence centres. The thermoluminescence measurement emission gives us information on the defect centres and its corresponding energy levels [195]. The glow curve of the samples deposited at different values of the TEOS are shown in Fig. 9.7. From Fig. 9.7, we can see that the samples deposited at TEOS concentration of 0.021 and 0.015M have higher thermoluminescence intensity which can be ascribed to high defect levels compared to the other synthesis conditions [248]. The estimated kinetic energy and the trapping parameters calculated from the glow curve of Fig. 9.7 have been calculated by Chene's peak shape equation [226]. The activation energy has been calculated using the kinetic parameters ( $\tau$ ,  $\delta$  and  $\omega$ ) which are defined in equation (6.4). The average activation energy of each kinetic parameters is given by is given in equation (6.5). The value of  $\mu_g$  is between 0.42 and 0.52. If the value of  $\mu_g$  is around 0.42 it is called first order and when it is 0.52 it is called second order.  $\mu_g$  is independent of the activation energy but it depends on the order of kinetics (b) [249]. The frequency factor (S) can be calculated from E and b by chen's and Kirsh relation [195] as given in equation (6.6).

Using equation (6.5) and (6.6) the activation energy and frequency factor are summarized in the table below.

Table 9.1: kinetic and trapping parameters of the UV- irradiated  $Y_2SiO_5:Ce^{3+}$  nano crystalline phosphor powders

TEOS values in (moles)	$T_1$ (k)	$T_m$ (k)	$T_2$ (k)	$\omega$	$\tau$	$\delta$
0.011	314.05	387.84	417.18	103.13	73.79	29.34
0.014	354.94	389.62	421.63	66.69	34.68	32.01
0.015	357.61	394.06	426.97	69.36	36.45	32.91
0.021	326.5	397.624	430.52	104.02	71.124	32.896

Table 9.2: Trap parameters and order of kinetics for UV-irradiated  $Y_2SiO_5:Ce^{3+}$  phosphor powders.

TEOS values (moles)	in	$T_m(K)$	Order of kinetics $\mu_g(b)$	Activation energy (eV)				Frequency factor ( $S^{-1}$ )
				$E_\tau$	$E_\delta$	$E_\omega$	$E_{av}$	
0.011		387.84	0.285	0.126	0.006	0.076	0.065	$2.19 \times 10^4$
0.014		389.62	0.480	0.513	0.577	0.546	0.545	$3.42 \times 10^4$
0.015		394.06	0.474	0.491	0.557	0.524	0.524	$2.95 \times 10^4$
0.021		397.624	0.316	0.151	0.090	0.123	0.121	$1.73 \times 10^4$

As we can see from table 9.2 maximum activation energy have been observed at synthesis TEOS concentration of 0.015 and 0.014 M respectively and minimum activation energy were calculated from the glow curve of the samples synthesised at a concentration of 0.011 and 0.021 M respectively. The higher activation energy is related to high trap depth, the higher the trap depth high activation energy is required to excite the electron or hole which was previously trapped there. And the lower activation energy observed at TEOS concentration of 0.011 and 0.021 M are ascribed to shallow depth.

## Conclusion

The phosphor powder was synthesised at different molar concentration of TEOS. The synthesised powder was annealed at  $800\text{ }^\circ\text{C}$  for 4 hours. Small agglomeration has been observed in both TEM images deposited at 0.014 and 0.015 M. The average nanoparticle size was 13.8 nm. The phosphor powder prepared at molar concentration of 0.015 M shows stable slope than the phosphor powder prepared at a TEOS concentration of 0.014 M. Moreover, a high percentage of weight loss observed at 0.014 M. The two DGTAs downward peaks observed at  $95\text{ }^\circ\text{C}$  and  $600\text{ }^\circ\text{C}$  are due to the evaporated deionized water and the residual organic materials. Three excitation peaks are observed at 220, 308 and 340 nm which ascribes to the transition of electron from the ground state of  $^2F_{5/2}$  to the crystal field splitting of the 5d states of  $Ce^{3+}$  ions. A broad emission has observed at 483 nm, this emission ascribes to electronic transition from 5d to 4f energy states of  $Ce^{3+}$  ions. Maximum TL emission were observed at TEOS concentration of 0.021 and 0.015 M respectively. Maximum activation energy was observed at a molar concentration of 0.014 and 0.015 M respectively. The activation energy is related to the depth of the trap. When the trap depth is high, maximum energy is required to excite the electron from the trapped position.



## Chapter 10: conclusion, future work and Recommendation

### 10.1: Conclusion

$\text{Y}_2\text{SiO}_5:\text{Ce}^{3+}$  thin films were successfully deposited by pulsed laser deposition method with different deposition conditions. The phosphor powder was also synthesized by combustion method. Different characterization techniques were used to investigate the effect of variable deposition parameters on the structural, morphological, photoluminescence, thermoluminescence and other properties of the thin films and the synthesized phosphor powder. In all deposition conditions the structure of the thin films was found to be monoclinic with different lattice sizes. The average crystalline size was found to be 37 nm when it was deposited with various substrate distances from the target material. For all excitation's wavelengths, used in all deposition conditions it was observed that the corresponding emission wavelength were observed at a blue electromagnetic spectrum band. The emissions are ascribed to the electronic transitions between the 5d and 4f energy levels of the  $\text{Ce}^{3+}$  ions where the 4f and 5d are the ground state and excited state energy levels of the  $\text{Ce}^{3+}$ , which could be created due to the electrostatic interaction between the ions and crystalline field of the host at the expense of surrounding charges. Highest emission intensity was observed at a substrate distance of 5 cm when the films was deposited at various substrate distances. The material properties of  $\text{Y}_2\text{SiO}_5:\text{Ce}^{3+}$  were also investigated at different substrate temperatures. At a deposition temperature of 450 °C a crystalline thin film with an excitation and emission wavelength of 337 and 465 nm were observed respectively with better crystallinity than the other films deposited with another substrate temperature. In this deposition condition the nanoparticles were distributed with some agglomerations which might be due to the high deposition rate. Structural, morphological, photoluminescence, thermoluminescence and U.V absorbance of the thin films were also investigated with different deposition gases (Oxygen, argon, nitrogen and vacuum). Thin films with different textures and topographies were observed in all deposition gases. The average nanoparticle size was found to be 28.1 nm. In all EDS measurements all the constituent elements of the complex compound were detected with their respective atomic ratios. Maximum UV absorbance has been observed at argon deposition gas and minimum absorbance were also observed at vacuum deposition. The value of the absorption is ascribed to the thickness of the film. The excitation was probed at 370 nm with corresponding emission of 420 and 457 nm. The calculated activation energy was ranged between 0.1733 and 0.1938 eV. A prominent diffraction peak was observed at a diffraction peak of  $2\theta = 28.9^\circ$ . The crystallinity of the films was supported by the Raman spectroscopy measurement. Morphological and structural variation have been observed both in the SEM and AFM measurements. The grains are structurally spherical in shape. The average diameter of the nanoparticles was 0.54, 0.49, 0.39 and 0.55  $\mu\text{m}$  for the deposition pressure of 1.5, 20, 60 and 100

mTorr respectively. Higher surface roughness and rms roughness was observed at a deposition pressure of 60 mTorr. Maximum and minimum absorbance were detected at a deposition pressure of 60 and 100 mTorr, respectively, which ascribes to the surface thickness of the deposited film. The maximum TL intensity was also observed at a deposition pressure of 60 and 100 mTorr which is due to the defect levels present on the interacting surface. The average activation energy was varied between 0.349 and 0.438 eV. At a deposition pressure of 1.5 mTorr, maximum activation energy was calculated. The higher the activation energy, the greater the depth of the traps. When the thin films are deposited at different oxygen deposition condition the prominent diffraction peak were observed at  $30.6^\circ$  in all deposition conditions. In the Raman measurements, the value of Rayleigh, stokes and anti-stokes were observed at 536, 6.9 and  $980\text{ cm}^{-1}$ , respectively. Very intense peak was observed at a deposition time of 120 minute which ascribes to good crystallinity of the thin film for this deposition time. The average nanoparticle size was varied between 0.2 and  $0.4\ \mu\text{m}$ . More atomic percentage of silicon were observed and the atomic percentage of cerium increases as the deposition time increases. The maximum absorbance observed at a deposition time of 120 minute could be due to the thickness of the film. The band gap of the thin films at deposition time of 90 and 120 were 2.49 and 1.79 eV, respectively. The excitation wavelength was observed at 269 and 282 nm and the corresponding emission was detected at 473 nm where this emission is due to the radiative transition of  $\text{Ce}^{3+}$  electrons from the 5d to the 4f energy states. The phosphor powder synthesized by combustion were investigated by measurements of TEM, TGA, DTGA, PL and TL measurements. The nanoparticle size from the TEM measurement was obtained to be 13.8 nm. The de-ionized water and the residual organic materials were evaporated at  $95^\circ\text{C}$  and  $600^\circ\text{C}$ , respectively. Maximum TL emission were observed at TEOS concentration of 0.021 M. Maximum activation energy were observed at a TEOS concentration of 0.014 and 0.015 M respectively which is related to the trap depth of the trapped electrons.

## **10.2: Future work and Recommendations**

Besides the investigations we have implemented with different conditions, further study with different deposition condition and measurements is compulsory to get better and sustainable results which is easily suitable for the display applications. The films should be deposited with a wider background gas, with different laser source like 193 and 248 nm ArF to get better optimized results and make comparison between the two. Where the deposition laser we have used was 266 nm Nd: YAG. Deposition parameters or conditions like laser spot size, pulse width, pulse repetition rate and substrate type are some of the deposition conditions which should be employed in future studies to get full information on the material properties of the thin films for possible display applications. Post deposition of the thin films with reactive and non-reactive environments is also our plan in

order to study the corresponding effects on the structural, photoluminescence, thermoluminescence and other properties of the material. Other important recommendations to the reader is implementation of the off-axis deposition technique could better helps to minimize the formation of particulates on the surface of the thin films. The off-axis technique is a deposition technique where the substrate mounts at some angle in which the plasma plume is not directly focused on the substrate. The other future work we have planned to do is studying the material properties of the host material with different dopants and co-dopants like Eu, Gd, Tb and Dy to get suitable photoluminescence results for the possible implementation on the display applications.

## Publications

1. H.T. Haile, F.B. Dejene, Effect of substrate temperature on the material properties of the  $Y_2SiO_5:Ce^{3+}$  thin films by pulsed laser deposition (PLD) method. *Optik - International Journal for Light and Electron Optics*: 184(2019) 508–517: <https://doi.org/10.1016/j.ijleo.2019.05.003>
2. H.T. Haile, F.B. Dejene, Effect of target to substrate distance on the material properties of  $Y_2SiO_5:Ce^{3+}$  thin films by pulsed laser deposition. *Applied physics A (Materials science and processing)* 172(2019) 125-172. <https://doi.org/10.1007/s00339-019-2473-4>.
3. H T Haile and F B Dejene, the influence of deposition gases on the material properties of  $Y_2SiO_5: Ce^{3+}$  thin films deposited by pulsed laser deposition (PLD) method 2020 *Mater. Res. Express* 7 076406: <https://doi.org/10.1088/2053-1591/ab88fd>.
4. H.T. Haile, F.B. Dejene; Influence of oxygen deposition pressure on the structural, morphological, photoluminescence and thermoluminescence properties of  $Y_2SiO_5:Ce^{3+}$  by pulsed laser deposition method (under Review): *Inorganic Chemistry communications; Manuscript Number: INOCHE-D-20-00927-Under Review*.
5. H.T. Haile, F.B. Dejene, the influence of deposition time on the structural, photoluminescence, morphological and optical properties of  $Y_2SiO_5:Ce^{3+}$  thin films deposited by Pulsed Laser (Ready to journal submission)
6. H.T. Haile, F.B. Dejene, Synthesis and characterization of  $Y_2SiO_5:Ce^{3+}$  phosphor powder by combustion method (Ready for submission).

## Conferences and Workshops

1. Workshop on pulsed laser deposition Universidade Eduardo Mondlane, Mozambique, 28<sup>th</sup> July-7<sup>th</sup> August, 2018, Maputo, Mozambique.
2. H. T. Haile, F. B. Dejene, the influence of deposition gases on the material properties of  $Y_2SiO_5: Ce^{3+}$  thin films deposited by pulsed laser deposition (PLD) method, 12<sup>th</sup> African

laser centre (ALC) Student Workshop, 20<sup>th</sup> - 23<sup>rd</sup> November 2019, Zevenwacht Wine Estate, Stellenbosch, South Africa.

3. Workshop on Laser Spectroscopy and Laser Imaging, 25-27<sup>th</sup> November 2019, Zevenwacht Wine Estate, Stellenbosch, South Africa

## References

- [1] C.Feldmann, T.Jüstel, C.R.Ronda, and P.J.Schmidt, "Inorganic luminescent materials: 100 years of research and application," *Advanced Functional Materials*, vol.13, no.7, pp.511-516, 2003.
- [2] V.Țucureanu and D.Munteanu, "Enhanced optical properties of YAG: Ce yellow phosphor by modification with gold nanoparticles," *Ceramics International*, vol. 45, no.6, pp.7641-7648, 2019.
- [3] R.H.Petrucci, W.S. Harwood, and F.G.Herring, *General chemistry*. Prentice Hall, 1993.
- [4] E.S. Grew, A.J. Locock, S.J.Mills, I.O.Galuskina, E.V.Galuskin, and U.Hålenius, "Nomenclature of the garnet supergroup," *American Mineralogist*, vol. 98, no. 4, pp. 785-811, 2013.
- [5] L.Shirmane and V. Pankratov, "Emerging blue-UV luminescence in cerium doped YAG nanocrystals," *physica status solidi (RRL)–Rapid Research Letters*, vol.10, no.6, pp.475-479, 2016.
- [6] M.Nazarov, *New generation of europium-and terbium-activated phosphors: from syntheses to applications*. Pan Stanford, 2011.
- [7] G.Blasse and B.Grabmaier, "How Does a Luminescent Material Absorb Its Excitation Energy?," in *Luminescent materials*: Springer, 1994, pp. 10-32.
- [8] P. Kumari, P. Baitha, and J. Manam, "Structural and photoluminescence properties of red-light emitting YVO<sub>4</sub>: Eu<sup>3+</sup> phosphor synthesized by combustion and solid-state reaction techniques: a comparative study," *Indian Journal of Physics*, vol. 89, no. 12, pp. 1297-1306, 2015.
- [9] B.Choudhury and A.Choudhury, "Tailoring luminescence properties of TiO<sub>2</sub> nanoparticles by Mn doping," *Journal of Luminescence*, vol. 136, pp. 339-346, 2013.
- [10] R.Vacassy, S. M. Scholz, J. Dutta, C.J. G. Plummer, R. Houriet, and H. Hofmann, "Synthesis of controlled spherical zinc sulfide particles by precipitation from homogeneous solutions," *Journal of the American Ceramic Society*, vol. 81, no. 10, pp. 2699-2705, 1998.
- [11] S. D. Meetei et al., "Crystal structure and photoluminescence correlations in white emitting nanocrystalline ZrO<sub>2</sub>: Eu<sup>3+</sup> phosphor: Effect of doping and annealing," *Journal of Luminescence*, vol. 132, no. 2, pp. 537-544, 2012.
- [12] T. Wang, W. Bian, D. Zhou, J. Qiu, X. Yu, and X. Xu, "Tunable LLP via Energy Transfer between Na<sub>2-y</sub>(Zn<sub>1-x</sub>Ga<sub>x</sub>) GeO<sub>4</sub> Sosooid Host and Emission Centers with the Assistance of Zn Vacancies," *The Journal of Physical Chemistry C*, vol. 119, no. 25, pp. 14047-14055, 2015.
- [13] L. Muresan et al., "Tunable luminescence of broadband-excited and narrow line green emitting Y<sub>2</sub>SiO<sub>5</sub>: Ce<sup>3+</sup>, Tb<sup>3+</sup> phosphor," *Journal of Alloys and Compounds*, vol. 658, pp. 356-366, 2016.
- [14] D. Fu et al., "Comprehensive study of the metal-insulator transition in pulsed laser deposited epitaxial VO<sub>2</sub> thin films," *Journal of Applied Physics*, vol. 113, no. 4, p. 043707, 2013.

- [15] J.T.Stock, "Edgar Buckingham: Fluorescence of quinine salts," *Bull. Hist. Chem*, vol. 27, no. 1, pp. 57-61, 2002.
- [16] B.Valeur and M. N. Berberan-Santos, "A brief history of fluorescence and phosphorescence before the emergence of quantum theory," *Journal of Chemical Education*, vol. 88, no. 6, pp. 731-738, 2011.
- [17] J.R.Cooper, K. Randle, and R. S. Sokhi, *Radioactive releases in the environment: impact and assessment*. John Wiley & Sons, 2003.
- [18] B.R.Masters, "Molecular Fluorescence: Principles and Applications," *Journal of Biomedical Optics*, vol. 18, no. 3, p. 039901, 2013.
- [19] C.R.Ronda, *Luminescence: from theory to applications*. John Wiley & Sons, 2007.
- [20] A.Kitai, *Luminescent materials and applications*. John Wiley & Sons, 2008.
- [21] N.T. Kalyani, H. C. Swart, and S. J. Dhoble, *Principles and applications of organic light emitting diodes (OLEDs)*. Woodhead Publishing, 2017.
- [22] J.R. Gispert, *Coordination chemistry*. Wiley-VCH Weinheim, 2008.
- [23] O.Dincer and A. Ege, "Synthesis and luminescence of Tb<sup>3+</sup> doped lithium borate (LiBO<sub>2</sub>)," *Journal of luminescence*, vol. 138, pp. 174-178, 2013.
- [24] N.Kucuk, I.Kucuk, M.Cakir, and S.K. Keles, "Synthesis, thermoluminescence and dosimetric properties of La-doped zinc borates," *Journal of luminescence*, vol.139, pp.84-90, 2013.
- [25] C.Reuven and M.S.WS, *Theory of Thermoluminescence and Related Phenomena*. World Scientific, 1997.
- [26] D.Vij and N. Singh, *Luminescence and related properties of II-VI semiconductors*. Nova Publishers, 1998.
- [27] C.Falcony, M.Garcia, A.Ortiz, and J.Alonso, "Luminescent properties of ZnS: Mn films deposited by spray pyrolysis," *Journal of applied physics*, vol.72, no.4, pp.1525-1527, 1992.
- [28] S.W.McKeever, *Thermoluminescence of solids*. Cambridge University Press, 1988.
- [29] C.Varney, D.Mackay, A.Pratt, S.Redda, and F.Selim, "Energy levels of exciton traps in yttrium aluminum garnet single crystals," *Journal of Applied Physics*, vol. 111, no. 6, p. 063505, 2012.
- [30] A.R.Barron, "Physical Methods in Chemistry and Nano Science," 2015.
- [31] M.J.Simpson and A.J.Simpson, *NMR spectroscopy: a versatile tool for environmental research*. John Wiley & Sons, 2014.
- [32] G.Kickelbick, *Hybrid materials: synthesis, characterization, and applications*. John Wiley & Sons, 2007.
- [33] A.Mitchell and M.W.Zemansky, *Resonance Radiation*. Cambridge, 1934.
- [34] R.S.Becker and R.S.Becker, *Theory and interpretation of fluorescence and phosphorescence*. Wiley Interscience New York, 1969.
- [35] B.Valeur, "Molecular fluorescence," *digital Encyclopedia of Applied Physics*, pp. 477-531, 2003.
- [36] C.E.Moore, *Atomic Energy Levels as Derived from the Analyses of Optical Spectra: The spectra of hydrogen, deuterium, tritium, helium, lithium, beryllium, boron, carbon, nitrogen, oxygen, flourine, neon, sodium, magnesium, aluminum, silicon, phosphorus, sulfur, chlorine, argon, potassium, calcium, scandium, titanium, and vanadium*. US Department of Commerce, National Bureau of Standards, 1949.
- [37] J.Röhler, "X-ray absorption and emission spectra," *Handbook on the physics and chemistry of rare earths*, vol. 10, pp. 453-545, 1987.
- [38] D.Favrholdt, *Complementarity Beyond Physics (1928-1962)*. Elsevier, 2013.
- [39] P. J. Mohr, B. N. Taylor, and D. B. Newell, "CODATA recommended values of the fundamental physical constants: 2006," *Journal of Physical and Chemical Reference Data*, vol. 80, no. 3, pp. 633-1284, 2008.
- [40] D. C. Harris, *Quantitative chemical analysis*. Macmillan, 2010.

- [41] J. Solé, L. Bausa, and D. Jaque, *An introduction to the optical spectroscopy of inorganic solids*. John Wiley & Sons, 2005.
- [42] J. A. DeLuca, "An introduction to luminescence in inorganic solids," ed: ACS Publications, 1980.
- [43] R. Saraf, "Facile synthesis of metal tungstates,  $\text{Eu}^{3+}$ -activated metal molybdates and bismuth oxyhalides nanophosphors: Applications in white LEDs and photocatalysis," MTEch thesis, University of Rajasthan and Indian Institute of Science, 2014.
- [44] T. Hussain et al., "Enabling low amounts of YAG:  $\text{Ce}^{3+}$  to convert blue into white light with plasmonic Au nanoparticles," in *Solid-State and Organic Lighting*, 2015, p. JTU5A. 1: Optical Society of America.
- [45] M. Nikl, "Scintillation detectors for x-rays," *Measurement Science and Technology*, vol. 17, no. 4, p. R37, 2006.
- [46] A. Huignard, T. Gacoin, and J.-P. Boilot, "Synthesis and luminescence properties of colloidal  $\text{YVO}_4$ : Eu phosphors," *Chemistry of materials*, vol. 12, no. 4, pp. 1090-1094, 2000.
- [47] F. B. Dejene and M. Tsega, "Blue-red emitting  $\text{BaAl}_x\text{O}_y$ : $\text{Eu}^{2+}$ , $\text{Dy}^{3+}$  nanophosphors synthesized using solution-combustion method: The effect of boric acid," *Optik*, vol. 127, pp. 1975–1979, 2016.
- [48] X. W. Sun and H. S. Kwok, "Pulsed laser deposition of silicate phosphor thin films," *Applied Physics A*, journal article vol. 69, no. 1, pp. S39-S43, December 01 1999.
- [49] X. Zhang, L. Zhou, Q. Pang, J. Shi, and M. Gong, "Tunable luminescence and  $\text{Ce}^{3+} \rightarrow \text{Tb}^{3+} \rightarrow \text{Eu}^{3+}$  energy transfer of broadband-excited and narrow line red emitting  $\text{Y}_2\text{SiO}_5$ :  $\text{Ce}^{3+}$ ,  $\text{Tb}^{3+}$ ,  $\text{Eu}^{3+}$  phosphor," *The Journal of Physical Chemistry C*, vol. 118, no. 14, pp. 7591-7598, 2014.
- [50] L. Muresan, B. Oprea, A. Cadis, I. Perhaita, and O. Ponta, "Studies on  $\text{Y}_2\text{SiO}_5$ : Ce phosphors prepared by gel combustion using new fuels," *Journal of Alloys and Compounds*, vol. 615, pp. 795-803, 2014.
- [51] J. Gonzalez-Ortega, N. Perea, and G. Hirata, "White light emission from  $\text{Y}_2\text{SiO}_5$ : Ce, Tb films excited by electroluminescence," *Optical Materials*, vol. 29, no. 1, pp. 47-50, 2006.
- [52] T. Aitasalo, J. Hölsä, M. Lastusaari, J. Legendziewicz, J. Niittykoski, and F. Pellé, "Delayed luminescence of  $\text{Ce}^{3+}$  doped  $\text{Y}_2\text{SiO}_5$ ," *Optical materials*, vol. 26, no. 2, pp. 107-112, 2004.
- [53] A. Meijerink, W. Schipper, and G. Blasse, "Photostimulated luminescence and thermally stimulated luminescence of  $\text{Y}_2\text{SiO}_5$ -Ce, Sm," *Journal of Physics D: Applied Physics*, vol. 24, no. 6, p. 997, 1991.
- [54] S. H. Shin, D. Y. Jeon, and K. S. Suh, "Emission band shift of the cathodoluminescence of  $\text{Y}_2\text{SiO}_5$ : Ce phosphor affected by its activator concentration," *Japanese Journal of Applied Physics*, vol. 40, no. 7R, p. 4715, 2001.
- [55] H. Jiao, F. Liao, S. Tian, and X. Jing, "Influence of Rare Earth Sc and La to the Luminescent Properties of FED Blue Phosphor  $\text{Y}_2\text{SiO}_5$ : Ce," *Journal of The Electrochemical Society*, vol. 151, no. 7, pp. J39-J42, 2004.
- [56] J. Wang, S. Tian, G. Li, F. Liao, and X. Jing, "Influence of Rare Earth Elements (Sc, La, Gd, and Lu) to the Luminescent Properties of FED Blue Phosphor  $\text{Y}_2\text{SiO}_5$ : Ce," *Journal of The Electrochemical Society*, vol. 148, no. 6, pp. H61-H66, 2001.
- [57] T. Aitasalo, J. Hölsä, M. Lastusaari, J. Niittykoski, and F. Pellé, "Delayed luminescence of  $\text{Ce}^{3+}$  doped  $\text{X}_1$  form of  $\text{Y}_2\text{SiO}_5$ ," *Optical Materials*, vol. 27, no.9, pp.1511-1515, 2005.
- [58] D. Cooke et al., "Luminescent properties and reduced dimensional behavior of hydrothermally prepared  $\text{Y}_2\text{SiO}_5$ : Ce nanophosphors," *Applied physics letters*, vol. 88, no. 10, p. 103108, 2006.
- [59] P. Dorenbos, "5d-level energies of  $\text{Ce}^{3+}$  and the crystalline environment. IV. Aluminates and "simple" oxides," *Journal of Luminescence*, vol.99, no.3, pp.283-299, 2002.
- [60] J. J.Chambers, "Reactions for yttrium silicate high-K dielectrics," 2000.

- [61] E.Coetsee, “Luminescent properties of  $Y_2SiO_5: Ce$  thin films,” University of the Free State, 2010.
- [62] R. G. Burns and R. G. Burns, Mineralogical applications of crystal field theory. Cambridge university press, 1993.
- [63] B. N. Figgis and M. A. Hitchman, Ligand field theory and its applications. Wiley-Vch New York, 2000.
- [64] J. Han, “Synthesis and luminescence properties of rare earth activated phosphors for near UV-emitting LEDs for efficacious generation of white light,” UC San Diego, 2013.
- [65] W.Carnall, G.Goodman, K.Rajnak, and R.Rana, “A systematic analysis of the spectra of the lanthanides doped into single crystal  $LaF_3$ ,” The Journal of Chemical Physics, vol.90, no.7, pp. 3443-3457, 1989.
- [66] O.Laporte and W.F.Meggers, “Some rules of spectral structure,” JOSA, vol. 11, no. 5, pp. 459-463, 1925.
- [67] M.Nazaraov, “Luminescence mechanism of highly efficient YAG and TAG,” Mold J Phys Sci, vol. 4, pp. 347-56, 2005.
- [68] H. N. Russell and F. A. Saunders, “New regularities in the spectra of the alkaline earths,” The Astrophysical Journal, vol. 61, p. 38, 1925.
- [69] L.B.Freund and S. Suresh, Thin film materials: stress, defect formation and surface evolution. Cambridge University Press, 2004.
- [70] O.Sneh, R.B.Clark-Phelps, A.R.Londergan, J.Winkler, and T.E.Seidel, “Thin film atomic layer deposition equipment for semiconductor processing,” Thin solid films, vol. 402, no. 1-2, pp. 248-261, 2002.
- [71] V.Pokropivny, R.Lohmus, I.Hussainova, A.Pokropivny, and S.Vlassov, Introduction to nanomaterials and nanotechnology. Tartu University Press Tartu, Estonia, 2007.
- [72] C.R. Kagan and P. Andry, Thin-film transistors. CRC Press, 2003.
- [73] K.S.Harsha, Principles of vapor deposition of thin films. Elsevier, 2005.
- [74] M.Ohring, Materials science of thin films. Elsevier, 2001.
- [75] J.Creighton and P.Ho, “Introduction to chemical vapor deposition (CVD),” Chemical vapor deposition, vol. 2, pp. 1-22, 2001.
- [76] K.Ostrikov, “Colloquium: Reactive plasmas as a versatile nanofabrication tool,” Reviews of modern physics, vol. 77, no. 2, p. 489, 2005.
- [77] R.W.Johnson, A.Hultqvist, and S. F.Bent, “A brief review of atomic layer deposition: from fundamentals to applications,” Materials today, vol. 17, no. 5, pp. 236-246, 2014.
- [78] S.Haukka and H.Huotari, “Method of producing thin films,” ed: Google Patents, 2009.
- [79] T. Schneller, R.Waser, M. Kosec, and D.Payne, Chemical solution deposition of functional oxide thin films. Springer, 2013.
- [80] J.Wen and G.L.Wilkes, “Organic/inorganic hybrid network materials by the solgel approach,” Chemistry of Materials, vol. 8, no. 8, pp. 1667-1681, 1996.
- [81] R.W.Kelsall, I.W.Hamley, and M.Geoghegan, Nanoscale science and technology. Wiley Online Library, 2005.
- [82] R.Behrisch, “Sputtering by particle bombardment Springer Verlag,” ed: Berlin-Heidelberg, 1981.
- [83] D.M.Mattox, Handbook of physical vapor deposition (PVD) processing. William Andrew, 2010.
- [84] D.M.Mattox, “The foundations of vacuum coating technology. 2003,” Norwich, NY: Noyes Publications/William Andrew Pub.
- [85] L.Huang et al., “Preparation of large-scale cupric oxide nanowires by thermal evaporation method,” Journal of Crystal Growth, vol.260, no. 1-2, pp.130-135, 2004.
- [86] X.Chen, J.Cheng, and X.Yin, “Advances and applications of electrohydrodynamics,” Chinese Science Bulletin, vol.48, no.11, pp.1055-1063, 2003.
- [87] S.M.Metev and V.P.Veiko, Laser-assisted microtechnology. Springer Science & Business Media, 2013.

- [88] P. Willmott and J. Huber, "Pulsed laser vaporization and deposition," *Reviews of Modern Physics*, vol.72, no.1, p.315, 2000.
- [89] D.B.Chrisey and G.K. Hubler, "Pulsed laser deposition of thin films," 1994.
- [90] M.R.Vaziri, F.Hajiesmaeilbaigi, and M.Maleki, "Microscopic description of the thermalization process during pulsed laser deposition of aluminium in the presence of argon background gas," *Journal of Physics D: Applied Physics*, vol. 43, no. 42, p. 425205, 2010.
- [91] T.Ohnishi, K. Shibuya, T.Yamamoto, and M. Lippmaa, "Defects and transport in complex oxide thin films," *Journal of Applied Physics*, vol.103, no. 10, p.103703, 2008.
- [92] J. Ferguson, G.Arikan, D. Dale, A. Woll, and J. Brock, "Measurements of surface diffusivity and coarsening during pulsed laser deposition," *Physical review letters*, vol. 103, no. 25, p. 256103, 2009.
- [93] G. Koster, B. L.Kropman, G.J.Rijnders, D.H. Blank, and H.Rogalla, "Quasi-ideal strontium titanate crystal surfaces through formation of strontium hydroxide," *Applied Physics Letters*, vol. 73, no. 20, pp. 2920-2922, 1998.
- [94] A. Ohtomo and H. Y. Hwang, "Growth mode control of the free carrier density in SrTiO<sub>3-δ</sub> films," *Journal of Applied Physics*, vol. 102, no. 8, p. 083704, 2007.
- [95] M. Lippmaa, N. Nakagawa, M. Kawasaki, S. Ohashi, and H. Koinuma, "Growth mode mapping of SrTiO<sub>3</sub> epitaxy," *Applied Physics Letters*, vol. 76, no. 17, pp. 2439-2441, 2000.
- [96] R. J. Tilley, *Crystals and crystal structures*. John Wiley & Sons, 2006.
- [97] C. Guozhong, *Nanostructures and nanomaterials: synthesis, properties and applications*. World scientific, 2004.
- [98] H. Agiwaan, "Thesis: Thermal Stability of cubic and nanocrystalline arc evaporated TiCrAlN coatings," 2014.
- [99] A. Jalaukhan, "Microstructure and Optoelectronics Characterizations of GaxSb1-x/GaAs Heterojunction," 2012.
- [100] S.Werta, O. Echendu, and F. Dejene, "Physico-chemical studies of Cd<sub>1-x</sub>Zn<sub>x</sub>S thin films produced by simple two-electrode electrodeposition system for solar cell application," *Journal of Materials Science: Materials in Electronics*, vol. 30, no. 6, pp. 6201-6211, 2019.
- [101] A.D.McNaught and A.D.McNaught, *Compendium of chemical terminology*. Blackwell Science Oxford, 1997.
- [102] N.G.Debelo, "Structural and luminescence properties of re doped fluoride and silicate phosphors," *University of the Free State (Qwaqwa Campus)*, 2017.
- [103] S.Agrawal and E. Kingsley, "High-intensity, persistent photoluminescent formulations and objects, and methods for creating the same," ed: Google Patents, 2011.
- [104] K. Mishra, S. K. Singh, A. K. Singh, M. Rai, B. K. Gupta, and S. B. Rai, "New perspective in garnet phosphor: low temperature synthesis, nanostructures, and observation of multimodal luminescence," *Inorganic chemistry*, vol. 53, no. 18, pp. 9561-9569, 2014.
- [105] W.M.Yen and H.Yamamoto, *Measurements of Phosphor Properties*. CRC Press, 2018.
- [106] M. Kira, F. Jahnke, and S. W. Koch, "Quantum theory of secondary emission in optically excited semiconductor quantum wells," *Physical review letters*, vol. 82, no. 17, p. 3544, 1999.
- [107] D.Abo-Kahla, M. Ahmed, and A. Makram-Allah, "Analytical solution of a three-level atom coupled to four systems of N-two-level atoms," *Optical Review*, vol. 26, no. 6, pp. 699-708, 2019.
- [108] H. Haug and S. W. Koch, *Quantum Theory of the Optical and Electronic Properties of Semiconductors: Fifth Edition*. World Scientific Publishing Company, 2009.
- [109] D.A.Skoog, F.J.Holler, and S.R.Crouch, *Principles of instrumental analysis*. Cengage learning, 2017.
- [110] H.-H. Perkampus, *UV-VIS Spectroscopy and its Applications*. Springer Science & Business Media, 2013.



- [111] P.J.Goodhew and J. Humphreys, *Electron microscopy and analysis*. CRC Press, 2000.
- [112] M. Walock, "Nanocomposite coatings based on quaternary metal-nitrogen and nanocarbon systems," 2012.
- [113] G.E.Lloyd, "Atomic number and crystallographic contrast images with the SEM: a review of backscattered electron techniques," *Mineralogical Magazine*, vol. 51, no. 359, pp. 3-19, 1987.
- [114] B.Cappella and G. Dietler, "Force-distance curves by atomic force microscopy," *Surface science reports*, vol. 34, no. 1-3, pp. 1-104, 1999.
- [115] N. Jalili and K. Laxminarayana, "A review of atomic force microscopy imaging systems: application to molecular metrology and biological sciences," *Mechatronics*, vol. 14, no. 8, pp. 907-945, 2004.
- [116] P.C.Braga and D.Ricci, *Atomic force microscopy: biomedical methods and applications*. Springer Science & Business Media, 2004.
- [117] P. Hansma et al., "Tapping mode atomic force microscopy in liquids," *Applied Physics Letters*, vol. 64, no. 13, pp. 1738-1740, 1994.
- [118] L. Gross, F. Mohn, N. Moll, P. Liljeroth, and G. Meyer, "The chemical structure of a molecule resolved by atomic force microscopy," *Science*, vol. 325, no. 5944, pp. 1110-1114, 2009.
- [119] C. E. Lyman et al., *Scanning electron microscopy, X-ray microanalysis, and analytical electron microscopy: a laboratory workbook*. Springer Science & Business Media, 2012.
- [120] J. P. Sibilila, *A guide to materials characterization and chemical analysis*. John Wiley & Sons, 1988.
- [121] R. Jenkins and J. L. De Vries, *Practical X-ray spectrometry*. Macmillan International Higher Education, 1970.
- [122] P. Taunk, R. Das, D. Bisen, R. Tamrakar, and N. Rathor, "Synthesis and optical properties of chemical bath deposited ZnO thin film," *Karbala International Journal of Modern Science*, vol. 1, no. 3, pp. 159-165, 2015.
- [123] M. Leskelä and M. Ritala, "Rare-earth oxide thin films as gate oxides in MOSFET transistors," *Journal of Solid State Chemistry*, vol. 171, no. 1-2, pp. 170-174, 2003.
- [124] X. Ouyang, A. Kitai, and R. Siegle, "Rare-earth-doped transparent yttrium silicate thin film phosphors for colour displays," *Thin Solid Films*, vol. 254, no. 1-2, pp. 268-272, 1995.
- [125] G. Blasse and B. Grabmaier, "Energy transfer," in *Luminescent Materials*: Springer, 1994, pp. 91-107.
- [126] B. D. Cullity and S. R. Stock, *Pearson New International Edition: Elements of X-Ray Diffraction*, 3<sup>rd</sup> ed. Printed in the United States of America: Pearson Education Limited 2014.
- [127] S. C. Singh, H. Zeng, C. Guo, and W. Cai, *Nanomaterials: processing and characterization with lasers*. John Wiley & Sons, 2012.
- [128] R. Eason, *Pulsed laser deposition of thin films: applications-led growth of functional materials*. John Wiley & Sons, 2007.
- [129] H. Huang and B. Yan, "In situ sol-gel composition of multicomponent hybrid precursors to luminescent novel unexpected microrod of Y<sub>2</sub>SiO<sub>5</sub>: Eu<sup>3+</sup> employing different silicate sources," *Solid state communications*, vol. 132, no. 11, pp. 773-777, 2004.
- [130] T. Böttger, C. Thiel, R. Cone, and Y. Sun, "Effects of magnetic field orientation on optical decoherence in Er<sup>3+</sup>: Y<sub>2</sub>SiO<sub>5</sub>," *Physical Review B*, vol. 79, no. 11, p. 115104, 2009.
- [131] B. Comaskey, G. Albrecht, R. Beach, B. Moran, and R. Solarz, "Flash-lamp-pumped laser operation of Nd<sup>3+</sup>: Y<sub>2</sub>SiO<sub>5</sub> at 1.074 μm," *Optics letters*, vol. 18, no. 23, pp. 2029-2031, 1993.
- [132] B. Lauritzen et al., "Telecommunication-wavelength solid-state memory at the single photon level," *Physical review letters*, vol. 104, no. 8, p. 080502, 2010.

- [133] Z. Cole et al., "Coherent integration of 0.5 GHz spectral holograms at 1536 nm using dynamic biphasic codes," *Applied Physics Letters*, vol. 81, no. 19, pp. 3525-3527, 2002.
- [134] Y. Ogura, M. Kondo, T. Morimoto, A. Notomi, and T. Sekigawa, "Oxygen permeability of  $\text{Y}_2\text{SiO}_5$ ," *Materials transactions*, vol. 42, no. 6, pp. 1124-1130, 2001.
- [135] H. M. O'Bryan, P. K. Gallagher, and G. Berkstresser, "Thermal expansion of  $\text{Y}_2\text{SiO}_5$  single crystals," *Journal of the American Ceramic Society*, vol. 71, no. 1, 1988.
- [136] M. Aparicio and A. Duran, "Yttrium silicate coatings for oxidation protection of carbon-silicon carbide composites," *Journal of the American Ceramic Society*, vol. 83, no. 6, pp. 1351-1355, 2000.
- [137] T. Minami, T. Miyata, S. Takata, and I. Fukuda, "High-luminance green  $\text{Zn}_2\text{SiO}_4$ : Mn thin-film electroluminescent devices using an insulating  $\text{BaTiO}_3$  ceramic sheet," *Japanese journal of applied physics*, vol. 30, no. 1B, p. L117, 1991.
- [138] J. Dolo et al., "The effect of oxygen pressure on the structure, morphology and photoluminescence intensity of pulsed laser deposited  $\text{Gd}_2\text{O}_2\text{S}:\text{Tb}^{3+}$  thin film phosphor," *Applied Physics A*, vol. 101, no. 4, pp. 655-659, 2010.
- [139] F. Dejene, M. Kebede, M. Redi-Abshiro, and B. Kgarebe, "Structural and photoluminescence properties of  $\text{Dy}^{3+}$  co-doped and  $\text{Eu}^{2+}$  activated  $\text{MAAl}_2\text{O}_4$  (M= Ba, Ca, Sr) nanophosphors," *Optical Materials*, vol. 35, no. 11, pp. 1927-1931, 2013.
- [140] J. Felsche, "The crystal chemistry of the rare-earth silicates," in *Rare earths*: Springer, 1973, pp. 99-197.
- [141] K. Liddell and D. Thompson, "X-ray diffraction data for yttrium silicates," *Trans. J. Br. Ceram. Soc.*, vol. 85, no. 1, pp. 17-22, 1986.
- [142] A. G. De Mesquita and A. Bril, "Preparation and cathodoluminescence of  $\text{Ce}^{3+}$ -activated yttrium silicates and some isostructural compounds," *Materials Research Bulletin*, vol. 4, no. 9, pp. 643-650, 1969.
- [143] M. Leskelä and J. Suikkanen, " $\text{Ce}^{3+}$ - and  $\text{Tb}^{3+}$ -activated rare earth oxyorthosilicates," *Journal of the Less common Metals*, vol. 112, no. 1-2, pp. 71-74, 1985.
- [144] J. Shmulovich, G. Berkstresser, C. Brandle, and A. Valentino, "Single-Crystal Rare-Earth-Doped Yttrium Orthosilicate Phosphors," *Journal of The Electrochemical Society*, vol. 135, no. 12, pp. 3141-3151, 1988.
- [145] A. Mostako and A. Khare, "Effect of target-substrate distance onto the nanostructured rhodium thin films via PLD technique," *Applied Nanoscience*, vol. 2, no. 3, pp. 189-193, 2012.
- [146] D. Nečas and P. Klapetek, "Gwyddion: an open-source software for SPM data analysis," *Open Physics*, vol. 10, no. 1, pp. 181-188, 2012.
- [147] Taylor and F. Group, *New Generation of Europium and Terbium Activated Phosphors from syntheses to applications*. U.S. : PAN STANFORD, 2012.
- [148] A. Kuznetsov, "Photoluminescence of cathodoluminophores with short afterglow," *Journal of Applied Spectroscopy*, vol. 20, no. 5, pp. 622-625, 1974.
- [149] D. Bimberg, D. Robbins, D. Wight, and J. Jeser, " $\text{CeP}_5\text{O}_{14}$ , a new ultrafast scintillator," *Applied Physics Letters*, vol. 27, no. 2, pp. 67-68, 1975.
- [150] X. Sun and H. S. Kwok, "Pulsed laser deposition of silicate phosphor thin films," *Applied Physics A*, vol. 69, no. 1, pp. S39-S43, 1999.
- [151] E. Zych, C. Brecher, A. Wojtowicz, and H. Lingertat, "Luminescence properties of Ce-activated YAG optical ceramic scintillator materials," *Journal of luminescence*, vol. 75, no. 3, pp. 193-203, 1997.
- [152] L. E. Shea, J. McKittrick, O. A. Lopez, and E. Sluzky, "Synthesis of red-emitting, small particle size luminescent oxides using an optimized combustion process," *Journal of the American Ceramic Society*, vol. 79, no. 12, pp. 3257-3265, 1996.
- [153] E. Coetsee, J. Terblans, O. Ntwaeaborwa, and H. Swart, "Luminescent mechanism of  $\text{Y}_2\text{SiO}_5$ : Ce phosphor powder," *Physica B: Condensed Matter*, vol. 404, no. 22, pp. 4426-4430, 2009.

- [154] L.Zheng et al., “Crystal growth and spectroscopic properties of praseodymium and cerium co-doped  $Y_2SiO_5$ ,” *Journal of Luminescence*, vol. 145, pp. 547-552, 2014.
- [155] J.Gonzalo, R.G.San Román, J.Perriere, C.N. Afonso, and R.P.Casero, “Pressure effects during pulsed-laser deposition of barium titanate thin films,” *Applied Physics A*, vol. 66, no. 5, pp. 487-491, 1998.
- [156] S.Yi, J.Bae, B.Moon, J.Jeong, I.Kim, and H.Park, “Photoluminescence behavior of pulsed laser deposited  $ZnGa_2O_4$  thin-film phosphors grown on various substrates,” *Applied Physics A*, vol.76, no.3, pp. 433-437, 2003.
- [157] S.Dlamini, H.Swart, J.Terblans, and O.Ntwaeaborwa, “The effect of different gas atmospheres on the structure, morphology and photoluminescence properties of pulsed laser deposited  $Y_3(Al, Ga)_5O_{12}: Ce^{3+}$  nano thin films,” *Solid State Sciences*, vol. 23, pp. 65-71, 2013.
- [158] P. Thiyagarajan, M. Kottaisamy, and M.R. Rao, “Structural and luminescence properties of pulsed laser deposited green-emitting  $Zn_2SiO_4: Mn$  phosphor thin films,” *Scripta materialia*, vol.57, no.5, pp.433-436, 2007.
- [159] S.Jones, D.Kumar, R.K.Singh, and P. Holloway, “Luminescence of pulsed laser deposited Eu doped yttrium oxide films,” *Applied physics letters*, vol. 71, no. 3, pp. 404-406, 1997.
- [160] J. Robertson, “Pulsed laser deposition of silicate phosphor thin films,” *Thin Solid Films*, vol. 141, pp.221-224, 1984.
- [161] N.Debelo, F.Dejene, and K.Roro, “Pulsed laser deposited  $KY_3F_{10}: Ho^{3+}$  thin films: Influence of target to substrate distance,” *Materials Chemistry and Physics*, vol.190, pp. 62-67, 2017.
- [162] S.A.-J.Jassim, A.A.R. A.Zumaila, and G.A.A.Al Waly, “Influence of substrate temperature on the structural, optical and electrical properties of CdS thin films deposited by thermal evaporation,” *Results in Physics*, vol. 3, pp. 173-178, 2013.
- [163] S. Proyer, E. Stangl, M. Borz, B. Hellebrand, and D. Bäuerle, “Particulates on pulsed-laser deposited YBaCuO films,” *Physica C: Superconductivity*, vol. 257, no. 1-2, pp. 1-15, 1996.
- [164] Y.Parganiha, J. Kaur, V.Dubey, and K.V.R.Murthy, “Near UV–blue emission from Ce doped  $Y_2SiO_5$  phosphor,” *Materials Science in Semiconductor Processing*, vol.31, pp.715–719, 2015.
- [165] X.Han et al., “Fabrication, patterning and luminescence properties of  $X_2Y_2SiO_5: A$  ( $A= Eu^{3+}, Tb^{3+}, Ce^{3+}$ ) phosphor films via sol–gel soft lithography,” *Solid state sciences*, vol. 6, no. 4, pp. 349-355, 2004.
- [166] J.Wang, J.H. Hao, and P.A. Tanner, “Persistent luminescence upconversion for  $Er_2O_3$  under 975 nm excitation in vacuum,” *Journal of Luminescence*, vol. 164, pp. 116-122, 2015.
- [167] G.Ju, Y.Hu, L.Chen, and X.Wang, “Persistent luminescence and its mechanism of  $Ba_5(PO_4)_3Cl: Ce^{3+}, Eu^{2+}$ ,” *Journal of Applied Physics*, vol. 111, no. 11, p. 113508, 2012.
- [168] K.Tshabalala et al., “Luminescent properties and X-ray photoelectron spectroscopy study of  $ZnAl_2O_4: Ce^{3+}, Tb^{3+}$  phosphor,” *Journal of Alloys and Compounds*, vol. 509, no. 41, pp. 10115-10120, 2011.
- [169] W.M.Yen and H.Yamamoto, *Practical applications of phosphors*. CRC press, 2018.
- [170] K.N.Shinde, S.Dhoble, H.Swart, and K.Park, *Phosphate phosphors for solid-state lighting*. Springer Science & Business Media, 2012.
- [171] B.C.G.G.Blasse, *Luminescent Materials*. Springer. VerJag Berlin Heidelberg 1994.
- [172] H.Q.Wang, M.Batentschuk, A.Osvet, L.Pinna, and C. J. Brabec, “Rare-earth ion doped up-conversion materials for photovoltaic applications,” *Advanced Materials*, vol. 23, no. 22-23, pp. 2675-2680, 2011.
- [173] A.J.Khimani, S.H.Chaki, S.M.Chauhan, A.V.Mangrola, R.R.Meena, and M.Deshpande, “Synthesis, characterization, antimicrobial and antioxidant study of the facile

- sonochemically synthesized SnS<sub>2</sub> nanoparticles,” *Nano-Structures & Nano-Objects*, vol. 18, p. 100286, 2019.
- [174] M. N. Ashfold, F. Claeysens, G.M. Fuge, and S.J. Henley, “Pulsed laser ablation and deposition of thin films,” *Chemical Society Reviews*, vol. 33, no. 1, pp. 23-31, 2004.
- [175] H. Haile and F. Dejene, “Effect of target to substrate distance on the material properties of the Y<sub>2</sub>SiO<sub>5</sub>: Ce<sup>3+</sup> thin film by pulsed laser deposition,” *Applied Physics A*, vol. 125, no. 3, p. 172, 2019.
- [176] Y. Parganiha, J. Kaur, V. Dubey, and K. Murthy, “Near UV–blue emission from Ce doped Y<sub>2</sub>SiO<sub>5</sub> phosphor,” *Materials Science in Semiconductor Processing*, vol. 31, pp. 715-719, 2015.
- [177] G. Ramakrishna, H. Nagabhushana, D. Sunitha, S. Prashantha, S. Sharma, and B. Nagabhushana, “Effect of different fuels on structural, photo and thermo luminescence properties of solution combustion prepared Y<sub>2</sub>SiO<sub>5</sub> nanopowders,” *Spectrochimica Acta Part A: Molecular and Biomolecular Spectroscopy*, vol. 127, pp. 177-184, 2014.
- [178] A. Bos, “High sensitivity thermoluminescence dosimetry,” *Nuclear Instruments and Methods in Physics Research Section B: Beam Interactions with Materials and Atoms*, vol. 184, no. 1-2, pp. 3-28, 2001.
- [179] J. Azorin, G. González, A. Gutiérrez, and R. Salvi, “Preparation and dosimetric properties of a highly sensitive CaSO<sub>4</sub>: Dy thermoluminescent dosimeter,” *Health physics*, vol. 46, no. 2, pp. 269-274, 1984.
- [180] A. Monshi, M. R. Foroughi, and M. R. Monshi, “Modified Scherrer equation to estimate more accurately nano-crystallite size using XRD,” *World journal of nano science and engineering*, vol. 2, no. 3, pp. 154-160, 2012.
- [181] G. Socol et al., “Pulsed laser deposition of transparent conductive oxide thin films on flexible substrates,” *Applied surface science*, vol. 260, pp. 42-46, 2012.
- [182] A. J. Khimani, S. H. Chaki, S. M. Chauhan, and M. Deshpande, “Influence of deposition techniques on quality and photodetection properties of tin disulfide (SnS<sub>2</sub>) thin films,” *Journal of Materials Science: Materials in Electronics*, vol. 30, no. 14, pp. 13118-13133, 2019.
- [183] Z. Zhang et al., “Effects of oxygen pressures on pulsed laser deposition of ZnO films,” *Physica E: Low-dimensional Systems and Nanostructures*, vol. 39, no. 2, pp. 253-257, 2007.
- [184] A. Bailini, P. Ossi, and A. Rivolta, “Plume propagation through a buffer gas and cluster size prediction,” *Applied surface science*, vol. 253, no. 19, pp. 7682-7685, 2007.
- [185] S.S. Kim and B.-T. Lee, “Effects of oxygen pressure on the growth of pulsed laser deposited ZnO films on Si (001),” *Thin Solid Films*, vol. 446, no. 2, pp. 307-312, 2004.
- [186] R.P. Scott, “Measuring the thickness of thin metal films,” Brigham Young University–Idaho, 2012.
- [187] J. Tauc, R. Grigorovici, and A. Vancu, “Optical properties and electronic structure of amorphous germanium,” *physica status solidi (b)*, vol. 15, no. 2, pp. 627-637, 1966.
- [188] G. F. Neumark, I. L. Kuskovsky, and H. Jiang, *Wide bandgap light emitting materials and devices*. Wiley Online Library, 2007.
- [189] Y.C. Kang, I.W. Lenggoro, S.B. Park, and K. Okuyama, “Y<sub>2</sub>SiO<sub>5</sub>: Ce phosphor particles 0.5–1.4 μm in size with spherical morphology,” *Journal of Solid State Chemistry*, vol. 146, no. 1, pp. 168-175, 1999.
- [190] Y. Wang et al., “Luminescence of Ce<sup>3+</sup> activated NaCaPO<sub>4</sub> under VUV–UV and X-ray excitation,” *Optical Materials*, vol. 34, no. 7, pp. 1214-1218, 2012.
- [191] T.A. O’Brien, P.D. Rack, P.H. Holloway, and M.C. Zerner, “Crystal field and molecular orbital calculation of the optical transitions in Ce doped alkaline earth sulfide (MgS, CaS, SrS, and BaS) phosphors,” *Journal of luminescence*, vol. 78, no. 4, pp. 245-257, 1998.

- [192] J.-S. Bae, K.-S. Shim, S. Kim, J.-H. Jeong, S.-S. Yi, and J. Park, "Photoluminescence characteristics of pulsed laser deposited  $Y_{2-x}Gd_xO_3: Eu^{3+}$  thin film phosphors," *Journal of crystal growth*, vol. 264, no. 1-3, pp. 290-296, 2004.
- [193] A.V.Bulgakov, "Mass spectrometric study of gas-phase oxidation reactions during laser ablation of YBaCuO," in *Laser-Induced Thin Film Processing*, 1995, vol. 2403, pp. 75-87: International Society for Optics and Photonics.
- [194] G.Blasse and B.Grabmaier, "A general introduction to luminescent materials," in *Luminescent materials*: Springer, 1994, pp. 1-9.
- [195] R.Chen and Y.Kirsh, *The analysis of thermally stimulated processes*. Elsevier, 2013.
- [196] R.Chen, "Glow curves with general order kinetics," *Journal of the electrochemical society*, vol. 116, no. 9, pp. 1254-1257, 1969.
- [197] R. Chen and Y. Kirsh, "Analyses of Thermally Stimulated Processes," ed: Pergamon Press, 1981.
- [198] D. Shenker and R. Chen, "Numerical curve fitting of general order kinetics glow peaks," *Journal of Physics D: Applied Physics*, vol. 4, no. 2, p. 287, 1971.
- [199] P. Kivits and H. Hagebeuk, "Evaluation of the model for thermally stimulated luminescence and conductivity; reliability of trap depth determinations," *Journal of Luminescence*, vol. 15, no. 1, pp. 1-27, 1977.
- [200] S. Shionoya, W. M. Yen, and H. Yamamoto, *Phosphor handbook*. CRC press, 2018.
- [201] G. Blasse, "Scintillator materials," *Chemistry of Materials*, vol. 6, no. 9, pp. 1465-1475, 1994.
- [202] T. Jüstel and H. Nikol, "Optimization of luminescent materials for plasma display panels," *Advanced Materials*, vol. 12, no. 7, pp. 527-530, 2000.
- [203] H. Tanno, S. Zhang, T. Shinoda, and H. Kajiyama, "Characteristics of photoluminescence, thermoluminescence and thermal degradation in Eu-doped  $BaMgAl_{10}O_{17}$  and  $SrMgAl_{10}O_{17}$ ," *Journal of luminescence*, vol. 130, no. 1, pp. 82-86, 2010.
- [204] J. Reichardt, M. Stiebler, R. Hirtle, and S. Kemmler-Sack, "Cathodo-and Photoluminescence in Oxyorthosilicates of  $X_1$  and  $X_2$  Type: System  $Y_{2-x}Gd_xSiO_5: Tb^{3+}$ ," *physica status solidi (a)*, vol. 119, no. 2, pp. 631-642, 1990.
- [205] J.Wang, S.Tian, G.Li, F.Liao, and X.Jing, "Preparation and X-ray characterization of low-temperature phases of  $R_2SiO_5$  (R= rare earth elements)," *Materials research bulletin*, vol.36, no. 10, pp.1855-1861, 2001.
- [206] Y.Liu, C.Xu, H.Chen, and H.Tateyama, "Influence of calcining temperature on photoluminescence and thermal quenching in europium-doped  $Y_2SiO_5$  using the MOD process," *Journal of luminescence*, vol.97, no.2, pp.135-140, 2002.
- [207] A.Gupta, "Gas-phase oxidation chemistry during pulsed laser deposition of  $YBa_2Cu_3O_{7-\delta}$  films," *Journal of applied physics*, vol. 73, no. 11, pp. 7877-7886, 1993.
- [208] S. Bharadwaja and S. Krupanidhi, "Growth and study of antiferroelectric lead zirconate thin films by pulsed laser ablation," *Journal of applied physics*, vol. 86, no. 10, pp. 5862-5869, 1999.
- [209] T.Nakamura, Y.Yamanaka, A.Morimoto, and T.Shimizu, "Effect of oxygen pressure on  $(Ba_xSr_{1-x})TiO_3$  thin films by pulsed laser ablation," *Japanese journal of applied physics*, vol.34, no. 9S, p. 5150, 1995.
- [210] Y.Ding, J.Wu, Z.Meng, H.Chan, and Z.Choy, "Oxygen pressure dependence of structural and tunable properties of PLD-deposited  $Ba_{0.5}Sr_{0.5}TiO_3$  thin film on  $LaAlO_3$ -substrate," *Materials chemistry and physics*, vol.75, no.1-3, pp. 220-224, 2002.
- [211] J. Han, G.Hirata, J.Talbot, and J.McKittrick, "Luminescence enhancement of  $Y_2O_3:Eu^{3+}$  and  $Y_2SiO_5: Ce^{3+}, Tb^{3+}$  core particles with  $SiO_2$  shells," *Materials Science and Engineering: B*, vol. 176, no.5, pp.436-441, 2011.
- [212] L.Muresan, B.Oprea, A.Cadis, I.Perhaita, and O.Ponta, "Studies on  $Y_2SiO_5: Ce$  phosphors prepared by gel combustion using new fuels," *Journal of alloys and compounds*, vol.615, pp.795-803, 2014.

- [213] U.Holzwarth and N. Gibson, "The Scherrer equation versus the 'Debye-Scherrer equation'," *Nature nanotechnology*, vol. 6, no. 9, pp. 534-534, 2011.
- [214] P.Vandenabeele, *Practical Raman spectroscopy: an introduction*. John Wiley & Sons, 2013.
- [215] J.Gonzalo, R.G.San Román, J.Perriere, C.Afonso, and R.P.Casero, "Pressure effects during pulsed-laser deposition of barium titanate thin films," *Applied Physics A*, vol.66, no.5, pp.487-491, 1998.
- [216] M.Liu et al., "The effect of nitrogen pressure on the two-step method deposition of GaN films," *Applied Physics A*, vol. 85, no. 1, pp. 83-86, 2006.
- [217] L.-C. Lin and L. Chen, "Particulates generated by pulsed laser ablation," *Pulsed Laser Deposition of thin films*, pp. 167-198, 1994.
- [218] A.Kisiel, "Synchrotron Methods of the Conduction Band Electronic Structure Analysis," *Acta Physica Polonica-Series A General Physics*, vol.114, no.2, p.287, 2008.
- [219] A. Abdelghany, E. Abdelrazek, S. Badr, and M. Morsi, "Effect of gamma-irradiation on (PEO/PVP)/Au nanocomposite: materials for electrochemical and optical applications," *Materials & Design*, vol. 97, pp. 532-543, 2016.
- [220] S.Rotman and C.Warde, "Defect luminescence in cerium-doped yttrium aluminum garnet," *Journal of applied physics*, vol. 58, no. 1, pp. 522-525, 1985.
- [221] K. Cho, D. Kumar, S. Jones, D. Lee, P. Holloway, and R. K. Singh, "Growth and Characterization of Eu: Y<sub>2</sub>O<sub>3</sub> Thin-Film Phosphors on Silicon and Diamond-Coated Silicon Substrates," *Journal of the Electrochemical Society*, vol.145, no.10, pp.3456-3462, 1998.
- [222] K.A. Gschneidner, J.-C.G. Bunzli, and V.K.Pecharsky, *Handbook on the physics and chemistry of rare earths: optical spectroscopy*. Elsevier, 2011.
- [223] G. Blasse and A. Bril, "Investigation of some Ce<sup>3+</sup>-activated phosphors," *The journal of chemical physics*, vol. 47, no. 12, pp. 5139-5145, 1967.
- [224] L. Muresan, M. Ayvacikli, J. G. Guinea, A. Canimoglu, Y.Karabulut, and N.Can, "Preparation and characterization of Yttrium based luminescence phosphors," *Optical Materials*, vol. 74, pp. 150-158, 2017.
- [225] P. Saadatkia, C.Varney, and F.Selim, "Trap Level Measurements in Wide Band Gap Materials by Thermoluminescence," *Luminescence-An Outlook on the Phenomena and their Applications*, 2016.
- [226] Y.Chen, C.Shi, and G.Hu, "Influence of Sb doping on the luminescent properties of PbWO<sub>4</sub> single crystals," *Journal of Applied Physics*, vol. 87, no.3, pp. 1503-1506, 2000.
- [227] C.Cannas et al., "Advances in the structure and microstructure determination of yttrium silicates using the Rietveld method," *Journal of Solid State Chemistry*, vol.178, no.5, pp.1526-1532, 2005.
- [228] E.Bosze, J.McKittrick, and G.Hirata, "Investigation of the physical properties of a blue-emitting phosphor produced using a rapid exothermic reaction," *Materials Science and Engineering: B*, vol. 97, no. 3, pp. 265-274, 2003.
- [229] Y.-Q. Wang, J.-F. Huang, L.-Y.Cao, and X.-R. Zeng, "Direct Preparation of Y<sub>2</sub>SiO<sub>5</sub> Nanocrystallites by a Microwave Hydrothermal Process," *ISRN Nanotechnology*, vol. 2011, 2011.
- [230] L. Xiujian, J. Huan, W. Xiaoming, Z. Zhengzhi, and J. Xiping, "Y<sub>2</sub>SiO<sub>5</sub>: Ce<sup>3+</sup> particle growth during sol-gel preparation," *Journal of Rare Earths*, vol.28, no.4, pp.504-508, 2010.
- [231] H.-S. Kang, Y.-C. Kang, H.-D. Park, and Y.-G. Shul, "Green-emitting yttrium silicate phosphor particles prepared by large scale ultrasonic spray pyrolysis," *Korean Journal of Chemical Engineering*, vol.20, no.5, pp. 930-933, 2003.
- [232] H. Jiao, X. Wang, S.Ye, and X.Jing, "Morphology of Gd<sup>3+</sup>-doped Y<sub>2</sub>SiO<sub>5</sub>: Ce," *Journal of luminescence*, vol. 122, pp. 113-116, 2007.

- [233] P. Korir and F. Dejene, "The effect of deposition time on the structural, morphological and luminescence properties of  $Y_2O_3: Eu^{3+}$  thin films prepared by pulsed laser deposition," *Applied Physics A*, vol. 124, no. 5, p.356, 2018.
- [234] K.S.Cho, N.-M. Park, T.-Y. Kim, K.-H. Kim, G.Y.Sung, and J. H. Shin, "High efficiency visible electroluminescence from silicon nanocrystals embedded in silicon nitride using a transparent doping layer," *Applied Physics Letters*, vol. 86, no. 7, p. 071909, 2005.
- [235] Y.Nakanishi, H. Wada, H. Kominami, M. Kottaisamy, T. Aoki, and Y. Hatanaka, "Growth and characterization of  $Y_2O_3: Tm$  thin-film blue-emitting phosphor," *Journal of the Electrochemical Society*, vol. 146, no. 11, p. 4320, 1999.
- [236] A. Patterson, "The Scherrer formula for X-ray particle size determination," *Physical review*, vol. 56, no. 10, p. 978, 1939.
- [237] J.G. Grasselli and B. J. Bulkin, *Analytical raman spectroscopy*. 1991.
- [238] H. Suzuki, T.Tombrello, C.Melcher, and J.Schweitzer, "UV and gamma-ray excited luminescence of cerium-doped rare-earth oxyorthosilicates," *Nuclear Instruments and Methods in Physics Research Section A: Accelerators, Spectrometers, Detectors and Associated Equipment*, vol.320, no.1-2, pp.263-272, 1992.
- [239] L.Pidol, O.Guillot-Noël, A.Kahn-Harari, B.Viana, D.Pelenc, and D.Gourier, "EPR study of  $Ce^{3+}$  ions in lutetium silicate scintillators  $Lu_2Si_2O_7$  and  $Lu_2SiO_5$ ," *Journal of Physics and Chemistry of Solids*, vol.67, no.4, pp.643-650, 2006.
- [240] R.Reisfeld and C.K.Jorgensen, *Lasers and excited states of rare earths*. Springer Science & Business Media, 2012.
- [241] F.-h.Kan, *Optical and spectroscopic properties of glass*. 1992.
- [242] W.Zhu, *Vacuum microelectronics*. John Wiley & Sons, 2001.
- [243] S.-h.Park, J.-h.Gwak, Y.-w. Jin, V.Vorobyov, and E.Morozov, "Yttrium silicate based phosphor having effective emission at low voltages and method for synthesizing the same," ed: Google Patents, 2003.
- [244] X.Ouyang, A.Kitai, and T.Xiao, "Electroluminescence of the oxide thin film phosphors  $Zn_2SiO_4$  and  $Y_2SiO_5$ ," *Journal of applied physics*, vol. 79, no. 6, pp. 3229-3234, 1996.
- [245] H.Huang and B.Yan, "Sol-gel preparation and luminescence properties of nanophosphors  $Y_{2-x}Tb_xSiO_5$  derived from in situ assembling hybrid precursors," *Journal of non-crystalline solids*, vol. 351, no.6-7, pp.618-621, 2005.
- [246] K.Patil, *Chemistry of nanocrystalline oxide materials: combustion synthesis, properties and applications*. World Scientific, 2008.
- [247] D.Geng, M.Shang, Y.Zhang, H.Lian, Z.Cheng, and J.Lin, "Tunable luminescence and energy transfer properties of  $Ca_5(PO_4)_2SiO_4: Ce^{3+}/Tb^{3+}/Mn^{2+}$  phosphors," *Journal of Materials Chemistry C*, vol. 1, no. 12, pp. 2345-2353, 2013.
- [248] A.Fasasi, F.Balogun, M.Fasasi, P.Ogunleye, C.Mokobia, and E.Inyang, "Thermoluminescence properties of barium titanate prepared by solid-state reaction," *Sensors and Actuators A: Physical*, vol.135, no.2, pp.598-604, 2007.
- [249] R.Chen, "Glow curves with general order kinetics," *Journal of the electrochemical society*, vol. 116, no. 9, p.1254, 1969.